

# An engineering characterisation of shaken bioreactors: flow, mixing and suspension dynamics

Gregorio Rodriguez

A thesis submitted for the degree of  
Engineering Doctorate

The Advanced Centre for Biochemical Engineering  
Department of Biochemical Engineering  
University College London



**UCL ENGINEERING**  
Change the world

June 2016



I, Gregorio Rodriguez confirm that the work presented in this thesis is my own.  
Where information has been derived from other sources, I confirm that this has  
been indicated in the thesis.

Signed,

*For my family.*

## Abstract

The thesis describes an experimental investigation of the flow, mixing and suspension dynamics in cylindrical orbitally shaken bioreactors (OSRs). Amongst the plethora of bioreactor types and geometries available for cell culture, the OSR is ubiquitous in bioprocess research and development. Offering a well defined liquid-gas interface, high throughput potential and experimental flexibility, it is the vessel of choice in early bioprocess research, either as microtiter-plates, Erlenmeyer flasks or other geometries. Despite recent advances in the field, an accurate and exhaustive engineering characterisation of OSRs from this point of view is lacking. In the present study a mixing time estimation methodology is developed and employed to assess the effect of operational parameters on the mixing of cylindrical OSRs. Particle Image Velocimetry measurements are carried out to evaluate the effect of vessel geometry modifications on the flow. Laser Induced Fluorescence is used to produce accurate description of the micro-mixing. Solid suspension studies are also undertaken to assess potential strategies to improve microcarrier culture in OSRs.

Accurate determination of the mixing time in OSRs is essential for the optimisation of mixing processes and minimization of concentration gradients that can be deleterious to cell cultures. The Dual Indicator System for Mixing Time (DISMT) is employed, together with a purposely built image processing code to objectively measure mixing

times in cylindrical and Erlenmeyer flask bioreactors. Relevant data acquisition aspects to optimise the accuracy of DISMT measurements are discussed in detail, with direct comparison of different mixing time measurement methodologies, including DISMT, pH probe and iodine-thiosulfate decolourisation results obtained in two types of stirred reactors.

The DISMT is employed to determine mixing characteristics of OSRs at different flow conditions and develop an effective feeding strategy, by evaluating the effect of the position of the feed at different radial locations in the vessel. At low  $Fr$  the flow presents a toroidal vortex below the free surface, which controls mass transport process across the entire vessel and defines two distinct regions in and outside of the vortex exhibiting different mixing rate. At higher  $Fr$  the axial flow enhances the mixing of the fluid located next to the wall as the mean flow transition to axial flow coincides with a regime flow transition and onset of turbulence fluctuations. By controlling the locations of feed addition, the flow characteristics can be exploited to enhance initial distribution of the added liquid and decrease the time required to reach homogeneity. The mixing number is highly dependent on the position of the feeding pipe. Insertion close to the vessel walls, and in the periphery of the toroidal vortex, where local shear stresses and deformation rates are highest, were found to significantly enhance mixing.

In order to provide an effective scaling methodology, the results obtained in OSRs are compared with data previously reported in the literature for both cylindrical reactors and Erlenmeyer flasks. The employment of a critical Froude number shows promise for the es-

establishment of a scaling law for mixing time across various types and sizes of shaken bioreactors.

The flow dynamics in cylindrical shaken bioreactors of different conical bottom geometries (inward facing) is investigated by means of phase-resolved Particle Image Velocimetry. The cylindrical bioreactor with a conical bottom geometry is selected to assess its potential application in three-dimensional cultures, and improve solid suspension in shaken systems. The effects of conical shaped bottoms of different heights on the fluid flow are evaluated for different operating conditions with water being the working fluid. The results provide evidence that the presence of the conical bottom affects the transition from laminar to turbulent flow, increases the vorticity and generates shear stresses at well defined locations.

The increased kinetic energy content measured with PIV in cylindrical OSRs with a conical bottom is found to effectively enhance solid suspension in microcarrier or embryod body cell culture. The dynamics of solid suspension is studied using commercially available Cytodex-3, stained with trypan blue for improved visual contrast and image acquisition. The presence of the conical bottom improves solid suspension by requiring lower agitation rates for the microcarriers to lift from the bottom completely. The critical Froude, which determines the flow type controlling the bioreactor, can also be used to scale the suspension of microcarriers in OSRs.

Full characterisation of macro- and micro- mixing scales in OSRs for highly viscous is obtained by DIMST and pLIF, respectively. This data also provides an effective visualisation of the flow structures con-

trolling the bioreactor transport processes.

The mixing characteristics of high viscosity fluids in OSRs are investigated by means of DISMT and pLIF, for the macro- and micro-scales of mixing, respectively. Fluids of viscosities 2-14 times that of water, exhibit flow characteristics different to those observed at  $\nu=10^{-6}\text{m}^2\text{s}^{-1}$ . A toroidal vortex, similar to that observed in water, is present at low  $Fr$ . Small increments of agitation rate provide transition to other flow structures, never reported in the literature. The pLIF measurements allow to characterise the small scale features of the flow not observable from phase averaged PIV, and visualise well defined elongation and striation dynamics for different regimes.

Although extensively used, OSRs are yet to be fully characterised. Further research is required on the hydrodynamic phenomena dominating orbitally shaking vessels, to enable the development of scale-up platform to simplify and speed progress from cell line development to industrial production of bio-products. The development of the scale-up platform must be made considering the advantages and requirements of single-use technology, to provide the industry with robust and reproducible scale-up model.

## Acknowledgements

I would like to acknowledge the precious help of my two supervisors, Dr. Micheletti and Dr. Ducci for their expert guidance and constant encouragement throughout the period of the Engineering Doctorate. They have provided me with invaluable support in fulfilling the requirements of this degree, accessing the appropriate sources of information, empowering me to take control of the direction of my research and being supportive in addressing issues arising throughout the EngD.

I also must acknowledge the expert help of Prof. Yianneskis in presenting my work to the scientific community and Dr. Balabani for making important equipment available to me.

The results of this research would not have been as impactful if it were not for the collaboration and exchange of knowledge with other PhD students, namely Weheliye, Irene and Francesco, with whom I have shared equipment and supervisors, faced problems and engineered solutions together.

In the quest of completing the task of this research I have been accompanied by fellow students and friends that have supported me in a variety of ways, ranging from equipment training to shared jokes. Amongst these I wish to include the various generations of the Cloisters office, from the old guard Anand, Alex T and S, Matthew, Georgina

to the young newcomers, Asma, Billy, Elisabetta, Jasmin, Joe, Lara, Rachel, Roberto, Thomas. Friendly support has also come from the old friends on the Strand, Andreas, Dimitris, Joao, Neil, Hugo and Angela. On this front I must again thank Martina and Andrea for not only guiding me academically but also becoming my friends. A research degree is, inevitably, the summation of the experiences, difficulties and joys that occur during its course and in this regard I must mention Nicola, Viola, Sissi, Alessandro, Greta, Luca and Sole.

Finally and most importantly, I am indebted to my family for their trust and endless support throughout my studies. My mother and father have been an example of dedication and commitment in completing the task at hand. My siblings have always provided me with the confidence I needed. C, C, S and C know that they represent for me the inspiration for more beautiful things, the ambition to academic excellence, the ambition to dutiful and enthusiastic persistence and the love for life.

My research has been funded by the Engineering and Physical Sciences Research Council (EPSRC), for whose support I am most grateful. I also wish to thank my industrial sponsor, Kühner AG, for providing equipment and financial support for the completion of this work.

# Contents

<b>Abstract</b>	<b>v</b>
<b>Acknowledgements</b>	<b>ix</b>
<b>Table of Contents</b>	<b>xv</b>
<b>Nomenclature</b>	<b>xvi</b>
<b>List of Tables</b>	<b>xxii</b>
<b>List of Figures</b>	<b>xxiii</b>
<b>1 Introduction</b>	<b>1</b>
1.1 Background . . . . .	1
1.2 Literature review . . . . .	5
1.3 Flow dynamics . . . . .	5
1.3.1 Power consumption . . . . .	7
1.3.2 Flow characterisation and transition . . . . .	10
1.3.3 Flow in fluids of high viscosity . . . . .	14
1.3.4 Vessel geometry fluid mixing enhancement . . . . .	15
1.4 Mixing Time . . . . .	15
1.5 Mechanical stress in OSRs and effects on cell culture . . . . .	20
1.6 Solid suspension . . . . .	22

1.6.1	Engineering aspects of microcarrier culture . . . . .	23
1.7	Main Findings . . . . .	26
1.8	Aims and objectives . . . . .	29
1.9	Thesis outline . . . . .	30
<b>2</b>	<b>Methodology</b>	<b>32</b>
2.1	Introduction . . . . .	32
2.2	Bioreactor vessels . . . . .	33
2.2.1	OSR Vessel v.1 . . . . .	33
2.2.2	Feed insertion rig . . . . .	33
2.2.3	OSR Vessel v.2 . . . . .	34
2.2.4	Shaken platform . . . . .	35
2.2.5	Other bioreactors used . . . . .	36
2.3	Mixing Time experiments . . . . .	37
2.3.1	Iodine-Thiosulfate decolourisation . . . . .	37
2.3.2	Water blue Dye . . . . .	37
2.3.3	pH Meter . . . . .	38
2.3.4	Dual Indicator System for Mixing Time . . . . .	38
2.3.5	Experimental rig . . . . .	39
2.3.6	Experimental conditions . . . . .	41
2.4	Solids suspension . . . . .	42
2.5	Particle Image Velocimetry . . . . .	44
2.5.1	PIV Introduction . . . . .	44
2.5.2	PIV experimental setup . . . . .	45
2.5.3	Selection of PIV software and analysis parameters . . . . .	47
2.6	Planar Induced Fluorescence . . . . .	49
2.6.1	Combined pLIF and PIV experimental set up . . . . .	49
2.7	Concluding Remarks . . . . .	50

<b>3</b>	<b>Mixing time methodology development and mixing time in low viscosity fluids</b>	<b>69</b>
3.1	Introduction . . . . .	69
3.2	Image processing code development . . . . .	71
3.2.1	Comparison between RGB and HSV colour model . . . . .	72
3.2.2	Mixing time code I: pixel by pixel maps . . . . .	74
3.2.3	Mixing time code II: interrogation box and normalisation . . . . .	75
3.2.4	Mixing time code III: Standard deviation and mixed pixel occurrence . . . . .	76
3.3	Experimental reproducibility of DISMT . . . . .	78
3.3.1	Appraisal of different methodologies for the determination of mixing time . . . . .	78
3.3.2	Definition of mixing criterion . . . . .	80
3.3.3	Validation of DISMT with pH probe in STRs . . . . .	81
3.4	Flow visualisation with DISMT . . . . .	83
3.4.1	Mixing Maps . . . . .	84
3.4.2	Path of fluid parcel in the flow . . . . .	85
3.5	Mixing Transients . . . . .	87
3.6	Mixing time in OSRs . . . . .	88
3.6.1	Mixing time in OSRs at different feed insertion locations . . . . .	89
3.6.2	Mixing time in OSRs at different fill volumes . . . . .	91
3.6.3	Mixing time in OSRs at different internal diameters . . . . .	92
3.7	Mixing time scaling . . . . .	93
3.7.1	Mixing cylindrical OSRs and Erlenmeyer flasks . . . . .	93
3.7.2	Mixing scale-up in OSRs . . . . .	94
3.8	Concluding Remarks . . . . .	97
<b>4</b>	<b>Fluid flow and solid suspension in cylindrical OSRs with conical</b>	

<b>bottoms</b>	<b>128</b>
4.1 Introduction . . . . .	128
4.2 Effects of conical bottom on fluid flow . . . . .	130
4.2.1 Effects of bottom design on flow dynamics and vorticity . .	130
4.2.2 Effects of bottom design on shear rates . . . . .	133
4.2.3 Effects of bottom design on local flow direction . . . . .	137
4.2.4 Effects of bottom design on energy content . . . . .	139
4.3 Solid Suspension . . . . .	140
4.3.1 Effect of orbital diameter on solid suspension . . . . .	142
4.3.2 Effect of vessel bottom geometry on solid suspension . . .	143
4.3.3 Scaling of solid suspension mechanism . . . . .	145
4.4 Concluding Remarks . . . . .	147
<b>5 Flow and mixing dynamics in fluids of high viscosity</b>	<b>175</b>
5.1 Introduction . . . . .	175
5.2 Mixing dynamics in highly viscous fluids . . . . .	177
5.2.1 Effects of fluid viscosity on mixing time . . . . .	181
5.2.2 Caverns in toroidal vortex flows . . . . .	182
5.2.3 Segregated mixing time . . . . .	184
5.2.4 Diffusion coefficient . . . . .	185
5.3 Micro-mixing of highly viscous fluids . . . . .	187
5.3.1 Material line elongation of Rhodamine dye . . . . .	191
5.4 Concluding Remarks . . . . .	194
<b>6 Conclusions and recommendations for future work</b>	<b>224</b>
6.1 The present contribution . . . . .	224
6.2 Main findings of the investigation . . . . .	227
6.3 Recommendations for future work . . . . .	230

Appendices	233
A DISMT experimental procedure	233
References	235

# Nomenclature

## Abbreviations

AFT After Flow Transition

3D Three-Dimensional

2D Two-Dimensional

BFT Before Flow Transition

BHK Baby Hamster Kidney

hMSC Human Mesenchymal Stem Cells

CFD Computational Fluid Dynamics

DISMT Dual Indicator System for Mixing Time

HSV 3D colour space representation

LHS Left hand side

OSR Orbital Shaker Reactor

pLIF	planar Induced Fluorescence
PIV	Particle Image Velocimetry
RGB	Red Green Blue space representation
RHS	Right hand side
STR	Stirred Tank Reactor

### Greek Symbols

$\alpha_c$	Angle from horizontal of conical bottom	°
$\Delta\alpha_u$	Change of direction of the velocity field	°
$\theta$	Free surface angle	°
$\nu$	Kinematic viscosity	m <sup>2</sup> /s <sup>1</sup>
$\nu_w$	Kinematic viscosity of water	m <sup>2</sup> /s <sup>1</sup>
$\varphi$	Phase angle of the table	°
$\rho$	Fluid density	kg/m <sup>3</sup>
$\rho^*$	Relative fluid density	-
$\sigma_{G^*}$	Standard deviation of the normalised green channel	-
$\tau_{max}^*$	Maximum shear strain	s <sup>-1</sup>
$\omega_i$	Vorticity components in the $i$ th direction	s <sup>-1</sup>

## Roman Symbols

$a_o$	Constant of proportionality	-
$a_{ow}$	Constant of proportionality for water	-
$B_{ij}^*$	Normalised blue channel pixel value	-
$C_l$	Lift Coefficient	-
$C$	Concentration	moles/m <sup>3</sup>
$d_i$	Inner diameter of the cylinder	m
$d_o$	Orbital diameter	m
$D$	Diffusion coefficient	m <sup>2</sup> /s <sup>1</sup>
$d_{50}$	Mass median diameter	m
$d_{imp}$	Impeller diameter in STR	m
$d_f$	Inner diameter of the Erlenmeyer flask	m
$Fr$	Froude number $Fr = \frac{2(\pi N)^2 d}{g}$	-
$Fr_a$	Axial Froude number	-
$Fr_{do}$	Froude number based on the orbital diameter	-
$Fr_{cr}$	Critical/transitional Froude number	-
$Fr_{js}$	Just-suspended Froude number	-

$F_l$	Lift Force	Kg m / s <sup>2</sup>
$g$	Gravitational acceleration	m/s <sup>2</sup>
$G_{ij}^*$	Normalised green channel pixel value	-
$h$	Fluid height at rest	m
$H$	Height of cylinder	m
$h_{imp}$	Impeller distance from bottom in STR	m
$\Delta h$	Free surface height	m
$h_c$	Height of truncated conical bottom	m
$h_f$	Fluid height height at rest in OSRs with conical bottom	m
$I_B$	Image brightness index	-
$I_B^*$	Normalised image brightness index	-
$J$	Diffusive flux	mol m <sup>-2</sup> s <sup>-1</sup>
$k_{ij}$	Kinetic energy of the periodic motion estimated from the $i$ th and $j$ th velocity components	m <sup>2</sup> /s <sup>2</sup>
$k_{ij}^*$	Space average of the kinetic energy of the periodic motion	m <sup>2</sup> /s <sup>2</sup>
$k'_{ij}$	Kinetic energy due to the random velocity fluctuations in the $i$ th and $j$ th directions	m <sup>2</sup> /s <sup>2</sup>

$k_{ij}^*$	Space average of the kinetic energy due to the random velocity fluctuations	$\text{m}^2/\text{s}^2$
$M$	Global degree of mixedness	-
$N$	Shaking frequency	$\text{s}^{-1}$
$N_{cr}$	Critical/transitional shaking frequency	$\text{s}^{-1}$
$Ne'$	Modified Newton number	-
$Ne$	Newton number	-
$N_{js}$	Just-suspended shaking frequency	$\text{s}^{-1}$
$Nt_m$	Mixing number	-
$P$	Power consumption	$\text{kg m}^2/\text{s}^3$
$Ph$	Phase number	-
$p_{ij}$	Greyscale value of pixel	-
$P_L$	Principal vortical cell on LHS	
$p_v$	Perimeter of the vortical cell	$\text{m}$
$p_v^*$	Normalised perimeter of the vortical cell	-
$P_R$	Principal vortical cell on RHS	
$Re$	Reynolds number	-

$Re_c$	Centrifugal Reynolds number	-
$Re_f$	Film Reynolds number	-
$R_{ij}^*$	Normalised red channel pixel value	-
$S_{ij}$	Strain rate tensor	$s^{-1}$
$S_L$	Secondary vortical cell on LHS	
$S_R$	Secondary vortical cell on RHS	
$T_L$	Tertiary vortical cell on LHS	
$t_m$	Mixing time	s
$T_R$	Tertiary vortical cell on RHS	
$u_i$	Velocity in the $i$ th direction,	m/s
$\langle u_i \rangle$	Phase average of the velocity component in the $i$ th direction	m/s
$u'_i$	Random velocity fluctuations in the $i$ th direction	m/s
$U$	Velocity field of the flat bottom OSR	m/s
$U_c$	Velocity field of the conical bottom OSR	m/s
$V$	Nominal fluid volume	$m^3$
$V_f$	Measured fluid volume	$m^3$
$X$	Local degree of mixedness	-

# List of Tables

1.1	Mixing time results available in the literature for OSRs and STRs.	31
2.1	Conditions for mixing time experiments in OSRS and STRs. . . .	52
4.1	Suspension studies with constant fluid height: $(h/d_i) \Leftrightarrow \sqrt{d_o/d_i}$ relationship and $Fr_{cr}$ based on Equation 1.8 and 1.7 . . . . .	150
4.2	Suspension studies with constant volume: $(h/d_i) \Leftrightarrow \sqrt{d_o/d_i}$ relationship and $Fr_{cr}$ based on Equation 1.8 and 1.7. . . . .	150
5.1	Fluid properties of the aqueous glycerol solutions. . . . .	198

# List of Figures

2.1	Diagram of the cylindrical OSR v.1 . . . . .	53
2.2	Sketch of the cylindrical OSR with feed insertion position. . . . .	54
2.3	(a) Schematic and (b) Exploded views of the cylindrical OSR v.2 . . . . .	55
2.4	(a) Benchtop Kühner LS-X lab-shaker; (b) Kühner SR-200 shaker. . . . .	56
2.5	Sketch of the positions assumed by a cylindrical OSR on the circular orbit of the shaker, and visualisation of the laser measurement plane projection (dashed line) with increasing phase angle. . . . .	57
2.6	(a) Picture and (b) diagram of the Mobius CellReady reactor. . . . .	58
2.7	NewBrunswick BioFlo 110 stirred tank reactor. . . . .	59
2.8	a) Experimental rig for mixing time estimation within the cylindrical OSR v1, b) Side view of the reactor and feed insertion device. . . . .	60
2.9	Schematic diagram showing PIV working principle (www.dantecdynamics.com). . . . .	61
2.10	Sketch of the arrangement of the high speed camera, OSR, and Laser for PIV experiments. . . . .	62
2.11	Sketch representing the alignment of the vertical laser sheet with experimental rig's reference holes. . . . .	63
2.12	Typical velocity vector field for $\varphi = 0^\circ$ ( $h/d_i=0.5$ and $N=105$ RPM). . . . .	64
2.13	Effect of interrogation window size on velocity profiles at a height $z/d_i=0.15$ : (a) $u_r$ and (b) $u_z$ . . . . .	65

2.14	Effect of image masking and vector validation on velocity profiles at $z/d_i=0.15$ : (a) $u_r$ and (b) $u_z$ . . . . .	66
2.15	Comparison of DynamicStudio, JPiv and PIVLab software: (a) $u_r$ and (b) $u_z$ . . . . .	67
2.16	Experimental rig arrangement for simultaneous PIV and pLIF experiments. Highspeed cameras in red, dichroic mirror in yellow, laser arm optics in green. (a) side view, (b) top view. . . . .	68
3.1	Time evolution of the mixing dynamics inside the bioreactor for conditions characteristics of in-phase flow: $Fr_{do}=0.11$ , $h/d_i=0.5$ , $d_o/d_i=0.25$ . . . . .	100
3.2	Time evolution of the mixing dynamics inside the bioreactor for conditions characteristics of out-of-phase flow $Fr_{do}=0.23$ , $h/d_i=0.5$ , $d_o/d_i=0.25$ . . . . .	100
3.3	(a) Location of points in the cylindrical OSR for RGB channel evaluation with DISMT; (b) Variation of red, green and blue values at the nine points shown in (a). . . . .	101
3.4	Variation with orbital revolutions, $Nt$ , of the three channels in the RGB space representation ( $r/d_i=0.375$ , $z/d_i=0.25$ ). . . . .	102
3.5	Variation with orbital revolutions, $Nt$ , of the three channels in the HSV space representation of colour ( $r/d_i=0.375$ , $z/d_i=0.25$ ). . . . .	103
3.6	Characteristic mixing map generated from the pixel-by-pixel mixing time algorithm. . . . .	104
3.7	Visualisation of the area used to determine the reactor mixing time. . . . .	105
3.8	Variation in time of the standard deviation across the investigation region of the normalised green channel $G^*$ ( $Fr_{do}=0.17$ , $h/d_i=0.5$ , $d_o/d_i=0.25$ ). . . . .	106

3.9	Percentage of mixed pixels of the normalised green channel $G^*$ as a function of shaker table revolution ( $Fr_{do}=0.17$ , $h/d_i=0.5$ , $d_o/d_i=0.25$ ). . . . .	107
3.10	Variation of the average mixing time with increasing random sample size ( $Fr_{do}=0.17$ , $h/d_i=0.5$ , $d_o/d_i=0.25$ ). . . . .	108
3.11	Time evolution of the mixing dynamics inside the CellReady 3 L STR for three mixing time methodologies: Dual Indicator System for Mixing Time and pH probe (a-d); Iodine-Sodium Thiosulfate (e-h); Waterblue dye (i-l). . . . .	109
3.12	Comparison of Mixing Time measurement in the CellReady at $V_f=2L$ using DISMT ( $\bullet$ ), Iodine-Sodium thiosulfate ( $\square$ ), Waterblue dye ( $\nabla$ ) and pH probe methodologies ( $\triangleright$ ). . . . .	110
3.13	Variation in time of the percentage of pixels mixed, $M$ , against the local mixing threshold selected, $X$ , for a Mobius CellReady reactor, with $V_f=2 L$ , $N=50$ RPM ( $Re=14000$ ). . . . .	111
3.14	Variation in time of the pH probe readings and of the standard deviation of the normalised green channel output, $\sigma_{G^*}$ , for New Brunswick Bioreactor (the horizontal lines indicate the pH threshold for the fluid to turn from red to yellow). . . . .	112
3.15	Variation in time of the pH probe readings and of the standard deviation of the normalised green channel output, $\sigma_{G^*}$ , for CellReady Bioreactor (the horizontal lines indicate the pH threshold for the fluid to turn from red to yellow). . . . .	113
3.16	Characteristic mixing time maps for different Froude number ( $h/d_i=0.5$ ; $d_o/d_i=0.25$ ): (a) $Fr_{do}=0.11$ (b) $Fr_{do}=0.23$ . . . . .	114
3.17	Variation in time of the normalised green and red indices, $G_{i,j}^*$ and $R_{i,j}^*$ , for the point of the bioreactor at the centre of the area delimited in the inset image. . . . .	115

3.18	Colour evolution in time within the area highlighted in the inset image of Figure 3.17. . . . .	115
3.19	Variation in time of the standard deviation of the normalised green channel output, $\sigma_G^*$ , for different orbital speeds. All data are for a cylindrical OSR with $d_i=100$ mm, $d_o=25$ mm. . . . .	116
3.20	Non-dimensional mixing time in a cylindrical bioreactor ( $d_i=100$ mm, $d_o=25$ mm, $h=50$ mm) at increasing $Fr_{d_o}$ . . . . .	117
3.21	Mixing time maps for two DISMT experiments at same conditions: $h/d_i=0.5$ , $d_o/d_i=0.25$ , $Fr_{d_o}=0.12$ . (a) $Nt_m=350$ Nt; (b) $Nt_m=160$ Nt. . . . .	118
3.22	Variation of the mixing number with radial feed position and $Fr_{d_o}$ . $h/d_i=0.5$ ; $d_o/d_i=0.25$ . Insertion point (a): P1= $\diamond$ , P2= $\nabla$ , P3= $\square$ , P4= $*$ , Average P1-P7= $\bullet$ , $\pm$ one standard deviation= (- - -); (b) P4= $*$ , P5= $\square$ , P6= $\nabla$ , P7= $\diamond$ , Average P1-P7= $\bullet$ , $\pm$ one standard deviation= (- - -). . . . .	119
3.23	Variation of the mixing number with radial feed position at different $Fr_{d_o}$ . ( $h/d_i=0.5$ ; $d_o/d_i=0.25$ ). ( $\times$ ) experimental result, ( $\circ$ ) average with error bar; $Fr_{d_o} =$ (a) 0.11, (b) 0.14, (c) 0.17, (d) 0.2, (e) 0.24. . . . .	120
3.24	Variation of the mixing number with $Fr_{d_o}$ for constant $d_o/d_i=0.25$ and different fluid height: ( $\square$ ) $h=30$ mm, ( $\triangleright$ ) $h=50$ mm, ( $\diamond$ ) $h=70$ mm. . . . .	121
3.25	Variation of the mixing number with $Fr_{d_o}$ for constant $d_o/d_i=0.25$ and $h/d_i=0.5$ : ( $\square$ ) $d_i=70$ mm and $h=35$ mm, ( $\triangleright$ ) $d_i=100$ mm and $h=50$ mm, ( $\diamond$ ) $d_i=130$ mm and $h=65$ mm. . . . .	122

3.26	Comparison of $Nt_m$ versus $Fr_{do}$ curves obtained in cylindrical and Erlenmeyer OSRs against those reported by Tissot <i>et al.</i> (2010) and Tan <i>et al.</i> (2011): ( $\circ$ ) Cylindrical OSR, $d_i=100$ mm, $h=50$ mm, $V_f=0.4$ L, ( $\bullet$ ) Cylindrical OSR, $d_i=130$ mm, $h=65$ mm, $V_f=0.85$ L, ( $\square$ ) Tissot <i>et al.</i> (2010) OSR, $d_i=100$ mm, $h=125$ mm, $V_f=1$ L, ( $\blacktriangle$ ) Erlenmeyer Flask, $d_i=131$ mm, $V_f=0.4$ L, ( $\triangle$ ) Erlenmeyer Flask, $d_i=166$ mm, $V_f=0.8$ L, ( $\blacksquare$ ) Tan <i>et al.</i> (2011), Erlenmeyer Flask, $d_i=105$ mm, $V_f=0.05$ L. . . . .	123
3.27	Variation of the mixing time with dimensional shaking speed for cylindrical OSRs. . . . .	124
3.28	Variation of the mixing number with $Fr_{do}/Fr_{cr}$ , for cylindrical OSRs. . . . .	125
3.29	Comparison of the present cylindrical OSR mixing data with those reported by Tissot <i>et al.</i> (2010), in terms of mixing time against shaking speed (dimensional). . . . .	126
3.30	Comparison of the present cylindrical OSR mixing data with those reported by Tissot <i>et al.</i> (2010), in terms of mixing number against the proposed scaling factor $Fr_{do}/Fr_{cr}$ (non-dimensional). . . . .	127
4.1	Cross-sectional view of the orbitally shaken cylindrical bioreactor with the cylindrical bottom. . . . .	151
4.2	Phase-resolved non-dimensional velocity fields and contours of the tangential component of vorticity, $\omega_\theta$ , for flat bottom geometry at (a-d) $Fr_{do}=0.10, 0.14, 0.17, 0.18$ ( $N=85, 100, 110, 115$ RPM). . .	152
4.3	Phase-resolved non-dimensional velocity fields and contours of the tangential component of vorticity, $\omega_\theta$ , for conical A bottom geometry at (a-d) $Fr_{do}=0.10, 0.14, 0.17, 0.18$ ( $N=85, 100, 110, 115$ RPM). . . . .	153

4.4	Phase-resolved non-dimensional velocity fields and contours of the tangential component of vorticity, $\omega_\theta$ , for conical B bottom geometry at (a-d) $Fr_{do}=0.10, 0.14, 0.17, 0.18$ ( $N=85, 100, 110, 115$ RPM). . . . .	154
4.5	(a) Variation of the spaced-averaged non-dimensional vorticity with increasing $Fr_{do}$ : flat bottom ( $\circ$ ), Conical A ( $\triangle$ ), and Conical B ( $\square$ ); (b) Visualization of the area $\omega_\theta = 0.1\pi N$ used to determine the average vorticity. . . . .	155
4.6	Principal component of strain rate tensor at $\varphi = 0^\circ$ for conical B geometry ( $Fr_{do}=0.14, N=100$ RPM) (a) Compression strain rate $S_1$ , (b) Stretching strain rate $S_2$ . . . . .	156
4.7	Contour maps of the maximum shear strain rate of the flow at $\varphi = 0^\circ$ for (a) flat, (b) conical A, (c) conical B geometries at $Fr_{do}=0.14$ ( $N=100$ RPM). . . . .	157
4.8	Variation of the spaced-averaged non-dimensional maximum shear rate, $\tau_{max}^*$ , with increasing $Fr_{do}$ : flat bottom ( $\circ$ ), Conical A ( $\triangle$ ), and Conical B ( $\square$ ). . . . .	158
4.9	(a) Comparison of the vertical profiles of the radial velocity component for a flat bottom (red) and Conical B bottom (blue) at two shaker speeds $N=80$ RPM ( $\square$ ) and $N=100$ RPM ( $\times$ ); (b) Profiles of the radial velocity component with a coordinate system $(z - h)/d_i$ for a flat bottom (red) and Conical B bottom (blue) at two shaker speeds $N=80$ RPM ( $\square$ ) and $N=100$ RPM ( $\times$ ); (c) Diagram of the location of the radial profiles at coordinates $r/d_i=0$ and 0.25. . . . .	159

4.10	Velocity field for $Fr_{do}=0.14$ ( $N=100$ RPM) for flat bottom (white vector field) and conical B (black vector field); contour of the angle difference, $\Delta\alpha_u$ , between velocity fields. Inset: detail of the velocity field. . . . .	160
4.11	Scatter plot of the velocity ratio, $U/U_c$ , and angle difference, $\Delta\alpha_u$ , for $Fr_{do}=0.14$ ( $N=100$ RPM). . . . .	161
4.12	Variation of the spaced-averaged non dimensional kinetic energy of the random velocity fluctuations, $k'_{rz}$ with increasing $Fr_{do}$ : flat bottom ( $\circ$ ), Conical A ( $\triangle$ ), and Conical B ( $\square$ ). . . . .	162
4.13	Visualisation of the suspension mechanism for a flat bottom OSR $d_i=100$ mm, $d_o=25$ mm, $h=45$ mm at varying $N$ , (a-h): 90, 100, 105, 110, 112, 115, 118 and 121 RPM. . . . .	163
4.14	Visualisation of the suspension mechanism for a flat bottom OSR $d_i=100$ mm, $d_o=25$ mm, $h=70$ mm at varying $N$ , (a-h): 90, 100, 110, 115, 120, 123, 126 and 129 RPM. . . . .	164
4.15	Variation of the normalised brightness index, $I^*$ , with agitation rate, $N$ , with reference (a-h) to Figure 4.13. $d_i=100$ mm, $d_o=25$ mm, $h=70$ mm at varying $N$ . . . . .	165
4.16	Variation of $I^*$ with shaker speed for different orbital diameters in a Flat bottom $d_i=100$ mm OSR with (a) $h=45$ mm and (b) $h=70$ mm. . . . .	166
4.17	Variation of $I^*$ with shaker speed for different orbital diameters in a conical A bottom $d_i=100$ mm OSR with (a) $h=45$ mm and (b) $h=70$ mm. . . . .	167
4.18	Variation of $I^*$ with shaker speed for different orbital diameters in a conical B bottom $d_i=100$ mm OSR with (a) $h=45$ mm and (b) $h=70$ mm. . . . .	168

4.19	Variation of suspension speed, $N_s$ , with orbital diameter, $d_o$ , for $d_i=100$ mm, $h=45$ mm (○) flat bottom, (□) Conical A, (△) Conical B and $h=70$ mm (○) flat bottom, (□) Conical A, (△) Conical B. . . . .	169
4.20	Variation of suspension speed, $N_s$ , with conical bottom height, $h_c$ , for $d_i=100$ mm, $h=45$ mm: (○) $d_o=15$ mm, (□) $d_o=25$ mm, (△) $d_o=50$ mm; and $h=70$ mm: (○) $d_o=15$ mm, (□) $d_o=25$ mm, (△) $d_o=50$ mm. . . . .	170
4.21	Variation of suspension speed, $N_s$ , with conical bottom height, $h_c$ , for $d_i=70$ mm, $V_f=115$ mL: (○) $d_o=15$ mm, (□) $d_o=25$ mm, (△) $d_o=50$ mm; and $V_f=192$ mL: (○) $d_o=15$ mm, (□) $d_o=25$ mm, (△) $d_o=50$ mm. . . . .	171
4.22	Variation of $I^*$ with $Fr_s/Fr_{cr}$ for different orbital diameters in a Flat bottom $d_i=100$ mm OSR with (a) $h=45$ mm and (b) $h=70$ mm.	172
4.23	Variation of $I^*$ with $Fr_s/Fr_{cr}$ for different orbital diameters in a Conical B bottom $d_i=100$ mm OSR with (a) $h=45$ mm and (b) $h=70$ mm. . . . .	173
4.24	Variation of the suspended to critical Froude number ratio, $Fr_s/Fr_{cr}$ , with critical heigh ratio, $(h/d_i)/\sqrt{(d_o/d_i)}$ , for all the conditions investigated. . . . .	174
5.1	Time evolution of the mixing dynamics inside the $d_i=100$ mm bioreactor for a glycerol solution of viscosity $\nu=1.9 \times 10^{-6}$ m <sup>2</sup> s <sup>-1</sup> for two speeds; (a-d) $N=105$ RPM, (e-h) $N=120$ RPM. ( $h/d_i=0.32$ , $d_o/d_i=0.25$ ). . . . .	199

5.2	Time evolution of the mixing dynamics inside the $d_i=100$ mm bioreactor for a glycerol solution of viscosity $\nu=4.37 \times 10^{-6} \text{ m}^2\text{s}^{-1}$ for two speeds; (a-d) $N=110$ RPM, (e-h) $N=120$ RPM. ( $h/d_i=0.32$ , $d_o/d_i=0.25$ ). . . . .	200
5.3	Time evolution of the mixing dynamics inside the $d_i=100$ mm bioreactor for a glycerol solution of viscosity $\nu=1.37 \times 10^{-5} \text{ m}^2\text{s}^{-1}$ for three speeds; (a-d) $N=110$ RPM, (e-h) $N=112$ RPM, (i-l) $N=115$ RPM. ( $h/d_i=0.32$ , $d_o/d_i=0.25$ ). . . . .	201
5.4	Detail of Figure 5.3 (d), showing the location of secondary vortical cells. . . . .	202
5.5	Variation of mixing number, $Nt_m$ , with increasing Froude for fluids of different viscosity: ( $\square$ ) $\nu=1.9 \times 10^{-6} \text{ m}^2 \text{ s}^{-1}$ , ( $\triangleright$ ) $\nu=4.37 \times 10^{-6} \text{ m}^2 \text{ s}^{-1}$ and ( $\circ$ ) $\nu=1.37 \times 10^{-5} \text{ m}^2 \text{ s}^{-1}$ . . . . .	203
5.6	Variation of mixing number, $Nt_m$ , with $Fr_{d_o}/Fr_{cr}$ for fluids of different viscosity: ( $\square$ ) $\nu=1.9 \times 10^{-6} \text{ m}^2 \text{ s}^{-1}$ , ( $\triangleright$ ) $\nu=4.37 \times 10^{-6} \text{ m}^2 \text{ s}^{-1}$ and ( $\circ$ ) $\nu=1.37 \times 10^{-5} \text{ m}^2 \text{ s}^{-1}$ . Shaded area representing mixing numbers for water-like fluids (see Figure 3.28). . . . .	204
5.7	Mixing time map of a $d_i=100$ mm bioreactor for glycerol solution $\nu=4.37 \times 10^{-6} \text{ m}^2\text{s}^{-1}$ , $h/d_i=0.32$ , $d_o/d_i=0.25$ , $N=110$ RPM (a) whole field of view, (b) slow mixing region, (c) fast mixing region. . . . .	205
5.8	Mixing time map of a $d_i=100$ mm bioreactor for glycerol solution $\nu=1.37 \times 10^{-5} \text{ m}^2\text{s}^{-1}$ , $h/d_i=0.32$ , $d_o/d_i=0.25$ , $N=110$ RPM (a) whole field of view, (b) slow mixing region, (c) fast mixing region. . . . .	206
5.9	Variation in time of the (a) standard deviation of the Green channel output, $\sigma_{G^*}$ , and of (b) the percentage of mixed pixels, $M$ , in the ( $\square$ ) slow mixing and ( $\circ$ ) fast mixing regions. All data are for $d_o=100$ mm, $\nu=4.37 \times 10^{-6}$ , $h/d_i=0.32$ , $d_o/d_i=0.25$ , $N=110$ RPM. . . . .	207

5.10	Variation in time of the (a) standard deviation of the Green channel output, $\sigma_{G^*}$ , and of (b) the percentage of mixed pixels, $M$ , in the ( $\square$ ) slow mixing and ( $\circ$ ) fast mixing regions. All data are for $d_o=100$ mm, $\nu=1.37 \times 10^{-5}$ , $h/d_i=0.32$ , $d_o/d_i=0.25$ , $N=110$ RPM.	208
5.11	(a) Visualisation of the major and minor axis of the elliptical cross-section of the LHS vortical cell. (b) Time evolution of the normalised perimeter of the vortical cell with linear fit for: ( $\circ$ ) $\nu=4.37 \times 10^{-6}$ ; ( $\square$ ) $\nu=1.37 \times 10^{-5}$ ( $d_o=100$ mm, $h/d_i=0.32$ , $d_o/d_i=0.25$ , $N=110$ RPM).	209
5.12	pLIF images of the cylindrical OSR, for $d_i=100$ mm, $\nu=1.37 \times 10^{-5}$ $\text{m}^2\text{s}^{-1}$ , $h/d_i=0.5$ , $d_o/d_i=0.5$ , $N=80$ RPM: (a) $Nt=63$ , (b) $Nt=105$ , (c) $Nt=150$ . (d) Schematic diagram of the flow configuration.	210
5.13	pLIF images of the cylindrical OSR, for $d_i=100$ mm, $\nu=1.37 \times 10^{-5}$ $\text{m}^2\text{s}^{-1}$ , $h/d_i=0.5$ , $d_o/d_i=0.5$ , $N=85$ RPM: (a) $Nt=20$ , (b) $Nt=31$ , (c) $Nt=93$ . (d) Schematic diagram of the flow configuration.	211
5.14	pLIF images of the cylindrical OSR, for $d_i=100$ mm, $\nu=1.37 \times 10^{-5}$ $\text{m}^2\text{s}^{-1}$ , $h/d_i=0.5$ , $d_o/d_i=0.5$ , $N=90$ RPM: (a) $Nt=33$ , (b) $Nt=44$ , (c) $Nt=108$ . (d) Schematic diagram of the flow configuration.	212
5.15	pLIF images of the cylindrical OSR, for $d_i=100$ mm, $\nu=1.37 \times 10^{-5}$ $\text{m}^2\text{s}^{-1}$ , $h/d_i=0.5$ , $d_o/d_i=0.5$ , $N=100$ RPM: (a) $Nt=37$ , (b) $Nt=62$ , (c) $Nt=93$ . (d) Schematic diagram of the flow configuration.	213
5.16	pLIF images of the cylindrical OSR, for $d_i=100$ mm, $\nu=1.37 \times 10^{-5}$ $\text{m}^2\text{s}^{-1}$ , $h/d_i=0.5$ , $d_o/d_i=0.5$ , $N=105$ RPM: (a) $Nt=21$ , (b) $Nt=74$ , (c) $Nt=182$ . (d) Schematic diagram of the flow configuration.	214
5.17	pLIF images of the cylindrical OSR, for $d_i=100$ mm, $\nu=1.37 \times 10^{-5}$ $\text{m}^2\text{s}^{-1}$ , $h/d_i=0.5$ , $d_o/d_i=0.5$ , $N=115$ RPM: (a) $Nt=9$ , (b) $Nt=16$ , (c) $Nt=62$ .	215

5.18	Schematic diagrams of the flow structures observed from the pLIF images for $\nu=1.37 \times 10^{-5} \text{ m}^2\text{s}^{-1}$ at different $N$ : (a) 80 RPM, (b) 85 RPM, (c) 90 RPM, (d) 100 RPM, (e) 105 RPM. . . . .	216
5.19	Detail of the elongation of Rhodamine dye on the LHS of a $d_i=100$ mm OSR, glycerol solution $\nu=1.37 \times 10^{-5} \text{ m}^2\text{s}^{-1}$ , $h/d_i=0.5$ , $d_o/d_i=0.5$ $N=80$ RPM: (a-g) $Nt=25-31$ . (h) Elongation of material lines per shaker revolution, with the colour change indicating each complete revolution. . . . .	217
5.20	Detail of the elongation of Rhodamine dye on the RHS of a $d_i=100$ mm OSR, glycerol solution $\nu=1.37 \times 10^{-5} \text{ m}^2\text{s}^{-1}$ , $h/d_i=0.5$ , $d_o/d_i=0.5$ $N=80$ RPM: (a-g) $Nt=42-48$ . (h) Elongation of material lines per shaker revolution, with the colour change indicating each complete revolution. . . . .	218
5.21	Detail of the elongation of Rhodamine dye on the LHS of a $d_i=100$ mm OSR, glycerol solution $\nu=1.37 \times 10^{-5} \text{ m}^2\text{s}^{-1}$ , $h/d_i=0.5$ , $d_o/d_i=0.5$ $N=85$ RPM: (a-e) $Nt=26-30$ . (f) Elongation of material lines per shaker revolution, with the colour change indicating each complete revolution. . . . .	219
5.22	Detail of the elongation of Rhodamine dye on the RHS of a $d_i=100$ mm OSR, glycerol solution $\nu=1.37 \times 10^{-5} \text{ m}^2\text{s}^{-1}$ , $h/d_i=0.5$ , $d_o/d_i=0.5$ $N=85$ RPM: (a-h) $Nt=28-35$ . (i) Elongation of material lines per shaker revolution, with the colour change indicating each complete revolution. . . . .	220
5.23	Detail of the elongation of Rhodamine dye on the LHS of a $d_i=100$ mm OSR, glycerol solution $\nu=1.37 \times 10^{-5} \text{ m}^2\text{s}^{-1}$ , $h/d_i=0.5$ , $d_o/d_i=0.5$ , $N=90$ RPM: (a-e) $Nt=31-35$ . (f) Elongation of material lines per shaker revolution, with the colour change indicating each complete revolution. . . . .	221

5.24	Detail of the elongation of Rhodamine dye on the RHS of $d_i=100$ mm OSR, glycerol solution $\nu=1.37\times 10^{-5}$ m <sup>2</sup> s <sup>-1</sup> , $h/d_i=0.5$ , $d_o/d_i=0.5$ $N=90$ RPM: (a-k) $Nt=49-59$ . (l) Elongation of material lines per shaker revolution, with the colour change indicating each complete revolution. . . . .	222
5.25	Evolution in time of the material line growth ratio, $\frac{\ell(t)-\ell_0}{\ell_0}$ for the (a) LHS of bioreactor; (b) RHS of bioreactor: ( $\square$ ) $N=80$ RPM, ( $\triangle$ ) $N=85$ RPM and ( $\circ$ ) $N=90$ RPM. . . . .	223

# Chapter 1

## Introduction

### 1.1 Background

Mammalian cell cultures have been widely used for the production of therapeutic proteins and vaccines. Monoclonal antibodies, in particular, represent a class of therapeutics that has shifted the treatment paradigm in the fields of oncology and immunology by improving the quality of life for the patient during cancer treatment (Pavlou and Reichert, 2004; Reichert *et al.*, 2005). Manufactured biologics are used for the diagnosis and treatment of a variety of patient conditions, such as rheumatoid arthritis (Adalimumab), leukemia (Ofatumumab), colonrectal cancer (Panitumumab) (Walsh, 2014; Zhang, 2010). Mammalian cells are usually preferred to other host cells, such as yeast, bacteria, insects and plants, because of their favourable folding characteristics as well as assembly and post-translational abilities, which define the efficacy and functioning of an antibody (Wurm, 2004).

Commercial production of antibodies relies on the development of cost-effective large-scale cultivation methods of genetically engineered mammalian cells. At lab-

oratory scale, cells are usually grown in low shear devices, with orbitally shaken bioreactors (OSRs) being largely employed in the early stages of bioprocess development because they offer an effective solution to screen several conditions in parallel. Process development studies are typically performed at small scale, in either microwell plate formats or Erlenmeyer flasks. The low energy demand and the well-defined gas-liquid interface make OSRs a favourable solution that provides a promising environment for mammalian cell cultivation in terms of oxygen transfer and nutrient requirements. Once the process is optimised at small scale, it is then adapted to stirred tank reactors (STRs), which is the type of bioreactor most commonly used at production level. STRs consist of an impeller for culture medium agitation, spargers for gas aeration, pH and temperature control systems and their flow, mixing and suspension dynamics have been thoroughly characterized in the literature (see for example the works on STR mixing and fluid dynamics of Doulgerakis *et al.* 2009; Escudié and Liné 2003; Kresta and Wood 1993; Yianneskis *et al.* 1987 to name a few).

The scale translation from OSRs to conventional stirred tank reactors currently represents a bottleneck at the process development stage due to the significant differences in geometry and mixing dynamics, and has generated interest in large scale OSRs for facilitating bioprocess development. Laboratory and production scale OSRs are now on the market (see for example Kühner SB50-X and SB200-X) allowing users to select the same bioreactor geometry at multiple scales, thus facilitating scaling-up and simplifying regulatory approval. The bioprocess industry has also been investigating implementation of OSRs to provide a single piece of equipment for different cell culture processes at multiple scales, because of the possibility to implement more efficiently single-use manufacturing processes while taking advantage of the flexibility and adaptability of this technology. An opposite strategy to facilitate process scale-up is based on the scaling down of STRs

to mL scale. The AMBR-15 (Sartorius Stedim), arguably the most popular small scale STRs, provides a microscale high throughput technology to achieve swift time-to-clinic and has resulted successful particularly for platform development of drug products (Siva *et al.*, 2015).

Cell growth and environmental conditions vary significantly between shaken cultures and those encountered in large STRs. The differences between OSR and STR may result in inadequate mass transfer characteristics, cell damage and reduced antibody productivity in scaling up/down processes. Studies of animal cell cultures have focused on optimising the chemical environment and culture media in order to enhance antibody productivity (Bibila *et al.*, 1994; Schröder *et al.*, 2004), but studies of the engineering characteristics relevant to the optimisation of bioreactor geometry and operating conditions are still lacking. While growth rates in mammalian cell cultures are slower than those in microbial systems, the need for a well-mixed environment has been acknowledged in terms of the quality of cell suspension and gas supply and removal (Lara *et al.*, 2006; Nienow *et al.*, 1996; Ozturk, 1996; Serrato *et al.*, 2004). Recent studies in STRs have shown that shear stresses do not significantly affect cell growth of animal cells (Nienow, 2006; Nienow *et al.*, 2013), however there is a growing interest in understanding the effect of shear stress on stem cells and cells for therapy, and the low shear levels present in OSRs could potentially make this device a suitable option for scaling up stem cell expansion using suspension cultures (Sargent *et al.*, 2010). From this point of view operating conditions should be carefully selected by comparing the Kolgomorov length scale to the size of the microcarriers or cell aggregates (King and Miller, 2007). Despite recent progress of shaken bioreactor platforms, supported by recent development of optical sensors and control loops to improve automation in mL scale, the number of publications which address scaling up/down aspects of shaken bioreactors is very limited (Klößner *et al.*,

2012).

The motivation of the present study is to further the knowledge of the mixing processes, fluid dynamics and suspension mechanisms in OSR in order to develop an effective and reliable scaling method. To this end it is fundamental to shed light on the magnitude and local variations of the mixing, the flows present in OSRs at different operating conditions, the intensity of shear rates and their peak location in the bioreactor, the nature and dynamics of solid suspension (single cell, microcarrier or cell aggregates). Amongst the variety of geometries available for shaken bioreactors, the simple cylindrical geometry was chosen to develop a fundamental understanding of the flow and mixing mechanisms in OSRs. The research was undertaken using techniques and methodologies applied to a variety of applications throughout the field of fluid mixing and flow dynamics, specifically applied to reactor vessels, such as the Dual Indicator for Mixing Time, Particle image Velocimetry, solid suspension studies and planar Laser Induced Fluorescence. The following section contains a detailed review of the findings of previous investigations of the engineering aspects of OSRs, which sets the foundation of the present work. The objectives of the present investigation are formulated at the end of this chapter and are based on the literature survey. Finally, the chapter concludes with an outline of the Thesis.

## 1.2 Literature review

The aim of the literature survey is to provide an accurate account of the findings of the works dealing with OSRs and the development of the experimental methods applied in the present research. The literature review will be presented in sections, each highlighting current knowledge in the three following engineering aspects of OSRs:

- Flow dynamics
- Mixing dynamics
- Solid suspension dynamics

## 1.3 Flow dynamics

The oscillatory motion of a shaker table causes the deformation of the free surface in a partially filled cylindrical vessel, which in turn induces fluid flow inside the container. Under shaking conditions the free surface raises and lowers periodically due to centrifugal, inertial and gravitational forces. Shaker tables perform an orbital motion at different speeds to achieve agitation of the fluid in the vessel. A number of variables, in addition to fluid physical properties, are to be considered for a shaken bioreactor: vessel size, geometry, type, surface finish, baffles (if any), shaking frequency, shaking diameter and fluid height (i.e. fluid volume).

The study of Gardner and Tatterson (1992) is one of the first reported in the published literature that investigates the flow and mixing dynamics in a shaken, partially-filled, cylindrical vessel. Dye visualization techniques with different degree of mixture of water and corn syrup were employed to assess the variation of

the homogenization time with increasing Reynolds number,  $Re = NT^2/\nu$ , where the characteristic length scale,  $T$ , is obtained as the cubic root of the filling volume,  $V_f^{1/3}$ , while  $N$  and  $\nu$  are the shaker table rotational speed and fluid viscosity, respectively. The authors identified three mixing regimes: i) a laminar regime,  $Re=0.8-1000$ , controlled by a toroidal vortex and characterised by the homogenization time being inversely proportional to  $Re$ ; ii) a transitional regime, for  $Re \sim 1000$ , characterised by a vertical axial vortex inducing unmixed dye regions at the top and at the bottom of the filling volume; iii) a turbulent regime at higher  $Re$ , where the flow is dominated by severe splashing and the homogenization time is nearly constant. It should be noted that, in the experiments of Gardner and Tatterson (1992), the addition of the dye occurred prior to the shaker motion; hence diffusion would start before the flow structures would have been established.

Kim and Kizito (2009) performed numerical analysis to study the flow present in a shaken system with emphasis on the deforming free surface. They found that the flow was quasi-steady when a coordinate system rotating with the shaker table was considered. More specifically, the highest free surface height occurred on the vertical plane identified by the directions of the centrifugal and gravitational accelerations. This plane changes its orientation in space and rotates around the bioreactor axis as the shaker table proceeds along its circular orbit. Their numerical simulations showed that the velocity field of the deforming free surface is  $90^\circ$  out of phase with the centrifugal body force. The time-averaged flow fields showed the presence of two strong vortical flow structures, with their axis in the tangential direction, in proximity of the cylindrical vessel walls. As the fluid viscosity was increased, the two vortices were pushed towards the centre of the bioreactor, and the thickness of the boundary layers next to the cylinder walls grew in size. Kim and Kizito (2009) assessed their numerical results against flow visualizations

obtained in a cylindrical vessel of 43.5 mm internal diameter, for a shaking diameter  $d_o=20$  mm and a shaking frequency  $N=60$  RPM. Water-ethylene glycol mixtures were used as the working fluid, while a laser was employed to illuminate the cross-section of the cylinder. Experimental results confirmed the presence of large vortices on the side walls, which created a strong upstream flow in the core region of the vessel. The sizes of the vortical structures depended on fluid height and viscosity. Kim and Kizito (2009) concluded that mixing processes were driven by these side vortices when the aspect ratio  $h/d_i = 1$ , where  $h$  and  $d_i$  are the fluid height and cylindrical vessel diameter, respectively. At higher aspect ratios mixing was found to be primarily caused by the free surface travelling wave. Apart from the work of Kim and Kizito (2009), other numerical simulation studies are those carried out by Zhang *et al.* (2005, 2008) on 250 mL Erlenmeyer flask and 24- and 96 microwell bioreactors, respectively. These analyses aimed at estimating macro-parameters, such as power consumption, from the integral of the viscous dissipation rate of kinetic energy, interfacial area and volumetric mass transfer coefficients for different types of bioreactor, but do not provide insight into the flow and mixing dynamics occurring inside the bioreactor.

### 1.3.1 Power consumption

Büchs *et al.* (2000b) estimated the power consumption in Erlenmeyer flasks by measuring the torque on the drive acting upon the shaker table and taking into account friction and other system losses. Several operating conditions were investigated by varying the size of the container, filling volume, shaking diameter, shaking frequency and liquid viscosity. The results showed that at certain agitation regimes an ‘out-of-phase’ condition occurs, and the liquid in the shaken flask does not move in synchrony with the shaker table. The variation of a modified Newton number  $Ne'$  (i.e. power number) with  $Re$  showed that for in-phase con-

ditions a logarithmic correlation is present between the two parameters, while for out-of-phase flow the modified Newton number exhibits a significant drop over the range of  $Re$  investigated, and the data are scattered in the  $Re - Ne'$  plane. The non-dimensional phase number,  $Ph$ , of Equation 1.1 was found to distinguish between in-phase and out-of-phase conditions.

$$Ph = \frac{d_o}{d_f} (1 + 3 \log_{10} Re_f) \quad (1.1)$$

where  $d_o$  and  $d_f$  are the orbital and flask base diameters, respectively, and  $Re_f$  is the film Reynolds number  $\left( Re_f = Re \frac{\pi}{2} \left( 1 - \sqrt{1 - \frac{\pi}{4} \left( \frac{V_f^{1/3}}{d} \right)^2} \right)^2 \right)$ .

Büchs *et al.* (2000b) reported that Equation 1.1 is only valid for an axial Froude number based on the orbital diameter  $d_o$ ,  $Fr_a = \frac{2\pi^2 N^2 d_o}{g} > 0.4$  and in-phase conditions occur for  $Ph > 1.26$ . A correlation was found from experimental data for the modified Newton number,  $Ne'$ , reported in Equation 1.2.

$$Ne' = 70 Re^{-1} + 25 Re^{-0.6} + 1.5 Re^{-0.2} \quad (1.2)$$

where  $Ne'$  comprises a laminar ( $Re^{-1}$ ), transition ( $Re^{-0.6}$ ) and turbulent ( $Re^{-0.2}$ ) term. The  $Ne'$  can be used to calculate the specific power consumption by rearranging Equation 1.3.

$$Ne' = \frac{P}{\rho N^3 d_f^4 V_f^{1/3}} \quad (1.3)$$

where  $P$  is the power consumption,  $\rho$  the density,  $N$  the agitation rate,  $d_f$  the flask inner diameter and  $V_f$  the fill volume (Büchs *et al.*, 2000b).

Klockner and Büchs (2012) extended the work of Büchs *et al.* (2000b) to estimate the power consumption of cylindrical shaken bioreactors. A Buckingham  $\pi$ -theorem analysis was carried out to determine the variation of the Newton

number,  $Ne'$ , with Reynolds number,  $Re = Nd_i^2/\nu$ , centrifugal Froude number,  $Fr = N^2d_i/g$ , volume number,  $V_f/d_i^3$ , and orbital to cylinder diameter ratio,  $d_o/d_i$  (see Equation 1.4).

$$Ne' = 9 Re^{-0.17} \left( \frac{N^2d_i}{g} \right)^{0.42} \left( \frac{V_f}{d_i^3} \right)^{0.44} \left( \frac{d_o}{d_i} \right)^{0.42} \quad (1.4)$$

Contrary to the results obtained for Erlenmeyer flasks (see Equation 1.2), the diameter ratio  $d_o/d_i$  was found to affect the power number in cylindrical OSRs, as greater orbital diameters are associated with a higher inclination of the fluid inside the bioreactor and a greater wetted wall surface. The authors concluded that this correlation is not valid in Erlenmeyer flasks because the conical shape in the upper part of the flask suppresses the distribution of the liquid over a larger wetted area. The second and fourth terms on the right hand side of Equation 1.4 have the same exponent (i.e. 0.42) and after simplification it can be concluded that the power number,  $Ne'$ , depends only on a Froude number,  $Fr$ , based on the orbital diameter,  $d_o$ , as the characteristic length scale. The correlation of Equation 1.5 was also found to estimate the critical shaking speed,  $N_{cr}$ , which for this type of bioreactor replaces the phase number,  $Ph$ , that characterises only Erlenmeyer flasks and is used to identify ‘suitable’ shaking conditions associated with a measurable power number and in-phase flow. They concluded that for this critical condition the hydrodynamics in the bioreactor are such that the centrifugal acceleration overcomes inertial forces.

$$N_{cr} = \frac{1}{d_i^2} \sqrt{0.28 V_f g} \quad (1.5)$$

The validity of the correlation found for  $N_{cr}$  was assessed by comparing the measured values of  $Ne'$  and those predicted using Equations 1.4 and 1.5. The comparison was carried out only for those operating conditions denoted as ‘suitable’, which are those characterised by an in-phase fluid motion induced in the

bioreactor. Predicted and measured values of  $Ne'$  showed a general agreement with a margin of  $\pm 20\%$  between the two shown on a logarithmic scale.

Scaling protocols based on power consumption experiments have been applied to cell culture, such as in the work of Mehmood *et al.* (2010), who found a correlation between numerical estimates of the power dissipation and the production of pristinamycins by *Streptomyces pristinaespiralis* in a shaken bioreactor of conical shape (Erlenmeyer flask). From this study they identified an optimal production for a power consumption range of 5.5-8.5 kWm<sup>-3</sup>.

### 1.3.2 Flow characterisation and transition

The study of Weheliye *et al.* (2013) is the first to provide a thorough insight into the dynamics of the flow occurring inside a cylindrical shaken bioreactor, and to determine a flow scaling law based on physical considerations without resorting to the use of power law correlations. From their work phase-resolved velocity maps at low Froude number based on the  $d_o$ ,  $Fr_{d_o}$ , showed the presence of two completely separated counter-rotating vortices when the free surface is at its maximum inclination on the vertical plane of measurement ( $\varphi=0^\circ$ ). As the shaking speed,  $N$ , was increased, the counter-rotating vortices, often denoted as toroidal vortex to characterize the three-dimensionality of the flow, were observed to extend towards the bottom of the cylindrical bioreactor and increase in magnitude. When  $N$  was further increased, a mean flow transition was observed, with the flow being dominated by an axial vortex precessing around the axis of the bioreactor. The analysis was carried out for different combinations of internal diameter,  $d_i=100$  mm and 130 mm, fluid heights,  $h=30-70$  mm, orbital diameters,  $d_o=15-50$  mm, and agitation speeds  $N=60-140$  RPM and was based on phase-resolved PIV and free surface measurements. A scaling law was

derived by noting that the maximum free surface inclination,  $\Delta h$ , is proportional to the ratio between the centrifugal acceleration due to the orbital motion and the gravitational acceleration (see Equation 1.6).

$$\frac{\Delta h}{d_i} = a_o \left( \frac{2 (\pi N)^2 d_o}{g} \right) \quad (1.6)$$

The constant of proportionality,  $a_o$ , depends on the fluid considered and according to Weheliye *et al.* (2013), is  $a_o=1.4$  for water. The relationship of Equation 1.6 was tested for several combinations of non-dimensional fluid height,  $h/d_i=0.3-0.7$ , and orbital to cylinder diameter ratio  $d_o/d_i=0.14-0.5$ . The measured data and the correlation of Equation 4 showed very good agreement at low  $Fr_{d_o} < 0.15$ , when the free surface can be approximated by an inclined elliptic disk with the longer axis being constantly aligned with the plane defined by the direction of the gravitational and centrifugal accelerations. At greater  $Fr_{d_o}$  the free surface started exhibiting a more complex three-dimensional shape and the averaged profile inclination of the free surface started deviating from the relationship of Equation 1.6. Phase-resolved PIV measurements showed that the variation of free surface shape corresponded to the onset of a flow transition from a horizontal toroidal vortex to a vertical one precessing around the cylinder axis, dominating the flow dynamics inside the bioreactor before and after the transition, respectively. These results are in agreement with those described by the flow visualisations and numerical simulations of Gardner and Tatterson (1992) and Kim and Kizito (2009), respectively. The flow transition was described by Weheliye *et al.* (2013) by considering that an increase of the rotational speed,  $N$ , (i.e.  $Fr$ ) corresponded to a growth in size of the toroidal vortex until it extended to the bottom of the tank. Weheliye *et al.* (2013) concluded that the flow transition can be predicted using either Equation 1.7 or 1.8 depending whether  $h/d_i \leq (d_o/d_i)^{0.5}$  or  $h/d_i \geq (d_o/d_i)^{0.5}$ ,

respectively.

$$\frac{h}{d_i} = a_o \left( \frac{d_i}{d_o} \right)^{0.5} Fr_{d_o} \quad (1.7)$$

$$a_o Fr_{d_i} = 1 \quad (1.8)$$

where the Froude numbers  $Fr_{d_o}$  and  $Fr_{d_i}$  are estimated from Equation 1.9 using the orbital and cylinder diameters, respectively.

$$Fr = \frac{2 \pi^2 N^2 d}{g} \quad (1.9)$$

Given the broad range of definitions of Froude number available in literature, the definition of Equation 1.9 was selected for consistency with the works of Büchs *et al.* (2001, 2000b); Maier and Büchs (2001); Weheliye *et al.* (2013) and is used throughout the results discussed in the Thesis.

Rodriguez *et al.* (2013) evaluated the kinetic energy in OSRs, by distinguishing between the kinetic energy due to periodic flow energy content and that due to the random velocity fluctuations in phase-resolved measurements. The kinetic energy due to the mean flow was estimated according to the two-dimensional approximation of Equation 1.10, where indices  $i$  and  $j$  refer to the velocity components measured in the plane considered, while the third component contribution is estimated as the average of the other two (i.e.  $\langle u_k \rangle^2 = \frac{\langle u_i \rangle^2 + \langle u_j \rangle^2}{2}$ ).

$$k_{ij} = \frac{3}{4} \left( \langle u_i \rangle^2 + \langle u_j \rangle^2 \right) \quad (1.10)$$

Before flow transition (BFT) to an axial vortical structure, the kinetic energy of a plane parallel to the vessel bottom ( $k_{r\theta}$ ) was found to be of comparable magnitude to the kinetic energy on a plane bisecting the vessel axially ( $k_{rz}$ ). On the other hand at conditions after flow transition (AFT), the  $k_{r\theta}$  was found to be 3 times larger than  $k_{rz}$  and Rodriguez *et al.* (2013) determined that the flow was

dominated by a tangential component of velocity  $u_\theta$ . The kinetic energy due to the random velocity fluctuations,  $k'_{ij}$ , is defined as:

$$k'_{ij} = \frac{3}{4} \left( \langle u'_i \rangle^2 + \langle u'_j \rangle^2 \right) \quad (1.11)$$

The random velocity fluctuations were found to be nearly negligible BFT, as the average intensity of  $k'_{rz}$  was at least two orders of magnitude lower than the energy content of the periodic flow,  $k_{rz}$ , whilst at AFT conditions regions of higher content of kinetic energy associated to the random fluctuations were observed at the sides of the bioreactor. By estimating the space averaged values for  $k_{ij}$  and  $k'_{ij}$ . Rodriguez *et al.* (2013) concluded that at BFT the  $k_{ij}$  are of comparable magnitude in both  $r$ ,  $z$  and  $\theta$  and the  $k'_{ij}$  are negligible due to the flow being laminar. At higher  $Fr_{do}$ , for AFT conditions, the space averaged  $k'_{ij}$  becomes significant, particularly in the  $r$ - $\theta$  plane, indicating the initiation of a degree of turbulence in the flow.

The flow in a partially filled unbaffled Erlenmeyer flask is characterised by a strong circular solid-body-like movement along the  $r$ - $\theta$  axis (*i.e.* parallel to the vessel bottom) with high velocity regions close to the wall (Mancilla *et al.*, 2015). The authors found that fluid mixing was enhanced by the strong velocity on the annulus at the bottom of the flask, whilst little motion was present in the bulk of the fluid. Large turbulent intensities were also found at the periphery of the flask bottom. It was found that the mean turbulent intensity increased with agitation rate and that it could be used to determine the quality of the agitation as the degree of mixing is dependent on the fluctuations in the flow. Phase- and time-resolved measurements demonstrated that the velocity peaks of the instantaneous (time resolved) and mean flow (phase averaged) are both located at the periphery of the vessel bottom, although with different intensities due to the type of averaging performed. The pseudo-turbulence, calculated from the phase-

resolved measurements, proved that the tangential pseudo-turbulence is dominant on the radial one. Baffled Erlenmeyer flasks were proven to be characterised by a wider distribution of velocity intensities with an improvement of the radial component of velocity, greater average turbulent intensity and lower deformation rate magnitudes that may be detrimental to cell culture. Such improvements were not observed to increase with the number of baffles in the flasks; in fact above 4 baffles the average turbulent intensity was found to be lower than that of an unbaffled vessel.

### 1.3.3 Flow in fluids of high viscosity

Ducci and Weheliye (2014) investigated the effects of fluid viscosity in the flow in cylindrical OSR by means of PIV. It was found that, for conditions before flow transition, a linear relationship exists between the free surface wave, which drives the motion of the liquid, and the Froude number. The constant of free wave height and  $Fr$  proportionality,  $a_o$ , which Weheliye *et al.* (2013) proved to be 1.4 for water, was found to decrease with increasing viscosity by a power-law relationship of the type:

$$a_o = a_{ow} \left( \frac{\nu}{\nu_w} \right)^{-0.0256} \quad (1.12)$$

where  $a_o$ , is the constant at a given viscosity,  $a_{ow}$ , the constant for water,  $\nu_w$  and  $\nu$  the kinematic viscosity of water and the viscous fluid under study, respectively. Ducci and Weheliye found this relationship valid up to  $\nu = 1.7 \times 10^{-6} \text{ m}^2\text{s}^{-1}$ , with fluids below this viscosity value exhibiting the same flow structures as water. Above  $\nu = 1 \times 10^{-5} \text{ m}^2\text{s}^{-1}$  flow dynamics before flow transition are reported to be significantly different, consisting of a vortex region below the lowest edge of the wave with opposite vorticity as that normally found in water-like viscosities. A very weak vortex was reported on the high free surface side and the bottom

of the vessel. The three vortical structures were found to merge as  $Fr$  or  $\nu$  were increased. Critical  $Fr$  was reported to decrease with increasing  $\nu$ , with a flow structure reminiscent of the toroidal vortex present for the in-phase condition, but rotating in the opposite direction. At higher  $Fr$  or  $\nu$  a strong radial stream was recorded from the lowest side of the free surface wave.

### 1.3.4 Vessel geometry fluid mixing enhancement

The mentioned fluid dynamics studies and flow scaling law of shaken systems are limited to cylindrical and flask geometries, but several other designs have been proposed in the literature in an attempt to improve process mass transfer at different scales. For example, at small scale, a 6-petaled flower shape cross-section micro-titre plate geometry was found to be the most promising among all the proposed designs (Funke *et al.*, 2009). At large scale,  $V=50-1500$  L, Zhang *et al.* (2008) proposed a novel bioreactor configuration, where helical tracks were positioned on the cylindrical walls resulting in 10-fold increases in mass transfer in comparison to unbaffled cylinders. Monteil *et al.* (2013) investigated a shaker tube with a bottom equipped with a downward cone, reporting that a higher shaking speed was required to obtain the same mixing times as a flat bottom cylinder having a similar diameter.

## 1.4 Mixing Time

Mixing time is a convenient parameter to quantify the performance of a reactor. The mixing time can be defined as the “time taken to achieve a given degree of homogeneity following a perturbation” (Cabaret *et al.*, 2007). Melton similarly defines it as “the evolution in time of spatially dependent concentration towards a

final homogenous state” (Melton *et al.*, 2002). A practical way to measure mixing time is to measure the time taken to achieve the steady state condition once a perturbation has occurred. As the steady state conditions may require a long time to be reached, a suitable threshold can be determined, over which a fluid is regarded as mixed within acceptance. Kasat and Pandit (2004) defined the mixing time as the time taken to reach within 5% of the mixing process’ steady state value, whilst Delaplace *et al.* (2004) used 90% as the homogeneity threshold for mixing time definition.

The mixing number  $NT$  is often used as dimensionless unit for mixing performance and is defined as  $NT = N \times t$ , where  $N$  is the agitation speed and  $t$  is the time taken to achieve mixing.

From a homogenizing perspective, mixing can be divided in micro-, meso- and macro-mixing, depending on which scale the process occurs. Micro-mixing is associated with processes of molecular diffusion at scales close to the Batchelor scale, meso-mixing between the Batchelor and Kolmogorov scale, whilst macro-mixing refers to scales larger than Kolmogorov scale (Bałdyga and Bourne, 1999; Lehwald *et al.*, 2012). Mixing time measurements for mixing vessels can be broadly divided in two groups (Local and Global measurement methods) based on the volume of fluid that is considered in the mixing evaluation. Local methods rely on physical measurements at one location to give a measure of mixing time. Usually intrusive probes are required that modify or alter the dynamics of the fluid being agitated. Also numerous probes would be required to provide measurements at a number of locations sufficient to illustrate an accurate picture of the overall mixing performance. Examples of local measurement techniques use chemical sampling, thermal, conductometric and fluorimetric methods (Ducci and Yianneskis, 2007; Li and Humphrey, 1991; Margaritis and Sheppard, 1981).

Global methods consider the whole volume, or at least the bulk part of it, in evaluating mixing. Global methods are unintrusive, do not perturb the flow and rely on chemical reactions and optical detection. The greatest benefit of global methods is that unmixed zones within the vessel can be identified and that the end point of mixing for the entirety of fluid can be found. Its main drawbacks are that it can be inaccurate (subjectivity of operator's measurement interpretation) and that a transparent vessel is required for observation.

Muller *et al.* (2005) was the first to find a way to obviate for the subjectivity due to the judgement of the operator by a series of photographs of a tracer in a mixing vessel. Liquid crystals have been used by Lee and Yianneskis (1997) to determine the mixed state of a fluid in a stirred vessel. A small quantity of high temperature liquid was introduced in the bulk of colder temperature fluid. The color of the liquid crystals contained in the bulk liquid changed as contact with the higher temperature fluid occurred. The hue variation of the liquid crystals was used to measure mixing time. This method proved to work for chaotic flows but a binding requirement was that the liquid crystal microcapsules had to be neutrally buoyant (therefore fluid density had to be equal to the liquid crystals). Two coloured powders were used to find the mixing time of a vessel containing a high viscosity fluid (Le Coënt *et al.*, 2005). Image processing was used by Le Coënt in conjunction with a box-counting method to determine the position of the powder particles within the vessel. Mixing time measurements have also been done using planar Laser Induced Fluorescent method (Houcine *et al.*, 1996; Hu *et al.*, 2010). Such method investigates the mixing patterns on the plane on which the laser is shed.

One of the most promising approaches used in the measurement of mixing time is one involving fast acid-base reactions within a vessel (Cabaret *et al.*, 2007; Delaplace *et al.*, 2004; Melton *et al.*, 2002; Tan *et al.*, 2011; Tissot *et al.*, 2010).

pH indicators are used to visualize the mixing of the fluid in the vessel. Image processing has been used to obtain an objective estimate of the measured mixing time.

Mixing time studies based on a colorimetric method have been carried by Tissot *et al.* (2010) and Tan *et al.* (2011) in shaken cylinders and flasks, respectively. This approach has been widely used in stirred tanks, employing either a single or a combination of two pH indicators, and it has been thoroughly analysed by Cabaret *et al.* (2007) to optimise both the experimental and post-processing aspects of the colorimetric methodology. In his work, Cabaret *et al.* (2007) investigated the macro-mixing time of a stirred tank using a fast acid-base reaction and one pH indicator or tracer. Cabaret's experiments tracked the colour change of the fluid contained in the vessel as a strong acid is added. A distinction between macro- and micro-mixing is offered by the author. When the ratio between the acid and base equals 1 (neutralization method) what is observable is micro-mixing (Cabaret *et al.*, 2007). Macro-mixing instead can be easily observed with acid to base ratios greater than 2 and such experiments are reproducible (Godleski and Smith, 1962). Godleski found that using an acid-base ratio of 1 the mixing time measurements had an average deviation of 4.04%, whilst a lower 1.97% average deviation was recorded for a 2:1 ratio. Using 1:1 proportion of acid and base yields higher mixing times because stoichiometric amounts of acid and base must react. Cabaret specifies that macro-mixing time refers to the completion of the distribution of the tracer and not the actual pH level at various locations in the vessel.

Melton *et al.* (2002) Dual Indicator System for Mixing Time (DISMT) uses two pH indicators, Methyl red and Thymol blue. The first indicator is red in acidic conditions and turns yellow above pH 5.6 whilst the second is blue in base conditions and turns to yellow below pH 8. Melton's experiment comprised of mixing

two fluids in equal quantities (1:1). Tissot *et al.* (2010) used the DISMT to estimate from visual observations the variation of mixing time in shaken cylinders of different nominal volumes with shaken speed,  $N$ , cylinder diameter,  $d_i$ , orbital diameter,  $d_o$ , and fluid height,  $h$ . The experiments were filmed and image processing was performed on the videos. It was found that the green channel was the one to vary more significantly and was therefore selected to measure mixing time. The RGB values of the solution at time  $t=\infty$  was set as a benchmark for homogeneity. Then the software measured the time taken for each pixel to go from the initial green channel value to within a 3% of the steady state value. The images were selected so that the free surface would always have the same shape and be in the same position (phase-lock). By means of such selection, only frames belonging to the same specific position of the orbital shaker were used. Only the pixels that varied more than 30 in the green channel between beginning and end of experiment were considered for analysis.

The study by Tissot *et al.* (2010) showed the presence of different regions within the tank characterised by very different mixing dynamics: a slow mixing zone close to the cylinder bottom, where mixing was mainly determined by diffusion, and a region closer to the cylinder wall, where the high shear rates induced fastest mixing. Mixing times were found to be inversely proportional to Froude numbers, defined in that study as  $Fr = \frac{\pi N (d_o + d_i)}{\sqrt{g d_i}}$ , while a reduction in cylinder diameter,  $d_i$ , resulted in an increase of mixing times at constant  $N$ . Based on these considerations and the experiments they carried out in small ( $V=30$  L), and large ( $V=1500$  L) scale bioreactors, they empirically derived the correlation of Equation 1.13 to scale the mixing time,  $t_m$ .

$$t_{m,1500L} = t_{m,30L} \frac{d_{o,30L}}{d_{o,1500L}} \quad (1.13)$$

where  $t_{m,1500L}$  and  $t_{m,30L}$ ,  $d_{o,1500L}$  and  $d_{o,30L}$  are the mixing times and orbital

diameters for the 30 L and 1500 L bioreactors, respectively. Tan *et al.* (2011) employed a single indicator system to determine through visual inspection the mixing in an unbaffled Erlenmeyer shaken flask. They reported that mixing times obtained with a colorimetric method are only indicative of the time required to achieve colour uniformity within the tank upon reaching a preselected pH threshold, as this does not necessarily imply pH homogeneity, which is achieved only when the diffusion process is complete. Therefore comparison with mixing times obtained with other techniques should be made with care. Taking this into account, Tan *et al.* (2011) showed by means of a log-log plot that mixing times in shaken flasks exhibit a similar trend to those obtained in stirred tank reactors with different types of impellers, with a decrease of mixing number with increasing  $Re$ . In contrast to the study of Tissot *et al.* (2010) for a shaken cylinder, Tan *et al.* (2011) concluded that the shaking diameter  $d_o$  has no significant effect on the mixing time in unbaffled Erlenmeyer flasks. However it should be noted that the reported agreement between the mixing times obtained for  $d_o=25$  mm and 50 mm vessels was within a tolerance of  $\pm 30\%$ . Table 1.1 summarizes mixing time performances for a variety of bioreactor types and conditions found in the literature.

## 1.5 Mechanical stress in OSRs and effects on cell culture

Cells cultured in a bioreactor are subject to mechanical stresses due to the fluid dynamics developing within the system; however in the published literature no agreement has been reached on the qualitative and quantitative effects of flow shear stresses on mammalian cells and their metabolism. High shear forces at the air/liquid interface in sparged bioreactors were reported to be detrimental to cell

growth (Cherry and Hulle, 1992). Recent works by Nienow *et al.* (2013) proved that density and product titre of CHO cells were not affected by industrially relevant shear stress levels, both in laminar converging devices and turbulent bioreactors stirred by Rushton turbines. A low shear environment caused by the use of controlled agitation rates, on the other hand, has been reported to affect cell viability, growth and metabolism (Aloi and Cherry, 1996; Elias *et al.*, 1995; Keane *et al.*, 2003). The effect of sub-lytic shear stresses was evaluated for baby hamster kidney (BHK) cells in terms of cell morphology and viability by (Ludwig *et al.*, 1992) and critical shear stress levels of 0.8 to 1  $\text{Nm}^{-2}$  were reported. In the prospect of stem cells grown in 3-dimensional microcarrier cultures, flow shear becomes crucial with respect to cell proliferation and lineage selection (Li *et al.*, 2011).

Hydromechanical damage on microcarrier-cultured cells arises from inter-particles collisions and from turbulent eddies, whose characteristic dimension is similar to the microcarrier size (Cherry and Papoutsakis, 1988). Ismadi *et al.* (2014) investigated the effects of flow shear stresses on mouse induced pluripotent stem cells attached on microcarriers cultivated in spinner flasks, and reported an agitation of 25 RPM and 7 days culture time as the optimal conditions. Nienow *et al.* (2014) developed a new method for the harvesting of human mesenchymal stem cell (hMSC) in a spinner flask. Their study indicates that intense agitation for a short period (7 mins), under the presence of a suitable enzyme, can promote cell detachment without damaging the cells or affecting their attributes, with an overall harvesting efficiency above 95%. Studies on the effect of shear stresses on mammalian and stem cell cultures are generally limited to global considerations, where cell population properties, such as product titre and cell viability, are related to global flow characteristics based on volume average velocity and shear stress. From this point of view a rigorous quantification of local shear stresses

and their distribution in the bioreactor are crucial to better understand their effect on the process, and be able to design suitable operating conditions. This is especially important for novel technologies like stem cells and cells for therapy, where shear sensitivity has not been fully investigated, and where the direction and magnitude of shear stresses have been found to have a major impact on cell expansion and differentiation into cell lineages (Sargent *et al.*, 2010; Stolberg and McCloskey, 2009).

## 1.6 Solid suspension

Shaken bioreactors are often used in combination with microcarriers for the purpose of cultivating anchorage-dependant cells. Whilst often adapted to suspension cultures, hybridoma and other cells give increased product yields when cultured attached to a substrate, resulting in smaller fermentation runs at higher densities (up to  $2 \times 10^8$  cells/mL). Microcarriers are also used in tissue engineering and cell for therapy culture (Ferrari *et al.*, 2012). Stem cells are adherent-dependant cells and traditional 2-dimensional static cultures rely on disposable multilayer vessels, which have become the common route for stem cell expansion (Simaria *et al.*, 2014). Large scale production of stem cells would require the use of 3-dimensional dynamic culture methods by employing microcarrier technology, as demonstrated by Frauenschuh *et al.* (2007); Sart *et al.* (2009); Storm *et al.* (2010). Common microcarrier concentrations in cell culture are 1.5-12g/L.

Cells grow as monolayers on the surface of small spheres or as multilayers in the pores of macroporous structures that are usually suspended in culture medium by gentle stirring. Cultures are inoculated when the cells are in logarithmic growth to promote adhesion. Initial attachment efficiency is promoted by keeping the microcarriers static or with intermittent agitation. Microcarriers consist of spherical

beads with a size of 100-300  $\mu\text{m}$ , and can be made of a wide variety of materials, amongst others: plastics, glass, acrylamide, silica, silicone rubber, cellulose dextran and collagen. Extracellular matrices connect cells in vivo by means of collagens, proteoglycans or fibronectin which can be used to coat microcarriers to promote cell adhesion in vitro. Due to the animal origin of the aforementioned matrices, polymers which can be designed with specific binding sites, such as dextran, are the preferred material for microcarriers. Another way to enhance cell adhesion is to coat a microcarrier with an ionic surface charge, as all vertebrate cells possess a negative surface charge at physiological pH (Borysenko and Woods, 1979).

### 1.6.1 Engineering aspects of microcarrier culture

Whilst most studies have focused on investigating optimal compositions of microcarrier materials, their concentration and cell culture media, little research has been undertaken on the engineering aspects of microcarrier use. Efficient flow dynamics are desirable for complete suspension of microcarriers, prevention of agglomeration and spatial gradients of culture parameters that can affect cell growth (Lara *et al.*, 2006). Recently Olmos *et al.* (2015) determined the critical agitation speed for the suspension of microcarrier in shaken Erlenmeyer and cylindrical vessels. The critical agitation, or just-suspended agitation rate,  $N_{js}$  refers to the condition at which all particles are completely suspended. Olmos used the Vachy-Buckingham theorem to obtain the non-dimensional model of Equation 1.14:

$$\frac{N_{js}}{\sqrt{g/d_o}} = \sqrt{\frac{Fr_{js}}{2\pi^2}} = A \left(\frac{h}{d_i}\right)^{0.5} \left(\frac{d_o}{d_i}\right)^{0.25} (\rho^*) \left(\frac{d_p}{d_i}\right)^{-0.07} \quad (1.14)$$

where  $A$  is a constant depending on the type of geometry used (1.39 for cylinder, 0.12 for Erlenmeyer flask), and  $\rho^*$  and  $d_p$  are the relative density and diameter of the microcarriers, respectively. In their work, Olmos *et al.* (2015) used trypan blue to stain a range of microcarriers under investigation and a camera fixed to an orbital shaker to record the side-view of the particle suspension. Images were recorded as the the agitation speed was increased stepwise and full suspension was visually determined from the images. It was observed that microcarriers suddenly move from a completely settled state to a suspended one within a few RPM, yielding an accurate just-suspended speed observational measurement. It was found that the microcarrier concentration had little influence on the critical  $Fr_{js}$  for complete suspension and that suspension would occur when the toroidal vortices reached the bottom of the bioreactor, as described by Weheliye *et al.* (2013). Olmos *et al.* (2015) did not find a significant correlation between the power dissipation and  $Fr_{js}$ , concluding that large  $d_o$  are beneficial to the minimization of power dissipation required for complete suspension.

In their work, Pieralisi *et al.* (2015) analysed the two-phase flow dynamics occurring in a cylindrical shaken bioreactor when microcarriers are employed in suspension under realistic process concentrations. Just-suspended speed was calculated through measures of the light scattered by the microcarriers that remain at the bottom of the vessel, for an increasing shaking speed, when a laser is directed parallel to the bottom plane of the cylinder.

The just-suspended speed was obtained from the brightness of the images taken on the horizontal measurement plane, located immediately above the vessel bottom, which is directly proportional to the amount of microcarriers settled at the bottom of the cylinder. The image brightness,  $I_B(N)$ , for a shaking speed,  $N$ , is calculated by adding the pixel greyscale,  $p_{ij}$ , across the area delimited by the bioreactor

walls, as defined by Equation 1.15.

$$I_B = \sum_{N_{tot}} p_{ij} \quad (1.15)$$

where  $N_{tot}$  is the total number of pixels in the area. Peralisi *et al.* (2015) introduced a normalized brightness index  $I^*$  to account for material defects of the vessel and lighting and to compare results at different conditions:

$$I^* = \frac{I_B(N) - I_B(\infty)}{I_B(0) - I_B(\infty)} \quad (1.16)$$

where  $I_B(0)$  is the brightness at zero-speed, and  $I_B(\infty)$  is the brightness at the highest speed at which measurements are taken (i.e. solids fully suspended). The  $I^*$  values hence ranged between 0 and 1. Peralisi *et al.* (2015) fitted the data into a curve of the form:

$$I^* = \frac{1}{1 + e^{a(x-x_0)}} \quad (1.17)$$

where the parameters  $x_0$  and  $a$  position the curve along the  $x$  coordinate and control its rate of decay, respectively. The just-suspended speed considered to be attained when the brightness index  $I^*$  was 95% of the fully suspended condition. Solid suspension was found to be directly linked to the  $Fr_c$  for flow transition from toroidal to precessional axial vortex flow in single phase systems, as defined in Equations 1.7 and 1.8. Solid suspension was observed to occur at  $1.1 \times Fr_c$  when a configuration  $h/d_i \leq (d_o/d_i)^{0.5}$  was used and 1.2 when an axial vortex was present, or  $h/d_i \geq (d_o/d_i)^{0.5}$ . Microcarriers were observed to be pushed from the periphery to the centre of the bioreactor bottom along a spiral pattern and to be sucked into the the bulk flow depression created at the centre of the bioreactor by the toroidal or axial vortex, for in- and out-of-phase (or AFT and BFT) conditions respectively.

## 1.7 Main Findings

The preceding literature review highlighted five major aspects relevant to a complete engineering characterisation of cylindrical OSRs.

- **Flow dynamics** Deformation of the free surface occurs in an OSR under agitation, with the free surface wave being highest on the vertical plane identified by the directions of the centrifugal and gravitational accelerations. This plane changes its orientation in space and rotates around the bioreactor axis as the shaker table proceeds along its circular orbit. Two flow types can be identified: a toroidal vortex and an axial vortex. The flow transitions from one type to the other with the increase of  $Fr$ . The toroidal vortices, present at low  $Fr$  originate from the sides of the bioreactor below the free surface, expand towards the vessel bottom as  $Fr$  is increased. The toroidal vortex flow occurs when the fluid moves synchronously to the shaker vessel, in a condition called in-phase, which corresponds to an elliptical free surface. Out-of-phase occurs when the fluid lags the orbital motion of the bioreactor, coinciding with a precessional axial vortex and a three dimensional free surface. PIV results have shown that the toroidal vortex presents completely separated counter-rotating vortical cells on the measurement plane and expand in size as  $N$  is increased. The available literature has focused on the transition from toroidal to axial vortex by looking at the mean flow transition, either through power input measurements, CFD or PIV, neglecting to investigate the cycle-to-cycle fluctuations of velocity fields. Such variations are likely to be present and be a significant contributor to the characteristics of the flow and mixing dynamics.

A scaling law was formulated to determine the conditions for which flow transition occurs from in- to out-of-phase on the basis of the toroidal vortex

expansion being limited by the physical width of the bioreactor and its  $h/d_i$  ratio. The applicability of such scaling law has to be confirmed and possibly modified for different OSR geometries, which are commonly used in the bioprocess industry (i.e. Erlenmeyer flasks or conical bottom OSRs).

- **Effects of viscosity** The scaling law derived by Weheliye *et al.* (2013) for water-like viscosity fluids can be adapted to higher viscosity fluids by the proportionality between the free surface wave height and  $Fr$  by using a power law relationship between the normalised viscosity of the fluid (Ducci and Weheliye, 2014). Up to a fluid viscosity of  $\nu = 1.7 \times 10^{-6} \text{ m}^2\text{s}^{-1}$ , the flow presents the same flow characteristics exhibited for water, with the toroidal vortices rotating in a direction which results in an upstream flow from the bottom of the vessel towards the free surface at the centre of the bioreactor. Rotation of the vortical cells occur in the opposite direction above  $\nu = 1 \times 10^{-5} \text{ m}^2\text{s}^{-1}$ .

The information regarding the flow in high viscosity fluids in OSRs is limited, with few studies (Ducci and Weheliye, 2014). Due to the growing application of high density cell culture, which increase the viscosity of the cell culture media, questions regarding the nature of the flow at a range of viscosities need to be addressed.

- **Mixing time** Fast acid-base reactions in presence of pH indicators are an efficient means of estimating global mixing in OSRs. Amongst other mixing time measurement methodologies, DISMT provides details of the mixing magnitude and dynamics and has been tested in OSRs. Image processing via software can be used to perform an objective measurement of recorded experimental images. The literature is abundant in choice for mixing time experimental methodologies, although few of these have been

tested in different bioreactor types and compared to one another to obtain a robust methodology which paired with a software based image analysis eliminates discrepancies due to operator subjectivity.

Mixing time experiments in cylindrical OSR show that mixing number,  $Nt_m$ , decreases with increasing agitation,  $N$ , decreasing fluid height to vessel diameter ratio,  $h/d_i$ , and decreasing internal to orbital diameter ratios,  $d_i/d_o$ . With low agitation a slow mixing region can be observed below the free surface. With higher agitation faster mixing times are present in the fluid close to the walls and slower mixing occurs at the centre of the vessel. Despite mixing studies have assessed the performance of OSRs (and STRs) in achieving homogeneity no effort has been made to improve mixing by changing the feed/addition location. This can have significant benefits in fed-batch cultures, where highly concentrated media additions can result in pH or nutrient gradients, detrimental to the cell culture. Furthermore research is lacking in knowledge of mixing characteristics in high viscosity fluids, both on the macro- and micro-mixing scales.

- **Solid suspension** Microcarriers, used in the suspension culture of adherent cells, require agitation to achieve suspension. The transition from settled state to suspended occurs over few  $N$  increments. The just suspended speed,  $N_{js}$ , and the just suspended  $Fr_{js}$ , dependant on geometric and operational parameters, are related to the  $Fr_c$  for flow transition. The research on solid suspension in OSRs has concentrated on the dynamics of suspension in flat bottom cylindrical OSRs or Erlenmeyer flasks, without attempting to improve it by modifying the vessel geometry in such a way to embrace the characteristics of the flow. This becomes more relevant in perspective of cell culture on microcarriers and emboid bodies for regenerative medicine, which might be subject to greater drag forces due to their larger size when

compared to individual cells, requiring higher agitation for their suspension.

## 1.8 Aims and objectives

From the literature review it is clear that the flow dynamics, mixing time and suspension mechanism are crucial phenomena in orbitally shaken reactors which affect either directly or indirectly the parameters controlling cell growth and product expression in the bioreactor. The objectives of the present study have been summarised hereafter:

1. To develop, compare and validate a robust and effective mixing time estimation methodology and image processing algorithm, in a variety of different vessels and scales;
2. To determine the mixing dynamics characteristic of in- and out-of-phase flow for water-like viscosities in OSRs at increasing  $N$  for different combinations of  $h$ ,  $d_o$  and  $d_i$  and formulate a criterion enabling mixing time scaling between different scales and different OSR geometries;
3. To assess different locations for feed addition for mixing time experiments and identify regions of segregated mixing;
4. To evaluate the effects of a modified vessel geometry with a conical bottom of variable height on: flow velocity field, vorticity intensity, shear rates, energy content and solids suspension;
5. To investigate flow characteristics and mixing dynamics, including macro- and micro- mixing phenomena, in low Re fluids (i.e. high viscosity) using DISMT and pLIF.

## 1.9 Thesis outline

The remainder of this thesis is divided in five chapters. In Chapter 2 the experimental set-up and methodologies employed in the research are described in detail. The design of the bioreactors employed in the work are detailed alongside the mixing time estimation procedures. A brief outline of the principles that govern PIV and pLIF is given together with the selection of experimental conditions. Chapter 3 addresses with the development of an image processing algorithm for DISMT to estimate mixing time. Various important aspects are discussed with regards to the acquisition of accurate data from the measurement methodology. Chapter 3 also investigates the mixing in water-like fluids agitated in a cylindrical OSR for different combinations of  $d_o$ ,  $d_i$  and  $h$ . The mixing time results of this research are juxtaposed with data previously reported in the literature and a scaling law is suggested to scale mixing in OSRs of various geometries and sizes. Chapter 4 includes the study of the effects of a conical bottom geometry in a cylindrical OSR. The flow dynamics are studied by means of phase-resolved PIV and vorticity, shear rates and kinetic energy content are determined from the data, whilst highlighting the differences between a flat and conical bottom geometries. The potential improvement to solid suspension by a raised cone in the vessel is also investigated in Chapter 4 and a relationship between flow transition and solid suspension is suggested. In Chapter 5 the flow dynamic behaviour of fluids of higher viscosity are examined. The DISMT is used to evaluate macro-mixing performances and determine the location of segregated or slow mixing regions. The evolution of the flow structure with increasing  $N$  is described and the effects of shear rate are evaluated from pLIF measurements. The Thesis terminates with Chapter 6 where the conclusions are drawn and recommendations for future work are made.

Name	Bioreactor Type	Measurement Methodology	Nominal Volume [L]	Working Volume [L]	Fuid height, hf [cm]	Internal Diameter, di [cm]	Orbital Diameter, do [cm]	Agitation [RPM]	Froude Number, Fr	Mixing Time [s]	Mixing Number [-]	Reference	
Multiple Impeller	STR	Conductivity	65	63	90	30	-	100		90	150	Kasat, 2004	
								225		55	206		
								480		28	224		
Rounded Bottom Vessel	STR	DISMT	30	30	-	34.6	-	100 (gyration 19)		33	-	Delaplace, 2004	
BioWave	Wave	-	2	1	-	-	-	16		50	-	Eibl, 2010	
			200	100				6 degree angle		150			
Mobius CellReady	STR	-	3	-	-	-	-	-		-	34	Eibl, 2010	
Cylindrical Vessel	OSR	DISMT	30	13	20	28.7	2.5	5	90	0.95	40	60	Tissot, 2010
									110	1.16	25	46	
									140	1.47	15	35	
									90	0.88	70	105	
			2	1	13	10	5	110	1.07	30	55		
								140	1.36	18	42		
								100	0.79	110	183		
								110	0.87	50	92		
								130	1.03	25	54		
			3	1	7.5	13	5	100	0.83	60	100		
								110	0.92	40	73		
								130	1.08	15	33		
			1500	500	40.75	125	10	40	0.81	70	47		
50	1.01	18						15					
60	1.21	10						10					
Shake Flask	OSR	DISMT	500	50		10.5	5	100	0.80	10	16	Tan et al, 2011	
								150	1.20	7	18		
								350	2.80	2	12		

Table 1.1: Mixing time results available in the literature for OSRs and STRs.

# Chapter 2

## Methodology

### 2.1 Introduction

The research undertaken aims at characterising cylindrical OSRs from the perspective of mixing, flow dynamics and solid suspension. Several mixing time methodologies were employed on both OSRs and STRs to validate the DISMT and the home built code developed for objective mixing time estimation. The work was undertaken on OSRs of different internal diameter,  $d_i$ , some of which were designed with interchangeable bottoms. Iodine-Thiosulfate decolourisation, pH probe measurements and dye dissipation were used to assess mixing in STRs and validate the DISMT technique. Phase-resolved Particle Image Velocimetry (PIV) was used to measure the velocity field in OSRs with flat and conical bottoms. The effect of the conical bottom was also assessed in terms of solid suspension. The flow dynamics of high viscosity fluids was evaluated in terms of mixing, using DISMT, and flow visualisation, using pLIF.

## 2.2 Bioreactor vessels

### 2.2.1 OSR Vessel v.1

A 2L nominal volume vessel, previously used in the PhD work of Weheliye (2013) was also employed in this work (see Figure 2.1), and will be denoted in the remainder of this thesis as ‘cylindrical OSR v.1’. The internal diameter,  $d_i$ , height,  $H$ , and wall thickness,  $t_c$ , of the polished borosilicate glass cylindrical vessel measure 100, 250 and 5 mm, respectively. The cylinder was contained in a Plexiglass trough, with de-ionized water in between the cylinder and the squared trough to minimize diffraction. Water was chosen as its refractive index (1.33) is very close to those of glass (1.5) and Plexiglass (1.49). A steel structure encloses the trough and cylinder leaving the top of the cylinder open, while the flat bottom of the bioreactor was transparent to allow optical access. The glass cylinder and Plexiglass prism were held tightly together by an external steel structure that left the four sides of the trough unobstructed and the top of the cylinder open, so to ease volume filling/emptying and allow feed insertion from any location above the vessel. Adequate sealant was used to make the container watertight and avoid contamination between water contained in the trough and the fluid in the cylinder. In the rest of the thesis a cylindrical coordinate system,  $r, \theta, z$  is employed with the origin positioned at the cylinder axis on the bioreactor base.

### 2.2.2 Feed insertion rig

To perform mixing time experiments the orbital shaken reactor described in Section 2.2.1 was equipped with a feeding pipe which can be accurately located on the open end of the glass cylinder, at one of seven different radial positions (p1-p7) located along the diameter of the cylinder at 14 mm intervals (p4 was

on the cylinder axis, see Figure 2.2). The feeding pipe was constructed with microfluidics connectors (IDEX Health and Science) and was fed by a syringe pump. The Harvard Apparatus 11 Elite Infusion/Withdrawal Programmable syringe pump provides accurate automatized supply of  $\mu\text{L}$  volumes for the mixing time experiments performed.

### 2.2.3 OSR Vessel v.2

The rig described in Section 2.2.1 was redesigned to allow for replaceable cylinder bottoms. This bioreactor is denoted as ‘cylindrical OSR v.2’ for the purpose of this thesis. The redesigned cylindrical OSR is shown in the schematic and exploded view of Figure 2.3 (a) and (b), respectively. The new bioreactor vessel was designed to improve disassembly and cleaning as well as being able to change the geometry of the vessel bottom. The internal cylindrical vessel was identical to that of OSR v.1, with an acrylic trough and a steel enclosure. Water-tight seals were achieved with o-rings enabling ease of disassembly and vessel bottom replacement. Three bottom geometries were designed for this work: flat, conical A (cone height,  $h_c=5$  mm; angle from the horizontal,  $\alpha_c = 6.3^\circ$ ) and conical B (cone height,  $h_c=15$  mm; angle from the horizontal,  $\alpha_c = 18.4^\circ$ ). It should be noted that the conical bottoms used in this work were truncated cones, with a 10 mm upper face diameter. The bioreactor bottoms were manufactured on a lathe from a solid piece of Perspex and designed to be interchangeable on the cylindrical vessel. The manufacturing and polishing process allows good optical access to the measurement area, and refractive index matching with the working fluid minimises diffraction from the conical bottom profile. The OSRs vessel v.2 was manufactured in three sizes of different internal diameter:  $d_i = 70, 100$  and 130 mm with fixed cylinder height,  $H=250$  mm, and wall thickness,  $t=5$  mm.

## 2.2.4 Shaken platform

Two shaken platforms were used in this work: the Kühner L-SX and SR-200X shakers. The vessel assembly v.1 and v.2 were securely fastened on the two shaker tables. The L-SX shaker is a bench-top orbital shaker platform that uses magnetic direct drive (see Figure 2.4 a). The shaking diameter,  $d_o$ , can be varied between 15 and 50 mm and the range of shaking speed,  $N$ , is 20–500 RPM, controlled by a panel interface. The L-SX shaker tray has an array of threaded holes useful to secure containers or equipment. The shaker was equipped with a Hall-effect encoder. A magnet on the rotating shaft triggered the encoder at every revolution, with a  $1^\circ$  angular resolution, and could be used to trigger the measurement device (either DIMST, PIV or pLIF) at any specific angle over the  $360^\circ$  circular orbit. The SR-200X is a magnetic direct-driver shaker for heavy loads with a  $0.72 \text{ m}^2$  tray for bulky devices (see Figure 2.4 b). The shaking diameter,  $d_o$ , was fixed at 50 mm and the shaking speed,  $N$ , could be varied 20–300 RPM via a control panel interface. Similarly to the smaller shaker table an Hall-effect encoder was integrated also into this system to enable phase resolved triggering of external measurement devices.

Orbital shakers function by rotating on an off-centre axis, this results on the cylinder moving on a circular orbit. In this work an arbitrary reference field was introduced to consistently identify the angular position of the cylindrical OSR on the shaker’s orbit. The position furthest from the left was defined as  $\varphi = 0^\circ$  with  $\varphi$  increasing with the clockwise motion of the shaker as shown in Figure 2.5.

## 2.2.5 Other bioreactors used

Besides cylindrical OSRs v.1 and 2, mixing time experiments were performed in other types of bioreactors, both OSRs and STRs. The first STR was a single use 3L bench-scale Mobius CellReady shown in Figure 2.6. The bioreactor consisted of an unbaffled 137 mm diameter plastic tank with a height to diameter ratio of 1.8:1. The CellReady maximum and minimum working volumes were 2.4 and 1 L, respectively. It was agitated by a 3 blade, up-pumping marine impeller 76.2 mm in diameter, with 28 mm impeller clearance (Kaiser et al., 2011). In the mixing time experiments reported in Chapter 3, filling volumes of 1 and 2 L were used, while the impeller speed range was  $N=100-200$  RPM.

The second STR was a New Brunswick BioFlo-110 5.5 L glass vessel with a dome base and removable baffles, where agitation is accomplished with two Rushton impellers, as shown in 2.7. The vessel diameter and height were 190 mm and 290 mm, respectively, and mixing time experiments were carried out with a filling volume  $V_f = 4.5$  L for a rotational speed  $N=50$  RPM.

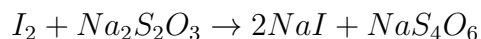
Mixing time experiments presented in Chapter 3 were also performed in DIN ISO 24450 wide mouth Erlenmeyer flasks. The two Erlenmeyer flasks had nominal volumes of 1 and 2 L with flask bottom diameters of 131 and 166 mm, respectively, with corresponding filling volumes of 400 and 800 mL. Experiments were carried out with an orbital diameter  $d_o=25$  mm, and agitation rates,  $N=100-200$  RPM.

## 2.3 Mixing Time experiments

Mixing time experiments were performed in various types of bioreactor vessels using different mixing time estimation techniques, both global and local, such as iodine-thiosulfate decolourisation, water-blue dye, pH probe and Dual Indicator System for Mixing Time (DISMT) (Melton *et al.*, 2002).

### 2.3.1 Iodine-Thiosulfate decolourisation

The reaction between Iodine and Sodium thiosulfate is a decolourization reaction, where the colour changes from deep orange to colourless. This methodology has been often applied in mixing time studies, i.e. such as in the work of Cronin (1992) where Iodine decolourisation due to Sodium thiosulphate was used to quantify liquid phase mixing times in aerated dual rushton STRs. The chemical reaction is shown below:



This method offered a very distinct end-point of homogenisation, and could be effectively used to visualise the hydrodynamics associated with mixing (Nienow *et al.*, 1996). The decolourisation between Iodine and Sodium thiosulfate required a 1% v/v addition of 1.8 M Sodium thiosulphate to a 5 mM Iodine solution and resulted in a colour change from deep orange to clear.

### 2.3.2 Water blue Dye

Colouring dyes are highly concentrated colouring agents that come in many different forms, such as powders or liquids, and do not change the property of

the solution they are added to. Mixing times and flow patterns can be estimated by adding the dye to a colourless fluid of known density and viscosity and measuring the time taken for colour homogeneity. In this work WaterBlue Dye (Fluka, Sigma-Aldrich, UK) was prepared in water at a 15 mg/L concentration. This methodology was used in the Mobius CellReady STR as described in Section 3.3.1. The dye was manually fed at the fluid free surface with concentration of 0.5 mL at a fixed location 50 mm from the impeller axis.

### **2.3.3 pH Meter**

Mixing time can be estimated by measuring pH variation in a fluid where a chemical reaction is occurring. A pH meter is used for measuring the acidity or alkalinity of a liquid. A typical pH meter consists of a glass electrode connected to an electronic meter that measures and displays the pH reading. pH provides a quantitative information by relating the degree of acidity or basicity of a solution to the hydrogen ion activity. The pH probe, consisting of concentric silver/silver chloride electrodes immersed in independently sealed buffer solutions, measures the potential difference between the ions  $H^+$  entering the inner glass electrode (through a thin glass bulb) and the reference buffer, which is shielded from the fluid to be measured.

### **2.3.4 Dual Indicator System for Mixing Time**

The Dual Indicator System for Mixing Time (DISMT), first developed by Melton *et al.* (2002), was the main methodology employed for the mixing time measurements carried out in shaken bioreactor systems.

DISMT comprises a fast acid-base reaction between Sodium Hydroxide (NaOH)

and Hydrochloric Acid (HCl) in the presence of two pH indicators, Methyl Red and Thymol Blue. The Methyl Red indicator turns from red to yellow in the pH interval 4.2-6, while Thymol Blue results in hues varying from yellow to blue for pH=8.0-9.6. The combination of such pH indicators results in the fluid being red for pH <6, blue for pH >8 and yellow for 6 <pH <8. The indicators were prepared in a volume of de-ionized water at a final concentration of 4.3 mg/L. This allowed mimicking typical media solutions used in mammalian cell cultures, which have water-like viscosities (Tissot *et al.*, 2010).

The fast acid-base reaction was initiated by inserting stoichiometric amounts of base (Sodium Hydroxide) in an acid solution of Type 2 pure Lab Water (ASTM D1193) and 0.5 mL/L of Hydrochloric Acid at a concentration of 0.75 M. At the beginning of the experiment the solution in the bioreactor was acidic (red). The base was inserted after the shaker table had completed at least ten revolutions and the flow inside the bioreactor was fully developed. A detailed description of the procedure can be found in the Appendix.

### **2.3.5 Experimental rig**

The experimental setup for mixing time measurements comprised of the following components: cylindrical OSR v.1 or v.2, shaking platform, camera, syringe-pump, encoder and desktop pc.

The vessel was positioned on a Kühner AG LS-X lab shaker equipped with a 360° encoder, as shown in Figure 2.8 (a) and (b). A feeding pipe constructed with microfluidics connectors (IDEX Health and Science) was connected to a Harvard Apparatus syringe pump, which was capable of providing accurate automatized supply of  $\mu\text{L}$  volumes of reagents for the mixing time experiments. A colour NET iCube camera was fixed to the shaker table to record the experiments in a

stationary reference system with respect to the cylindrical vessel. The camera had a global shutter, 1280x1024/SXGA resolution and 1/1.8" colour CMOS sensor. Placed 200 mm away from the vessel, the camera had the entire vessel's working volume in its field of view.

To reduce background noise an 8 LED OMC panel with a homogeneous 580 mcd white light source was positioned at the back of the experimental rig and rotated rigidly with the shaker table. The shaker table encoder and IDT MotionPro X Timing hub allowed complete synchronization of the motion of the table, the camera and the syringe pump insertion. The feed insertion was always made when the shaker table was at its position further to the left and it was nearly instantaneous, lasting around 2 ms (i.e. over an angle of rotation  $\Delta\varphi < 2^\circ$ ). Phase-locked images were recorded at every revolution for a phase angle  $\varphi = 0^\circ$  (see Figure 2.5), which corresponded to the orbital point furthest to the left when the system is viewed from the top. Phase-locked measurements allowed to 'freeze' the free surface motion at its maximum inclination position, resulting in a significant simplification of the image post-processing routines which did not need to take into account the cyclic variation of the fluid distribution inside the tank. Similar set ups, including an LED backlight for illumination, and a syringe pump for feed insertion at a fixed position above the working fluid surface, were also employed in mixing time measurements in BioFlo and CellReady STRs, but in this case it was not necessary to synchronise the iCube camera with the impeller, as it did not provide any advantages in terms of image-post processing (i.e. the free surface shape was fixed irrespective of the angular position of the impeller).

### 2.3.6 Experimental conditions

Mixing time was evaluated for a total of 5 OSRs and 2 STRs. DISMT was used in all of the OSRs, whilst a variety of mixing time estimation methodologies were used for the STRs. Three of the cylindrical OSRs were OSR v.1 and 2 of  $d_i=70$ , 100 and 130 mm and were operated at  $d_o=25$  mm, at different fluid heights and an agitation speed ranging  $N=70$ -220 RPM. The effect of feed insertion position was investigated for the  $d_i=100$  mm cylindrical OSR, whilst for all other experiment sets the feed position was kept constant at position 3 on the feeding rig, which was 14 mm from the cylinder axis on the high crest of the free surface wave.

The two Erlenmeyer flasks, 1 and 2 L nominal volume were used at agitation speed  $N=100$ -200 RPM, with feed insertion performed at the centre of the flask mouth with an automatic pipette. The orbital diameter was kept constant,  $d_o=25$  mm. For this set of experiments the fill to nominal volume ratio was kept constant at 40%, in order to perform experiments consistent to those carried out in cylindrical OSRs. It is worth to remark that this ratio is higher than those generally used in practical applications, for example in the study of Tan *et al.* (2011), where the fill and nominal volumes were 50 and 500 mL, respectively, with a volume ratio of 10%.

The New Brunswick BioFlo and Cellready STRs were run at different fill volumes and at varying stirrer speed. Different pH/colourisation methodologies were used to measure mixing in the STRs and their effectiveness at estimating mixing was evaluated: DISMT, Iodine-Thiosulfate decolourisation, Blue-dye dispersion and pH probe. The insertion position was fixed at 50 mm from the impeller axis.

The DIMST was performed concurrently to measurements taken by pH probes built into the New Brunswick BioFlo and Cellready STR bioreactors. This allowed to validate and further assess the mixing time estimates obtained from the

DISMT colorimetric methodology. In the new Brunswick BioFlo pH readings were acquired every 12 seconds by the BioFlo controller connected to a Hamilton Easyferm plus k8325 probe, while the data acquisition rate of the pH probe of the CellReady bioreactor was 1 Hz. The two off-the-shelf STRs were not equipped with an encoder, and, as a consequence, phase-resolved DIMST measurements could not be carried out as for the OSRs. For these sets of experiments the iCube camera was triggered at a constant frequency of 4 Hz, which is fast enough to capture the mixing dynamics of the bioreactors, and the pH measurements were started concurrently with the image acquisition at the instant of base addition. In the CellReady bioreactor, addition of a stoichiometric amount of NaOH was performed at the free surface using a port on the top cover at a radial position 50 mm from the impeller axis using the microfluidics connectors and syringe pump. Two fill volumes were investigated: 1 and 2 L at agitation rates ranging between 100-250 RPM. In the new Brunswick BioFlo experiments were performed with  $V_f=4.5$  L and  $N=50$  RPM. In agreement with previous studies (Cabaret *et al.*, 2007; Melton *et al.*, 2002; Tissot *et al.*, 2010), complete mixing was assumed to be achieved when pH variation measured by the pH probe due to a fast Sodium Hydroxide (NaOH) and Hydrochloric Acid (HCl) reaction were within 5% of the final pH average value.

Table 2.1 provides a summary of the different combinations of experimental conditions, mixing time methodologies and reactors investigated in this study.

## 2.4 Solids suspension

Two v.2 OSR cylindrical vessels ( $d_i=100$  and 70 mm) with interchangeable bottoms (see Section 2.2.3) were used for the evaluation of just-suspended speed with microcarriers. The OSRs were rigidly mounted to the Kühner LS-X shaker

together with the Net iCube camera and led backlight. Images were acquired at every revolution using the Hall-effect encoder. Cytodex 3 microcarriers (GE Healthcare Life Sciences) were used at a concentration of 1.5 g/L. The density of the swollen microcarrier was  $\rho=1.04 \mu\text{g/L}$  and the mass median diameter,  $d_{50}=175 \mu\text{m}$ . To enhance microcarrier visibility, they were immersed in Trypan Blue (ThermoFisher Scientific) for 12hrs from dry. Once completely swollen in Trypan, the Cytodex 3 microcarriers were filtered in a  $40 \mu\text{m}$  sieve to eliminate any Trypan which had not been absorbed by the microcarriers.

The stained microcarriers were added to de-ionised water in the OSRs and would settle within minutes on the bioreactor bottom. The experiment would start at low  $N$  ( $\sim 80$  RPM) and agitation increased step-wise until full suspension was obtained. Phase resolved images were taken at each  $N$  condition. Such procedure was repeated for the  $d_i=100$  and  $70$  mm OSR at an orbital diameter  $d_o=15, 25$  and  $50$  mm and for different fluid heights.

The acquired experimental images were analysed using a Matlab code, which measured the intensity of the greyscale of the liquid volume in the bioreactor. The Trypan-dyed microcarriers yielded a strong contrast in the clear DI water and the purpose built matlab code could measure the intensity of the image using the normalised brightness index defined in Equation 1.16. Similarly to the mixing time experiments, the settling time was estimated when the variation of the brightness index,  $I^*(N)$ , was within 5% of the final average value. A detailed description of the image processing algorithm, which relates the image greyscale to the local microcarrier suspension is provided in Section 4.3.

## 2.5 Particle Image Velocimetry

### 2.5.1 PIV Introduction

2D Particle image velocimetry (PIV) was used to study the flow inside cylindrical OSRs. The well-established technique consists of three fundamental elements: a laser light source, a high speed camera and a working fluid with tracer/seeding particles. The diameter of the flow tracing particles must be small enough not to interact with the flow. PIV allows to perform un-intrusive and whole field measurements of flows. Neutrally buoyant particle tracers are illuminated by a sheet of laser light with two short light pulses in a short time interval. The tracer particles scatter the light from the laser and the image is recorded by a high speed camera capable of taking single or double exposure frames of the scattered light from the two laser pulses. Fluorescently labelled particles can be used in combination with a wavelength-specific pass filter to remove background light.

The digitally acquired images are processed via software which measures the relative motion of the tracer particles between the image pairs. This is achieved by dividing the whole field image in ‘interrogation areas’ and calculating the relative motion of the particles within that area. The local displacement of the interrogation area is computed via statistical methods, such as auto- or cross-correlation. The interrogation area size is carefully selected so to include 3-10 tracer particles as it is assumed that all particles in that area move homogeneously. The schematic of the working principle of PIV is shown in Figure 2.9.

## 2.5.2 PIV experimental setup

The 2D PIV system employed in this study to determine velocity characteristics as well as estimates of local distribution of kinetic energy, shear rates and vorticity of the flow in the cylindrical OSR consisted of a continuous green diode laser, a cylindrical lens, a high speed intensified camera and a timing box. It should be noted that the laser, mirror and camera were all rigidly mounted on the tray of the shaker table. The laser employed has an output power of 300 mW with a wavelength of 532 nm and the size of the laser head is 30×50×120 mm. The intensifier in the camera amplified the photons entering the camera lens, allowing short exposure times (5  $\mu$ s) with the low power laser. A cylindrical lens was mounted in front of the laser to create a laser light sheet of approximately 1 mm thickness.

Schematic diagrams of the PIV system set up for measurements on vertical planes are provided in Figure 2.10. The rectangular mirror was placed below the bioreactor at a 45° angle so to reflect the laser sheet by 90° and illuminate the base along the vertical plane orthogonal to the camera bisecting the cylinder into two halves. Rhodamine-coated Polymethyl methacrylate spheres (50  $\mu$ m) were used for the PIV measurements in conjunction with a 570 nm orange cut-off filter mounted on the 60 mm camera lenses to minimize reflections of the laser.

The alignment of the laser plane was performed by using two reference holes of 4 mm diameter in the bottom and top steel plates of the cylindrical OSR, as shown in Figure 2.11. The bottom holes, in line with the diameter of the cylinder, let the laser sheet through the base, and allowed the laser light to reach the top plate, which was equipped with four holes in analogous position. Simultaneous passage of the laser through the base and the top holes ensured the laser was aligned with the cylinder internal diameter and perpendicular to the vessel bottom.

In order to carry out phase-resolved measurements the PIV system was synchronised with a magnetic encoder mounted on the shaker table. The encoder is placed on the shaker table while the magnet is fixed to the drive, so that a signal is triggered when the magnet faces the encoder at the position denoted by  $\varphi = 0^\circ$  in the sketch of Figure 2.5. The origin of the phase angular coordinate corresponds to the shaker being at the point furthest to the left along its clockwise circular orbit when seen from above. The encoder is connected to a timing box and a time delay can be selected through the Dantec Dynamic Studio software to trigger the camera at the desired angular positions of the shaker table and to collect the pair of images required to carry out PIV processing. 20-50  $\mu\text{m}$  rhodamine coated spherical particles were used for the PIV measurements because, together with the cut-off filter, helped minimise reflections at the walls and at the free surface.

An adaptive correlation analysis of the full image was applied with an initial interrogation window of  $256 \times 256$  pixels and a final window of  $32 \times 32$  pixels. A 50% window overlap was used for a final resolution of  $16 \times 16$  pixels, corresponding to an area of  $1.3 \times 1.3 \text{ mm}^2$  for a cylinder of diameter,  $d_i = 100 \text{ mm}$ . The adaptive correlation method is a multi-scale correlation approach, where velocity vectors estimated from larger area are used as input to the next correlation step. In this way a preliminary velocity direction is estimated to compute the final vector fields corresponding to the final interrogation area. The number of images obtained for each experiments varied in a range of 100-1000, while the image acquisition frame rates were set between 0.02-1 kHz. It should be noted that all the experiments carried out in this thesis were conducted at room temperature, controlled at  $20\text{C}^\circ$ .

### 2.5.3 Selection of PIV software and analysis parameters

The post-processing parameters for the PIV data were evaluated to find the most suitable for the experiments performed in this work. The PIV software, Dantec Dynamics Dynamic Studio, was evaluated against two other software: JPiv and PivLab.

A sample vector field for a flat bottom OSR,  $h/d_i=0.5$  and  $N=105$  RPM at  $\varphi=0^\circ$  is shown in Figure 2.12. It should be noted that reference is made to a negative radial coordinate,  $r$ , which is used to discriminate between points to the left and right hand sides of the bioreactor axis. Figure 2.12 shows separated counter-rotating vortical structures on the sides of the bioreactor as described by Weheliye *et al.* (2013). The phase resolved measurements, performed at the position furthest to the left, are defined as:

$$\langle \mathbf{u}_i \rangle = \frac{1}{N_\varphi} \sum_{i=1}^{N_\varphi} \mathbf{u}_i \quad (2.1)$$

where  $u_i$  is the instantaneous velocity field,  $N_\varphi$  is the number of measurements taken at a given phase angle  $\varphi$ .

The effect of mesh size on the calculation of vector fields in Dynamic Studio was studied for the velocity vector field in Figure 2.12 at a distance of  $z/d_i=0.15$  from the vessel bottom. The velocity profiles of the axial and radial components of velocity,  $u_r$  and  $u_z$  respectively, are shown in Figure 2.13 for two interrogation window (IW) sizes  $16 \times 16$  and  $32 \times 32$  pixels, both with a 50% window overlap. The velocity profiles for IW32 and IW16 do not differ by a large margin, but the latter showed higher levels of random error, because the  $16 \times 16$  pixel size was not the recommended 4 times larger than the maximum particle displacement and too few particles were present in the IW16. Therefore a IW32 was used in this

$\tilde{\text{work}}$ .

PIV processing software allow for different levels of analysis, such as image/vector masking and post processing averaging. Figure 2.14 compares the velocity profiles for  $h/d_i=0.5$ ,  $N=105$  RPM,  $\varphi = 0^\circ$  and  $z/d_i=0.15$  at a IW32 with and without image masking and vector validation. The validation was used to eliminate spurious vectors by applying a peak and local neighbourhood validation. Peak validation eliminates invalid vectors, where one peak is greater than another by a tuneable ratio, in this work set at 1.2. Peak validation can help identify invalid vectors, but is unable to produce an estimate of what the correct vector might be. With ‘Local neighborhood validation’, individual vectors are compared to the local vectors in the neighbourhood vector area. If a spurious vector is detected, it is removed and replaced by a vector, which is calculated by local interpolation of the vectors present in the area. Interpolation is performed using median or moving average methodology (with  $n$  iterations depending on the number of spurious vectors).

Figure 2.14 shows that a better velocity profile can be estimated close to the walls of the OSR walls by applying a mask, but no difference is made in the bulk of the liquid. Peak validation on the other hand removes random errors and local peaks smoothing the velocity profile. Although some information of the small scale velocity structures might be lost, the phase resolved flow over the entire bioreactor is measured more accurately by employing Local neighborhood vector validation.

The Dantec Dynamics Dynamic Studio software was evaluated against JPiv and PivLab, free-ware software for PIV analysis. The velocity profiles evaluated with the three softwares are shown in Figure 2.15. No significant difference was found in estimating the velocity vectors with the different software, and therefore Dy-

nostic Studio was selected for its superior flexibility and better integration with acquisition hardware.

## **2.6 Planar Induced Fluorescence**

Planar Laser Induced Fluorescence (pLIF) is an optical technique capable of measuring passive scalars such as concentration gradients in a flow. pLIF is based on the measurement of the fluorescence of a dye when illuminated by a laser. As the dye is excited by a pulsed laser, it emits energy photons at a specific wavelengths. The dye is chosen based on the absorption and emission wavelengths, and its quantum efficiency. The absorption and emission frequencies should not overlap to avoid auto-excitation of the dye, which is called self-quenching.

Rhodamine 6G was used in this work as it is highly soluble, chemically stable and has a high quantum efficiency. The absorption and emission wavelength are 532 and 560 nm, respectively. A cut-off orange filter (570 nm) was used to eliminate the light originated from the exciting laser.

### **2.6.1 Combined pLIF and PIV experimental set up**

To perform simultaneous pLIF and PIV measurements on cylindrical OSR vessels an experimental rig was arranged, consisting of two high speed cameras, 532 nm dual laser Litron Nano-L 50-100 mJ (Nd:YAG) laser, a laser arm, SR-200X shaker, a dichroic mirror. Silver coated glass spheres were used for the PIV measurements, whilst Rhodamine dye was employed for the pLIF measurements. High and low-pass filters on each camera allowed for one camera to film the Rhodamine dye and the other the tracer particles. The components were positioned as shown in

Figure 2.16. A Hall-effect sensor in the SR-200X shaker was used to provide an external trigger whilst Dantec Dynamic Studio was used to control laser pulses and image acquisition.

## 2.7 Concluding Remarks

In this chapter an overview of the bioreactor vessels and experimental methodologies is provided. The cylindrical bioreactor v.1 and v.2 with replaceable conical bottoms, their arrangement on the shaker platforms and synchronisation with camera recording equipment and feed insertion rig for mixing time studies is described. Other STRs employed in this work, namely the NewBrunswick BioFLo and Mobius Cellready, are briefly introduced. The different mixing time methodologies under consideration are detailed with the necessary reagents and pH indicators required. The complete list of mixing time experiments performed with the DISMT, Sodium-Thiosulfate, pH probe and blue dye in a total of 5 OSRs and 2 STRs is provided in Table 2.1.

The methodology to assess solid suspension of Cytodex 3 dyed in Trypan blue is specified in Section 2.4. The 12hr staining protocol was found to successfully generate contrast with the background enabling a home-built image processing code to assess the agitation rate required for complete microcarrier suspension.

A brief introduction of the principles of PIV is provided along with an explanation of the experimental arrangement used. Rhodamine-coated Polymethyl methacrylate spheres were used as tracers and a 570 nm orange cut-off filter enables to eliminate reflections of the laser wavelength. A comparison of three different PIV software and velocity vector validation parameters is presented, resulting in Dantec Dynamics Dynamic Studio as the software of choice for this study. The

discrepancies between the velocity profiles obtained with and without the masking are found to be negligible in the bulk of the field with exception of locations close to the vessel walls or free surface.

The principles of planar Laser Induced fluorescence are briefly explained along with the arrangement of the rig which included a high power laser source capable of exciting the Rhodamine 6G dye.

Vessel		MT Method	Shaking diameter, $d_o$ [mm]	Reactor diameter, $d_i$ [mm]	$h/d_i$	Fill, nominal volume, [l]	Fluid height, $h$ [mm]	Speed, $N$ [RPM]	Feed position
OSR	v.1 v.2	DISMT	25	70	0.5	0.135	35	110-220	3
				100	0.3	0.236	30	80-120	3
				100	0.5	0.393	50	70-120	1-7
				100	0.7	0.550	70	90-130	3
				130	0.5	0.862	65	90-200	3
	Erlenmeyer	DISMT	25	131		0.4, 1		100-200	
				166		0.8, 2		100-200	
STR	CellReady	DISMT, Iodine-Thiosulfate, Waterblue die, pH probe				1-2, 2.4		100-250	50mm from impeller axis
	BioFlo					4.5, 5.5		50	

Table 2.1: Conditions for mixing time experiments in OSRS and STRs.

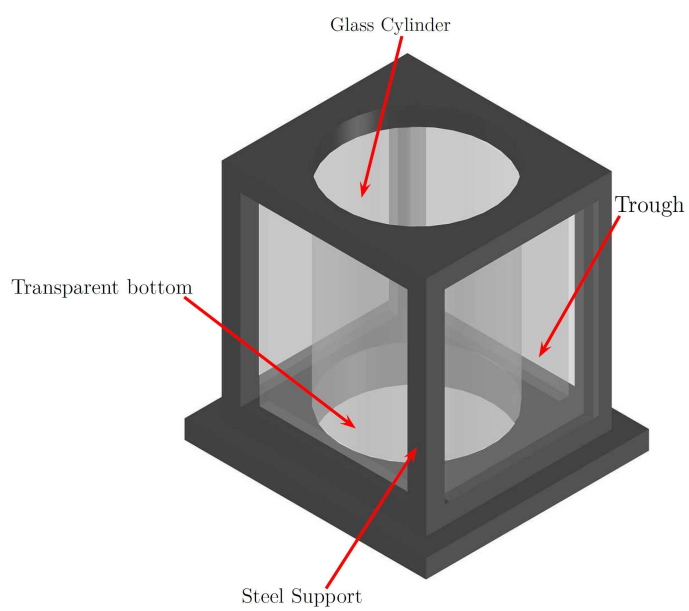


Figure 2.1: Diagram of the cylindrical OSR v.1

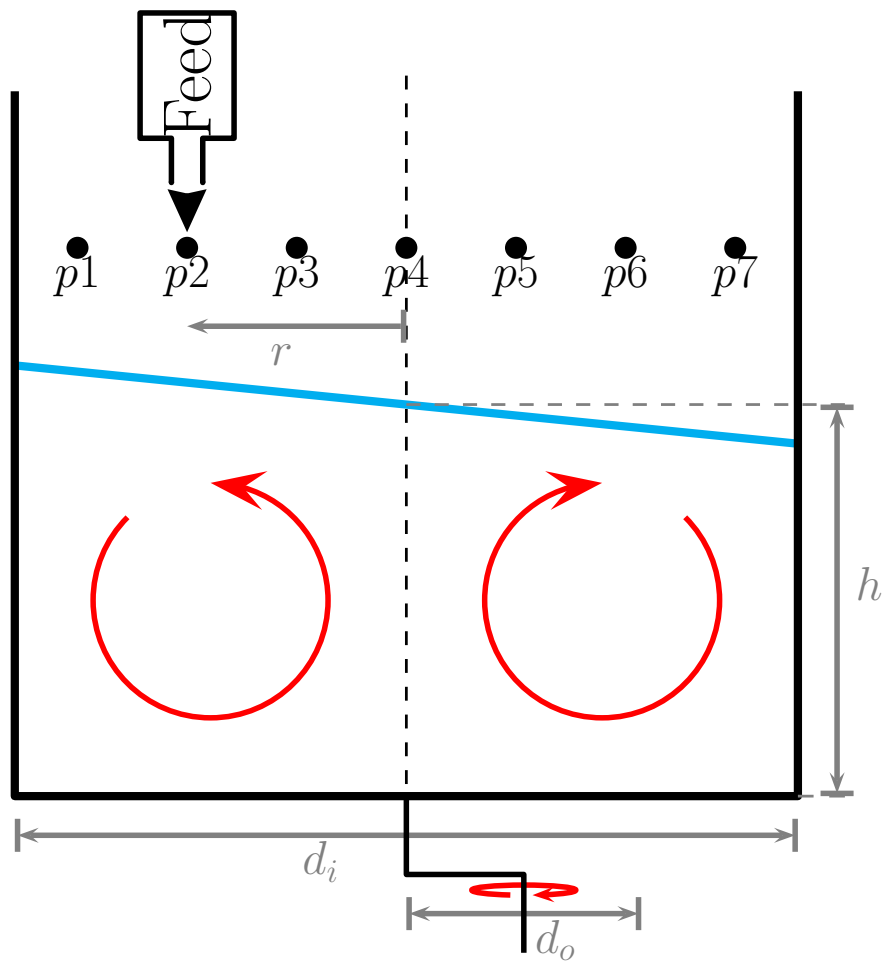
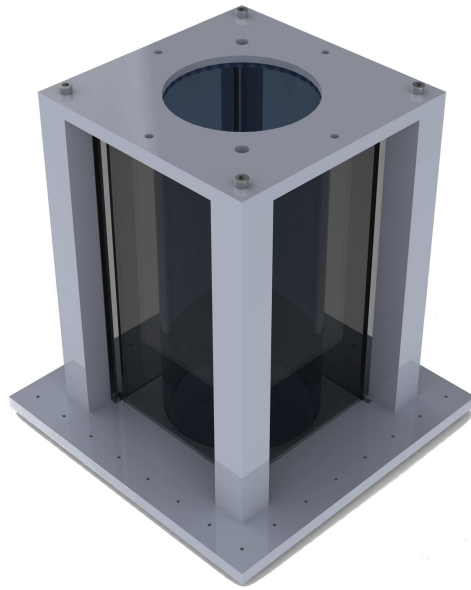
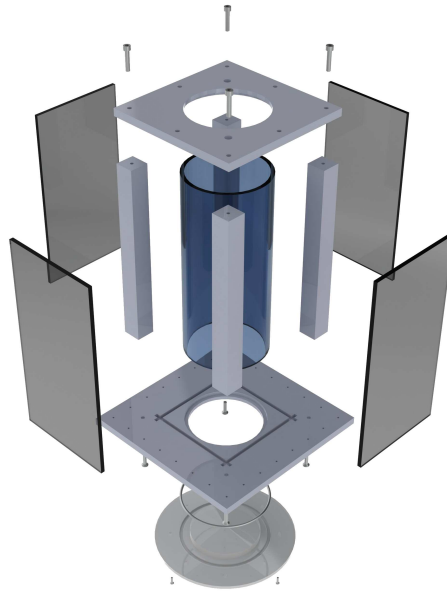


Figure 2.2: Sketch of the cylindrical OSR with feed insertion position.



(a)



(b)

Figure 2.3: (a) Schematic and (b) Exploded views of the cylindrical OSR v.2



(a)



(b)

Figure 2.4: (a) Benchtop Kühner LS-X lab-shaker; (b) Kühner SR-200 shaker.

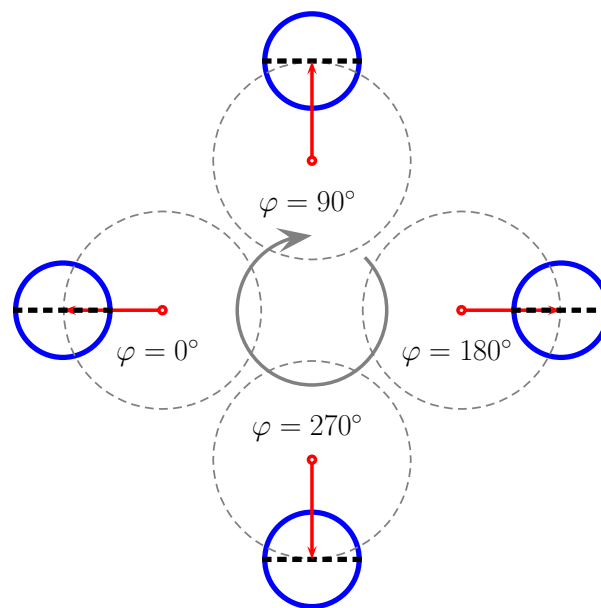
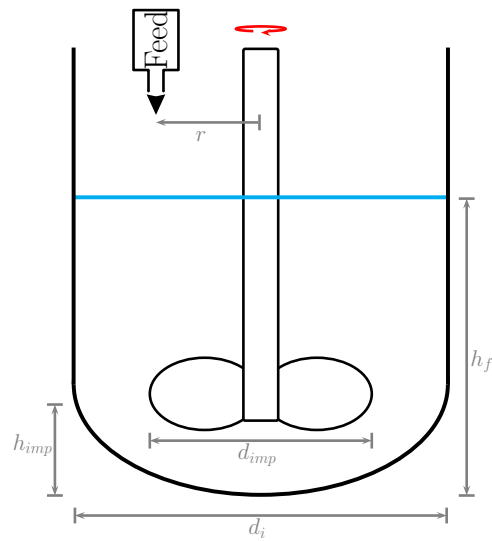


Figure 2.5: Sketch of the positions assumed by a cylindrical OSR on the circular orbit of the shaker, and visualisation of the laser measurement plane projection (dashed line) with increasing phase angle.



(a)



(b)

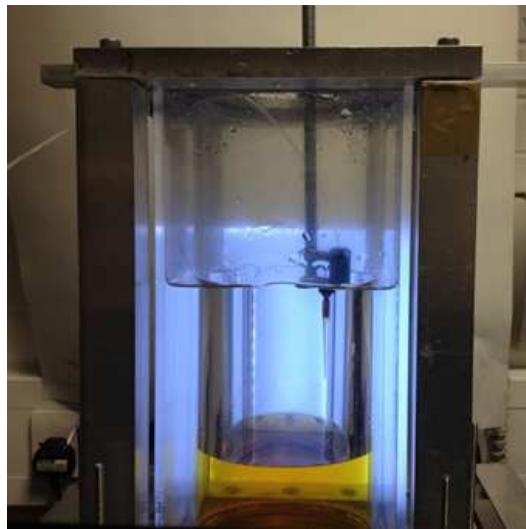
Figure 2.6: (a) Picture and (b) diagram of the Mobius CellReady reactor.



Figure 2.7: NewBrunswick BioFlo 110 stirred tank reactor.



(a)



(b)

Figure 2.8: a) Experimental rig for mixing time estimation within the cylindrical OSR v1, b) Side view of the reactor and feed insertion device.

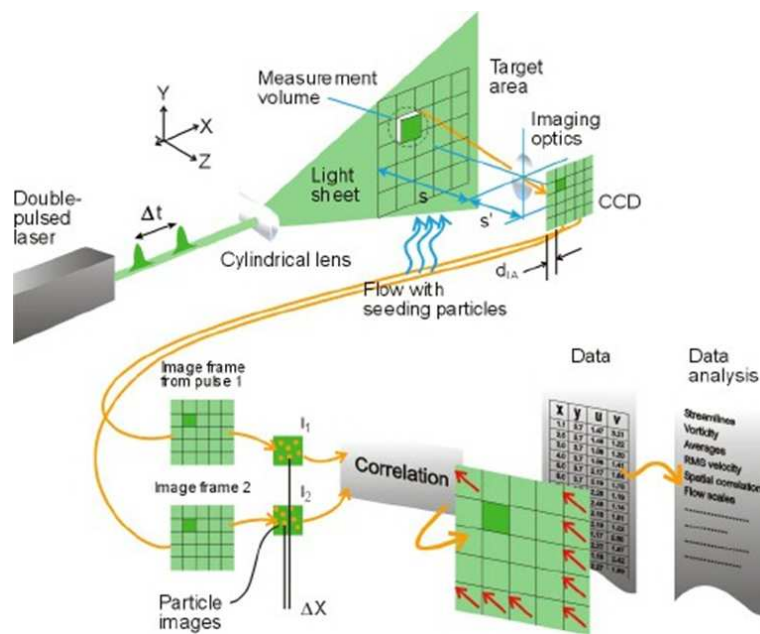


Figure 2.9: Schematic diagram showing PIV working principle (from [www.dantecdynamics.com](http://www.dantecdynamics.com)).

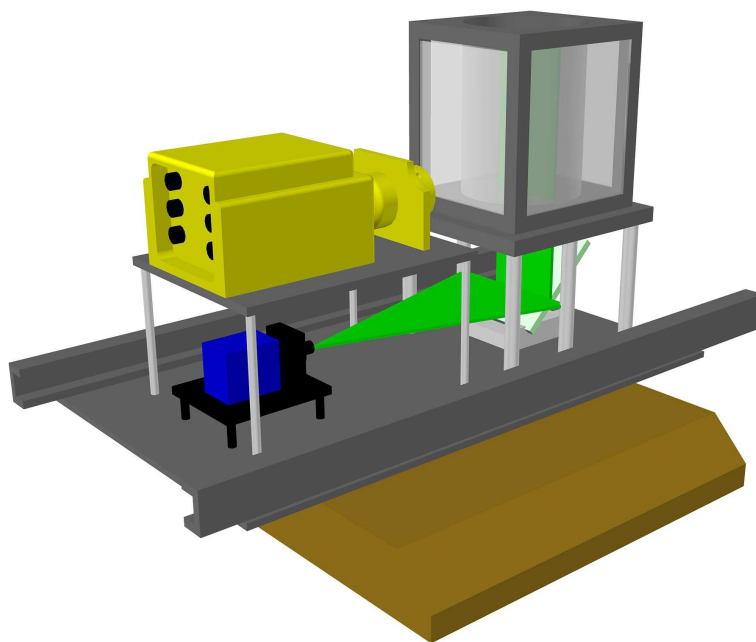


Figure 2.10: Sketch of the arrangement of the high speed camera, OSR, and Laser for PIV experiments.

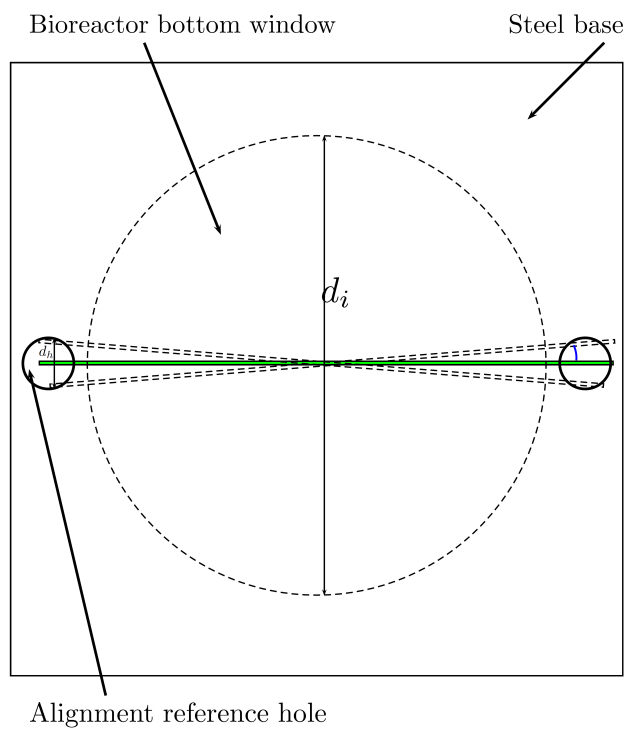


Figure 2.11: Sketch representing the alignment of the vertical laser sheet with experimental rig's reference holes.

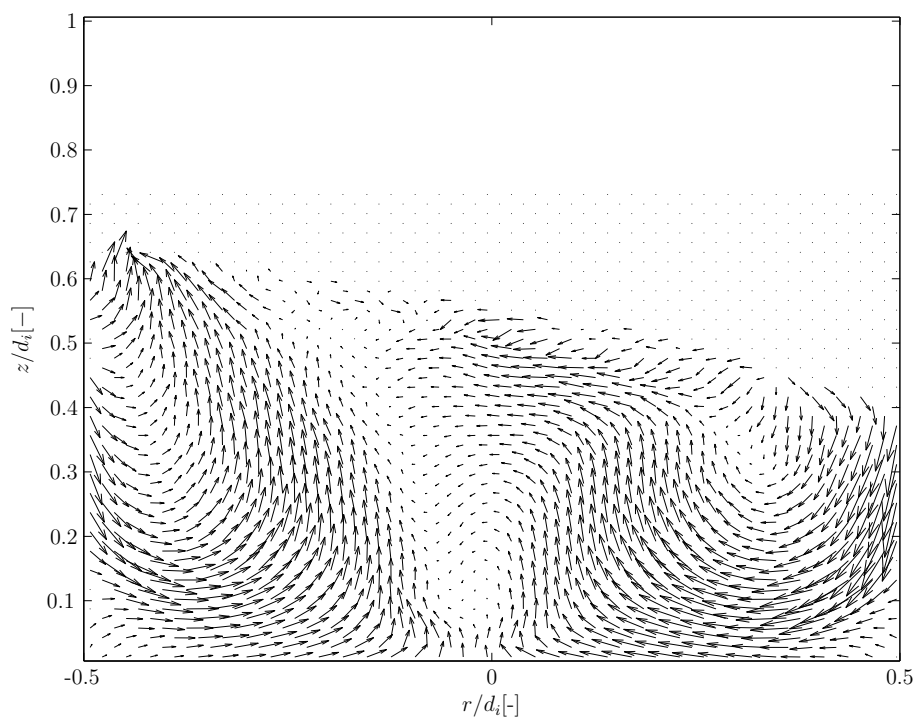


Figure 2.12: Typical velocity vector field for  $\varphi = 0^\circ$  ( $h/d_i=0.5$  and  $N=105$  RPM).

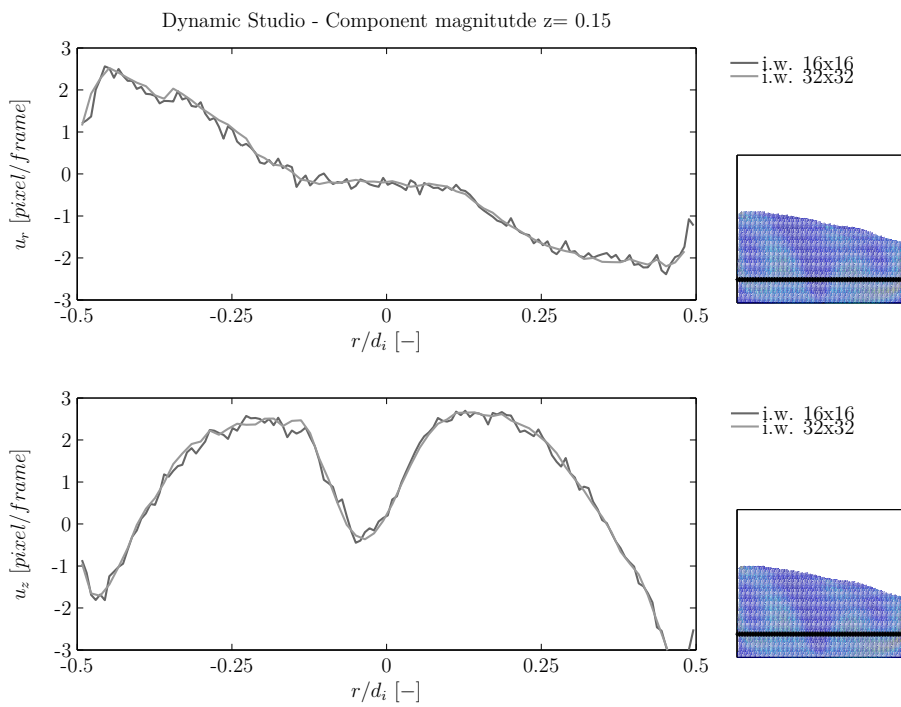


Figure 2.13: Effect of interrogation window size on velocity profiles at a height  $z/d_i=0.15$ : (a)  $u_r$  and (b)  $u_z$ .

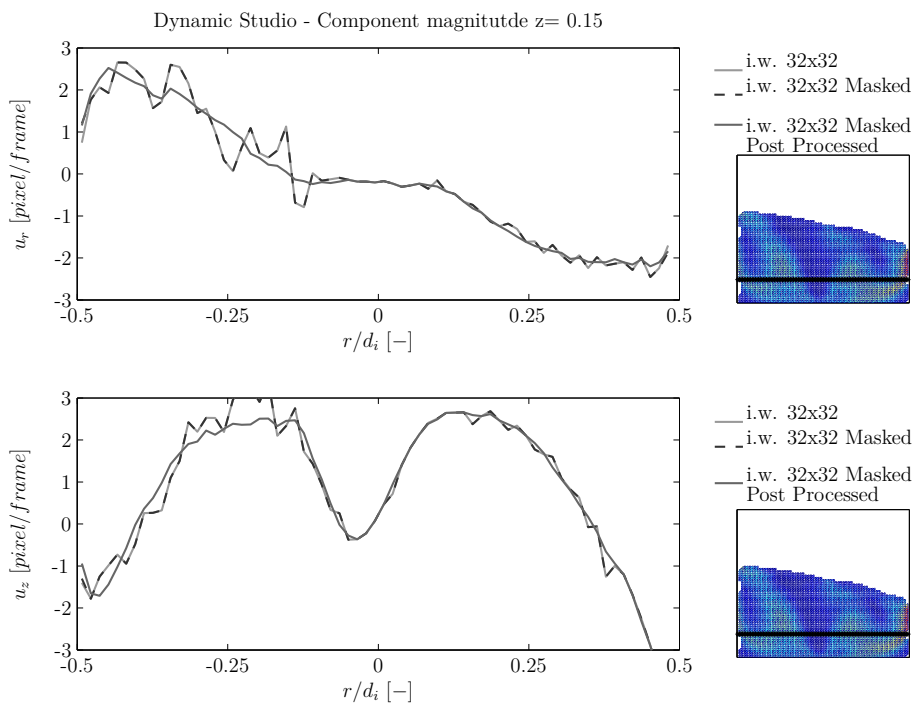


Figure 2.14: Effect of image masking and vector validation on velocity profiles at  $z/d_i=0.15$ : (a)  $u_r$  and (b)  $u_z$ .

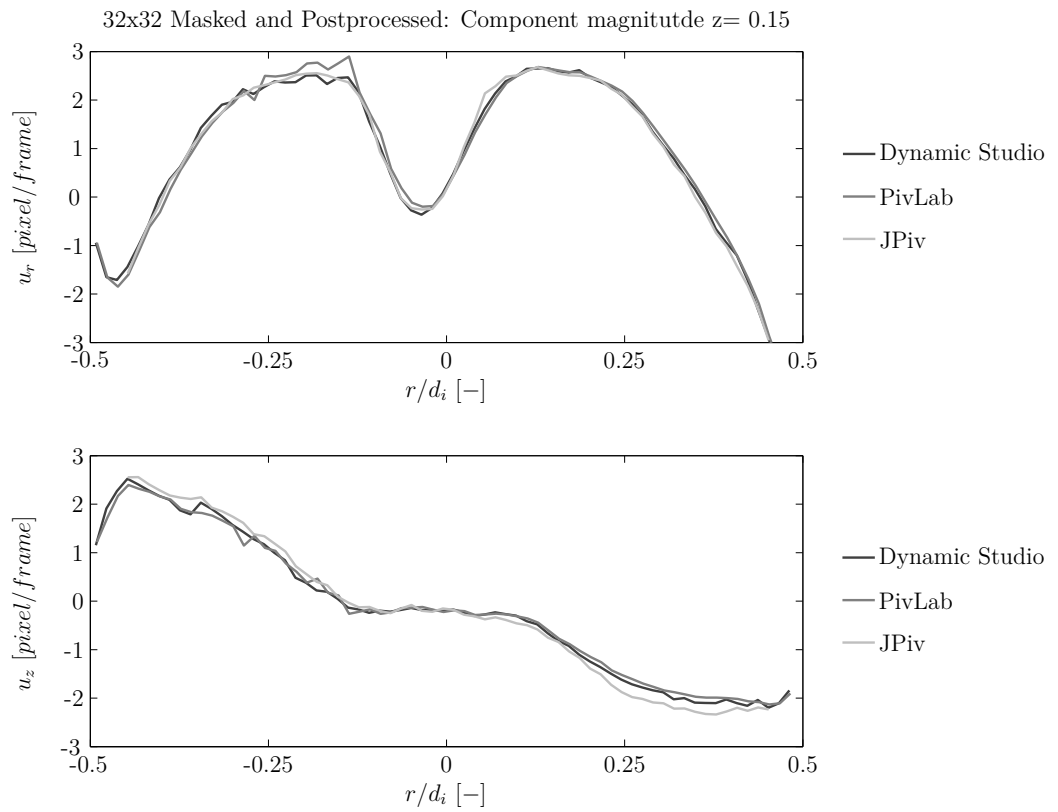
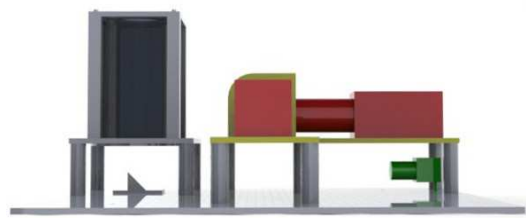
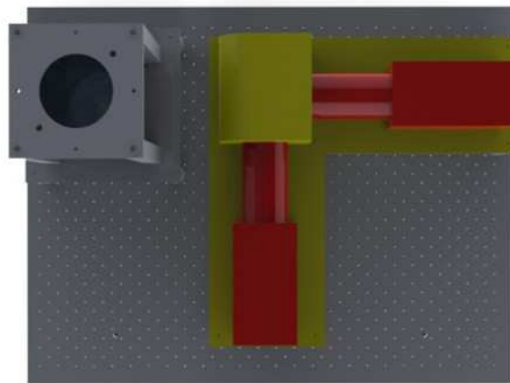


Figure 2.15: Comparison of DynamicStudio, JPiv and PIVLab software: (a)  $u_r$  and (b)  $u_z$ .



(a)



(b)

Figure 2.16: Experimental rig arrangement for simultaneous PIV and pLIF experiments. Highspeed cameras in red, dichroic mirror in yellow, laser arm optics in green. (a) side view, (b) top view.

# Chapter 3

## Mixing Time methodology development and Mixing Time in low viscosity fluids<sup>†</sup>

### 3.1 Introduction

This chapter provides an account of the development of the mixing time algorithm and its implementation in Matlab for the evaluation of mixing time in OSRs of different geometries. Mixing time is calculated from data generated from experiments using the Dual Indicator System for Mixing Time (Melton *et al.*, 2002), described in Section 2.3.4. Whereas mixing time measurements obtained from colorimetric and decolorization methods are often made visually by an operator

---

<sup>†</sup>Most of the results presented in this chapter are included in:

Rodriguez, G., Weheliye, W., Anderlei, T., Micheletti, M., Yianneskis, M. and Ducci, A. (2013), “Mixing time and kinetic energy measurements in a shaken cylindrical bioreactor”, *Chemical Engineering Research and Design*, vol 91, issue 11, pp. 2084-2097; and

Rodriguez, G., Anderlei, T., Micheletti, M., Yianneskis, M. and Ducci, A. (2014), “On the measurement and scaling of mixing time in orbitally shaken bioreactors ”, *Biochemical Engineering Journal*, vol 82, pp. 10-21

(Nienow *et al.*, 1996; Tan *et al.*, 2011), in this work an algorithm is implemented within Mathworks Matlab to process the images collected with the iCube camera. This approach eliminates the subjectivity of the operator in evaluating mixing times, especially with large datasets, and improves the reproducibility of the experiments in different laboratories. The aim of the code is to identify the colour change in the images and obtain objective mixing time estimates. The process of colour selection is explained in Section 3.2.1. Several different algorithms to measure the mixing time are developed, and are discussed in Section 3.2.2-3.2.4. The criterion for defining complete mixing is described in Section 3.3.2.

The DISMT is based upon the colour change due to pH neutralisation between acid and base in presence of pH indicators. The DISMT and the accompanying Matlab algorithms are evaluated against pH probe measurements, which, although offer a local measurement, give a direct reading of the pH value. The comparison is performed with data collected from DISMT experiments in two stirred tanks, the Mobius CellReady and the NewBrunswick (see Section 2.2.5).

The mixing experiments described in Section 3.4 provides data for flow visualisation in orbital shaken bioreactors, and confirms the presence of a toroidal vortex at low  $Fr$ , and a precessional axial vortex at high  $Fr$  as found by (Weheliye *et al.*, 2013) by means of PIV. This section also offers a study on the spatial distribution of mixing gradients and break-up dynamics of the fluid parcel.

Section 3.6 describes the mixing characteristics in cylindrical OSRs at different agitation rates, while Section 3.6.1 investigates the variation of mixing time when the feed addition is made at different radial positions. The parameters affecting mixing are discussed in Sections 3.6.2 and 3.6.3. A comparison is made between OSRs of cylindrical and conical shape in Section 3.7.1. Mixing in different scales, geometries and measurement techniques are discussed in Section 3.7.2, where a

scaling factor is proposed.

## 3.2 Image processing code development

The data collected from DISMT experiments, consists in phase-locked images acquired with the iCube camera system and are denoted by the colour change due to the acid-base reaction in presence of pH indicators. The time evolution of two samples of mixing time experiments are shown in Figures 3.1 and Figure 3.2, for high and low  $Fr$ , respectively. Figures 3.1-3.2 (i) refer to the beginning of the experiment, when the colour of the solution is red due to the acidic pH. A darker area can be seen which corresponds to the inserted base, determining the outset of the experiment. Figures 3.1-3.2 (ii-iv) refer to unspecified time intervals, and were selected to show characteristic colour change significantly during the DISMT experiments. In the transients Figure 3.1-3.2 (ii) and (iii) yellow, red and blue hues are simultaneously present, indicating that the acid-base reaction is under way.

The analysis of colour video images is a rather complex process that requires careful selection of the image processing methodology to ascertain the colour (and consequently, for the present application, the pH) exhibited by each pixel on an image. The iCube camera acquires images in RGB format, and the variation in colour of each pixel is a combination of the intensities of the red, green and blue channels. A preliminary validation step is performed to select the best RGB channel to measure mixing. Images from a flat bottom  $d_i=100$  mm,  $N=110$  RPM,  $h=50$  mm,  $d_o=25$  mm OSR experiment are used to evaluate the change of green, red and blue over time. Nine positions within the image were investigated and are shown and numbered in Figure 3.3 (a). Of such positions two (3 and 7) are purposely chosen outside the fluid undergoing mixing to evaluate the change

of RGB in the background. A Matlab script separates the red, green and blue values at pixels 1-9 for all the images in the experimental sequence, as the fluid experienced mixing, resulting in colour change from red to yellow. The variation of the RGB at each position during the experiment progression is shown in Figure 3.3 (b). These data indicate that all points within the fluid exhibited large variations, mostly in a sigmoidal curve, of the hue intensity of the three colour channels, while the RGB values at pixel 3 and 7 experienced little or no variation in intensity, as the background in the camera's field of view did not change during this time. These results proved to be very encouraging and confirmed that an algorithm based on RGB channels could be efficiently used to determine the mixing time in a bioreactor.

### 3.2.1 Comparison between RGB and HSV colour model

As explained in the previous chapter, colour may be apportioned to a pixel directly from the red, green and blue outputs of a camera (RGB), or alternatively via the hue, saturation and value (HSV) 3D colour space representation, that is derived from the RGB values. In effect, hue refers to the perceived colour, saturation to the amount of colour, and value to the brightness of each element of the analysed image.

A characteristic variation in time of the three RGB channels is given in Figure 3.4. In the abscissa the time is indicated by  $Nt$ , i.e. the number of shaker table revolutions from the start of the mixing process. The blue channel output varies the least, by around 50, while both the red and green channels show maximum variations of around 150 and 200, respectively, out of the 8bit camera full dynamic range, 255. The high initial value of red is consistent with the initial red colour of the acidic solution. In fact, the RGB value for pure red is  $[255\ 0\ 0]$ . After the

injection of NaOH the fluid experienced local alkali gradients but this does not correlate with significant changes of the blue value. At experiment completion the mixed fluid was observed to have a yellow/lime colour, which in the RGB space representation, is a mixture of red and yellow. The green channel consistently varies from an unmixed value of 50 to a mixed intensity level of 200.

On average, the time evolution of the green channel exhibits a sigmoidal shape, consistent with the colour change from red to yellow induced by the base insertion, while the red channel exhibits a U-shape indicating that a high level of red was also present in the final yellow hue achieved at the end of an experiment. Similar time variations to those shown in Figure 3.4 were exhibited by all three channels at all other points in the flow.

The variation of the HSV values with time at the same location as in Figure 3.4 is shown in Figure 3.5. As with the RGB data, similar HSV variations to those in Figure 3.5 were recorded at all other points in the flow. Although the V values exhibit the largest variation with time, it is the hue that was representative of colour, but it exhibits a far smaller variation. Consequently, the RGB data were preferred for the extraction of colour change information.

To reduce the computational cost of the data processing, and in agreement with the previous mixing time experiments of Cabaret *et al.* (2007) and Tissot *et al.* (2010), only the green channel was selected to measure the mixing time as it suffers from the least amount of background noise in comparison to the total intensity variation between the start and the end of the experiment. From this point of view it is clear that a composite index, made up of different percentages of the red, blue and green channels, would have been less effective at determining the colour variation than the green channel alone. This can be better understood when thinking at the extreme case of a grey scale space representation, where

all channels are weighted the same. The use of the blue and red channels would have dampened the greater variation associated to the green channel, resulting in a less effective composite index.

Three different algorithms/Matlab routines were developed to assess local and final mixing times of the OSR and are detailed in Sections 3.2.2-3.2.4.

### 3.2.2 Mixing time code I: pixel by pixel maps

A code was constructed in Matlab to evaluate mixing in the bioreactor vessel analysing every individual pixel. In the algorithm, first a mask is generated for each set of images of an experiment, so to exclude the background behind the mixing fluid. The mask is created by comparing the first and last frame of each experiment and all pixels whose green value did not vary by at least 50 units were ignored. The variation over time of the green channel for every individual pixel is measured, and the value at  $t_\infty$  is found. For each pixel the mixing process is assumed to be complete when the pixel's green value stays within  $\pm 5\%$  of the steady state value, in accordance to the mixing definition provided by Kasat and Pandit (2004). A matrix of individual pixel mixing times is generated and is used to find the volume's mixing time and to create 'mixing maps'. The ensemble of mixing times of each pixel in each experiment is represented as a contour plot, which highlighted areas of fast or slow mixing. A sample mixing map is shown in Figure 3.6 for a flat bottom,  $d_i=100$  mm,  $h=50$  mm,  $d_o=25$  mm,  $N=130$  RPM cylindrical OSR, with the colour bar representing the dimensionless mixing number  $Nt_{m_{ij}}$  for the  $i_{th}$  and  $j_{th}$  pixel.

### 3.2.3 Mixing time code II: interrogation box and normalisation

The algorithm for background elimination and pixel-by-pixel mixing time described previously proved to be computationally demanding and at times failed to correctly identify the control volume containing the liquid undergoing mixing, particularly at high agitation rates. Another approach is therefore taken to create a simpler Matlab routine: mixing time is measured in a specific area, called ‘interrogation box’. Mixing time is estimated based on the homogeneity of the colour within the interrogation box. The interrogation box A in Figure 3.7 was chosen in such a way to exclude the background and the borders of the reactor which are associated to a more noisy signal, but still capture the largest majority of the fluid being mixed.

It should be noted that the depth-of-field of the colour image in the three-dimensional reactor that is recorded by the two-dimensional camera sensor varies with radial coordinate or distance from the center of the vessel. Consequently, it should be determined to what extent the colour recorded at different radial coordinates was influenced by this effect. For example the intensity of the colour in a point on the axis of the cylinder,  $r/d_i=0$ , is determined by a horizontal volume of fluid which has a depth equal to the diameter of the cylinder. On the other hand, when considering points closer to the cylinder walls, at  $r/d_i=0.5$ , the depth of the fluid orthogonal to the camera field of view tends to zero at near-wall positions and the colour intensity decreases. This colour variation and the associated steady state inhomogeneity across the field of view introduces a systematic error in the final mixing time estimate. To eliminate this uncertainty, the green

intensity level of each pixel is normalized according to Equation 3.1.

$$G_{ij}^*(t) = \frac{G_{ij}(t) - G_{ij}(t_0)}{G_{ij}(t_\infty) - G_{ij}(t_0)} \quad (3.1)$$

The indices  $i$  and  $j$  denote a pixel in the field of view and  $G_{ij}(t)$ ,  $G_{ij}(t_0)$  and  $G_{ij}(t_\infty)$ , are the pixel green intensity at time  $t$ , at the start and at the end of the experiment, respectively. The steady-state (fully-mixed condition) green intensity  $G_{ij}(t_\infty)$  is obtained from the average of the last five data points on the time evolution curve. With this normalization procedure all pixels have the same  $G_{ij}^*$ , intensity at the beginning ( $G_{ij}^*=0$ ) and at the end ( $G_{ij}^* \approx 1$ ) of the experiment. Meeting these two conditions is essential for  $G_{ij}^*$  to reflect the homogeneity of the fluid both before the base insertion and at the fully-mixed state.

### 3.2.4 Mixing time code III: Standard deviation and mixed pixel occurrence

A third approach to estimate mixing time was developed, where two different methodologies are employed concurrently to measure the mixing time,  $t_m$ . In the first method the standard deviation of  $G_{ij}^*$  across the field of view is estimated at each instant, and the fully mixed condition is considered to be achieved when the standard deviation is below a selected threshold. A typical variation of the standard deviation,  $\sigma_{G^*}$ , with the number of bioreactor revolutions,  $Nt$ , is shown in Figure 3.8. The standard deviation is zero at the start of the experiment and rises rapidly after the insertion of the feed base. At high values of  $Nt$  the standard deviation tends towards a constant value close to zero. The mixing time is estimated according to Equation 3.2 as the average of the times necessary to achieve 13 different degrees of homogeneity, from 90% to 96%, with respect to the steady state value. This approach was implemented by Micheletti *et al.* (2003)

as it facilitates the minimization of scatter in the mixing time data due to signal noise. For example the time reported in Figure 3.8 is the one necessary to achieve 5% of the final  $\sigma_\infty$ .

$$Nt_m = \sum_{i=1}^{13} \frac{t_{i\%}}{13} \quad (3.2)$$

The second method for determination of the mixing time is based on the percentage of pixels,  $M$ , that have achieved the degree of mixing of Equation 3.3.

$$|G_{ij}^* - 1| < 0.05 \quad (3.3)$$

The mixing time corresponds to the instant when 95% of the pixels are mixed ( $M=95\%$ ). The variation of the percentage of mixed pixels with time is shown in Figure 3.9 for the same operating conditions,  $Fr_{do}=0.24$  and  $h/d_i=0.5$ , of Figure 3.8. The  $M$  curve is characterized by a sigmoidal shape with a sharp increase after 120 orbital revolutions and a final mixing number of 132. This is consistent with the mixing number of 128 obtained from the standard deviation methodology. A video (`Software_demonstration.avi`) is provided in the supplementary CD to show how the color variation occurring in the bioreactor during the pH experiment is converted into a mixing time using the two methodologies previously outlined.

Both approaches are useful for different purposes. The ‘cumulative’ method employing  $M$  might be thought of as more reliable if the time when fully-mixed conditions are achieved is the main requirement, as it is not so sensitive to variations during the mixing process. On the other hand, the  $\sigma_{G^*}$  approach indicates variations in the mixing conditions during the process that could help reveal undesirable concentration gradients that, for instance, may be harmful to cells suspended in the reactor.

### 3.3 Experimental reproducibility of DISMT

To evaluate the reproducibility of the DISMT and the image processing code, the same experiment is repeated 50 times at same operational conditions:  $N=110$  RPM,  $h=50$  mm,  $d_o=25$  mm,  $d_i=100$  mm and injection at position 6 (as labelled in Figure 2.2). The algorithm for mixing time evaluation consists of an average of the standard deviation and mixed pixel occurrence methodologies, as described in Section 3.2.4.

The mixing time results are calculated in terms of mixing number,  $\overline{Nt}_m$ , which was averaged over increasing randomly generated sample size. The  $\overline{Nt}_m$  for small samples has the greatest maxima and minima. The sample mean remains within a  $\pm 5\%$  of the total population average,  $\overline{Nt}_{m_n=50}$ , above a sample size of 20, as shown in Figure 3.10. Twenty repetitions of each experimental condition were therefore considered sufficient to accurately estimate mixing time within 5% accuracy, and such number of repetitions were performed for all the experimental conditions evaluated in this thesis.

#### 3.3.1 Appraisal of different methodologies for the determination of mixing time

The DISMT is evaluated against other methodologies in the estimation of mixing times in a Mobius CellReady 3 L STR (Section 2.2.5). A Iodine-Sodium thiosulfate reaction, a dye dispersion and pH probe method (see Section 2.3) are employed for this purpose. In all cases additions were made at the surface of the fluid and images were taken with the iCube camera. Mixing time is estimated using the code describe din Section 3.2.4. The CellReady bioreactor was filled with  $V_f=2$  L and operated at a range of  $N=100-250$  RPM.

Figure 3.11 shows the time evolution of the DISMT (a-d), Iodine-Sodium Thio-sulfate (e-h) and Water-blue dye (i-l) experiments performed in the 3 L Mobius CellReady. The image sequences depict the beginning of the experiment after reagent/dye addition (a, e, i), the ongoing mixing process (b, c, f, g, j, k) and the fully mixed state (d, h, l). It can be seen that addition was performed at the surface for all cases. The pH probe can be seen in Figure 3.11 (a) to the left of the impeller shaft. All methodologies visualize the characteristic axial vortex of unbaffled STRs.

Figure 3.12 shows the comparison between the DISMT Iodine-Sodium thiosulfate, Water-blue dye and pH probe methodologies for mixing time estimation. The DISMT and pH probe measurements were run concurrently for each investigated agitation speed and the data shows good agreement between the two methodologies. The volume of reagents added (acid and base) is less than 0.002% of the filling volume. The mixing number decreases at increasing  $Re$ . The simultaneous DISMT and pH probe measurements prove the effectiveness of the pH indicators to show when the pH reaches the mixed state at pH 7. The discrepancy between the DISMT and pH probe can be attributed to the fact that the pH probe is a local method, and hence more susceptible to local gradients.

The Iodine-Sodium thiosulphate method requires a reagent addition of 0.1% of the filling volume. Such a larger volume insertion affects the flow in the STR more significantly than that related to the DISMT method, resulting in a 20-30% lower mixing number due to shorter time taken for the added reagent to reach the highly turbulent region close to the impeller. Furthermore mixing time estimation with the Iodine-Sodium thiosulphate method might benefit from faster reaction times when compared to the reaction associated to the DISMT.

The Water-blue dye estimates faster mixing due to the large proportion of volume

added (0.05%) and the high solubility of the dye in water. The solution of dye in water under agitation from the impeller provides a measure of the macro-mixing in the STR, as no chemical reaction is required for colour change. Mixing at a molecular level is not required for the colour to change, resulting in mixing numbers 25% lower than that of reactive mixing methodologies (DISMT and Iodine-Sodium thiosulphate). Conversely to the other methodologies, the  $Nt_m$  is found to increase with  $Re$  (although mixing time in seconds remains constant at 20-25 s) with dye dispersion, suggesting that this is not a reliable method for mixing time estimation.

### 3.3.2 Definition of mixing criterion

The selection of mixing criteria is important in order to obtain objective and reliable estimates of mixing time. From this point of view, the detailed post-processing analysis of colorimetric data reported in Cabaret *et al.* (2007) for a stirred reactor distinguished between two main mixing thresholds: a local degree of mixedness,  $X$ , that is achieved in a single pixel when the condition  $G_{ij}^*(t) > X$  is met, and a global degree of mixedness,  $M$ , that represents the percentage of pixels that must achieve local mixing for the entire reactor to be considered as fully mixed. In their study Cabaret *et al.* (2007) built a mixing map,  $M-X$ , to establish whether an optimum range of the two thresholds exists to minimize the error made in the final mixing time. Their study highlighted that curves displaying the evolution in time of the global mixing index,  $M$ , against the local mixing threshold,  $X$ , selected were characterized by an inflection with nearly constant  $M=70\%$  for values of  $X$  in the range of 40-60%. This meant that in this range the final value of mixing time was less sensitive to small variations in  $M$  and  $X$ .

A similar analysis is carried out in the present study, and the resulting variation in time of  $M$ – $X$  curves for a mixing time experiment in the Mobius CellReady STR reactor, with a fill volume of 2 L agitated at  $N=150$  RPM, is shown in Figure 3.13. The present data show an opposite behavior to that reported by Cabaret *et al.* (2007), as in Figure 3.13 an inflection point occurs with nearly constant  $X=70\%$  for values of  $M$  in the range of 40-60%. The reason for this difference can be explained by considering that Cabaret *et al.* (2007) used a highly viscous fluid, which determined the formation of segregated regions in proximity of the impeller, where pockets of fluid with more base or acid concentrations were entrained in the vortex loops present above and below the impeller. This meant that in their case the percentage of the tank volume considered,  $M$ , affects the final mixing time for a given experiment to a greater extent, and, for example, lower mixing time values would be achieved if the analysis was restricted to the segregated regions. On the contrary, in the present case a water solution was used as working fluid, and therefore mixing dynamics are faster across the tank, and the final mixing time estimate is affected to a greater extent by the local mixing threshold selected, rather than by the size of the volume investigated. From the results of Figure 3.13 and related data across the vessel, the condition for which both  $M$  and  $X$  were 95%, indicated by an asterisk in the Figure, was selected as the threshold for complete mixing in the present work. Correspondingly, the mixing time used for the results hereafter is denoted as  $t_m$ , when 95% of the final value has been reached.

### 3.3.3 Validation of DISMT with pH probe in STRs

The DISMT is based on the colour change of the pH indicators generated by variation of the pH due to the acid-base reaction. The colour denotes a range of pH values, as mentioned in Section 2.3.4. It has been highlighted by Tan *et al.*

(2011) that what is indicated by the colour displayed in their single indicator experiments, is the transient time necessary for the entire fluid inside the flask to reach a certain pH threshold, which was not indicative of the mixing times necessary to achieve the final pH homogeneity.

To elucidate such effects, simultaneous measurements with the DISMT system and a pH probe were made both in the New Brunswick and in the CellReady STR bioreactors. Characteristic variations of the standard deviation of the normalised green channel output,  $\sigma_{G^*}$ , obtained with the DISMT method and of the pH measured with a pH probe are presented in Figure 3.14 and 3.15 for the New Brunswick and the CellReady STRs, respectively. The horizontal lines shown at pH=6 indicate the value for which the colour recorded with DISMT changes from yellow to red. The juxtaposition of the global (DISMT) with the local (pH probe) mixing results is made here solely to compare the qualitative trends indicated, not to consider quantitatively the level of mixing, as the local (probe) results are obviously not representative of the global state of mixing. In both pH probe curves the level varies slightly even after the  $Nt$  value for which the DISMT result indicates that mixing has been completed. This may be due to a small drift in the pH probes' output that may be encountered with such devices. In addition, the response time of pH probes is often limited, with readings being taken only every few seconds (1 s and 12 s for the CellReady and New Brunswick STR's controllers, respectively). The aforementioned limitations, single-point measurement and interference with the flow, make pH probes built in a bioreactor suitable only for monitoring the pH during the entire duration of a bioprocess (which involves long times scales, often of one or more days), but not very effective when estimates of the relatively fast mixing dynamics (with time scales of minutes or seconds) are required in OSR applications. Clearly the colour technique is much better suited for OSR measurements, but the range of pH indicated by

the reaction colours is finite and might affect the results obtained from visual inspection, whereas use of the  $\sigma_{G^*}$ , values allows far more accurate determination of mixing times. It may be inferred from the comparison of the probe and  $\sigma_{G^*}$  DISMT data, that they exhibit similar mixing times, for both the New Brunswick STR and CellReady cases. The effect that the finite band of pH indicated by the reaction colour may have on the accuracy of mixing time estimates obtained with visual inspection methods has not been quantified to date.

### 3.4 Flow visualisation with DISMT

The two time-sequences of Figures 3.1 and 3.2 were selected to visualize the different mixing dynamics occurring before and after the mean flow transition described in OSRs (Büchs, 2001; Weheliye *et al.*, 2013). Each sequence includes one image suddenly after injection (i), two during the mixing process (ii-iii) and one close to the fully mixed condition (iv). It should be noted that for the two experiments corresponding images are not necessarily associated to the same time instant from the start of the experiment.

The boundaries of a toroidal vortex can be distinguished in Figures 3.1 (ii-iv) from the red, blue and yellow regions denoting different levels of pH. More specifically for the experiment of Figure 3.1, the area outside the toroidal vortex is the one to turn yellow the fastest and to achieve the fully mixed condition. For this experiment the blue streaklines, denoting basic pH levels, visualise regions of higher shear rate that are located at the margin of the vortex and close to the cylinder walls. This enhances mixing in the bulk of the flow, but does not promote the pH-neutralization reaction within the toroidal vortex. It can be concluded that for the experiment of Figure 3.1 the rotational flow inside the vortex hinders mixing, which occurs in this region at slower rate and was highly determined by

the diffusion process of the base concentration towards the centre of the toroidal structure.

The experiment of Figure 3.2, at  $Fr_{d_o}=0.24$ , is characterised by completely different mixing dynamics to that identified in Figure 3.1 for  $Fr_{d_o}=0.11$ . Two regions denoted by different mixing rates can be distinguished also in this case from the red and yellow areas of Figures 3.2 (ii-iii). According to Weheliye *et al.* (2013) the mean flow at this Froude number has already undergone transition and it is controlled by a vortex with a vertical axis that precesses around the cylinder axis. From this point of view the red area of Figure 3.2 (iii) clearly visualises the region within the tank swept by this axial vortex. Similarly to the results of Figure 3.1 it can be concluded that the rotational flow within the vortical structure does not enhance mixing, which occurs at a faster rate closer to the bottom and lateral cylinder walls where viscous and turbulent shear are greater.

### 3.4.1 Mixing Maps

A better understanding of the different mixing dynamics of the experiments included in Figures 3.1 and 3.2 and a quantification of the local mixing time can be gained from the mixing maps of Figure 3.16 (a) and 3.16 (b) for  $Fr_{d_o}=0.11$  and 0.24, respectively. These mixing maps were reconstructed from the local mixing number,  $Nt_{m_{ij}}$ , of each single pixel  $(i, j)$ , when the condition of Equation 3.3 on the local degree of mixing is met. In agreement with the considerations previously made, the mixing map of Figure 3.16 (a) shows a slow mixing region in the upper section of the fluid, below the free surface. Such a slow mixing zone is generated by the entrainment and entrapment of part of the basic feed into the toroidal vortex. From this point of view it is worth noting that the non-dimensional mixing time,  $Nt_{m_{ij}}$ , inside the vortical structure is up to 250% of

that close to the wall and below the toroid. Such a difference can be explained by considering the results reported in Rodriguez *et al.* (2013) and the fact that at this  $Fr_{d_o}$  the flow has not developed any random/turbulent fluctuations that can enhance mixing.

Figure 3.16 (b) shows the mixing map for  $Fr_{d_o}=0.24$ , when a vortical structure with a vertical axis is present. Despite the difference in flow structures and mixing time distributions between Figure 3.16 (a) and 3.16 (b), analogous considerations can be made also for this  $Fr$  regime, with fast mixing times close to the vessel walls and a slow mixing zone present in the centre of the reactor in correspondence to the region swept by the vortex core along its orbital precession. It is also interesting to note that the slowest mixing zone occurs right below the free surface, where local entrainment of air might prevent mixing. However, the spread of local mixing times is significantly smaller for  $Fr_{d_o} = 0.24$  with mixing numbers in the fastest zones being only half of those encountered in the vortex core. This behaviour is in agreement with the kinetic energy content of the random/turbulent velocity fluctuations shown in Rodriguez *et al.* (2013, Figure 9b), where higher levels of turbulence were found to emanate from the side walls, and mixing was considerably improved.

### 3.4.2 Path of fluid parcel in the flow

The characteristic variation of the normalised green and red channels,  $G_{ij}^*$  and  $R_{ij}^*$ , with time, for the location  $r/d_i=0.375$ ,  $z/d_i=0.25$  on the right side of the  $d_i=100$  mm cylindrical bioreactor as shown in inset of Figure 3.17, is presented in Figure 3.17. The position of the measurement point is at the centre of the volume delimited by the white box in the inset in the figure. From Figure 3.17 it is evident that after normalization both channels satisfy the two conditions,

$G_{ij}^*(0) = 0$ ;  $G_{ij}^*(\infty) \approx 1$ , previously outlined. It is interesting to note that the variation of the normalized green and red channels data exhibits fluctuations, which, as expected, are similar to those of the non-normalized channels represented in Figure 3.4 and 3.5, but those of the red channel are greater in amplitude, and therefore  $R_{ij}^*$  represent a more meaningful parameter to study the mixing transient. These fluctuations are quasi-periodical for the first part of the trace, with a period of around 20 revolutions. These fluctuations stem from the movement of the reactants in the vessel and reflect the large changes of colour and pH that may be encountered at a point during the mixing process. The 10 triangular symbols in both curves of Figure 3.17 correspond to the 10 volume snapshots shown in Figure 3.18. The aforementioned large colour/pH variations can be clearly seen in Figure 3.18; the predominance of dark brown colour (i.e. high  $B_{ij}^*$ , and comparatively low  $R_{ij}^*$  and  $G_{ij}^*$  at  $Nt=20, 41$  and  $63$  corresponds to the fluctuation frequency mentioned above.

An assessment of this frequency is made from the circulation times estimated from the PIV measurements of Weheliye *et al.* (2013) for similar flow conditions. Figure 3.4, 3.5 and Figure 3.17 were obtained for incipient out-of-phase flow ( $N=90$  RPM;  $d_o=25$  mm,  $d_i=100$  mm,  $h=50$  mm), when the toroidal vortex extends to the bottom of the tank. From the ensemble-averaged data of Weheliye *et al.* (2013) the circulation time required for a fluid parcel to complete a loop around the toroidal vortex axis is estimated as approximately 1.67 shaker table revolutions. Similarly an estimate of 4 revolutions around the toroidal vortex axis (oriented along the azimuthal direction) is obtained for a fluid parcel to complete a loop around the cylinder axis (oriented in the vertical direction). Consequently, a parcel will proceed along a spiral path for  $4 \times 1.67=6.68$  shaker table revolutions, before occupying again its initial position in the cylinder. The mixing frames of Figure 3.18 were obtained from phase-resolved DIMST data that are under-

sampled, capturing only 1 of every 3 periods of the parcel motion (as  $3 \times 6.68 = 20$ ). It should be stressed that this analysis is approximate and any conclusions should be drawn with care, as a fluid parcel trajectory is being extrapolated from ensemble-averaged results.

### 3.5 Mixing Transients

Undesirable concentration gradients may be harmful for cell suspended in a bioreactor. The  $\sigma_{G^*}$ , methodology can help provide insights into the transient nature of the mixing process at different conditions and/or between different reactor geometries. A characteristic example is provided in Figure 3.19, where the variation of  $\sigma_{G^*}$ , with  $Nt$  in the  $d_i=100$  mm cylindrical bioreactor ( $h/d_i=0.5$ ,  $d_o/d_i=0.025$ ) is presented for five different speeds. It should be noted that for clarity only symbols corresponding to a few time instants are shown on each curve. All five curves indicate bell-shaped variations, but with notable differences: for the higher shaker table speeds, the curves have shapes akin to those of log-normal distributions, characterized by an initial rapid rise in  $\sigma_{G^*}$ , followed by a long tail at higher  $Nt$  values; at lower speeds the peak is skewed towards the higher values of  $Nt$ , with a slow rise of  $\sigma_{G^*}$  during the initial stages of mixing, while the variation for  $N=120$  RPM is more symmetrical. The two types of curves may be thought of as characteristic of OSR mixing, those for high  $Fr_{d_o}$  being more akin to the rapid mixing process similar to that that might be expected in a stirred tank reactor, while those for low  $Fr_{d_o}$  indicate a more gradual dispersion and mixing in the reactor.

### 3.6 Mixing time in OSRs

Mixing time experiments with the DISMT methodology were performed in the 100 mm cylindrical bioreactor ( $h/d_i=0.5$ ,  $d_o/d_i=0.025$ ) at varying speed,  $N=90$ -130 RPM ( $Fr_{d_o}=0.12$ -0.23) with a fluid of water-like viscosity and are shown in Figure 3.20. Mixing number steadily decreases to  $Nt_m=100$  with increasing  $Fr$  up to  $Fr_{d_o}=0.2$  after which the mixing number does not further decrease. The standard deviation, represented by the error bars in the Figure, are substantially larger at  $Fr_{d_o} < 0.2$ . The critical Froude (from Equation 1.7) for flow transition at the conditions of Figure 3.20 is  $Fr_{cr}=0.17$ . The mixing number hence decreases linearly when the flow is dominated by a toroidal vortex, with large variation between experiments, whilst at higher  $Fr_{d_o}$ , in presence of a precessional axial vortex, the mixing number does not further decrease.

The large experimental variation of  $Nt_m$  at  $Fr_{d_o} < 0.2$  is exemplified in Figure 3.21 (a) and 3.21 (b), which represent the local mixing number as mixing maps of two different experiments at identical conditions ( $N=90$  RPM,  $Fr_{d_o}=0.12$ ,  $h=50$  mm,  $d_o=25$  mm,  $d_i=100$  mm), which yield global mixing numbers of  $Nt_m=350$  and 160, respectively. Figure 3.21 (a) presents a slow mixing region close to the fluid surface, which achieves homogeneity much later than the fluid in the bottom half of the vessel. The added base remains entrained in the toroidal vortex and pH neutralisation takes longer, indicating large gradients in the bioreactor. Conversely, Figure 3.21 (b) presents homogenous local mixing number  $Nt_{m_{ij}} \simeq 160$  throughout the vessel, due to the added base breaking up early in the mixing process and quickly achieving homogeneity.

### 3.6.1 Mixing time in OSRs at different feed insertion locations

To minimise the experimental variability in mixing time estimation described in the previous section, a more thorough evaluation of the effects of the location of feed (NaOH) addition was performed using a syringe pump and a rig with seven positions along the radius of the vessel, as described in Section 2.2.2.

The variation of the mixing number,  $Nt_m$ , with orbital Froude number,  $Fr_{d_o}$ , is presented in Figure 3.22 (a) and 3.22 (b) for feed insertion points p1-p4 and p4-p7, respectively. The mixing time for each feed position and speed is averaged over 20 values. The black solid and dashed lines denote the average and standard deviation of the mixing time for the entire sample (i.e.  $7 \times 20 = 140$ ) of measurements obtained at a given speed irrespective of the feed position. The vertical dashed line indicates the  $Fr$  corresponding to flow transition for  $h/d_i = 0.5$  and  $d_o/d_i = 0.25$  (see Equations 1.7 and 1.8) with data points before and after the line being denoted as before flow transition, BFT, and after flow transition, AFT, respectively. The average mixing time exhibits the expected trend, with the first part before flow transition being characterised by a linear decrease and the second part after flow transition being denoted by a nearly constant mixing number. The behaviour in the BFT- $Fr$  range is in agreement with the results of Weheliye *et al.* (2013) who found that the size and height of the toroidal vortex present BFT increases with increasing  $Fr_{d_o}$  and therefore the basic solution fed into the reactor is subject to a circulation throughout the tank. On the contrary in the AFT- $Fr$  range turbulence starts to kick in and takes control of the mixing dynamics in the bioreactor.

When considering the data points associated to different feed insertion positions it is evident that only part of them display the expected and more intuitive

behaviour previously outlined for the average mixing time. For example,  $Fr_{d_o}$ - $Nt_m$  data variations for feed insertion positions p1 and p6-p7 in Figure 3.22 (a) and (b), respectively, exhibit again a linear decay before flow transition and a nearly constant mixing number afterwards. These similarities are explained by considering that all these insertions points are located closer to the walls where the shear induced by the boundary layer is higher and the initial drop fed into the system is more likely to be stretched by the local strain dynamics.

A more complex behaviour highly dependent on the local flow occurs for the other feed insertion positions. For example in Figure 3.23 the data of p2 show an increase of mixing number when the rotational speed of the shaker table is increased from the first to the second data points, while a similar increase occurs between the second and third data points of p3. This can be explained by considering that the growth of the toroidal vortex associated to the increase in  $Fr_{d_o}$  raises the probability of the feeding drop to be entrained and trapped inside the vortex despite the greater mean circulation associated to the higher  $Fr$  regime. A similar trend is exhibited by the mixing numbers associated to p5 in Figure 3.22 (b), which displays an increase of the mixing time corresponding to the growth of the vortical cell on the right hand side of the vessel. It is interesting to note that when data points after flow transition are considered only those corresponding to the insertion position p4 show a significant increase of mixing time outside the one standard deviation boundaries. This again has to be explained by a higher probability of a full insertion of the feed in the axial precessional vortex at the centre of the bioreactor.

The effect of the feed position is further highlighted by Figure 3.23, where for each  $Fr_{d_o}$  all the experimental results are shown alongside the mean value and error bar. At  $Fr_{d_o}=0.11$  longer mixing times were measured at p1, 2, 6 and 7 due to the likelihood of the base being fed inside to the toroidal vortex, which

at this  $Fr_{d_o}$  is small and close to the vessel walls. Entrainment in the toroidal structure is detrimental to mixing times as there is little fluid exchange between the interior of the vortex and the rest of the fluid. Feed position 4 also recorded long mixing times due to the feed being added at the centre of the vessel, where the shearing effect of the toroidal vortex are low as is the velocity of the fluid. At  $Fr_{d_o}=0.14$ , the toroidal vortex expands in size from the vessel walls towards the centre and bottom of the vessel, which results in lower mixing times for feed position p4, whilst p2 and p5 suffer higher likelihood of entrainment in the flow. Feed additions at position p7, which is located close to the wall on the lower free surface wave crest, result in large mixing numbers due to the toroidal vortex being compressed on the left side. At  $Fr_{d_o} > 0.17$  mixing numbers are less dependent on feed position, except for p4 which at  $Fr_{d_o}=0.24$  experienced longer mixing times due to entrainment of the added base in the precessional axial vortex.

### 3.6.2 Mixing time in OSRs at different fill volumes

The effect of filling volume in the  $d_i=100$  mm vessel on mixing time is investigated and the results are summarised in Figure 3.24. Three fluid heights,  $h=30, 50$  and  $70$  mm are used, corresponding to volumes of  $0.236, 0.393$  and  $0.550$  mL and  $h/d_i=0.3, 0.5$  and  $0.7$ . The orbital diameter is kept constant at  $d_o=25$  mm.

The  $h/d_i=0.3$  condition results in very long mixing times at low  $Fr$ . A steep decrease in  $Nt_m$  is measured for  $0.09 < Fr_{d_o} < 0.14$ , with the mixing number settling between  $80 < Nt_m < 130$  for  $Fr_{d_o} > 0.14$ . The flow transitions from toroidal to precessional axial vortex at  $Fr=0.11$ , corresponding to  $N=87$  RPM (as defined by Equation 1.7), which results in the mixing number slowly decreasing at  $Fr_{d_o} > 0.14$ . The  $h/d_i=0.5$  condition presents linear decrease of mixing number,  $Nt_m$ , for  $Fr_{d_o} < 0.2$  after which the mixing number settles on a value of  $Nt_m=30$ .

The  $Fr_{cr}$  for  $h/d_i=0.5$  and  $d_o/d_i=0.025$  is  $Fr_{cr}=0.18$ , after which the mixing number decreases asymptotically to  $Nt_m=50$ . With  $h/d_i=0.7$  and  $d_o/d_i=0.025$  the critical Froude number,  $Fr_{cr}=0.18$ , (as defined by Equation 1.8) but  $Nt_m$  decreases sharply up to  $Fr=0.4$ . At large agitation rates,  $Fr_{d_o} > 0.35$  the mixing number settles at  $Nt_m=40$ .

### 3.6.3 Mixing time in OSRs at different internal diameters

Mixing time experiments are performed for vessels of different vessel diameter,  $d_i=70, 100, 130$  mm whilst keeping the orbital diameter constant at  $d_o=25$  mm, as shown in Figure 3.25. The  $h/d_i$  is kept constant at 0.5, resulting in fluid heights of  $h=35, 50$  and 65 mm and volumes of  $V_f=135, 392$  and 862 mL, respectively.

At low speeds, the  $d_i=130$  mm vessel results in the largest mixing numbers, which linearly decreases from  $Nt_m=300$  at  $0.11 < Fr_{d_o} < 0.28$ , after which the  $Nt_m$  values settle at 60. The critical speed for this geometry is  $N_{cr}=99$  RPM or  $Fr_{cr}=0.13$  (from Equations 1.7 and 1.8) although the mixing number continues to decrease past the  $Fr_{cr}$ .

The  $d_i=70$  mm vessel achieves similar  $Nt_m$  values as the  $d_i=100$  mm vessel. Critical speed for the  $d_i=70$  mm vessel is  $N_{cr}=124$  RPM, or  $Fr_{cr}=0.21$  (from Equations 1.7 and 1.8), and  $Nt_m$  values linearly decrease at  $Fr_{d_o} < 0.3$ , after which the  $Nt_m$  does not further decrease. It must be noted that the drop between  $0.4 < Fr < 0.45$  is due to different experimental sets.

## 3.7 Mixing time scaling

The results described thus far show that mixing time is dependent on several factors such as orbital diameter,  $d_o$ , OSR internal diameter,  $d_i$ , fluid height,  $h$ , and Froude number,  $Fr_{d_o}$ . Experiments on cylindrical vessels are compared between sets, where one parameter at a time ( $d_i$ ,  $h$ , feed position) was evaluated against  $Fr_{d_o}$  for cylindrical OSRs, but in reality a plethora of geometries exist for OSRs, with the Erlenmeyer flask being used widely in shaken applications. Comparability with much larger cylindrical OSRs and Erlenmeyer flasks requires careful consideration for the formulation of a scale up factor for mixing in orbitally shaken systems.

### 3.7.1 Mixing cylindrical OSRs and Erlenmeyer flasks

Mixing time measurements obtained in 1 and 2 L Erlenmeyer flasks (as described in Section 2.3.6) with a fill volume of 40% are compared with previously reported data obtained by Tissot *et al.* (2010) in a cylindrical reactor and by Tan *et al.* (2011) in Erlenmeyer flasks, in an effort to identify potential similarities and scaling between OSRs of different sizes, shaking speeds, filling volumes and/or shapes.

Mixing time measurements were obtained in the Erlenmeyer flask bioreactors at agitation rate  $N=100-200$  RPM. The variations of mixing number,  $Nt_m$ , with  $Fr_{d_o}$  are presented in Figure 3.26. Of course, comparisons must be made with care, not only due to the differences in geometry and operating conditions, but also due to the different techniques employed. For example, Tissot *et al.* (2010) and Tan *et al.* (2011) determined the mixing time from visual observations, whereas for all the present experiments the DISMT data were processed using the

methodology outlined in Section 2.3.4 and the image processing code described in detail in Section 3.2.4.

The mixing numbers for the  $V_f=0.05$  L Erlenmeyer flask (Tan *et al.*, 2011) are much lower and cannot be readily compared with the rest. All other curves indicate that for  $Fr_{d_o}$  values less than around 0.3,  $Nt_m$  decreases with increasing  $Fr_{d_o}$ . For  $Fr_{d_o} > 0.3$  there is relatively little variation in  $Nt_m$ , except for the 0.4 L Erlenmeyer flask. The data exhibit scatter, as might be expected due to the aforementioned differences in geometry, measurement technique etc. Furthermore, the presentation of mixing time data against  $Fr_{d_o}$  does not take into consideration the change in the flow regime in a shaken reactor from in-phase to out-of-phase flow, as the critical speed,  $N_{cr}$ , at which such a change takes place is not accounted for. The different flow regimes encountered for varying conditions point to the need for a representation that can account for such changes and this is addressed in the following section.

### 3.7.2 Mixing scale-up in OSRs

The mixing time results for the  $d_i=70$  mm and  $h/d_i=0.5$ ,  $d_i=100$  mm and  $h/d_i=0.3$ ,  $d_i=100$  mm and  $h/d_i=0.5$ ,  $d_i=100$  mm and  $h/d_i=0.7$ ,  $d_i=130$  mm and  $h/d_i=0.5$  are presented in dimensional form in Figure 3.27. All the data indicate a similar variation, with the mixing time decreasing with shaking table speed from values of around 200 s at the low  $N$  range, tending nearly asymptotically to values of 20-30 s at speeds above 150 RPM. The range of variation of the data is indicated by the shaded area in Figure 3.27.

However, changes in flow regime will occur at different speeds when the filling volume, the orbital diameter or the reactor diameter is varied. An improved representation of the data is shown in Figure 3.28 where the same data as in

Figure 3.27 are plotted as variations of the mixing number  $Nt_m$  with the ratio  $Fr_{d_o}/Fr_{cr}$ , where the critical Froude number is estimated using the orbital diameter and the critical shaking speed obtained from either Equations 1.7 or 1.8 depending whether condition  $h/d_i < ((d_o/d_i)^{0.5})$  or  $h/d_i > ((d_o/d_i)^{0.5})$  is satisfied. This representation helps to account for the different critical speeds encountered with different  $d_o/d_i$  and  $h/d_i$ , as the definition of  $N_{cr}$  takes into consideration both  $d_o$  and  $V_f$ , the volume of fluid in the reactor. The data in Figure 3.28 show that, for the  $Fr$  range studied in this work, mixing numbers decrease with increasing  $Fr_{d_o}/Fr_{cr}$  up to 1.4 and remain approximately constant thereafter. Again, the range of variation of this set of data is indicated by a shaded area.

The potential of the proposed methodology for improved scaling protocols can be fully understood from Figure 3.29 and 3.30, where the experimental data acquired in this work for shaken bioreactors of cylindrical geometry are directly compared against those collected by Tissot *et al.* (2010) for the same geometry, but for rather different operating conditions. In Figure 3.29 a standard graph is made with dimensional axes ( $N$  versus  $t_m$ ). To improve the readability of the figure and reduce the clutter of curves, the data measured in this work are visualised by the grey shaded envelope. From Figure 3.29 two main differences can be seen between the current data and those of Tissot *et al.* (2010): (1) their data tend to reach a nearly constant mixing time at a lower speed; and (2) their constant mixing time is generally lower than the one found in this work. While the latter discrepancy can be justified by considering that in the two works a different methodology is used to determine the mixing time (visual versus post-processing analyses), the first one is more subtle and related to the onset of the flow transition reported by Rodriguez *et al.* (2013) and Weheliye *et al.* (2013). In the latter work it was shown that this flow transition is also related to the generation of turbulence, that enhances mixing. As mentioned before, this implies that the data of Tissot

*et al.* (2010), which were generally obtained in larger tanks and for greater fluid height to cylinder diameter ratios, will undergo flow transition at very different speeds to those reported in the current work.

From this perspective a more universal representation might be achieved if the ratio  $Fr_{d_o}/Fr_{cr}$  is considered. This would help account for differences in orbital diameters between experiments, as well as reactor diameter and filling volume. A compilation of the current and the previously reported cylindrical OSR data by Tissot *et al.* (2010) is shown in Figure 3.30, in terms of variation of the mixing number with  $Fr_{d_o}/Fr_{cr}$ . Similarly to Figure 3.29, the data from the present work are shown as a range, indicated by the grey shaded area for  $Fr_{d_o}/Fr_{cr} < 2.4$ . Although differences should be expected for data from such a wide range of configurations and obtained in different laboratories, Figure 3.30 clearly indicates the similarity of the variations of mixing number from different OSRs when considered against the normalised Froude number  $Fr_{d_o}/Fr_{cr}$ . The entire set of data in figure 3.30 indicates that the variation of  $Nt_m$  with  $Fr_{d_o}/Fr_{cr}$  may be represented by a power law relationship of the form:

$$Nt_m = a \left( \frac{Fr_{d_o}}{Fr_{cr}} \right)^{-b} + c \quad (3.4)$$

Such a relation would represent most sets of data included in Figure 3.30. The values of the factor  $a$  and of the exponent  $b$  might vary between different sets of data, to account for variations in the reactor size and operating parameters. At a sufficiently high  $Fr_{d_o}/Fr_{cr}$ ,  $Nt_m = c$  and assumes a constant value of around 25-30. Equation 3.4 at present offers a useful tool for the comparison of mixing time measurements in different cylindrical OSRs, and shows much promise for the development of a more universal scaling law for mixing in shaken bioreactors. At present, all the data included in Figure 3.30 can be correlated with the power law of equation in the form  $Nt_m = 100.7 (Fr_{d_o}/Fr_{cr})^{-1.245} + 25$ , albeit with a

correlation coefficient of 0.56. However, it should be expected that if a robust measurement protocol is developed and widely adopted, formulation of a more universal scaling law should be possible to correlate all data obtained with this protocol, and differences in the  $a$  and  $b$  values for various OSR conditions might be minimized.

### 3.8 Concluding Remarks

In this chapter the methodology of the DISMT technique for the measurement of mixing times in OSRs is assessed in detail. Various aspects of the data acquisition and processing procedures are considered and it is shown that utilisation of the standard deviation  $\sigma_{G^*}$  of the green colour values recorded during an experiment can help provide more reliable data that provide information not only on the final mixing time but also on the development of mixing during the process. It is noticed that, in agreement with the DISMT work of Cabaret *et al.* (2007) on STRs, care has to be exerted when selecting the fully-mixed criteria in an OSR.

DISMT measurements obtained in both a STR and an OSR are compared with simultaneously acquired pH probe data. The comparison indicated that the finite range of pH indicated by the colours displayed in the DISMT data can introduce uncertainties that should be further investigated in future.

Mixing time measurements highlight that the mixing number is highly dependent on the position of the feeding pipe, where a counter-intuitive increase of the mixing time corresponds to an increase of the shaker rotational speed. This is most likely to occur for feeding positions closer to the centre of the bioreactor when the probability of insertion into either the toroidal or axial vortices for

conditions BFT or AFT results in an entrainment of the base inserted volume into the vortex. The current data indicate that insertion should be made closer to the wall where shear stresses induced by the boundary layers enhance the dispersion and deformation of the initial blob and therefore the mixing dynamics of the bioreactor. Selection of positions closer to the wall is also advised at higher  $Fr$  regime after flow transition when turbulence starts to emanate from the boundary layers at the side walls. The present data have indicated that further optimization of mixing in shaken reactors may be achieved through a more thorough understanding of the processes involved in such systems. Furthermore, the results indicate that the use of baffles or different vessel geometries, that may help mix better the fluid that is trapped in the toroidal and axial vortices under certain operating conditions, should also be investigated.

The mixing time measurements obtained in cylindrical and Erlenmeyer shaken reactors for various operating conditions in the present work are compared with similar data previously reported in the literature. At low shaking table speeds the mixing number  $Nt_m$  decreases sharply with increasing speed and thereafter remains nearly constant. For some operating conditions mixing times as long as  $t_m=100$  s are obtained in cylindrical OSRs (see for example Figures 3.27 and 3.28), which may be related to the presence of inhomogeneity and local concentration gradients of pH and dissolved oxygen. These are extremely relevant in scaled up vessels, and for example the work of Serrato *et al.* (2004) highlighted that cell growth, metabolism, and glycosylation pattern of an IgG1 monoclonal antibody were severely affected by the time spent by the cells in low dissolved oxygen tension regions.

Differences between data obtained for various reactor diameters and filling volumes may be accounted for by considering the mixing time variation critical speed with  $N/N_{cr}$ , rather than simply  $N$ . This ratio accounts for the presence of in- or

out-of-phase flow conditions in the OSR. When different reactor diameters, orbital diameters and other operating conditions are concerned, it was shown that consideration of the variation of mixing number with  $Fr/Fr_{cr}$  can aid scaling between mixing time measurements in different systems: all sets of data exhibited a trend that may be described by an equation of the form  $Nt_m = a \left( \frac{Fr_{d\omega}}{Fr_{cr}} \right)^{-b} + c$ .

This relation provides a most useful scaling law for mixing time determination in OSRs. The factor  $a$ , the exponent  $b$  and the constant  $c$  are configuration- and protocol-dependent, but it is expected that with a properly and widely implemented robust measurement protocol more universal scaling laws could be developed. This could be facilitated by a better understanding of the physics of the related flow and mixing processes and future work to elucidate further the mixing mechanisms in shaken bioreactors is called for. Nevertheless, the results of the present work show promise for the more reliable and accurate characterization of OSR mixing and research is on-going at present to extend the proposed scaling to a more wide range of fluid properties and operating conditions.

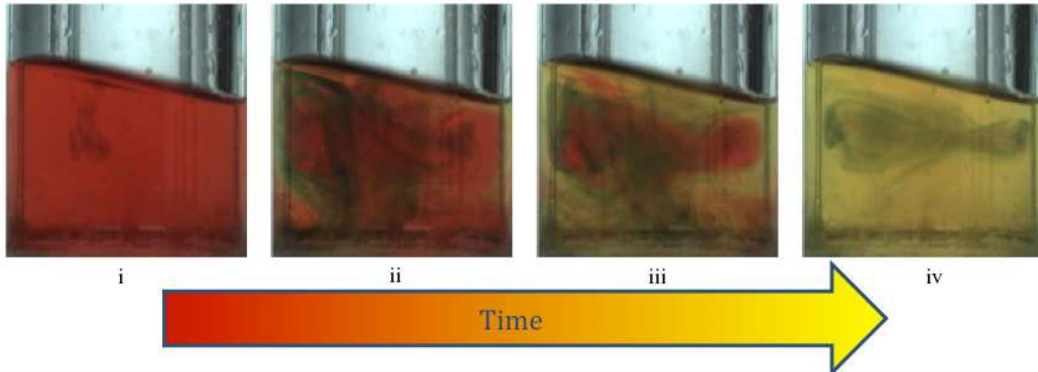


Figure 3.1: Time evolution of the mixing dynamics inside the bioreactor for conditions characteristic of in-phase flow:  $Fr_{do}=0.11$ ,  $h/d_i=0.5$ ,  $d_o/d_i=0.25$ .

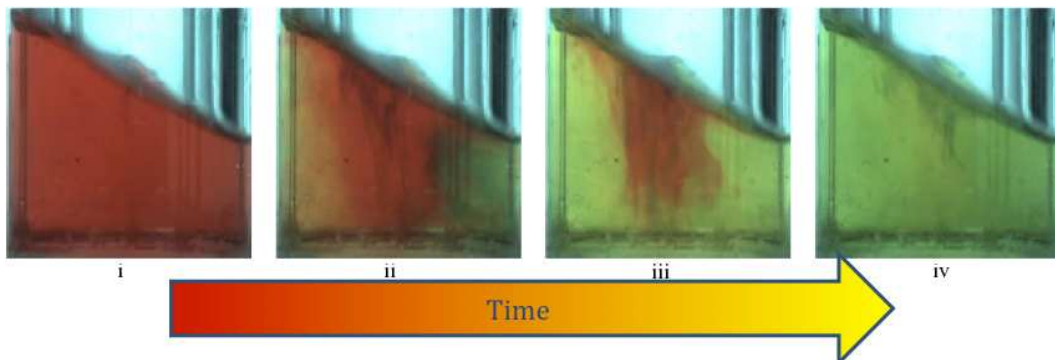
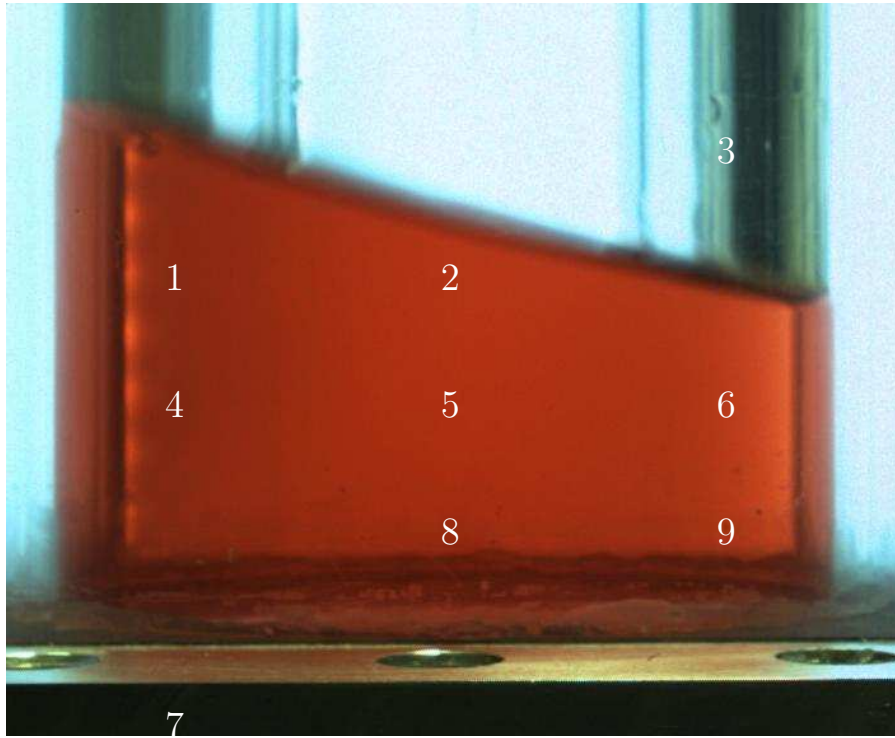
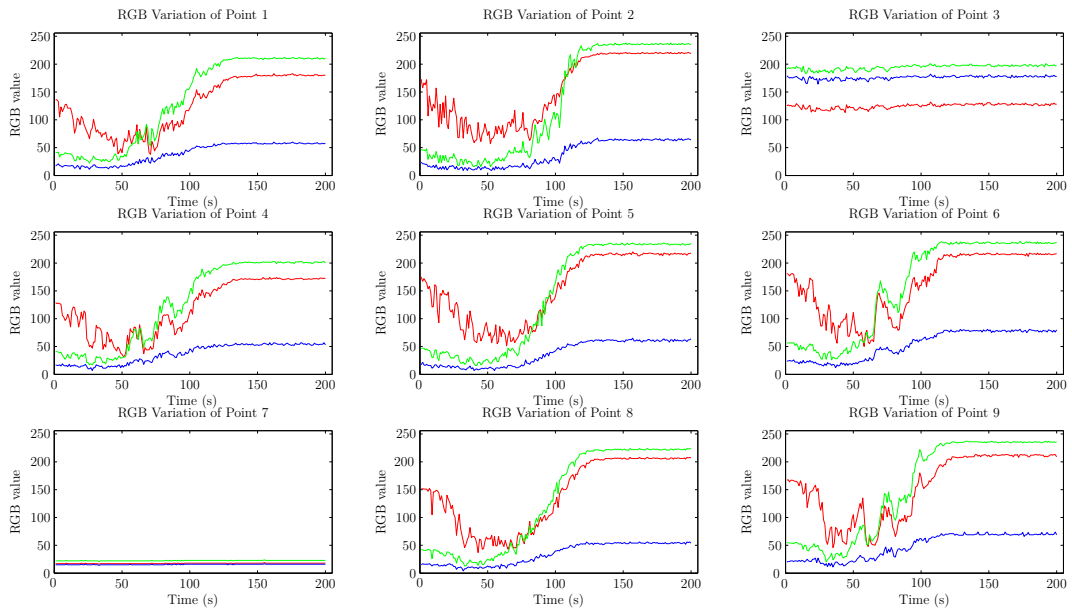


Figure 3.2: Time evolution of the mixing dynamics inside the bioreactor for conditions characteristic of out-of-phase flow  $Fr_{do}=0.23$ ,  $h/d_i=0.5$ ,  $d_o/d_i=0.25$ .



(a)



(b)

Figure 3.3: (a) Location of points in the cylindrical OSR for RGB channel evaluation with DISMT; (b) Variation of red, green and blue values at the nine points shown in (a).

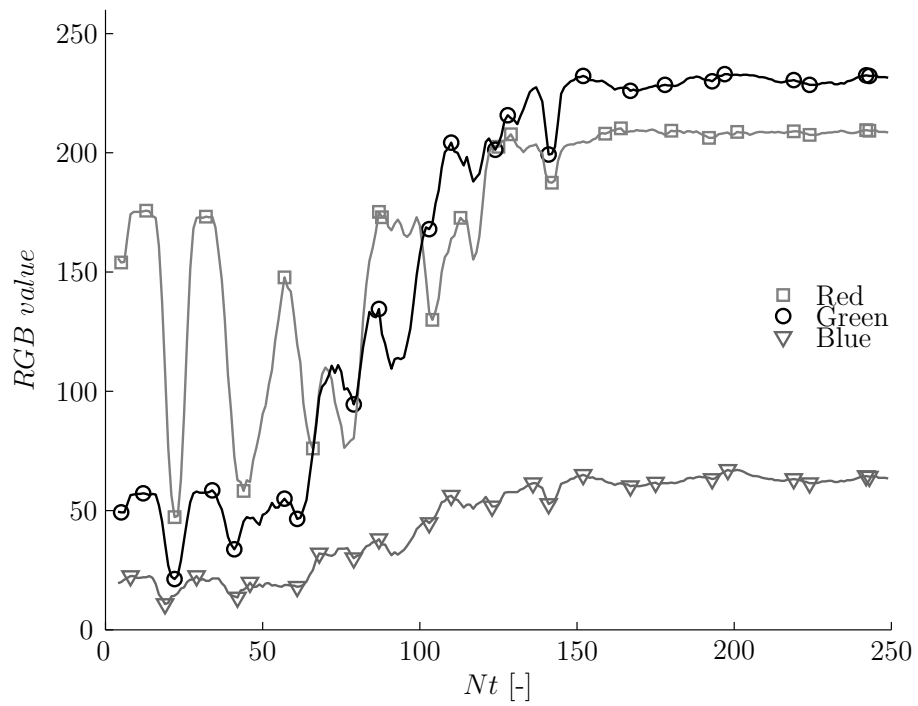


Figure 3.4: Variation with orbital revolutions,  $Nt$ , of the three channels in the RGB space representation ( $r/d_i=0.375$ ,  $z/d_i=0.25$ ).

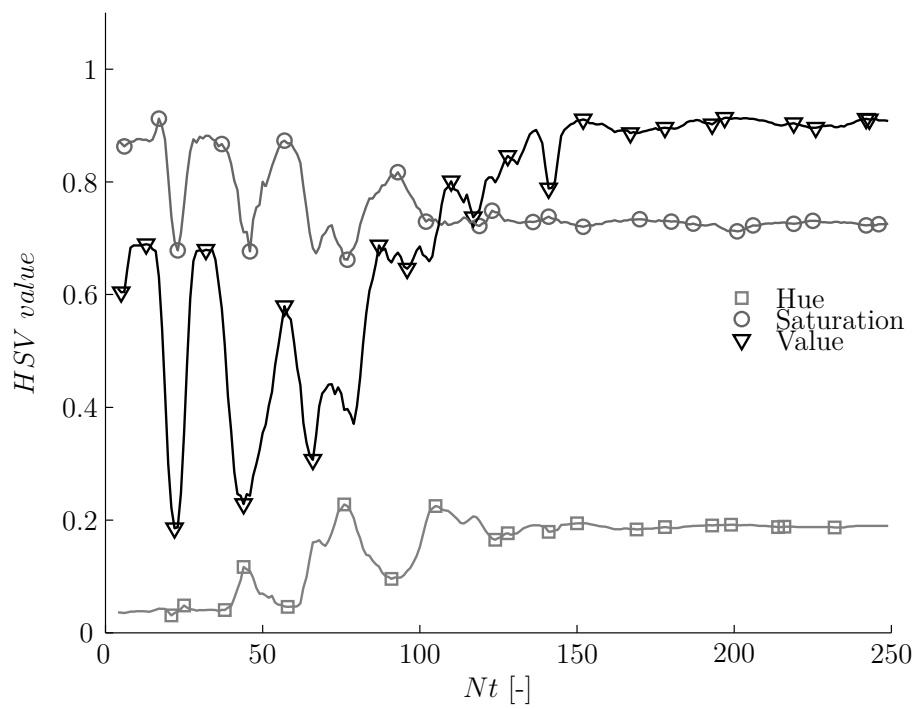


Figure 3.5: Variation with orbital revolutions,  $Nt$ , of the three channels in the HSV space representation of colour ( $r/d_i=0.375$ ,  $z/d_i=0.25$ ).

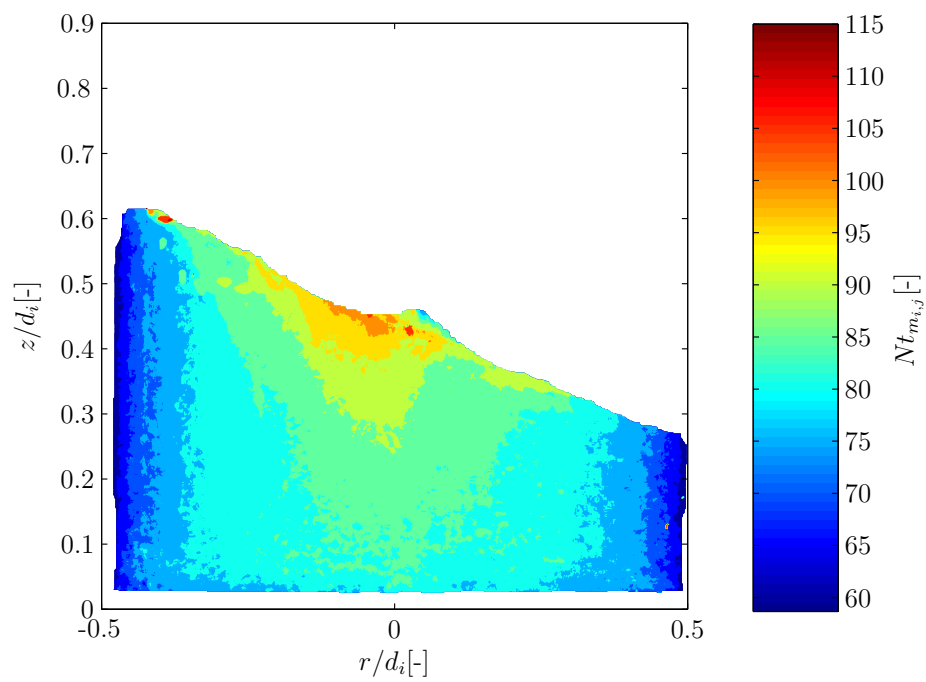


Figure 3.6: Characteristic mixing map generated from the pixel-by-pixel mixing time algorithm.

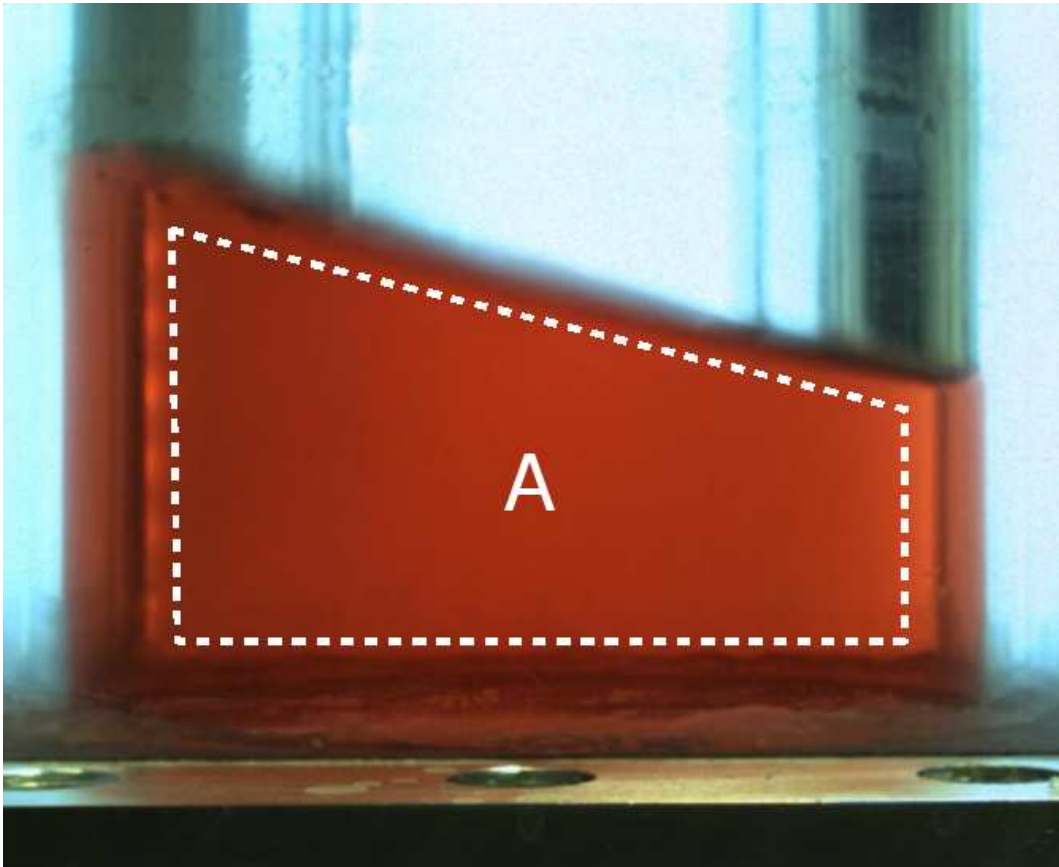


Figure 3.7: Visualisation of the area used to determine the reactor mixing time.

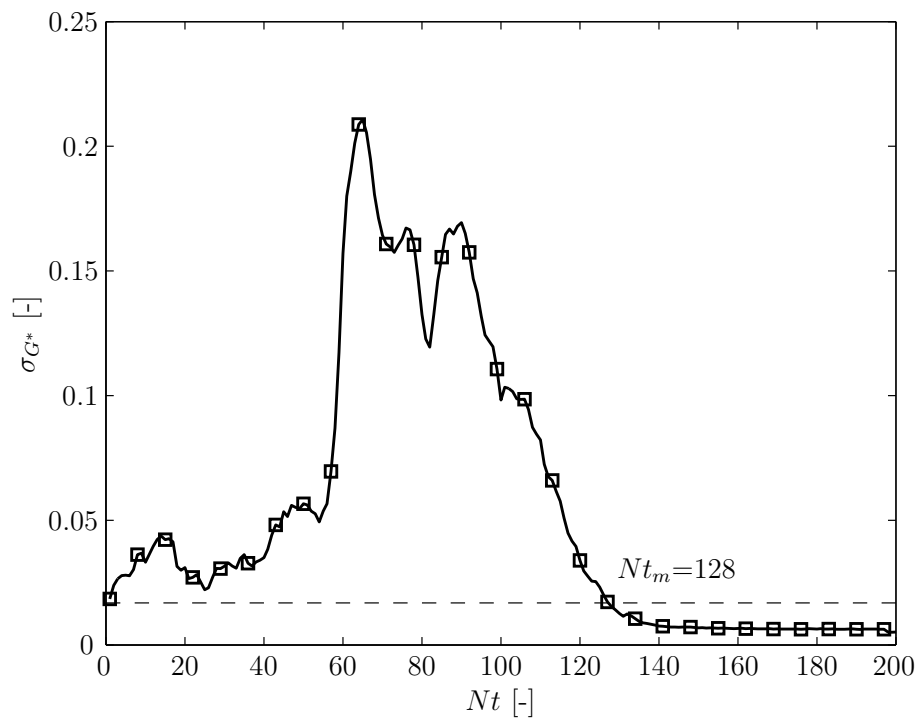


Figure 3.8: Variation in time of the standard deviation across the investigation region of the normalised green channel  $G^*$  ( $Fr_{do}=0.17$ ,  $h/d_i=0.5$ ,  $d_o/d_i=0.25$ ).

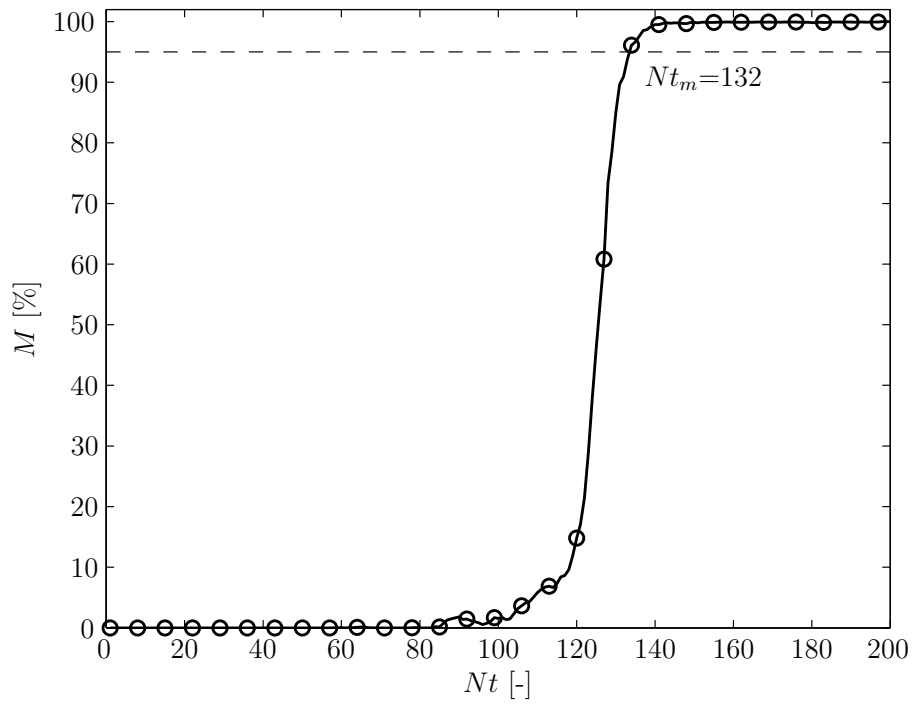


Figure 3.9: Percentage of mixed pixels of the normalised green channel  $G^*$  as a function of shaker table revolution ( $Fr_{do}=0.17$ ,  $h/d_i=0.5$ ,  $d_o/d_i=0.25$ ).

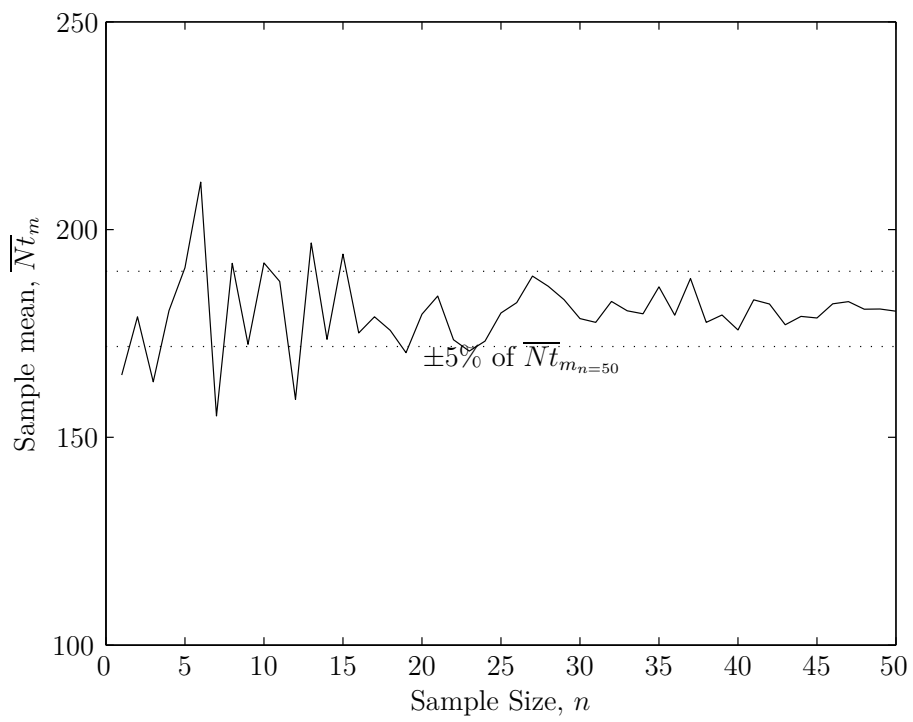


Figure 3.10: Variation of the average mixing time with increasing random sample size ( $Fr_{do}=0.17$ ,  $h/d_i=0.5$ ,  $d_o/d_i=0.25$ ).

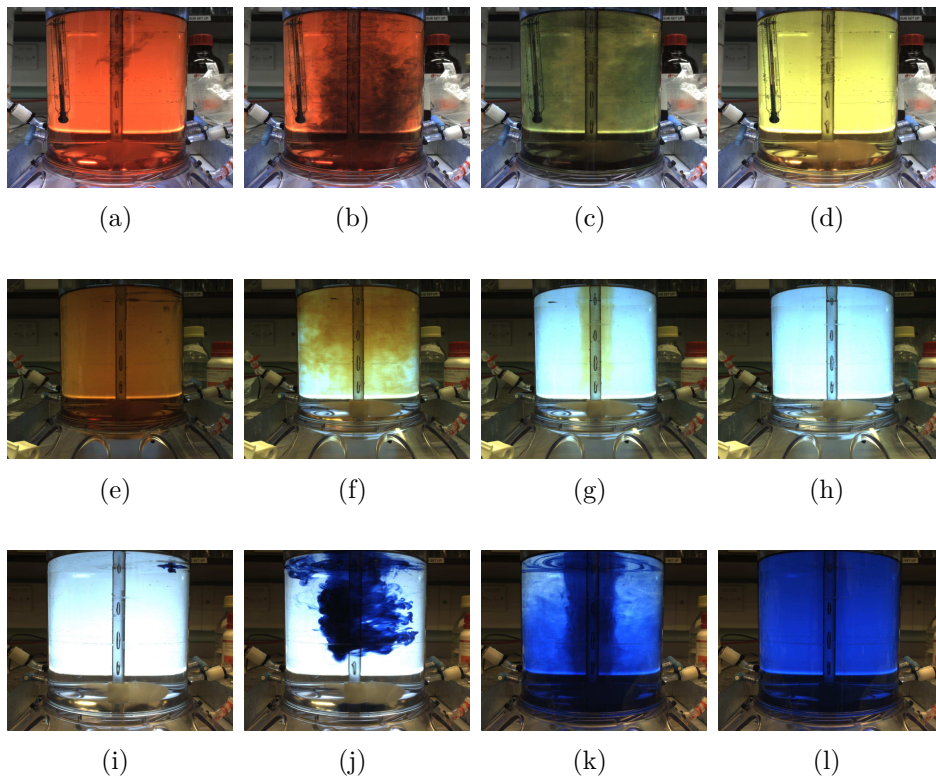


Figure 3.11: Time evolution of the mixing dynamics inside the CellReady 3 L STR for three mixing time methodologies: Dual Indicator System for Mixing Time and pH probe (a-d); Iodine-Sodium Thiosulfate (e-h); Waterblue dye (i-l).

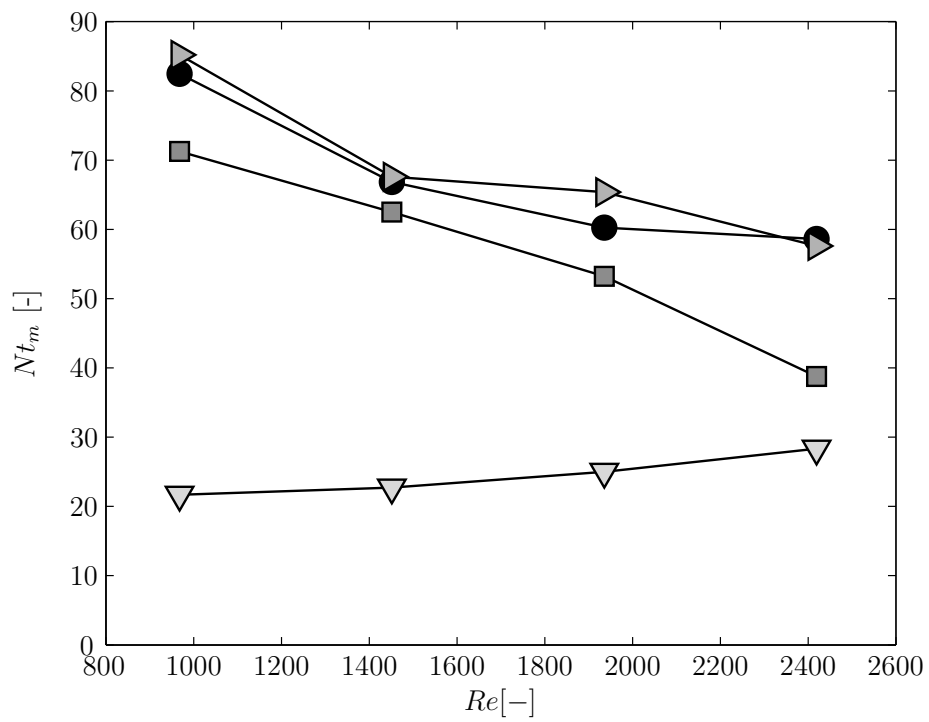


Figure 3.12: Comparison of Mixing Time measurement in the CellReady at  $V_f=2L$  using DISMT (●), Iodine-Sodium thiosulfate (□), Water-blue dye (▽) and pH probe methodologies (▷).

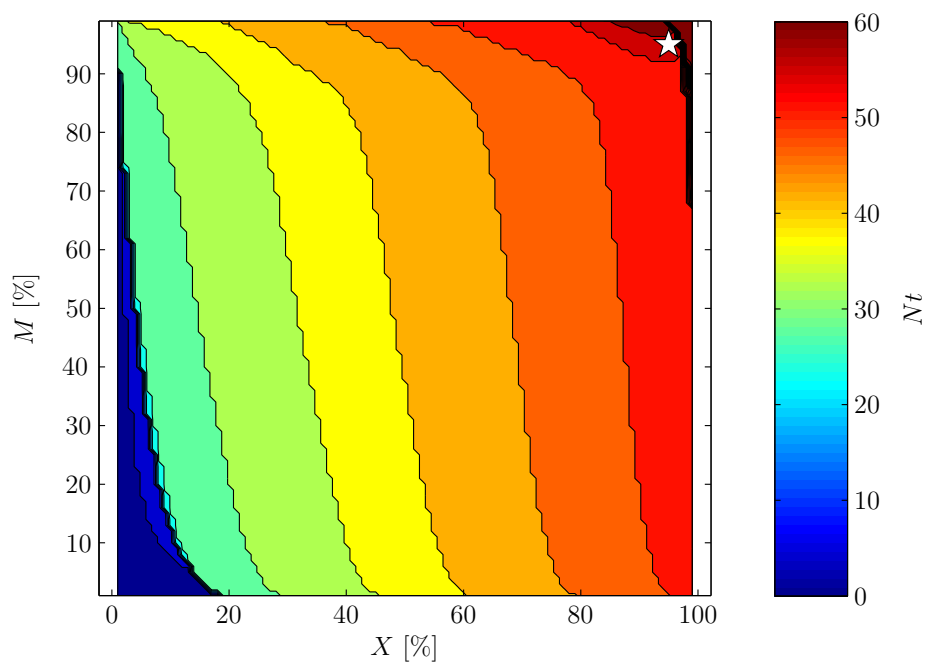


Figure 3.13: Variation in time of the percentage of pixels mixed,  $M$ , against the local mixing threshold selected,  $X$ , for a Mobius CellReady reactor, with  $V_f=2$  L,  $N=50$  RPM ( $Re=14000$ ).

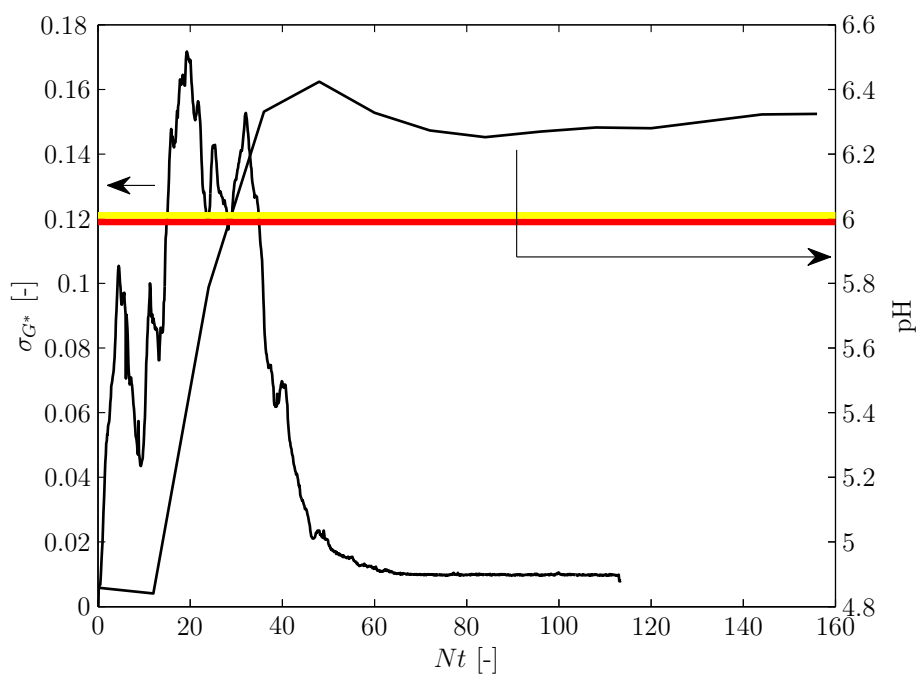


Figure 3.14: Variation in time of the pH probe readings and of the standard deviation of the normalised green channel output,  $\sigma_{G^*}$ , for New Brunswick Bioreactor (the horizontal lines indicate the pH threshold for the fluid to turn from red to yellow).

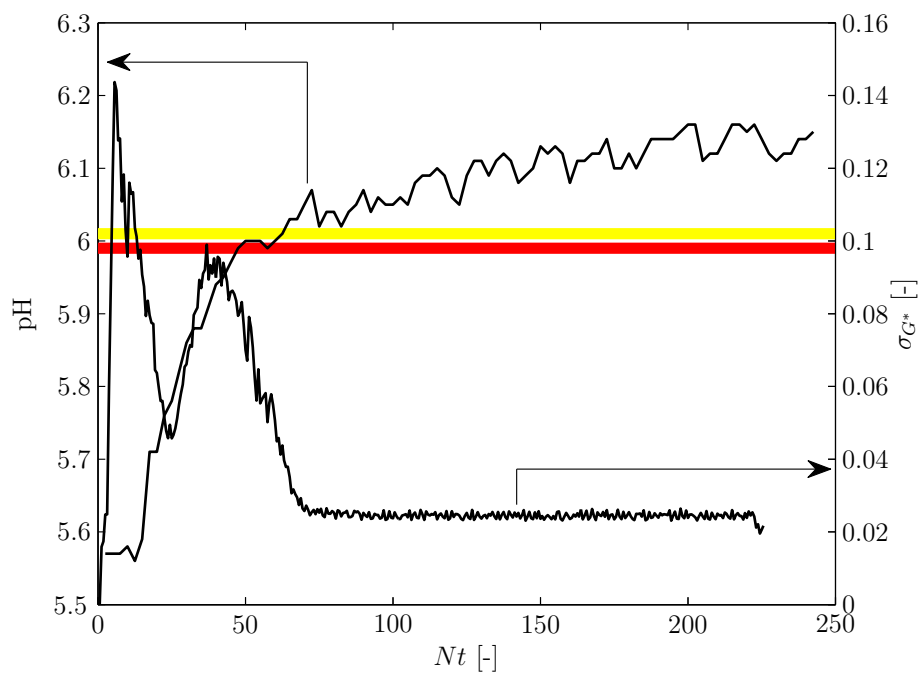
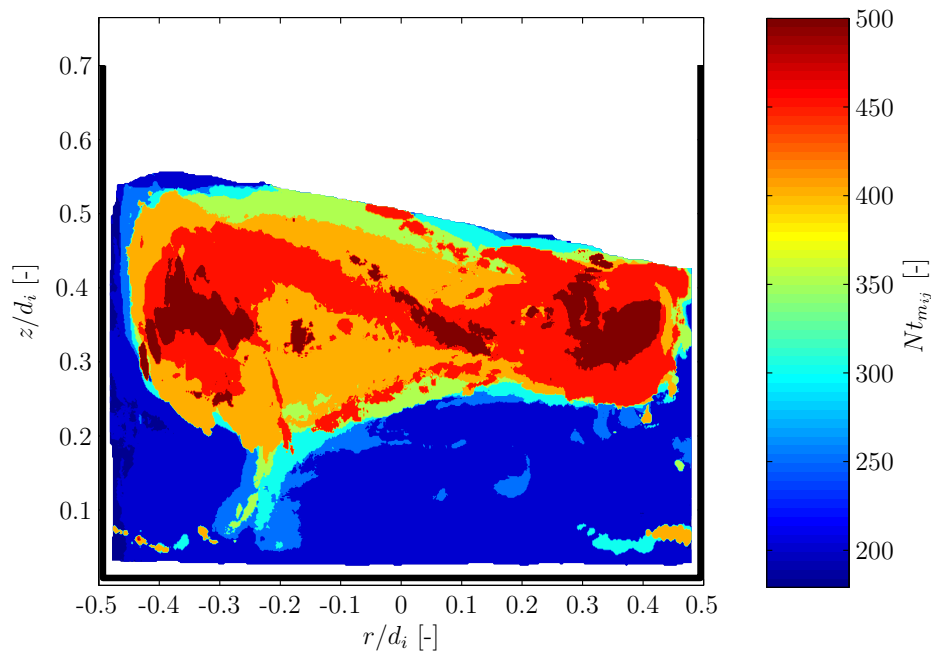
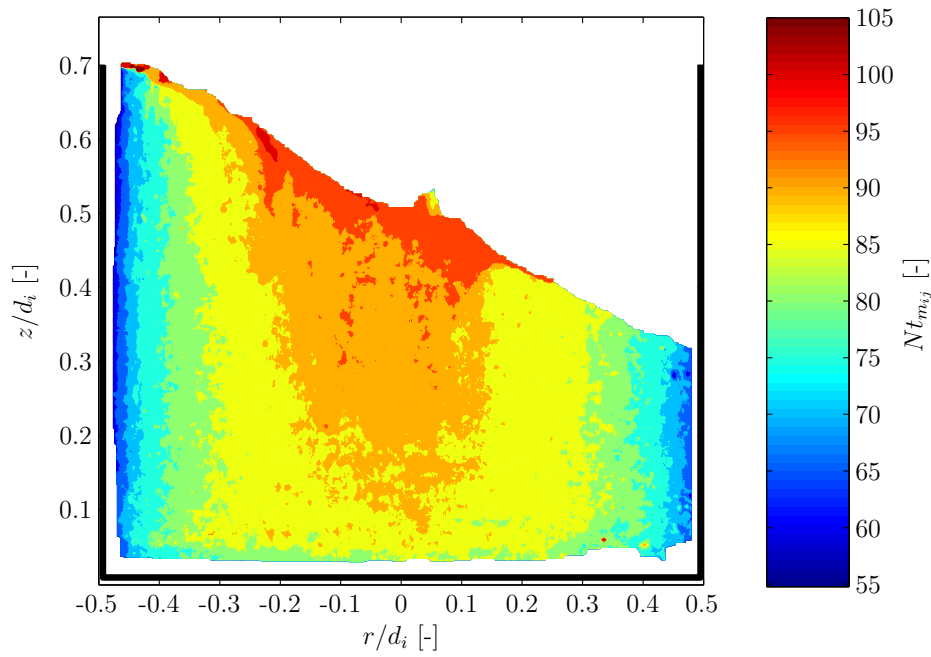


Figure 3.15: Variation in time of the pH probe readings and of the standard deviation of the normalised green channel output,  $\sigma_{G^*}$ , for CellReady Bioreactor (the horizontal lines indicate the pH threshold for the fluid to turn from red to yellow).



(a)



(b)

Figure 3.16: Characteristic mixing time maps for different Froude number ( $h/d_i=0.5$ ;  $d_o/d_i=0.25$ ): (a)  $Fr_{d_o}=0.11$  (b)  $Fr_{d_o}=0.23$ .

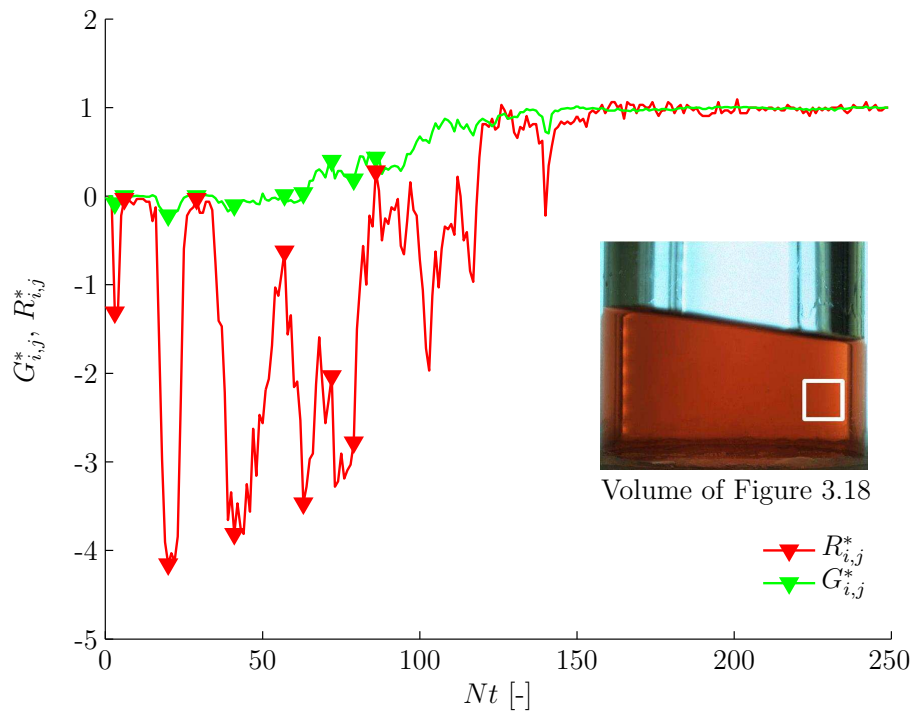


Figure 3.17: Variation in time of the normalised green and red indices,  $G_{i,j}^*$  and  $R_{i,j}^*$ , for the point of the bioreactor at the centre of the area delimited in the inset image.

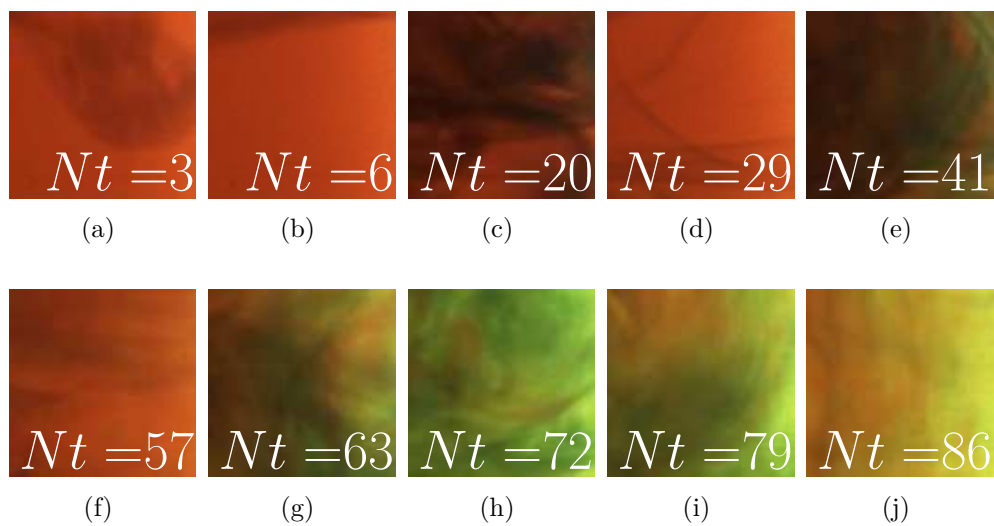


Figure 3.18: Colour evolution in time within the area highlighted in the inset image of Figure 3.17.

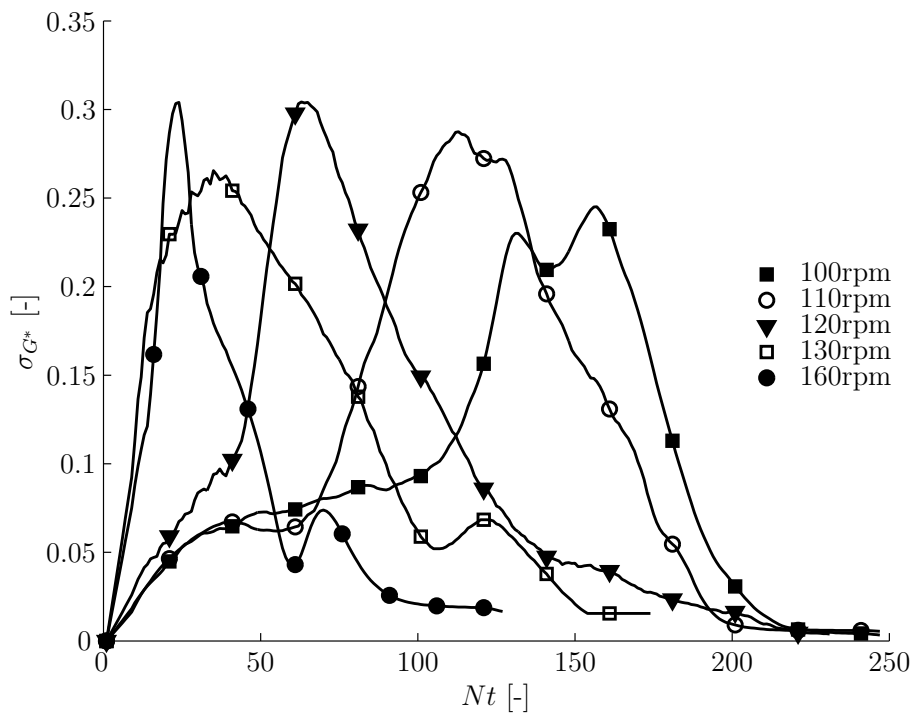


Figure 3.19: Variation in time of the standard deviation of the normalised green channel output,  $\sigma_{G^*}$ , for different orbital speeds. All data are for a cylindrical OSR with  $d_i=100$  mm,  $d_o=25$  mm.

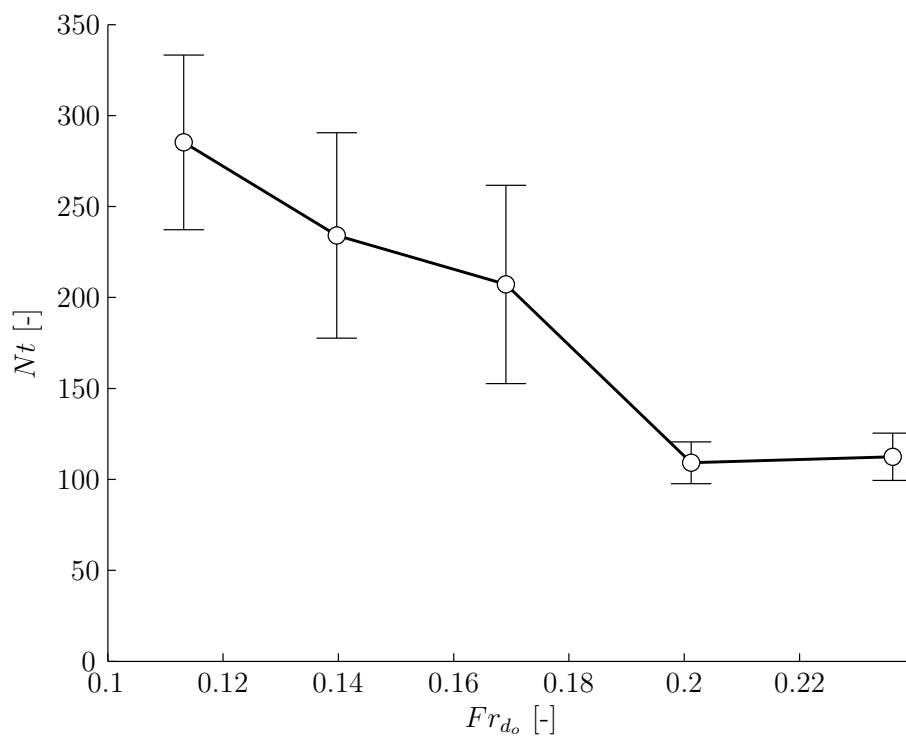


Figure 3.20: Non-dimensional mixing time in a cylindrical bioreactor ( $d_i=100$  mm,  $d_o=25$  mm,  $h=50$  mm) at increasing  $Fr_{d_o}$ .

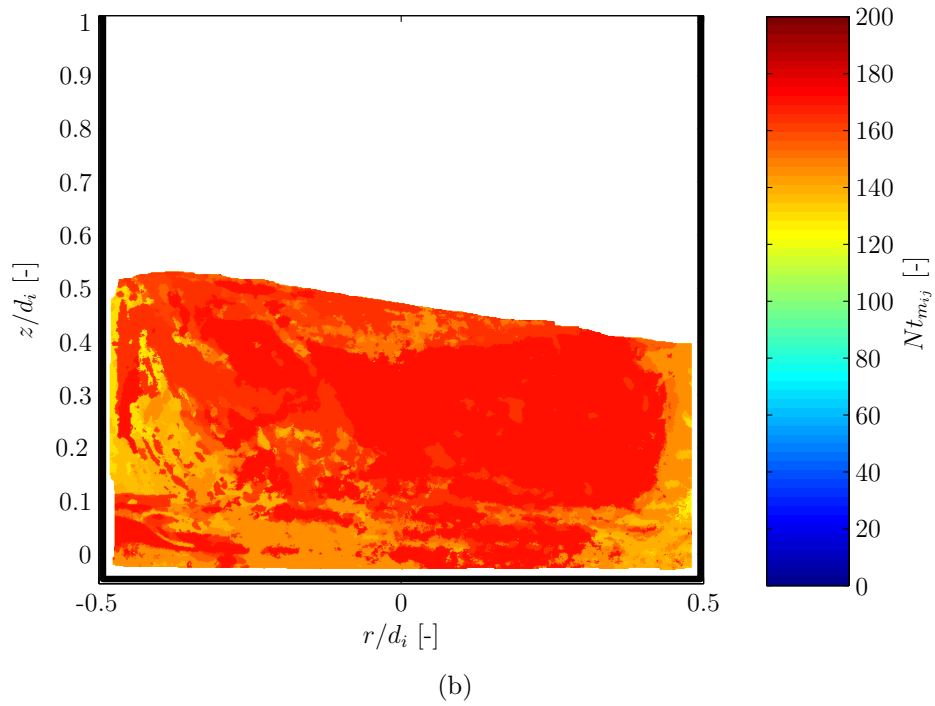
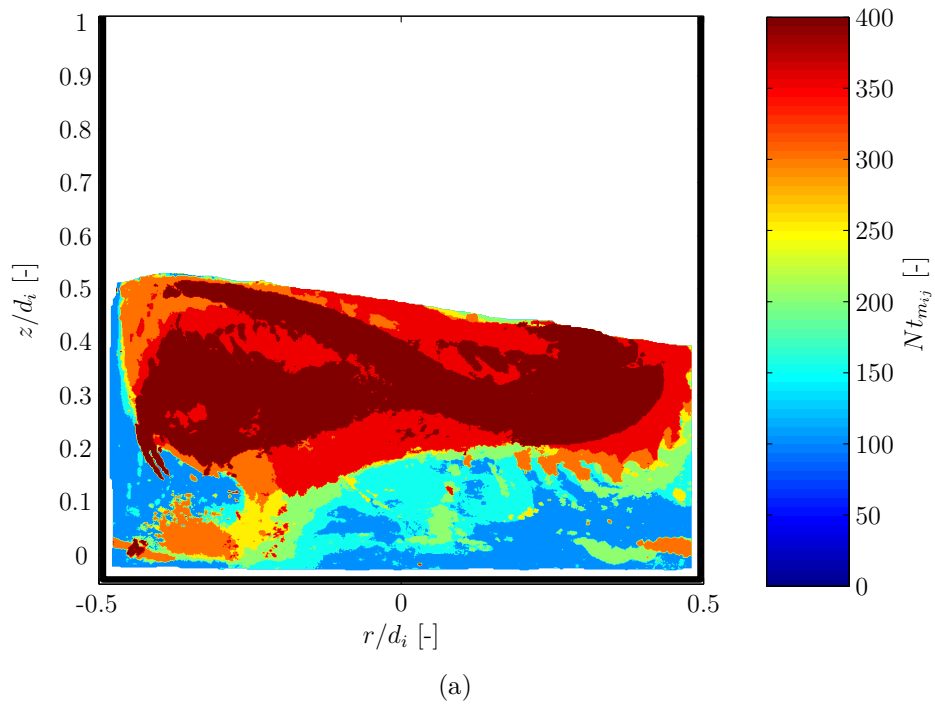


Figure 3.21: Mixing time maps for two DISMT experiments at same conditions:  $h/d_i=0.5$ ,  $d_o/d_i=0.25$ ,  $Fr_{d_o}=0.12$ . (a)  $Nt_m=350$  Nt; (b)  $Nt_m=160$  Nt.

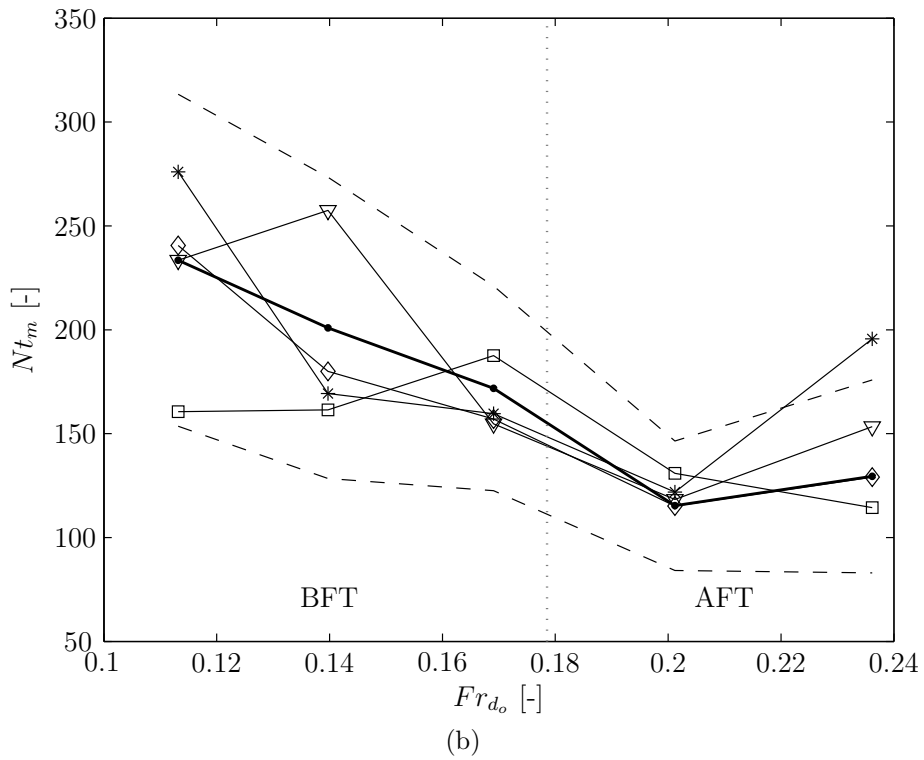
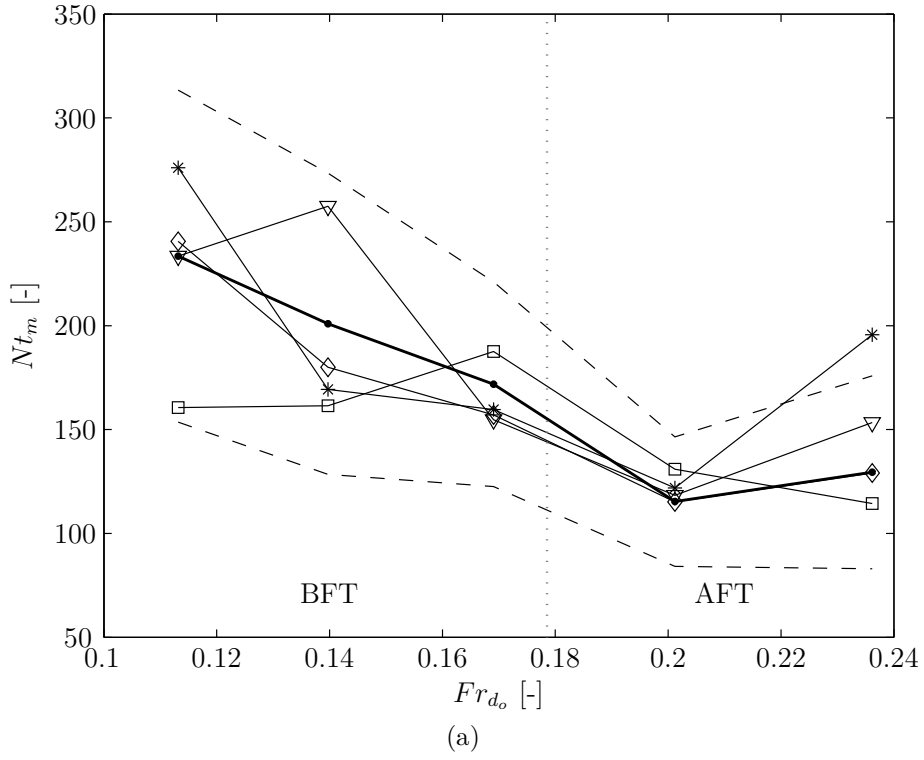


Figure 3.22: Variation of the mixing number with radial feed position and  $Fr_{d_o}$ .  $h/d_i=0.5$ ;  $d_o/d_i=0.25$ . Insertion point (a): P1= $\diamond$ , P2= $\nabla$ , P3= $\square$ , P4= $*$ , Average P1-P7= $\bullet$ ,  $\pm$  one standard deviation= $(- - -)$ ; (b) P4= $*$ , P5= $\square$ , P6= $\nabla$ , P7= $\diamond$ , Average P1-P7= $\bullet$ ,  $\pm$  one standard deviation= $(- - -)$ .

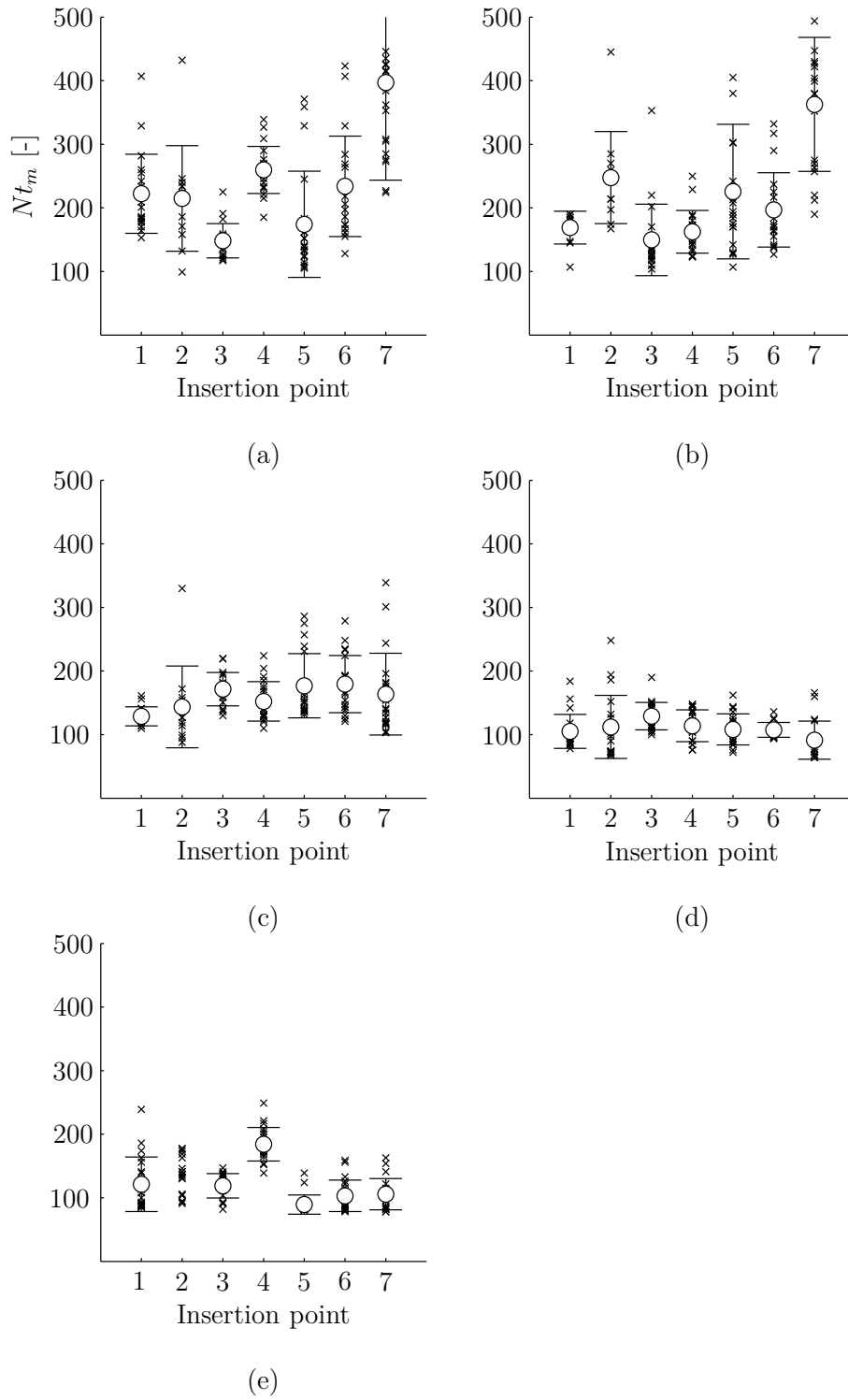


Figure 3.23: Variation of the mixing number with radial feed position at different  $Fr_{d_o}$ . ( $h/d_i=0.5$ ;  $d_o/d_i=0.25$ ). ( $\times$ ) experimental result, ( $\circ$ ) average with error bar;  $Fr_{d_o} =$  (a) 0.11, (b) 0.14, (c) 0.17, (d) 0.2, (e) 0.24.

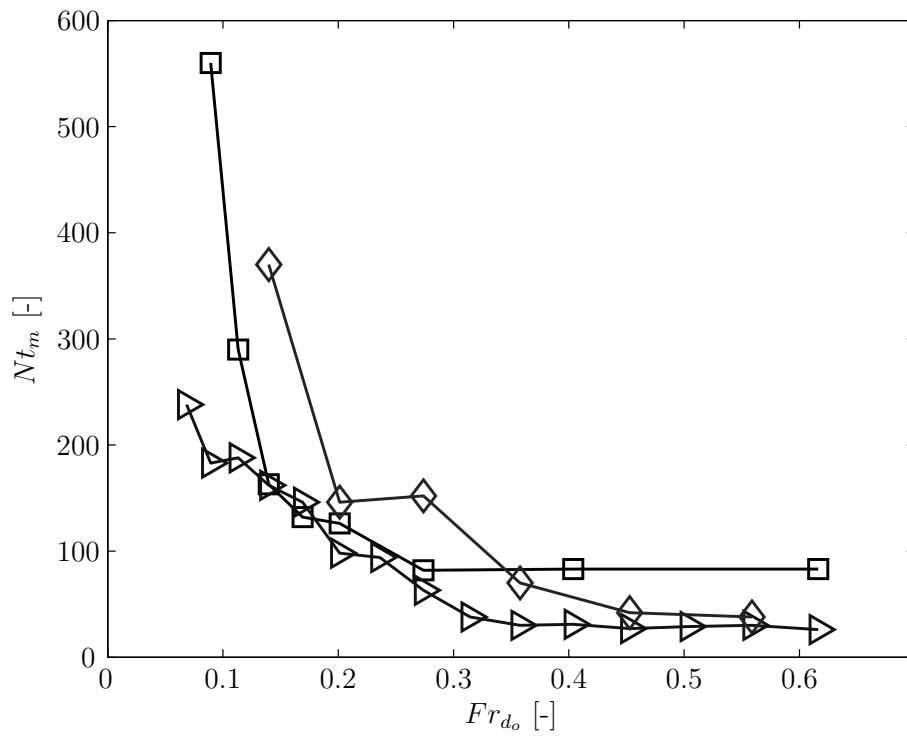


Figure 3.24: Variation of the mixing number with  $Fr_{d_o}$  for constant  $d_o/d_i=0.25$  and different fluid height: ( $\square$ )  $h=30$  mm, ( $\triangleright$ )  $h=50$  mm, ( $\diamond$ )  $h=70$  mm.

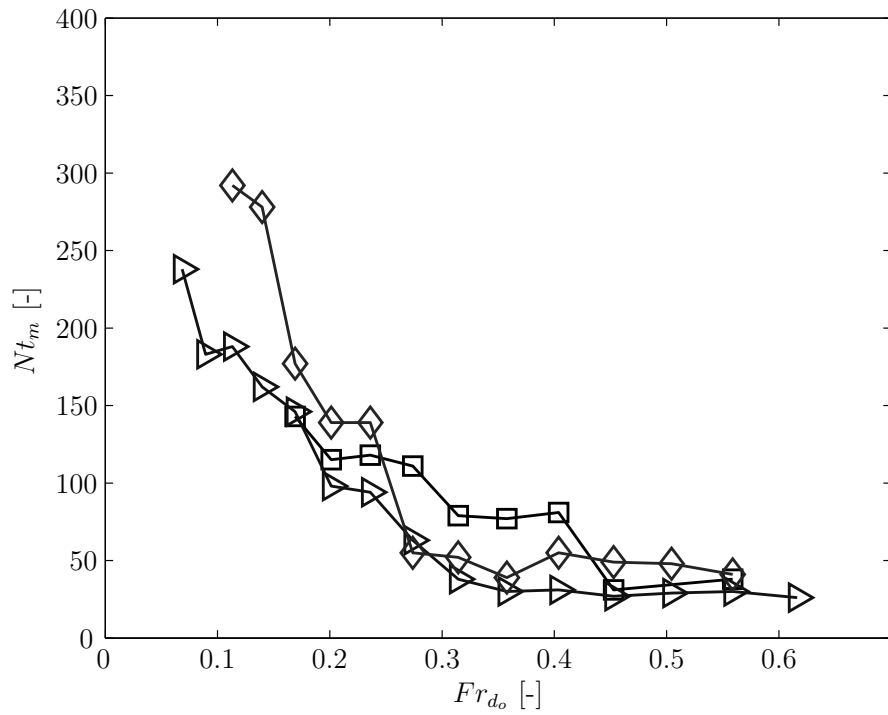


Figure 3.25: Variation of the mixing number with  $Fr_{d_o}$  for constant  $d_o/d_i=0.25$  and  $h/d_i=0.5$ : ( $\square$ )  $d_i=70$  mm and  $h=35$  mm, ( $\triangleright$ )  $d_i=100$  mm and  $h=35$  mm, ( $\diamond$ )  $d_i=130$  mm and  $h=65$  mm.

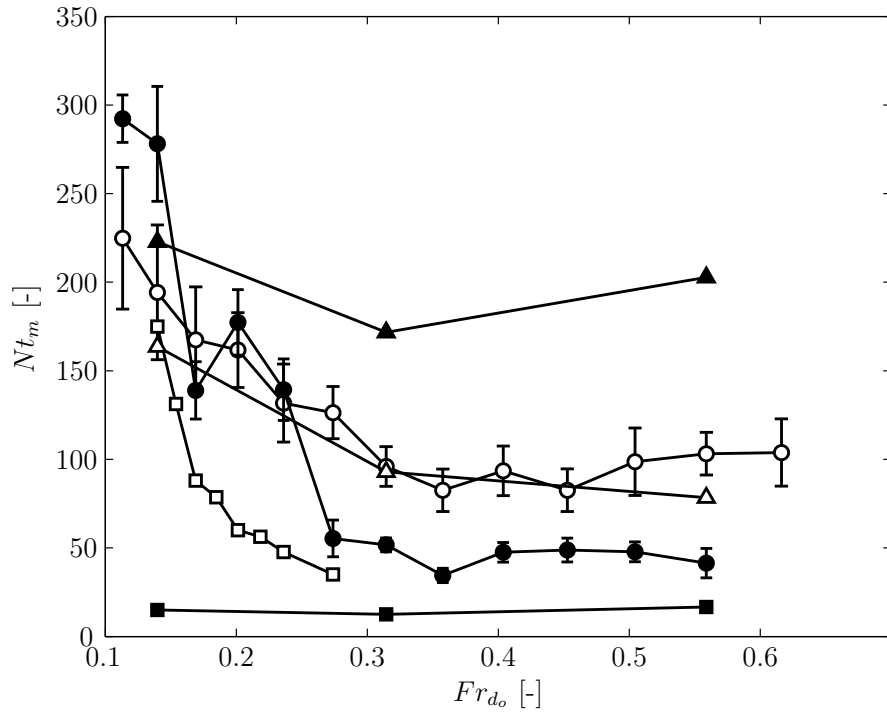


Figure 3.26: Comparison of  $Nt_m$  versus  $Fr_{d_o}$  curves obtained in cylindrical and Erlenmeyer OSRs against those reported by Tissot *et al.* (2010) and Tan *et al.* (2011):

- (○) Cylindrical OSR,  $d_i=100$  mm,  $h=50$  mm,  $V_f=0.4$  L,
- (●) Cylindrical OSR,  $d_i=130$  mm,  $h=65$  mm,  $V_f=0.85$  L,
- (□) Tissot *et al.* (2010) OSR,  $d_i=100$  mm,  $h=125$  mm,  $V_f=1$  L,
- (▲) Erlenmeyer Flask,  $d_i=131$  mm,  $V_f=0.4$  L,
- (△) Erlenmeyer Flask,  $d_i=166$  mm,  $V_f=0.8$  L,
- (■) Tan *et al.* (2011), Erlenmeyer Flask,  $d_i=105$  mm,  $V_f=0.05$  L.

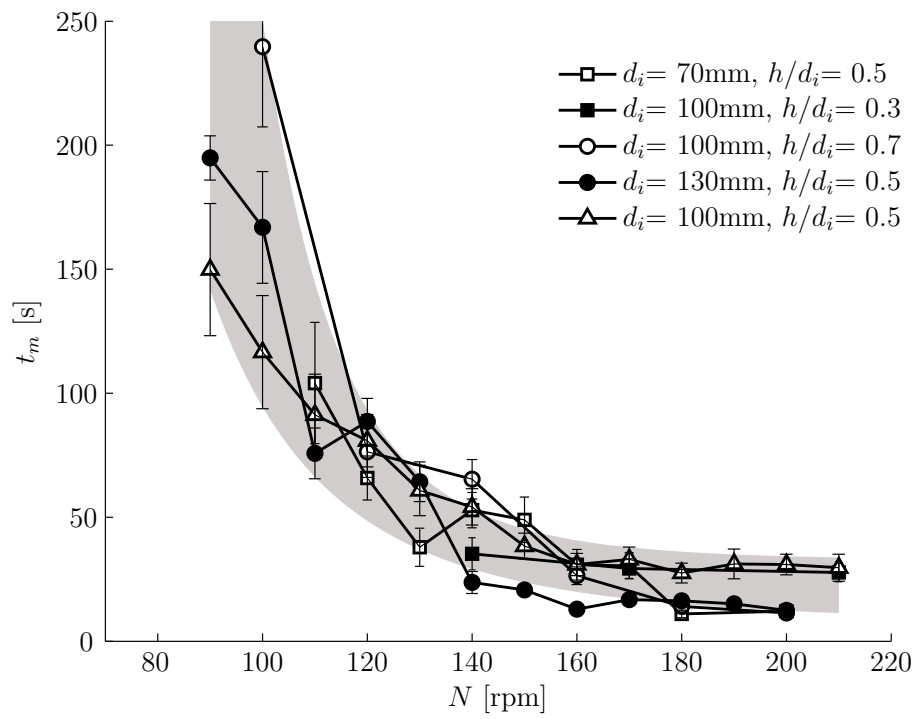


Figure 3.27: Variation of the mixing time with dimensional shaking speed for cylindrical OSRs.

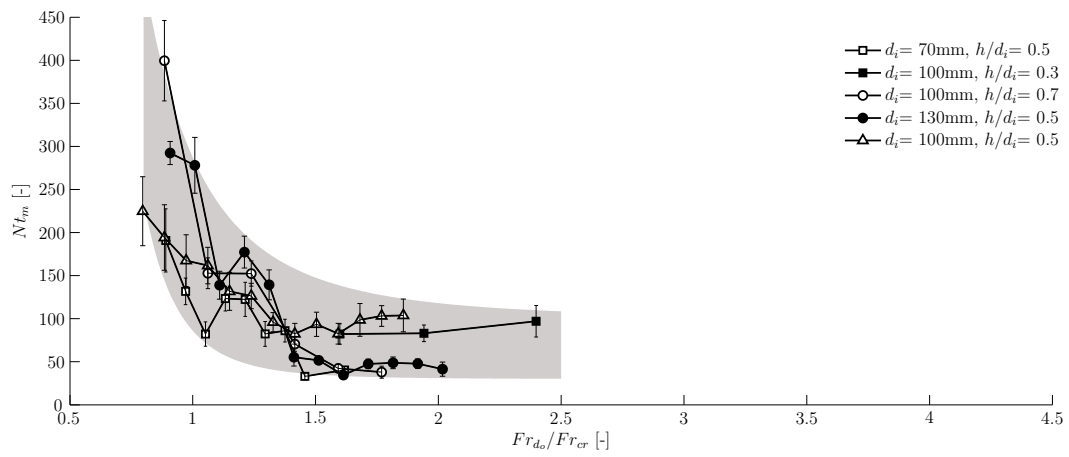


Figure 3.28: Variation of the mixing number with  $Fr_{do}/Fr_{cr}$ , for cylindrical OSRs.

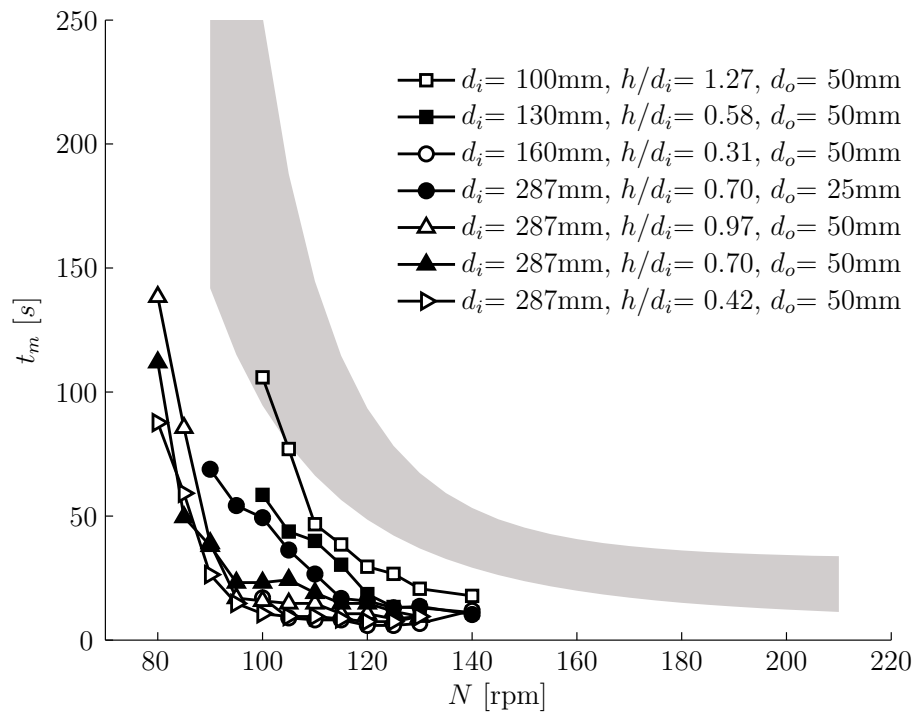


Figure 3.29: Comparison of the present cylindrical OSR mixing data with those reported by Tissot *et al.* (2010), in terms of mixing time against shaking speed (dimensional).

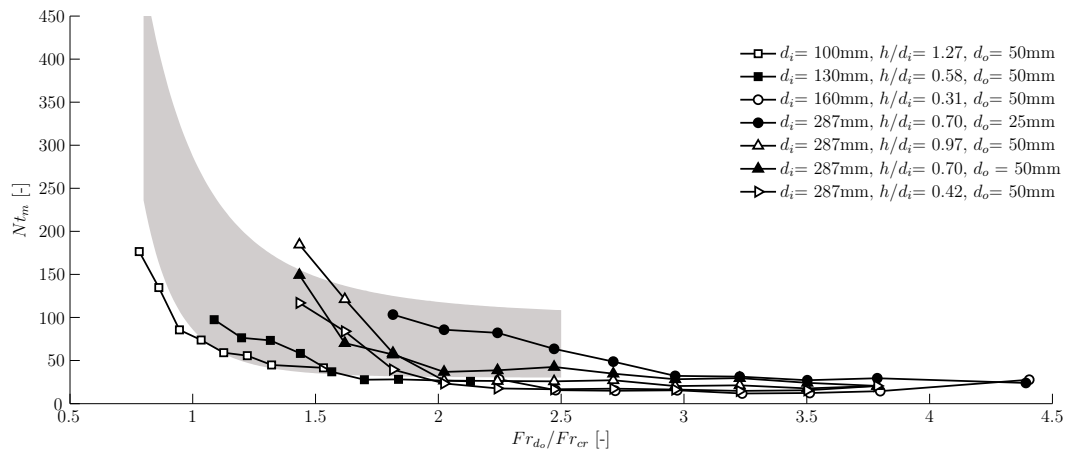


Figure 3.30: Comparison of the present cylindrical OSR mixing data with those reported by Tissot *et al.* (2010), in terms of mixing number against the proposed scaling factor  $Fr_{d_o}/Fr_{cr}$  (non-dimensional).

# Chapter 4

## Fluid flow and solid suspension in cylindrical OSRs with conical bottoms<sup>†</sup>

### 4.1 Introduction

This chapter investigates to what extent flow and suspension dynamics are affected when a conical bottom is used. The geometry of the OSR with conical bottom is described in Sections 2.2.1 and 2.2.3. Three bottom geometries were compared: flat, conical A (cone height,  $h_c=5$  mm; angle from the horizontal,  $\alpha_c=6.3^\circ$ ) and conical B (cone height,  $h_c=15$  mm; angle from the horizontal,  $\alpha_c=18.4^\circ$ ).

The flow dynamics in a flat bottom cylindrical OSR have been described by

---

<sup>†</sup>Most of the results presented in this chapter are included in:

Rodriguez, G., Perialisi, I., Anderlei, T., Ducci, A., Micheletti, M. (2015), "Appraisal of fluid flow in a shaken bioreactor with conical bottom at different operating conditions", *Chemical Engineering Research and Design*, vol 108, issue 11, pp. 186-197.

Weheliye *et al.* (2013) and Rodriguez *et al.* (2013). This chapter builds upon those findings to investigate the effects of a conical bottom geometry on the flow in a cylindrical OSR. Section 4.2.1 investigates the impact of a conical bottom of two different heights on the development of the vortical structures described by Weheliye *et al.* (2013), and on the intensity of the space-averaged vorticity. The principal components of the strain rate tensor were estimated over the entire flow field for the flat and conical B bottom geometries and, together with the intensity and position of maximum strain rate, are reported in Section 4.2.2. Section 4.2.3 provides an account on how and to what extent conical bottom geometries affect the flow at a phase angle,  $\varphi=270^\circ$ , which is characterized by a strong radial flow responsible for moving the fluid between opposite sides of the bioreactor (Rodriguez *et al.*, 2013). Section 4.2.4 shows how the conical bottom geometry affects the intensity of kinetic energy for increasing Froude number.

In Section 4.3 the effect of conical bottoms on solid suspension is evaluated using Trypan blue dyed GE Healthcare Life Science Cytodex 3 microcarriers, which are commonly used in cell culture for adherent cell lines (see Section 2.4). The suspended speed is associated to a condition of homogeneous dispersion of the microcarriers in the reactor. The process of dispersion is estimated through image processing from the blue intensity on the vertical field of view. The cylindrical OSR of orbital diameter  $d_i=100$  mm is used with flat, conical A and B bottom geometries at different orbital diameters ( $d_o=15, 25$  and  $50$  mm) and fluid heights ( $h=45$  and  $70$  mm). Further experiments are performed with a  $d_i=70$  mm vessel with flat and conical B geometry (cone height,  $h_c=10.5$  mm; angle from the horizontal,  $\alpha_c=18.4^\circ$ ) at  $d_o=15, 25$  and  $50$  mm and constant fill volume  $V_f=115$  and  $192$  mL, corresponding to  $h=30$  and  $33.8$  mm and  $h=50$  and  $53.8$  mm, respectively. The effect of the orbital diameter on solid suspension is estimated both in terms of dimensional  $N$  [RPM] and non-dimensional  $Fr_{d_o}$  characteristics, in an

attempt to determine a scaling factor related to suspension characteristics.

## 4.2 Effects of conical bottom on fluid flow

### 4.2.1 Effects of bottom design on flow dynamics and vorticity

Phase-resolved velocity fields and tangential vorticity contour maps were obtained for the three bottom geometries investigated (flat, conical A and conical B) in a cylindrical OSR of  $d_i=100$  mm. Figure 4.1 shows the truncated cone in position in the cylindrical OSR. The velocity fields are measured at a phase angle  $\varphi=0^\circ$ , when the OSR is at the point furthest to the left along the shaker orbit. The vertical plane of measurement bisects the cylindrical bioreactor into two halves. The phase-resolved velocity fields is calculated using Equation 4.1.

$$\langle u(r, z, \varphi) \rangle = \frac{\sum u(r, z, \varphi)}{N_\varphi} \quad (4.1)$$

where  $u(r, z, \varphi)$  is the instantaneous velocity field on the plane of measurement  $(r, z)$  and  $N_\varphi$  is the number of velocity fields obtained for each angular position,  $\varphi$ . In this work  $N_\varphi=500$  image pairs were used to calculate the phase-averaged velocity  $\langle u \rangle$ . The vorticity in the  $k^{th}$  direction,  $\omega_k$ , defined in Equation 4.2, was calculated from phase-averaged velocity fields on a two-dimensional grid using a central differentiation scheme.

$$\omega_k = \left( \frac{\partial u_i}{\partial x_i} - \frac{\partial u_j}{\partial x_j} \right) \quad (4.2)$$

where  $u_i$  and  $u_j$  indicate the velocity components in the  $i_{th}$  and  $j_{th}$  directions,

respectively. Velocity fields and vorticity contours are shown in Figures 4.2 to 4.4, for flat,  $h_c=5$  mm (conical A) and 15 mm conical (B) bottom cylinders, respectively. In all cases, the data shown were obtained at shaking speeds  $N=85, 100, 110$  and  $115$  RPM and  $Fr_{d_o}=0.10, 0.14, 0.17, 0.18$  (Figures 4.2 to 4.4 a-d). All vorticity contour maps are scaled according to the colour bars included in Figure 4.2 (d), 4.3 (d), 4.4 (d). Regions with red hues indicate a positive value of vorticity and counterclockwise rotation, whilst those in blue are associated to negative vorticity and clockwise rotation. Two counter-rotating vortical cells can be identified within the bulk of the fluid from all the vorticity contour maps considered. The cells represent a section of the toroidal vortex inclined below the free surface. In agreement with previous studies conducted using flat bottom bioreactors (Weheliye *et al.*, 2013), the size of the vortical cells increases and expands from the free surface towards the cylinder bottom as  $Fr_{d_o}$  is increased. Figure 4.2 (a) shows vortical cells present at a location close to the vessel walls and the free surface. As the shaking speed is increased the vortical cells increase in size and intensity, expanding toward the centre and bottom of the bioreactor (Figure 4.2 a-d), reaching the bottom at shaking speeds  $N > 110$  RPM ( $Fr_{d_o} > 0.17$  in Figure 4.2 d). The shaking speed at which flow transition occurs for the flat bottom bioreactor is in agreement with that indicated by Weheliye *et al.* (2013) for the geometrical configuration and operating conditions used in this study ( $h/d_i=0.5$  and  $d_o/d_i=0.25$ ).

A similar vortical cell expansion is observed for the conical bottom bioreactors investigated, however some differences with the flat bottom geometry can be noted from Figures 4.3 and 4.4. The shaking speed at which the vortices extend to the bottom decreases as the inclination of the conical bottom is increased. It is clear from Figures 4.4 (a-d) that the vortices reach the base of the bioreactor at a shaking speed  $N=100$  RPM for the most inclined conical bottom studied

in this work (see Figure 4.4 b), while the same phenomenon occurs at  $N=110$  and 115 RPM for the conical A (Figure 4.3 c) and flat bottom (Figure 4.2 d) designs, respectively. Despite the fact that the fully extended vortex configuration occurs at lower speeds when conical bottom geometries are used, Figures 4.4 (a-d) suggest that the vortical structures are still present at speeds higher than that associated to full vortex extension and the critical speed of the aforementioned mean flow transition is not affected by the bottom geometry. This could be due to the conical design influencing the shape of the vortical cells, pushing them closer to the vessel walls and away from each other reducing their interaction at the centre of the bioreactor.

Vorticity intensity increases as the shaking speed is increased for all bottom configurations investigated, as seen in Figures 4.2 to 4.4. The space-averaged non-dimensional vorticity,  $\omega_\theta^*$ , is defined in Equation 4.3 and its variation with  $Fr_{d_o}$  is provided in Figure 4.5 (a). The spaced-average is carried out inside the area delimited by a non-dimensional vorticity threshold of  $\omega_\theta > 0.1\pi N$ , which is shown for reference in Figure 4.5 (b) (conical A configuration,  $N=80$  RPM,  $Fr_{d_o}=0.09$ ).

$$\omega_\theta^* = \frac{\int_{A_\omega} |\omega_\theta| dA_\omega}{A_\omega} \quad (4.3)$$

As expected, the space-averaged non-dimensional vorticity,  $\omega_\theta^*$ , increases with  $Fr_{d_o}$  for flat, conical A and B bottoms (Figure 4.5 a). At shaking speeds corresponding to values of  $Fr_{d_o}$  below 0.12, similar values of  $\omega_\theta^*$  were obtained for all geometries investigated. At these conditions the toroidal vortices are present only in proximity of the free surface and vessel walls, as shown in Figures 4.2 (a), 4.3 (a) and 4.4 (a), respectively. The main flow does not extend to the bioreactor bottom, hence no effect of the conical bottom is observed. However for  $Fr_{d_o} > 0.12$  the rate of vorticity variation with  $Fr_{d_o}$  is more pronounced with increasing in-

clination of the conical bottom. Power curves fitted to the data points indicate that the space average vorticity for the conical B geometry is always higher than that of conical A for  $Fr > 0.12$ . This behaviour is in agreement with the description of the phase-resolved flow provided above, and indicates that the vorticity of the two cells is affected by the bottom geometry only for speed sufficiently large to determine full expansion to the bioreactor base. The greater space-averaged vorticity would benefit solid suspension as the solid lifting force,  $\mathbf{F}_1$  defined in Equation 4.4, is proportional to the slip velocity,  $\mathbf{u} - \mathbf{v}_p$ , and flow vorticity,  $\boldsymbol{\omega}$ , with  $d_p$ ,  $\mathbf{v}_p$ ,  $\rho_l$ ,  $\mathbf{u}$  and  $C_l$  being the solids diameter and velocity, the viscosity and velocity of the liquid phase and the lift coefficient, respectively.

$$\mathbf{F}_1 = \frac{\pi}{4} d_p^3 \frac{\rho_l}{2} C_l ((\mathbf{u} - \mathbf{v}_p) \times \boldsymbol{\omega}) \quad (4.4)$$

## 4.2.2 Effects of bottom design on shear rates

The effect of shear on cell metabolism and product expression has been a topic of discussion since mammalian cells became one of the major expression host for the production of antibodies and other therapeutics, and an agreement has yet to be reached on whether fluid stresses have a significant impact (Cherry and Hulle, 1992; Keane *et al.*, 2003; Ludwig *et al.*, 1992; Nienow *et al.*, 2013). It is clear, though, that a more rigorous quantification of fluid shear is needed in order, for example, to improve understanding of its effect on more delicate and shear-sensitive cells such as human stem cells. Maximum shear and strain rate components have therefore been quantified in this work. The strain rate tensor,  $S_{ij}$ , for the 2D flow measurements provided in this Thesis is defined in

Equation 4.5.

$$S_{ij} = \begin{pmatrix} \frac{\partial u_i}{\partial x_i} & \frac{1}{2}(\frac{\partial u_i}{\partial x_j} + \frac{\partial u_j}{\partial x_i}) \\ \frac{1}{2}(\frac{\partial u_j}{\partial x_i} + \frac{\partial u_i}{\partial x_j}) & \frac{\partial u_j}{\partial x_j} \end{pmatrix} \quad (4.5)$$

where indices  $i$  and  $j$  indicate the radial and axial directions, respectively. The strain rate tensor is a measure of local rate of stretching, compression and shear. When a local reference system aligned with the principal axes of  $S_{ij}$  is considered, the highest rate of stretching and compression can be determined. These are found from the principal components (eigenvalues)  $S_1$  and  $S_2$  of the strain rate tensor (Equation 4.5). Positive values of  $S_1$  and  $S_2$  indicate stretching, whilst negative values relate to compression (Bouremel *et al.*, 2009; Davidson, 2015). In this work only two velocity components were measured, therefore the  $S_3$  component of the strain rate tensor in the  $k$  direction orthogonal to the plane of measurement (i.e. azimuthal direction) was estimated using the continuity equation (Equation 4.6):

$$S_3 = -S_1 - S_2 \quad (4.6)$$

The principal components of the strain rate tensor,  $S_1$  and  $S_2$ , for the conical B geometry at  $Fr_{d_o}=0.14$  ( $N=100$  RPM) are shown in Figures 4.6 (a) and (b), respectively. It should be noted that the principal component  $S_1$  is negative across the entire field of view, and therefore it provides an estimate of the compression rates experienced by the cells. The direction of compression is not given in Figure 4.6 (a), but it is locally aligned with the direction of the first eigenvector of the local strain rate tensor. From the contour plot the highest compression rate is found at the margins of the counter-rotating vortices. The normal stress  $S_2$ , which is always positive and is associated to local stretching rates, reaches its maximum in the lower section of the toroidal vortices, at  $|r/d_i|=0.1-0.5$  and  $z/d_i=0.1-0.2$ , in proximity of the tips of the conical bottom upper surface (see

Figure 4.6 a).

The maximum shear rate,  $\tau_{max}$ , experienced at a specific location, can be found from the principal components of the strain rate tensor according to Equation 4.7.

$$\tau_{max} = \frac{(S_i - S_j)_{max}}{2} \quad (4.7)$$

where indices  $i$  and  $j$  are selected based on the maximum difference between any two principal components  $S_1$ ,  $S_2$  and  $S_3$ .

The contour plots of the phase-resolved maximum shear rates on the vertical plane ( $\varphi=0^\circ$ ) at  $Fr_{d_o}=0.14$  ( $N=100$  RPM) for flat, conical A and B geometries are shown in Figures 4.7 (a-c), respectively. This  $Fr_{d_o}$  number corresponds to in-phase flow condition for all the geometries investigated (according to the definition given by Weheliye *et al.* (2013), see Equations 1.7 and 1.8), but the toroidal vortices extend to the bottom of the vessel only for the conical B configuration (cf. from Figures 4.2 b, 4.3 b and 4.4 b). Values as high as  $\tau_{max}=0.13\pi N$  can be observed in Figure 4.7 (a) at the periphery of the toroidal vortical cells (shown in Figure 4.2 b). The maximum shear rate of Figure 4.7 (a),  $\tau_{max}=0.2\pi N$  occurs at  $r/d_i=0$ , in correspondence to the cylinder axis. This is probably due to inaccuracies in the PIV measurements as tracer particle agglomerates were visually observed at such location. The lowest  $\tau_{max}$  is found at the core of the cells ( $|r/d_i|=0.2$ ,  $z/d_i=0.2-0.3$ ), where quasi-solid body rotation occurs. Similarly, the shear rates for the conical A and B bottoms are characterized by low values at the core of the vortical cells and higher shear rates at the periphery (Figures 4.7 b-c). The maximum intensity of the shear rate occurs at the interfaces between the vortices and the fluid above the upper conical surface. Whilst Figure 4.7 (a) shows two distinct low shear regions in correspondence to the vortical cell cores, a third region of low  $\tau_{max}$  can be observed for conical geometries A and

B, above the truncated cone tip. When observing the high shear regions rising at the inner margins of the counterclockwise and clockwise vortices, it appears that all of them are locally orthogonal to the bioreactor base, i.e. vertical for the flat bottom (in Figure 4.7 (a) and outwards inclined in Figure 4.7 (b-c) for the conical bottom geometries. The maximum shear rate obtained in Figures 4.7 corresponds to dimensional shear stresses of  $0.001 \text{ Nm}^{-2}$ . As a reference stem cell proliferation is affected by shear stress greater than  $0.1 \text{ Nm}^{-2}$  (see Toh and Voldman, 2011), while mammalian cells damage occurs at value higher than  $0.15 \text{ Nm}^{-2}$  (Elias *et al.*, 1995), which are well above those reported in this work. It should be stressed that the shear stress reported in Figure 4.7 are related to the phase averaged flow field, but could be higher for instantaneous flows.

The variation of the average maximum shear stress,  $\tau_{max}^*$ , with  $Fr_{do}$  is shown in Figure 4.8 for the three bottom configurations investigated. The asterisk denotes the space-average of the absolute value of  $\tau_{max}$  over the vertical plane of measurement. Outlier values of  $\tau_{max}$  were not included in the space-average as caused by erroneous velocity vectors close to the free surface. For all cases  $\tau_{max}^*$  increases with  $Fr$ . Similarly to Figure 4.7 (a-c), the conical B geometry presents higher values of  $\tau_{max}^*$  for most  $Fr$ , as the toroidal vortices are more compressed towards the sides of the vessel, resulting in a more intense deformation rate. The maximum shear stress,  $\tau_{max}^*$ , increases up to  $Fr_{do}=0.17$ , then a sharp decrease can be observed, after which  $\tau_{max}^*$  increases again with  $Fr$ . This can be explained by the onset of the out-of-phase flow transition, where the tangential velocity component in the direction orthogonal to the plane of measurement is the most significant, and cannot be measured with the 2D PIV setup used in this work.

### 4.2.3 Effects of bottom design on local flow direction

A better understanding of the bioreactor flow can be gained from Figure 4.9 (a) where vertical profiles of the phase-averaged radial velocity component are plotted for a phase angle  $\varphi=270^\circ$ . In this figure the vertical profiles associated to a flat and conical B bottom geometries are compared at two radial coordinates,  $r/d_i=0$  and 0.25, indicated in Figure 4.9 (c), for two shaking speeds,  $N=80$  and 100 RPM. In Figure 4.9 (a) the non-dimensional velocity is on the abscissa, with magnitude increasing from right to left (negative values), while the distance from the vessel bottom is plotted on the ordinate axis. As expected the intensity of the radial velocity increases when moving closer to the free surface for the profiles plotted. It is evident that the two profiles for the flat and conical B bottom differ at a shaking speed  $N=100$  RPM, because at this regime the flow has nearly developed for both geometries all the way to the bottom of the reactor, and it is therefore affected by the bottom geometry. This does not occur when the lowest speed ( $N=80$  RPM) is considered as for both configurations the vortical flow has developed over a small region below the free surface, and therefore the differences in bottom geometries are less relevant. It can be observed that the curves seem to be shifted vertically between flat and conical B bottoms, this being more apparent at the higher shaking speed considered. It should be noted that both sets of measurements were obtained for the same filling volume and therefore the maximum height of the conical bottom is higher than for the flat one. This implies that points at the same height are further away from the free surface, which is the flow driving mechanism. The same data are presented in Figure 4.9 (b), where a normalized axial coordinate with origin on the free surface  $(z - h)/d_i$  is considered. The new axial coordinate system shown in Figure 4.9 (c) is more effective at capturing the similarity between the flow of the two geometries. From Figure 4.9 (b) it is evident that according to this reference

system the vertical profiles of the two configurations show an excellent match, particularly in proximity of the free surface where the local flow is less affected by the difference in bottom geometry.

The mean flow at a phase angle  $\varphi=270^\circ$  consists of fluid motion from one side to the other of the bioreactor. Figure 4.10 shows the velocity field for  $Fr_{d_o}=0.14$  ( $N=100$  RPM) for flat (white vector field) and conical B bottom geometries (black vector field). As can be seen in the inset of Figure 4.10, the velocity fields present differences in magnitude and direction between the two geometries. The contour describes the angle difference  $\Delta\alpha_u$  between the velocity fields of the flat bottom and conical B geometry, with a clockwise direction change in red and counterclockwise direction change in blue. The regions where the flow is most affected by the different bottom geometry are close to the conical bottom, with the ‘upstream’ side at the right of the cone experiencing a more significant change in velocity direction in comparison to the ‘downstream’ on the left. The condition  $Fr_{d_o}=0.14$  presents toroidal vortices expanded to the bioreactor bottom, as described in Figure 4.4, hence a large region of the flow is affected by the conical B geometry. The radial velocity ratio,  $U/U_c$ , is estimated to further assess the effect of the bottom geometry on the velocity field, where  $U$  and  $U_c$  are the velocity magnitude for the flat and conical B bottom geometries, respectively. A relation is sought between the change in  $\Delta\alpha_u$  and the change in velocity magnitude, and the results of this analysis are shown in Figure 4.11 for  $N=100$  RPM ( $Fr_{d_o}=0.14$ ). The  $U/U_c$  data shown in Figure 4.11 are limited to those points where  $|\Delta\alpha_u| > 10^\circ$ . The distribution of the data points on the positive  $\Delta\alpha_u$  axis, upstream side, is characterized by a narrower spread of  $U/U_c$  in comparison to the data points associated to the negative  $\Delta\alpha_u$ , downstream side (Figure 4.11). This implies that the upstream flow is mainly deflected, as indicated by the larger size of the region subject to an angle variation (cf. Figure 4.10), but its velocity

magnitude is less affected (cf Figure 4.11). The opposite occurs downstream of the conical bottom where the size of the region associated to a significant deflection is smaller (cf. Figure 4.10), but its velocity distribution is broader and  $U/U_c$  is larger.

#### 4.2.4 Effects of bottom design on energy content

Similarly to Rodriguez *et al.* (2013), in this work the velocity field is described using the Reynold's decomposition,  $u(r, z, t) = \langle u(r, z, \varphi) \rangle + u'(r, z, t)$ , with  $\langle u(r, z, \varphi) \rangle$  being related to flow periodic variations and  $u'(r, z, t)$  taking into account random fluctuations. The spaced-averaged non-dimensional kinetic energy of the random velocity fluctuations,  $k'_{rz}$ , is evaluated for the bioreactors under investigation according to the 2D approximation of Equation 4.8.

$$k'_{rz} = \frac{1}{A} \int_A \frac{3}{4} (\langle u_r'^2 \rangle + \langle u_z'^2 \rangle) dA \quad (4.8)$$

where  $\langle u_r'^2 \rangle$  and  $\langle u_z'^2 \rangle$  are phase-resolved terms of the random velocity fluctuations, and A is the area of the measurement field. The variation of  $k'_{rz}$  with  $Fr_{d_o}$  for all geometries under investigation is shown in Figure 4.12 at a phase angle  $\varphi = 0^\circ$ . Low values of kinetic energy  $k'_{rz}$  were measured for  $Fr_{d_o} = 0.9-0.14$  ( $N = 80-100$  RPM), followed by a sharp increase peaking at  $Fr_{d_o} = 0.17$ . Above  $Fr_{d_o} = 0.17$   $k'_{rz}$  drops to low values. This can be explained by considering that at  $Fr_{d_o} = 0.17$  the flow transition to a precessional vortex with a vertical axis occurs (Weheliye *et al.*, 2013). Above the critical flow-transition speed the main velocity component is aligned with the tangential direction which cannot be directly estimated from the vertical plane measurements presented in this work. The results presented in Figure 4.12 confirm that flow transition occurs at the same  $Fr_{d_o}$  numbers for all geometries considered. It can also be noted that the measured values of  $k'_{rz}$  for all

geometries were comparable up to  $Fr_{d_o}=0.14$ , whilst for  $Fr_{d_o} > 0.17$  lower values of kinetic energy were found for the conical B geometry when compared to the flat bottom (approximately 35% smaller). This suggests that the phase-resolved flow at conditions close to  $N_{cr}$  presents more stable vortical structures, with fewer velocity fluctuations for the conical configuration.

### 4.3 Solid Suspension

Solid suspension studies were performed in the  $d_i=100$  and 70 mm bioreactors using GE Healthcare Life Science Cytodex 3 microcarriers at a concentration of 1.5g/L, which have a swollen microcarrier density of  $\rho=1.04$  g/L and a median diameter  $d_{50}=175$   $\mu\text{m}$ . The Trypan blue dyed microcarriers were added to water in the bioreactor and agitation rate increased stepwise until full suspension. Solid suspension studies were performed in the  $d_i=100$  mm OSR using the same three bottom geometries designed for the flow studies discussed in Section 4.2, at  $d_o=15, 25$  and 50 mm with a fixed fluid height,  $h=45$  and 70 mm. Similarly experiments with conical bottom geometries were performed in the  $d_i=70$  mm OSR with a constant fill volume,  $V_f=115$  and 192 mL, which result in  $h=30$  and 33.5 mm for  $V_f=115$  mL and  $h=50$  and 53.5 mm for  $V_f=192$  mL. The fluid heights (and fill volumes) were selected so to have combinations of both  $(h/d_i) > \sqrt{d_o/d_i}$  and  $(h/d_i) < \sqrt{d_o/d_i}$ . These conditions correspond to configurations when the toroidal vortex can and cannot reach the bottom of the reactor, respectively.

Figures 4.13 (a-h) show a typical microcarrier suspension experiment for a flat bottom with  $d_i=100$  mm,  $d_o=25$  mm and  $h=45$  mm. Figure 4.13 (a-b) shows the microcarriers (stained in blue) settled at the bottom of the vessel for a low  $N$  value. For example at 105 RPM, few microcarriers start to be dragged up from the centre of the vessel bottom (Figure 4.13 c). Far more solids are forced into

suspension at 110-115 RPM, as can be seen in Figure 4.13 (d-f), and microcarriers are fully suspended above 118 RPM (Figure 4.13 g-h). The  $Fr_{cr}$  for this condition ( $(h/d_i) < \sqrt{d_o/d_i}$ ) is  $Fr_{d_o}=0.167$  ( $N_{cr} = 107$  RPM), which can be calculated using Equation 1.7. Figure 4.13 suggests that solid suspension commences at  $Fr_{cr}$  and complete homogeneous distribution of microcarriers is achieved at a higher agitation rate.

Figure 4.14 shows the suspension mechanism in a  $d_i=100$  mm,  $d_o=25$  mm,  $h=70$  mm where the condition  $(h/d_i) > \sqrt{d_o/d_i}$  is valid, and flow transition occurs at  $Fr_{cr}=0.179$  ( $N_{cr} =113$  RPM). The microcarriers are settled homogeneously at the bottom of the bioreactor at  $N=90$  RPM (Figure 4.14 a). As the speed is increased the solids start to concentrate at the centre of the bioreactors (Figure 4.14 b) and suspension begins from  $N \approx N_{cr}$  (see Figures 4.14 c-d). The suspension mechanism is not as immediate as in the case of  $(h/d_i) < \sqrt{d_o/d_i}$  (see Figure 4.13), but occurs over a wider range of  $N$  (Figures 4.14 e-g) and achieves full microcarrier dispersion at  $N=129$  RPM, a value significantly higher than the  $N_{cr}$ . As described in Section 1.6.1, the suspended speed is evaluated using the normalised brightness index (Equation 1.16) and fitting models of the form of Equation 1.17. It must be noted that the measurements taken by Pieralisi *et al.* (2015) were on a plane parallel to the OSR bottom, and the results provided give an estimation of the  $N$  required for the microcarriers to lift from the vessel bottom. As the measurements taken in this work are on a plane perpendicular to the vessel bottom, the field of view is the whole bioreactor. On this basis  $I^*$  not only gives a measure of the agitation required for microcarriers suspension but also their homogeneous distribution in the volume.

Figure 4.15 shows the variation of the normalised brightness index,  $I^*$ , with agitation rate,  $N$ . The letters (a-g) in the plot refer to the subplots of Figure 4.13 to better highlight the correlation between the solid suspension and the image

brightness.  $I^*$  does not change up to  $N=105$  RPM, which corresponds to the upper end of the speed range related to settled microcarriers in Figure 4.13 (a-c). As the toroidal vortices increase in size and intensity more solids are brought into suspension from the vessel bottom (Figure 4.13 d-f). Suspension is completed after  $N=118$  RPM as seen in Figure 4.13 (g-h). The suspended speed  $N_s$  is found when the fitted curve falls below a value  $I^*=0.05$  (i.e. 95% suspension).

### 4.3.1 Effect of orbital diameter on solid suspension

The effect of the variation of the shaking diameter,  $d_o$ , on the efficiency of microcarrier suspension in cylindrical OSRs of  $d_i=100$  mm is evaluated by plotting the normalised brightness index,  $I^*$ , against the agitation rate,  $N$ , for different orbital diameters  $d_o=15, 25, 50$  mm and at different fluid heights,  $h$ , as shown in Figure 4.16 (a-b) for a flat bottom vessel.

For  $h=45$  mm as the shaking diameter is increased, the suspended speed decreases with the data associated with  $d_o=50$  mm yielding the lowest  $N_s$  (see Figure 4.16 a). A similar trend can be observed in Figure 4.16 (b), for the  $h=70$  mm configuration. Similar trends to the flat bottom cylindrical bioreactor were found for the conical bottom vessels, when changing  $d_o$  (see Figures 4.17 and 4.18 for conical A and B geometries, respectively).

To put into perspective the normalised brightness index and its variation with respect to agitation rate, a summary of the flow transition speed and its relation to the transition condition  $(h/d_i) \Leftrightarrow \sqrt{d_o/d_i}$ , is provided in Table 4.1 for all the conditions investigated in Figures 4.16 to 4.18.

For  $h=45$  mm, all the configurations examined have distinct  $N_{cr}$ , which result in the  $I_B^*$  curves being apart for all the orbital diameters investigated. For  $h=70$

mm configuration, in Figure 4.16 (b), the improvement in solid suspension is marginal for  $d_o=15$  and 25 mm configuration which have the same critical speed  $N_{cr}$ , but substantial for  $d_o=50$  mm which has the lowest  $N_s$  of the experimental set.

The effect of  $d_o$  on the solid suspension is summarised in Figure 4.19, where the suspended speed,  $N_s$ , is plotted for all orbital diameters, all bottom geometries and fluid heights investigated in a  $d_i=100$  mm vessel. The suspension speeds for a larger fill volume are higher, with the  $h=70$  mm cases having a  $N_s \sim 15\%$  larger than the  $h=45$  mm data for the same  $d_o$  and geometry.  $N_s$  decreases for all geometries and fluid heights with increasing orbital diameter, but the largest decrease was observed between  $d_o=25$  and 50 mm. The orbital diameter has a greater influence on the suspended speed with the  $h=45$  mm fluid height, where  $N_s$  decreases by  $\sim 35\%$  between  $d_o=15$  and 50 mm, whilst the corresponding improvement for  $h=70$  mm over the same  $d_o$  range is 21%.

### 4.3.2 Effect of vessel bottom geometry on solid suspension

The effect of the presence of a truncated conical bottom in the bioreactor on microcarrier suspension was further investigated to best exploit the flow dynamics features identified in Section 4.2.1, where the conical B bottom provided higher space-averaged vorticity due to the interaction between the toroidal vortices occurring at lower  $N$ , when compared with a flat bottom geometry.

Figure 4.20 shows the variation of suspended speed for different  $d_o$  and  $h$  combination in a  $d_i=100$  mm conical OSR with flat, conical A and B geometry. For  $h=45$  mm (in black in Figure 4.20), the increase of conical bottom height was

found to lower the necessary agitation rate for microcarrier suspension, this is more pronounced for the conical B geometry ( $h_c=15$  mm). Only marginal improvements in  $N_s$  with increasing  $h_c$  were observed in the case of  $d_o=15$  mm  $h=45$ , as their operating condition falls into the  $(h/d_i) > \sqrt{d_o/d_i}$  category, meaning that the toroidal vortices in the flow do not fully extend to the vessel bottom, defeating the purpose of a modified geometry. The  $d_o=25$  and  $50$  mm,  $h=45$  mm configurations refers to  $(h/d_i) < \sqrt{d_o/d_i}$ , where the toroidal vortices are able to expand to the bottom resulting in an significant improvement in  $N_s$ .

With a larger fluid height,  $h=70$  mm, the addition of a conical bottom appear less effective at lowering the suspended speed. This can be explained by considering the fact that the toroidal vortices act from the free surface downwards, so at a higher fluid height less interaction occurs with the flow and particles at the bottom of the vessel.

The configurations discussed thus far for solid suspension in a  $d_i=100$  mm OSR were based on a constant fluid height for all bottom geometries, resulting in lower fill volumes of the bioreactor with conical bottoms. To investigate the effect of the conical bottom on solid suspension with constant fill volume, the  $d_i=70$  mm cylindrical vessel with constant fill volume was used with a flat and conical B bottom geometries. Two fill volumes were investigated,  $V_f=115$  and  $192$  mL which correspond to fluid heights with flat bottom of  $30$  and  $50$  mm, respectively, and  $33.8$  and  $53.8$  mm for the conical B geometry. The conditions with vortices reaching to the bottom ( $(h/d_i) < \sqrt{d_o/d_i}$ ) or not ( $(h/d_i) > \sqrt{d_o/d_i}$ ), together with critical speed  $N_{cr}$  associated to flow transition are shown in Table 4.2.

As shown in Figure 4.21, the  $N_s$  is lower when a conical B geometry is used. The  $N_s$  improves significantly at a  $V_f=115$  mL (corresponding to  $h=30$  and  $33.5$  mm) even though the  $Fr_{cr}$  for the conical B bottom is higher than that of a flat

bottom. In the case of  $V_f=192$  mL, there is a small decrease in  $N_s$  after the introduction of the conical bottom due to the large value of  $h/d_i$ , corresponding to  $(h/d_i) > \sqrt{d_o/d_i}$ .

### 4.3.3 Scaling of solid suspension mechanism

The results discussed thus far prove that the introduction of a conical bottom improves solid suspension in cylindrical OSRs and that, for the conditions investigated, a larger  $d_o$  is desirable to reduce  $N_s$ . To better understand the dependency of microcarrier suspension on the operational parameters, the  $Fr_s/Fr_{cr}$  ratio was introduced to scale the suspension speeds for different  $d_o$ ,  $h$ ,  $d_i$  and  $h_c$  combinations.  $Fr_s/Fr_{cr}$  is the ratio of the  $Fr_s$  for suspended speed ( $N_s$ ) and the  $Fr_{cr}$  for toroidal vortex expansion to the vessel bottom at given geometric parameters, as defined in Equations 1.7 and 1.8. The variation of  $I^*$  with  $Fr_{d_o}/Fr_{cr}$  is shown for the flat and conical B geometries in Figures 4.22 and 4.23, respectively. The Figures 4.22 and 4.23 present the same data as Figures 4.16 and Figures 4.18, although the  $Fr_{d_o}/Fr_{cr}$  is used as a scaling parameter on the abscissa.

According to the scaling factor, at a fluid height  $h=45$  mm, complete suspension/homogenisation occurs for all  $d_o$ 's at  $1.25 \times Fr_{cr}$  in Figure 4.22 (a). For the same  $h$  and  $d_o$ , but with the conical B geometry, Figure 4.23 (a), data associated to the  $d_o=25$  and 50 mm yield solid suspension at  $0.8 \times Fr_{cr}$ . This can be explained by the fact that at a fluid height  $h=45$  mm and  $d_o=25$  and 50 mm, the toroidal vortices reach full expansion to the bottom of the vessels earlier lifting the solids and the conical bottom enhances the suspension (see Section 4.2.1).

For  $h=70$  mm, in both the flat and conical B bottom geometries, solid suspension occurs at  $1.25 \times Fr_{cr}$  for  $d_o=15$  and 25 mm, whilst data related to  $d_o=50$  mm yield a  $Fr_s=0.75 \times Fr_{cr}$  (as shown in Figure 4.22 b and 4.23 b). The lower agitation

required by the  $d_o=50$  mm can be explained by the fact that the critical Froude number,  $Fr_{cr}$ , is lower than that of  $d_o=15$  and 25 mm. The presence of the conical bottom marginally improves the solid suspension for  $d_o=25$  mm, suggesting that at such conditions the microcarriers are subject to higher fluid velocity at lower  $N$  for the conical B geometry, thus anticipating solid suspension.

To compare the whole range of experimental conditions considered in the solid suspension studies, the  $(h/d_i) / \sqrt{d_o/d_i}$  ratio is introduced. Figure 4.24 collates the  $Fr_s/Fr_{cr}$  for all conditions investigated, with the left (right) quadrant on the x-axis including the  $(h/d_i) < \sqrt{d_o/d_i}$  ( $(h/d_i) > \sqrt{d_o/d_i}$ ) combinations. Each data point represents a different combination of  $h$ ,  $d_o$  and bottom geometry, with the largest  $d_o$  (50 mm) always being the lowest  $(h/d_i) / \sqrt{d_o/d_i}$  value within the triplets of data points. Despite some outliers, the solid lines indicate that the flat bottom geometry requires higher  $Fr_s/Fr_{cr}$  for solid suspension (i.e.  $1.2 < Fr_s/Fr_{cr} < 1.3$ ) than the conical bottom geometries.

The conical A geometry has a similar behaviour to that exhibited the flat geometry, with a constant reduction in  $Fr_s/Fr_{cr}$  throughout the  $(h/d_i) / \sqrt{d_o/d_i}$  range. The conical B bottom, with a 15 mm truncated cone, results in the lowest  $Fr_s/Fr_{cr}$  range required at  $(h/d_i) < \sqrt{d_o/d_i}$  indicating that for this configuration the conical shape affects to a larger extent the expansion of the toroidal vortices toward the bioreactor bottom. This is in agreement with the PIV measurements discussed in Section 4.2. For  $(h/d_i) > \sqrt{d_o/d_i}$ , the conical B geometry interacts less with the toroidal vortices expanding from the free surface, with the  $Fr_s/Fr_{cr}$  increasing linearly as  $(h/d_i)$  increases. The current results for the  $Fr_s/Fr_{cr}$  are in agreement with the work of Pieralisi *et al.* (2015), where the suspended speed was measured on a plane parallel to the cylindrical vessel. Pieralisi found that  $1.1 \times Fr_{cr}$  were sufficient to achieve suspension from the vessel bottom (with measurement plane parallel to the bottom), but when measurements were made

on the vertical plane (orthogonally to the bottom) a higher  $Fr \simeq 1.2$  was found to achieve complete suspension.

## 4.4 Concluding Remarks

The work described in this chapter evaluates the effect of the implementation of a conical bottom design in an orbital shaken bioreactor. Two truncated conical bottoms of  $h_c=5$  and 15 mm are used with an OSR, and the resulting flow and solid suspension dynamics are investigated in depth and compared with those obtained for a flat bottom configuration. Using PIV, the impact of the bottom geometry on the general flow characteristics at a phase angle  $\varphi=0^\circ$  is investigated first. It is found that the flow in cylindrical bioreactors with conical bottoms is characterised by toroidal vortices expanding towards the bottom with increasing  $Fr_{d_o}$ , as is the case for a standard flat configuration, while for the cone with the highest inclination examined (conical B) the vortices reached the bottom at a lower  $Fr_{d_o}$ . Despite this difference the Froude number associated to flow transition,  $Fr_{cr}$ , did not vary from the values reported for a flat bottom bioreactor. The space-averaged vorticity increases for all bottom geometries with  $Fr_{d_o}$ , however  $\omega_\theta^*$  increases at a higher rate in the conical B geometry when  $Fr_{d_o} > 0.12$ . This is explained by considering that for this configuration the interaction between the vortical cells and the bioreactor bottom starts to occur at lower speeds.

The proposed designs are also evaluated in terms of shear rates. It is found that the most intense deformations occur at the periphery of the toroidal vortices, with low shear rate values present at the centre of the vortical cells. For a given  $Fr_{d_o}$ , the vortical cells are closer to the vessel base with the conical bottom resulting in higher maximum shear rates,  $\tau_{max}$ , when the conical B configuration was analysed. The use of the conical geometry results in an area of low shear

rates at  $r/d_i=0.5$  as the inclined surfaces of the conical bottoms modified the shape of the vortical cells, resulting in the regions of largest shear deformation being orthogonal to the cone external walls. The space-averaged maximum shear rate variation is similar for all geometries considered at any given  $Fr_{d_o}$ , although slightly higher values were found for the highest cone investigated.

When the designs were evaluated at a different measurement angle,  $\varphi=270^\circ$ , which is characterized by a strong radial flow from one side to the other one of the bioreactor, it is observed that the region with the greatest change in velocity direction are in proximity of the inclined surfaces of the conical bottoms. The flow ‘upstream’ of the conical bottom experiences larger deflection with similar velocity magnitude between flat and conical B geometries, whilst the region ‘downstream’ of the conical bottom resulted in a greater range of velocity ratios. Finally, the variation of the kinetic energy content of the random (i.e. cycle-to-cycle) velocity fluctuations shows that the energy content increases with  $Fr_{d_o}$  for all designs, but the  $Fr_{cr}$  associated to flow transition is not affected.

The solid suspension methodology employed provides a measure for the suspension and homogeneous distribution of microcarriers within the fluid height. Results prove that, for same fluid height and geometry, a larger orbital diameter is beneficial for improved suspension. The increase of spaced averaged vorticity with the introduction of a conical bottom geometry, measured with PIV, resulted in improved suspension of microcarriers when for fluid height, orbital and internal diameter combinations corresponding to full extension of the toroidal vortices to the bioreactor bottom (i.e.  $(h/d_i) < \sqrt{d_o/d_i}$ ). For high  $(h/d_i)/\sqrt{d_o/d_i}$  ratios, only a limited effect of the conical bottom was observed. The scaling factor  $Fr_s/Fr_{cr}$  clearly indicates the improvement to solid suspension with conical B geometry, which achieves complete lift and homogeneous distribution of microcarriers at 85% of the critical Froude number  $Fr_{cr}$  required for flow transition,

which is in sharp contrast with  $1.25 \times Fr_{cr}$  found for a flat bottom.

			$d_o$ [mm]		
			15	25	50
$h$ [mm]	45	$(h/di) \Leftrightarrow \sqrt{d_o/d_i}$	>	<	<
		$N_{cr}$ [RPM]	113	107	90
	70	$(h/di) \Leftrightarrow \sqrt{d_o/d_i}$	>	>	<
		$N_{cr}$ [RPM]	113	113	112

Table 4.1: Suspension studies with constant fluid height:  $(h/di) \Leftrightarrow \sqrt{d_o/d_i}$  relationship and  $Fr_{cr}$  based on Equation 1.8 and 1.7

$V_f$ [ml]		$h$ [mm]		$d_o$ [mm]		
				15	25	50
115	Flat	3	$(h/di) \Leftrightarrow \sqrt{d_o/d_i}$	<	<	<
			$N_{cr}$ [RPM]	130	114	96
	Conical B	3.38	$(h/di) \Leftrightarrow \sqrt{d_o/d_i}$	>	<	<
			$N_{cr}$ [RPM]	135	121	102
192	Flat	5	$(h/di) \Leftrightarrow \sqrt{d_o/d_i}$	>	>	<
			$N_{cr}$ [RPM]	135	135	124
	Conical B	5.38	$(h/di) \Leftrightarrow \sqrt{d_o/d_i}$	>	>	<
			$N_{cr}$ [RPM]	135	135	129

Table 4.2: Suspension studies with constant volume:  $(h/di) \Leftrightarrow \sqrt{d_o/d_i}$  relationship and  $Fr_{cr}$  based on Equation 1.8 and 1.7.

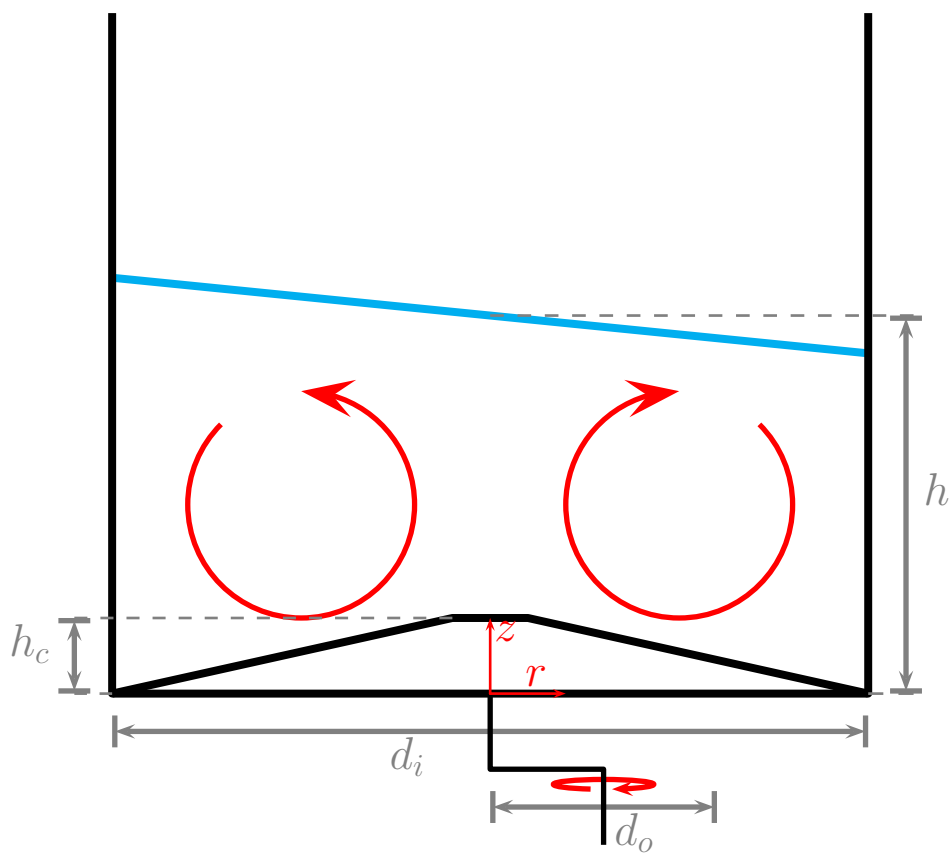


Figure 4.1: Cross-sectional view of the orbitally shaken cylindrical bioreactor with the cylindrical bottom.

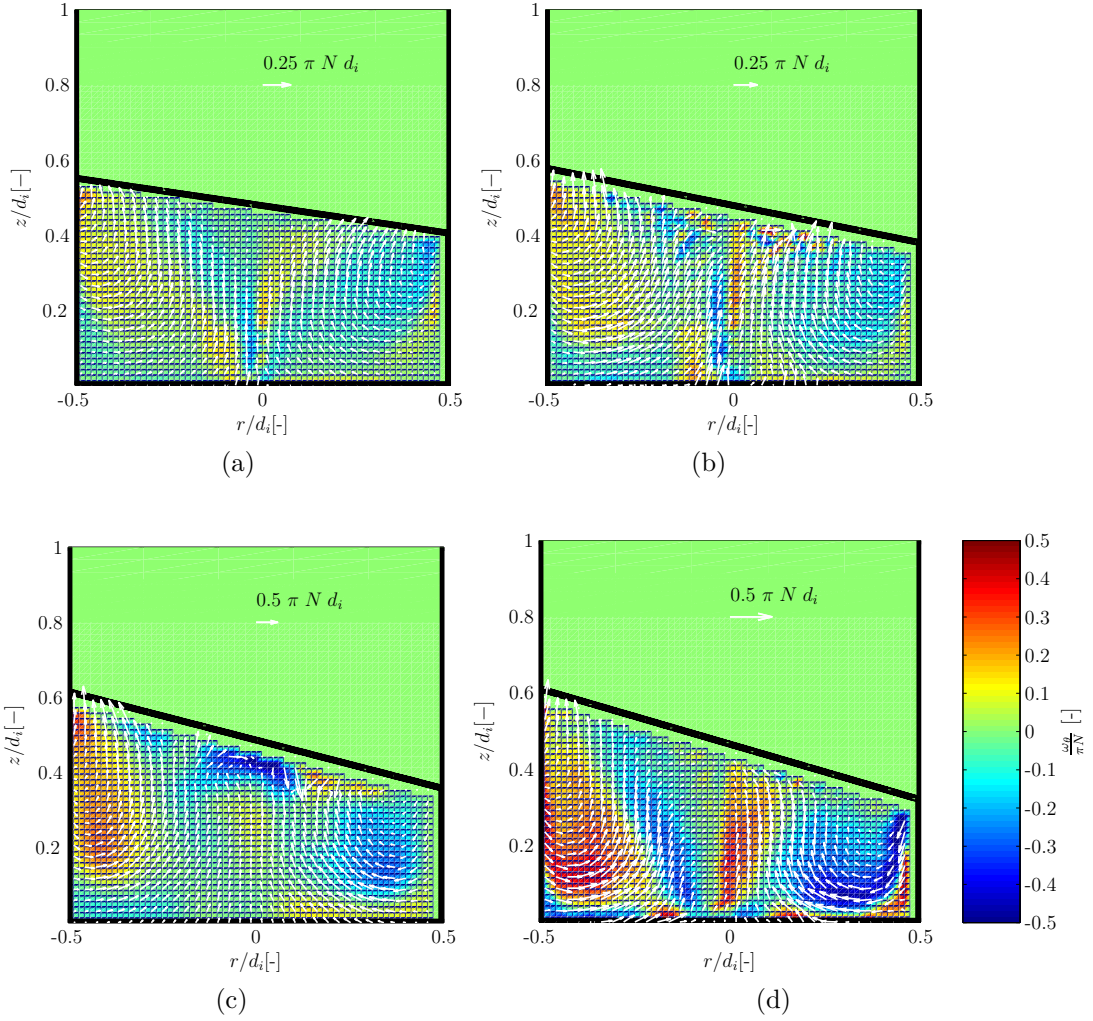


Figure 4.2: Phase-resolved non-dimensional velocity fields and contours of the tangential component of vorticity,  $\omega_\theta$ , for flat bottom geometry at (a-d)  $Fr_{do}=0.10, 0.14, 0.17, 0.18$  ( $N=85, 100, 110, 115$  RPM).

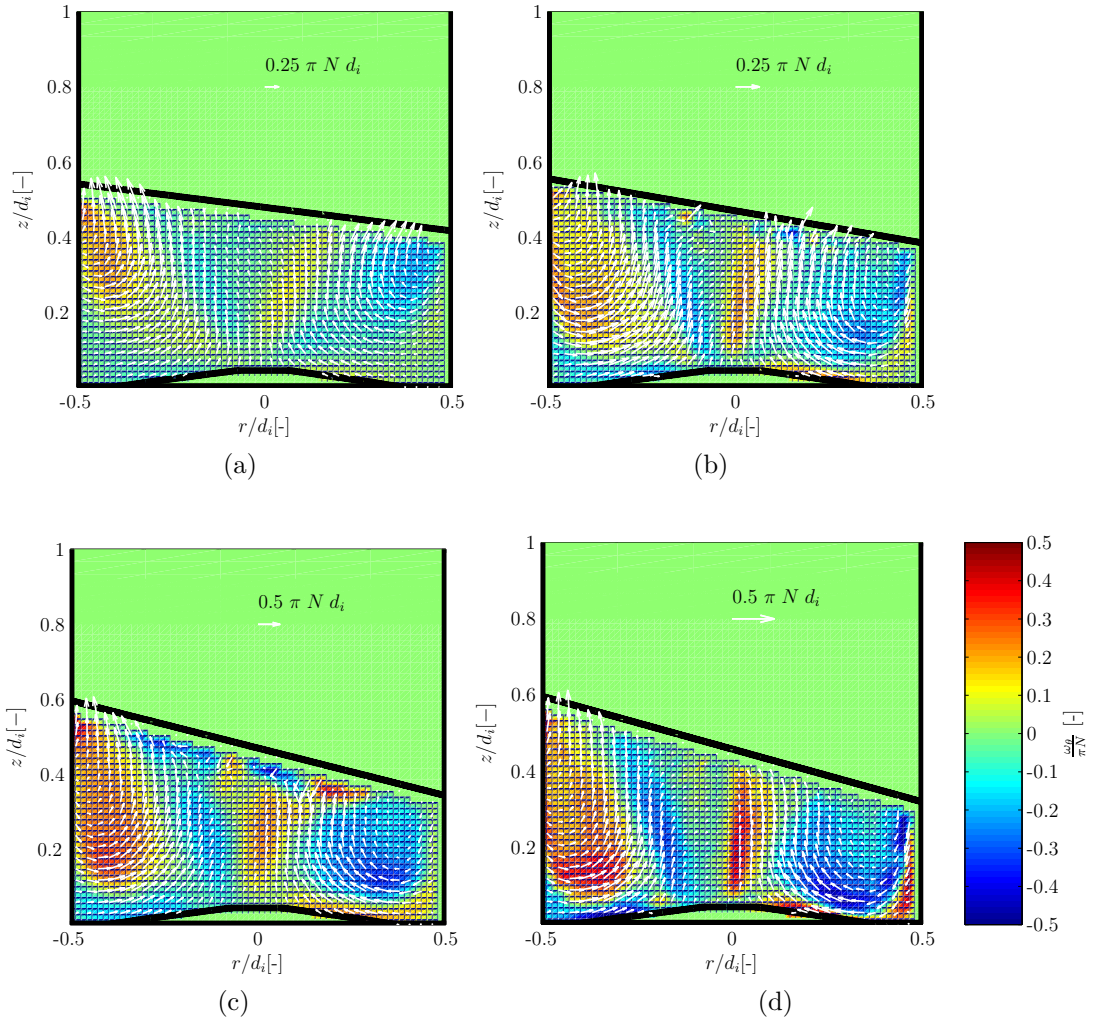


Figure 4.3: Phase-resolved non-dimensional velocity fields and contours of the tangential component of vorticity,  $\omega_\theta$ , for conical A bottom geometry at (a-d)  $Fr_{do}=0.10, 0.14, 0.17, 0.18$  ( $N=85, 100, 110, 115$  RPM).

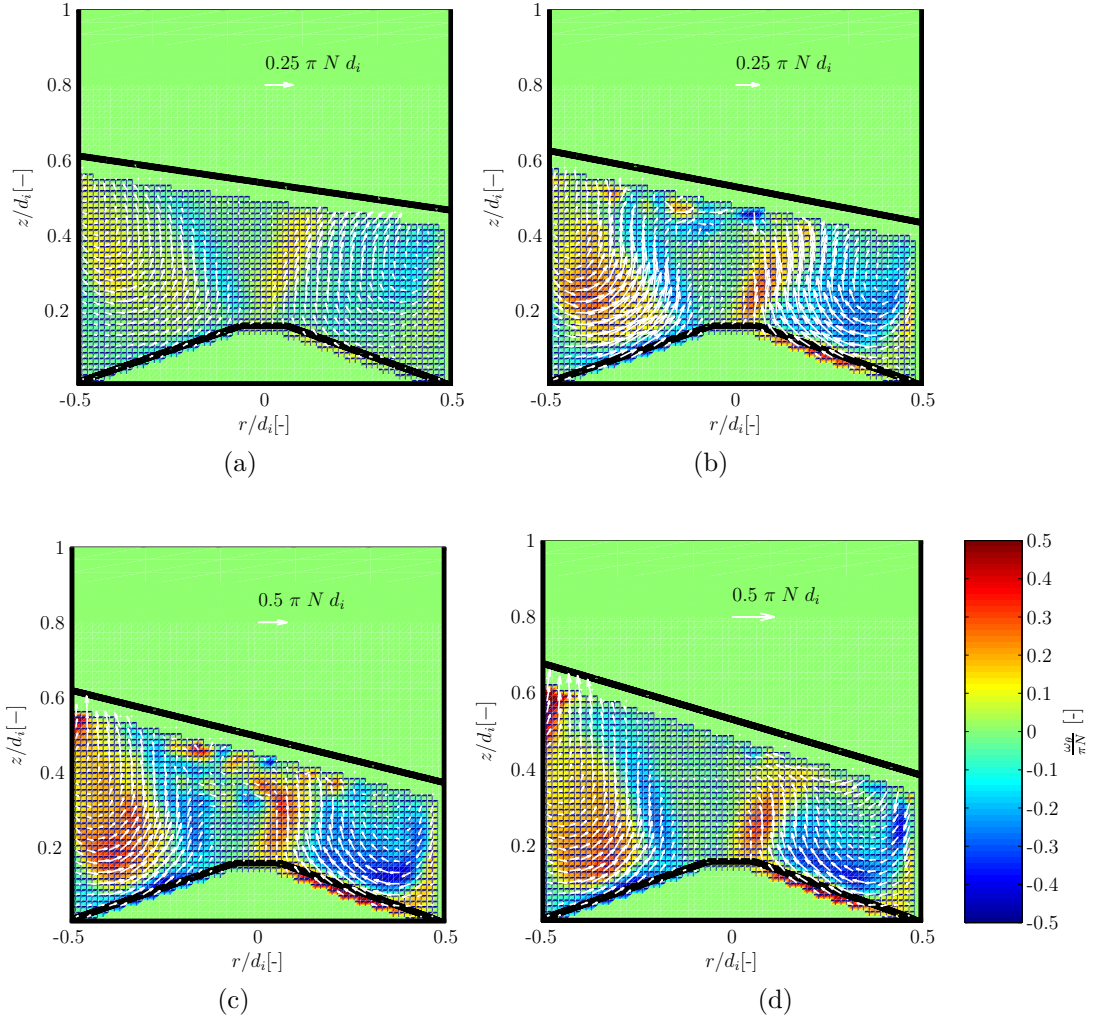
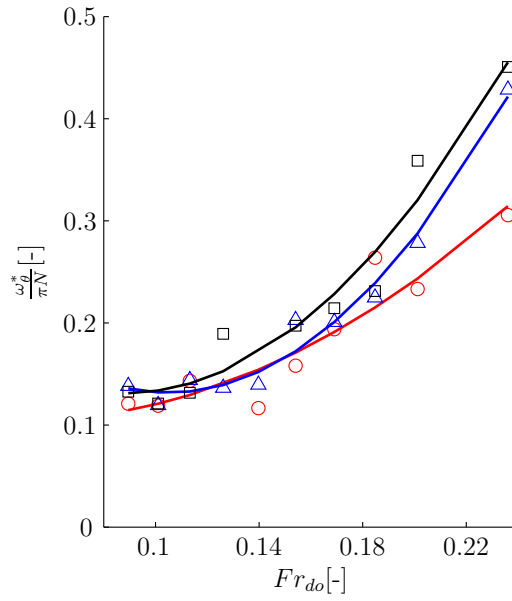
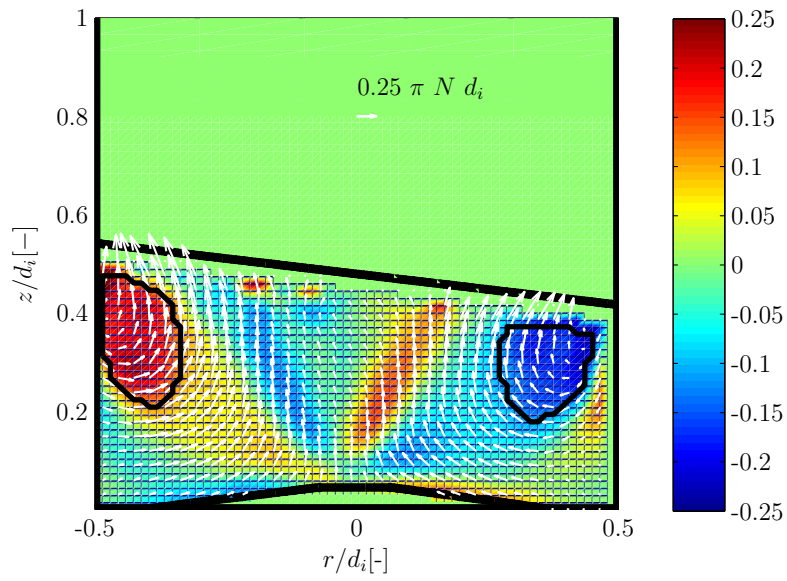


Figure 4.4: Phase-resolved non-dimensional velocity fields and contours of the tangential component of vorticity,  $\omega_\theta$ , for conical B bottom geometry at (a-d)  $Fr_{do}=0.10, 0.14, 0.17, 0.18$  ( $N=85, 100, 110, 115$  RPM).



(a)



(b)

Figure 4.5: (a) Variation of the spaced-averaged non-dimensional vorticity with increasing  $Fr_{do}$ : flat bottom ( $\circ$ ), Conical A ( $\triangle$ ), and Conical B ( $\square$ ); (b) Visualization of the area  $\omega_{\theta} = 0.1\pi N$  used to determine the average vorticity.

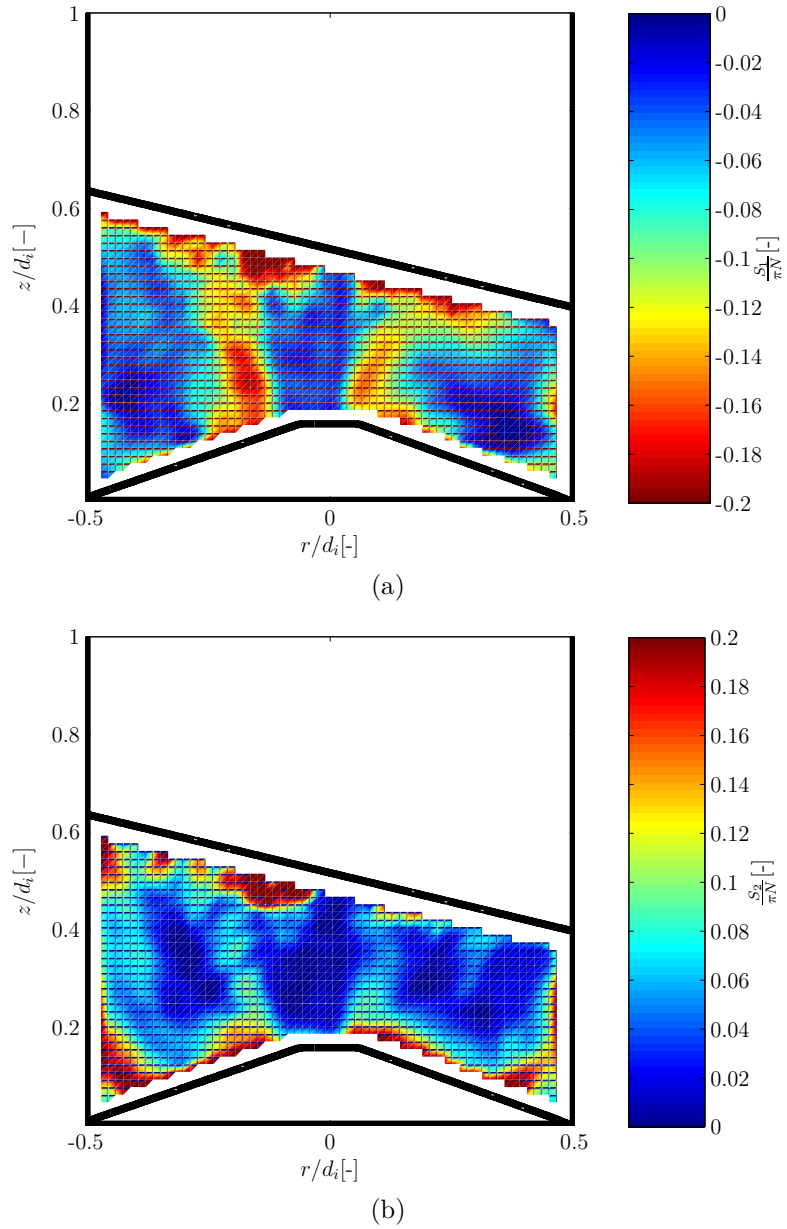


Figure 4.6: Principal component of strain rate tensor at  $\varphi = 0^\circ$  for conical B geometry ( $Fr_{do}=0.14$ ,  $N=100$  RPM) (a) Compression strain rate  $S_1$ , (b) Stretching strain rate  $S_2$ .

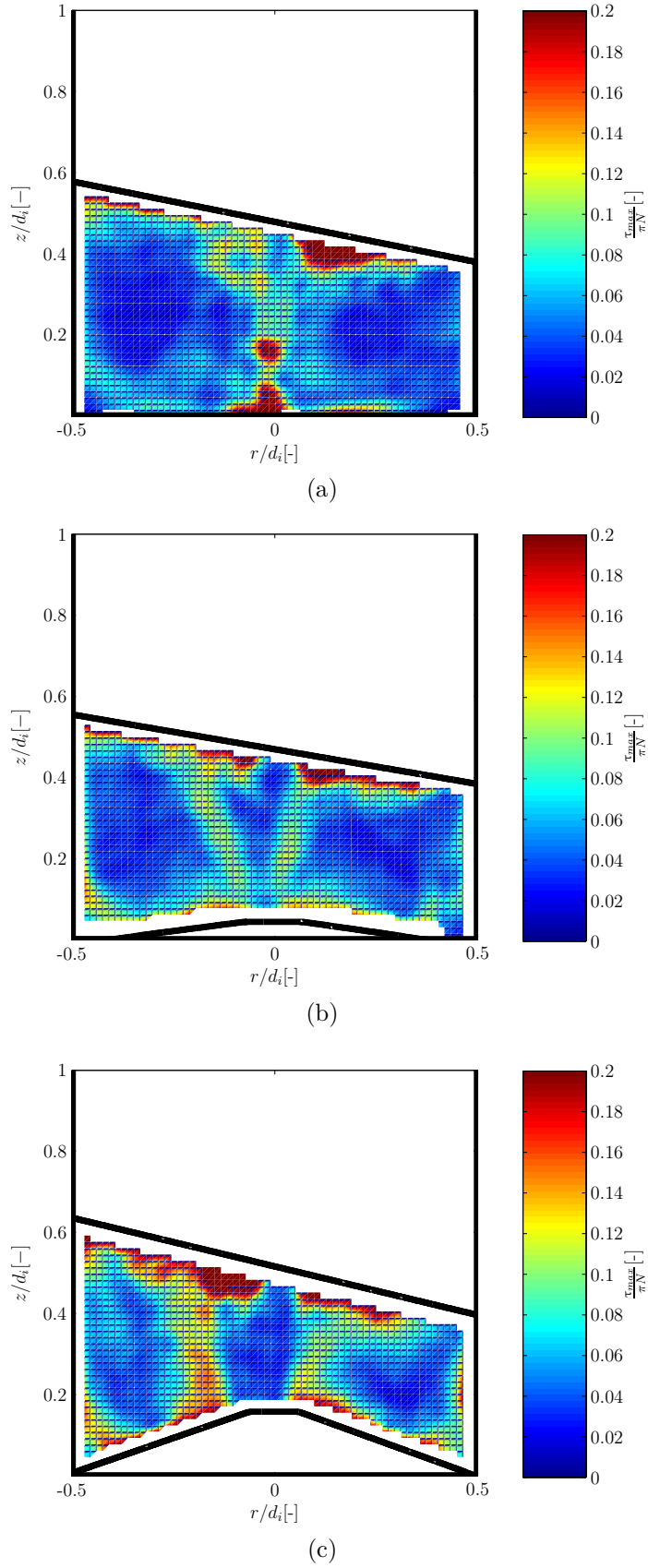


Figure 4.7: Contour maps of the maximum shear strain rate of the flow at  $\varphi = 0^\circ$  for (a) flat, (b) conical A, (c) conical B geometries at  $Fr_{do}=0.14$  ( $N=100$  RPM).

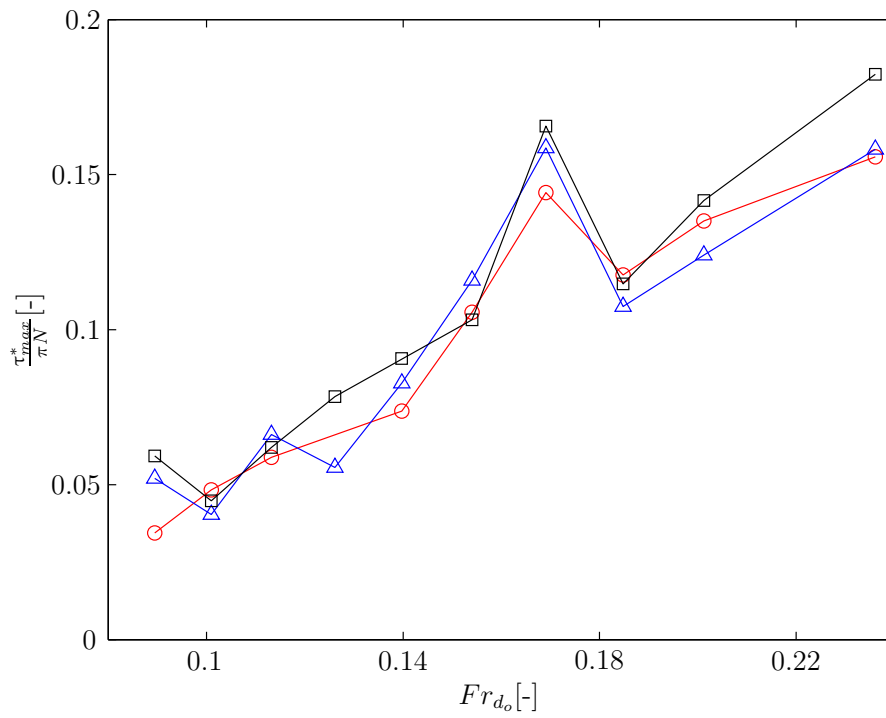


Figure 4.8: Variation of the spaced-averaged non-dimensional maximum shear rate,  $\tau_{max}^*$ , with increasing  $Fr_{do}$ : flat bottom ( $\circ$ ), Conical A ( $\triangle$ ), and Conical B ( $\square$ ).

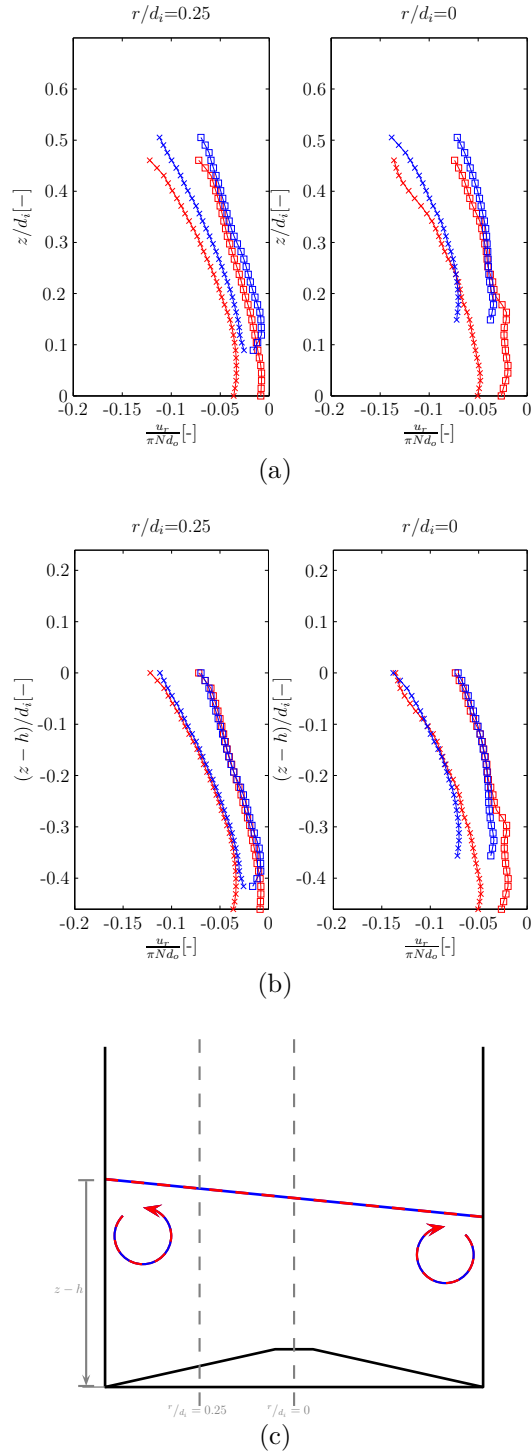


Figure 4.9: (a) Comparison of the vertical profiles of the radial velocity component for a flat bottom (red) and Conical B bottom (blue) at two shaker speeds  $N=80$  RPM ( $\square$ ) and  $N=100$  RPM ( $\times$ ); (b) Profiles of the radial velocity component with a coordinate system  $(z-h)/d_i$  for a flat bottom (red) and Conical B bottom (blue) at two shaker speeds  $N=80$  RPM ( $\square$ ) and  $N=100$  RPM ( $\times$ ); (c) Diagram of the location of the radial profiles at coordinates  $r/d_i=0$  and  $0.25$ .

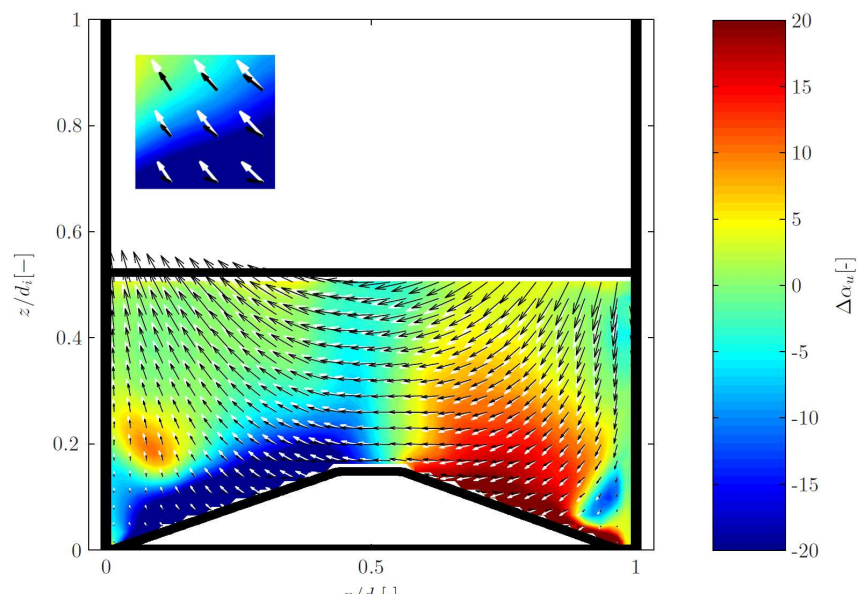


Figure 4.10: Velocity field for  $Fr_{do}=0.14$  ( $N=100$  RPM) for flat bottom (white vector field) and conical B (black vector field); contour of the angle difference,  $\Delta\alpha_u$ , between velocity fields. Inset: detail of the velocity field.

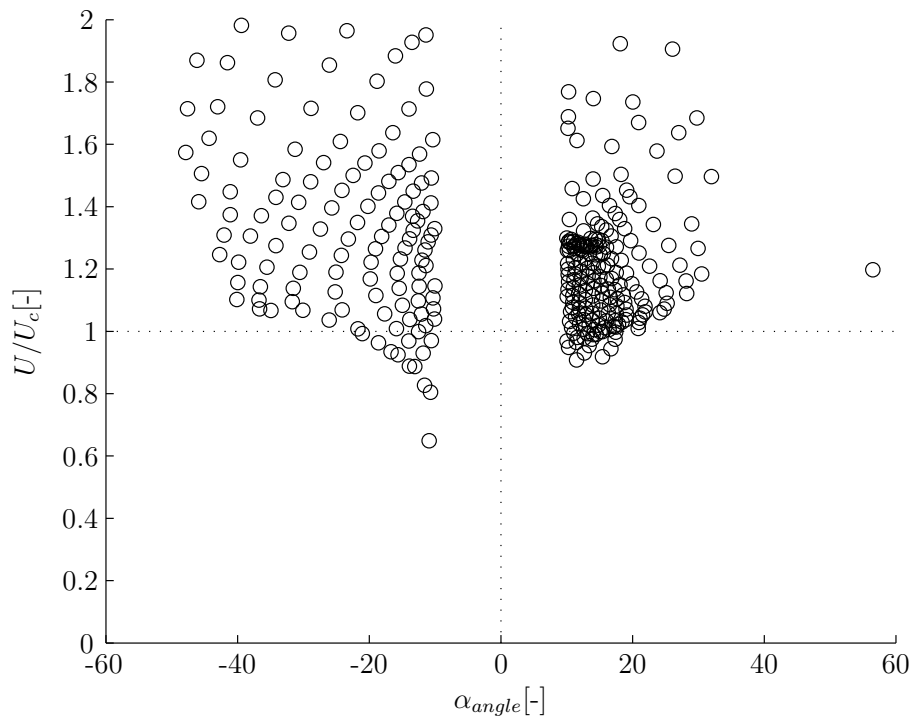


Figure 4.11: Scatter plot of the velocity ratio,  $U/U_c$ , and angle difference,  $\Delta\alpha_u$ , for  $Fr_{do}=0.14$  ( $N=100$  RPM).

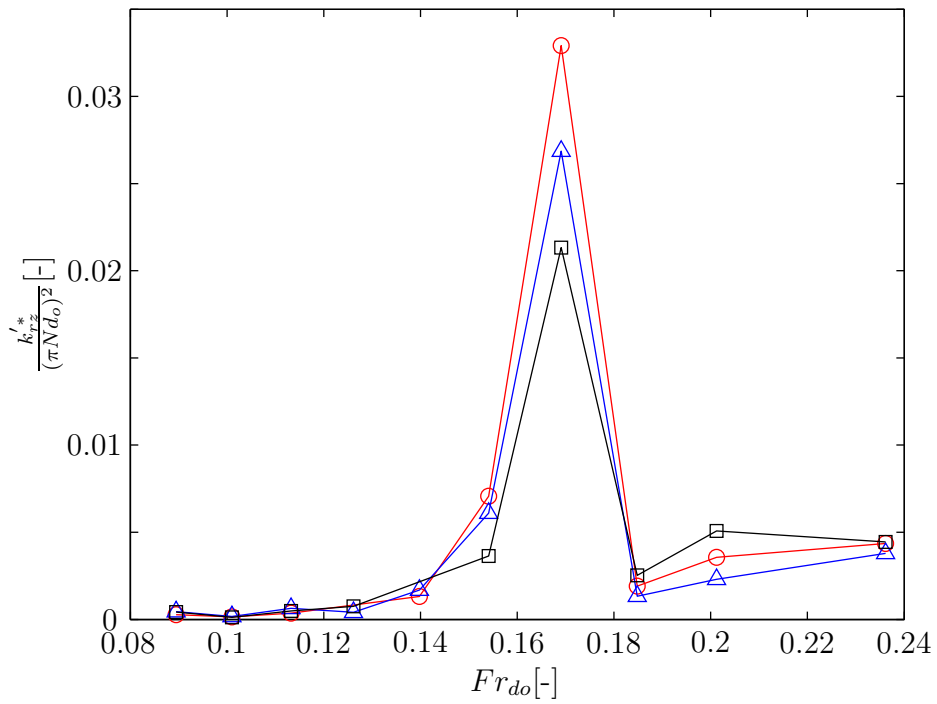


Figure 4.12: Variation of the spaced-averaged non dimensional kinetic energy of the random velocity fluctuations,  $k'_{rz}$  with increasing  $Fr_{do}$ : flat bottom (○), Conical A (△), and Conical B (□).

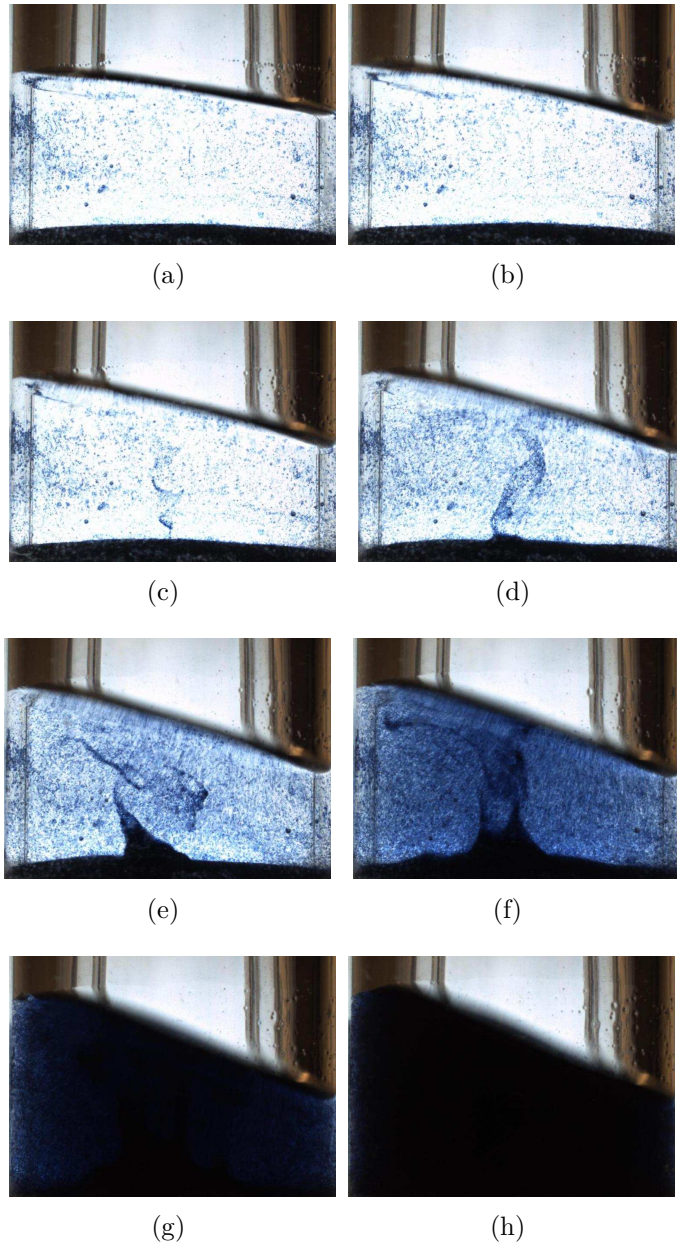


Figure 4.13: Visualisation of the suspension mechanism for a flat bottom OSR.  $d_i=100$  mm,  $d_o=25$  mm,  $h=45$  mm at varying  $N$ , (a-h): 90, 100, 105, 110, 112, 115, 118 and 121 RPM.

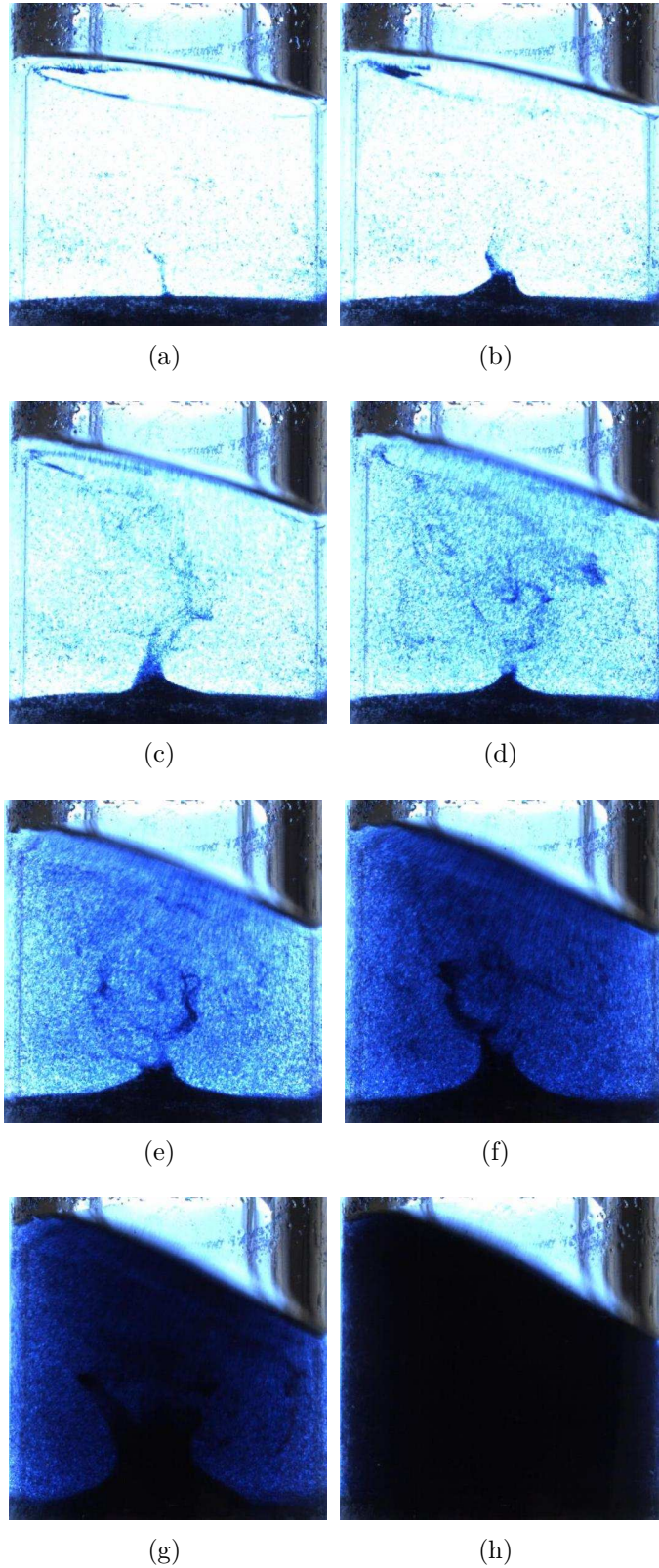


Figure 4.14: Visualisation of the suspension mechanism for a flat bottom OSR  $d_i=100$  mm,  $d_o=25$  mm,  $h=70$  mm at varying  $N$ , (a-h): 90, 100, 110, 115, 120, 123, 126 and 129 RPM.

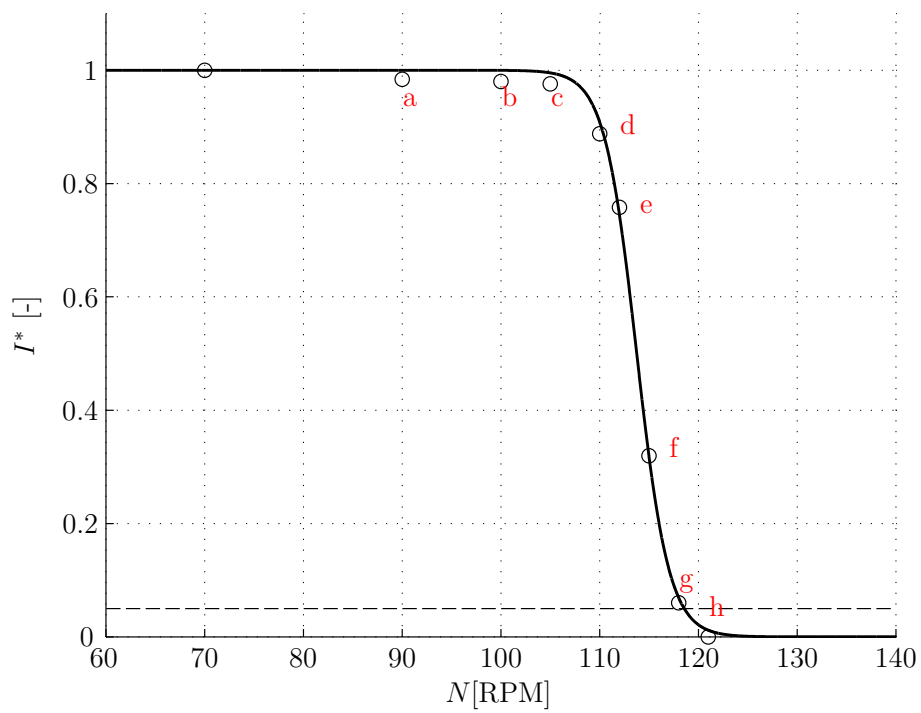
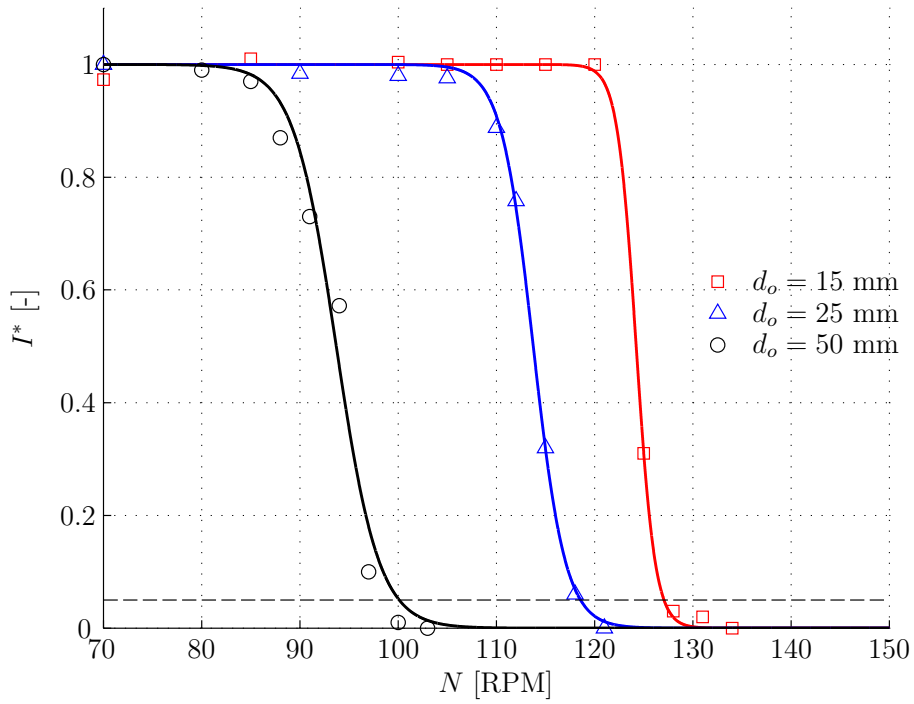
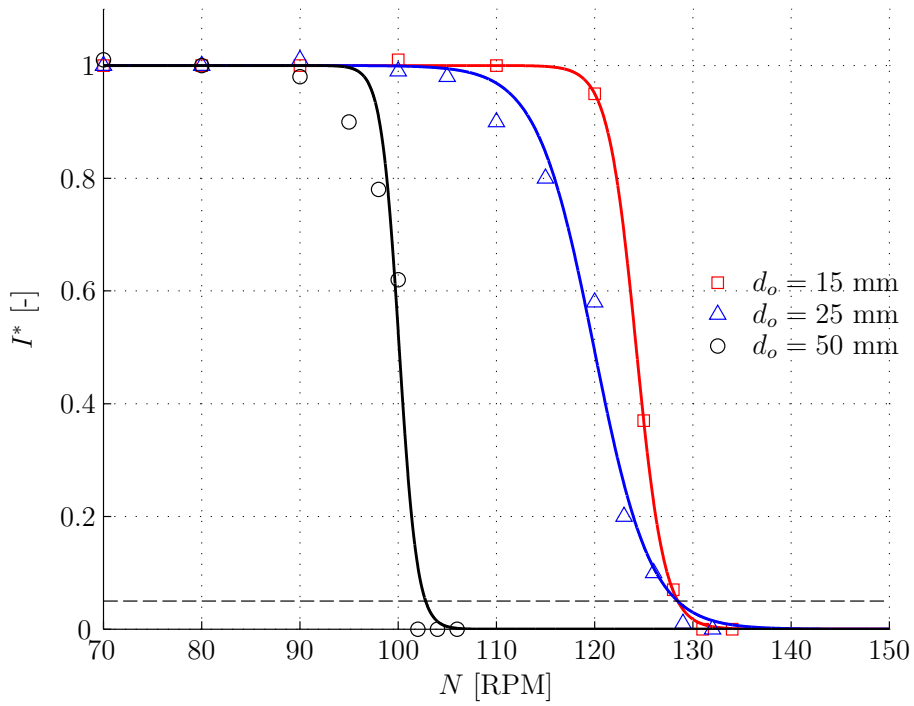


Figure 4.15: Variation of the normalised brightness index,  $I^*$ , with agitation rate,  $N$ , with reference (a-h) to Figure 4.13.  $d_i=100$  mm,  $d_o=25$  mm,  $h=70$  mm at varying  $N$ .

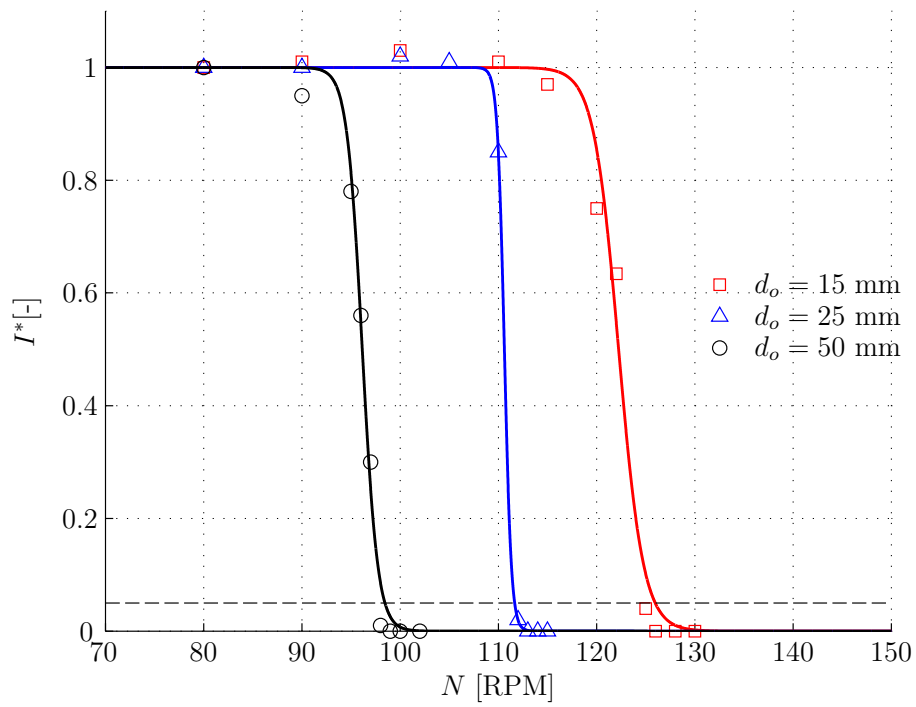


(a)

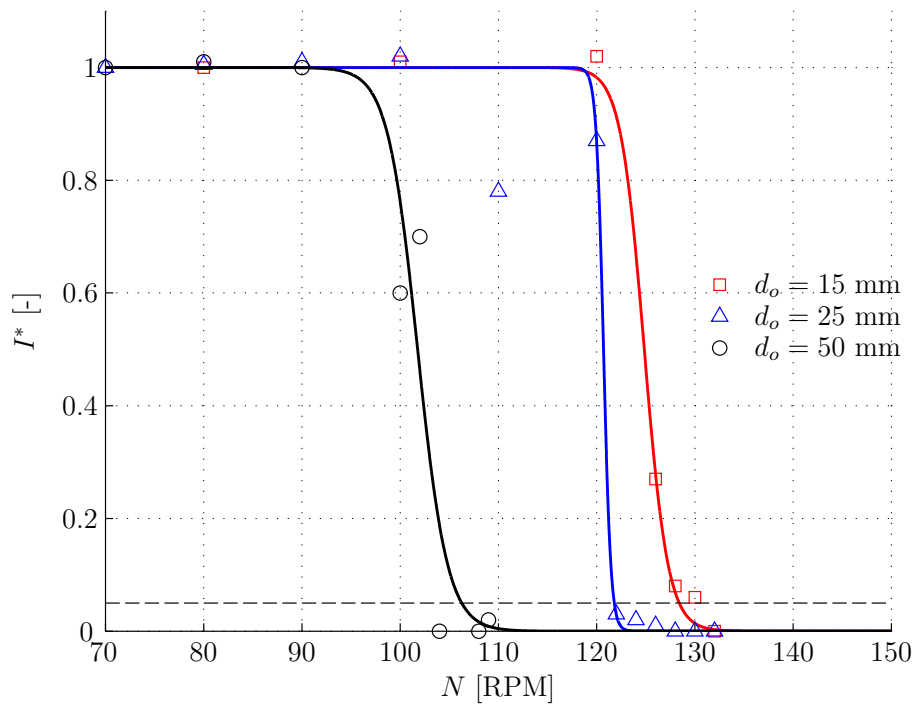


(b)

Figure 4.16: Variation of  $I^*$  with shaker speed for different orbital diameters in a Flat bottom  $d_i=100$  mm OSR with (a)  $h=45$  mm and (b)  $h=70$  mm.



(a)



(b)

Figure 4.17: Variation of  $I^*$  with shaker speed for different orbital diameters in a conical A bottom  $d_i=100$  mm OSR with (a)  $h=45$  mm and (b)  $h=70$  mm.

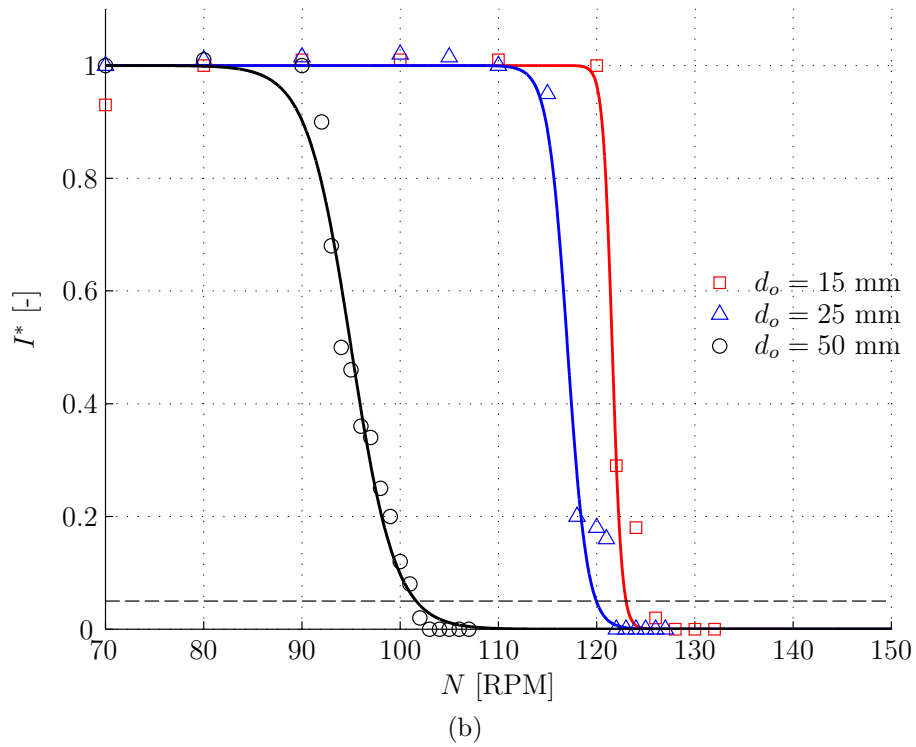
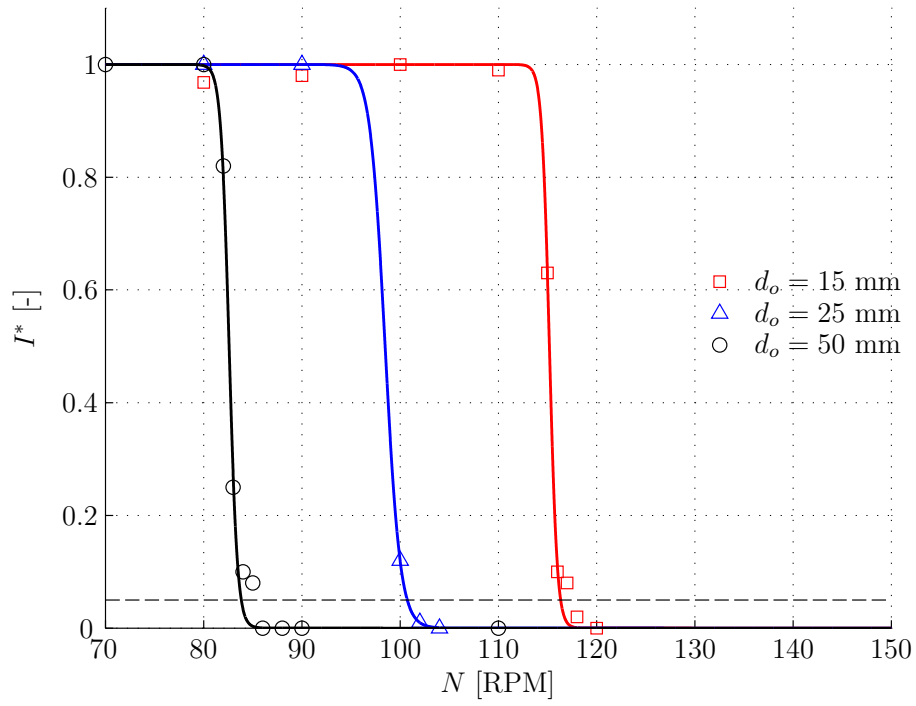


Figure 4.18: Variation of  $I^*$  with shaker speed for different orbital diameters in a conical B bottom  $d_i=100$  mm OSR with (a)  $h=45$  mm and (b)  $h=70$  mm.

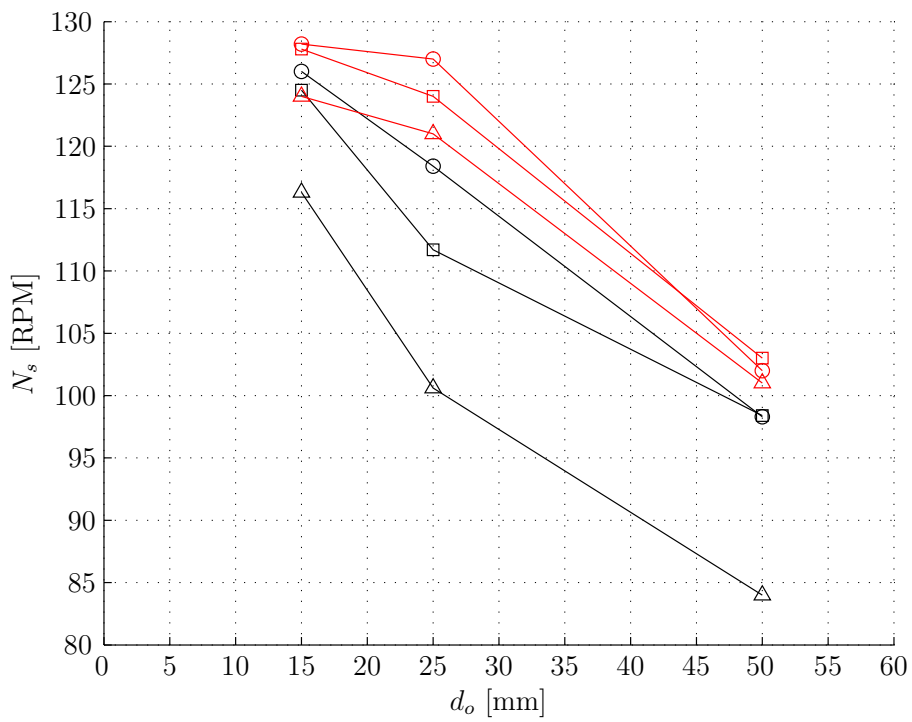


Figure 4.19: Variation of suspension speed,  $N_s$ , with orbital diameter,  $d_o$ , for  $d_i=100$  mm,  $h=45$  mm ( $\circ$ ) flat bottom, ( $\square$ ) Conical A, ( $\triangle$ ) Conical B and  $h=70$  mm ( $\circ$ ) flat bottom, ( $\square$ ) Conical A, ( $\triangle$ ) Conical B.

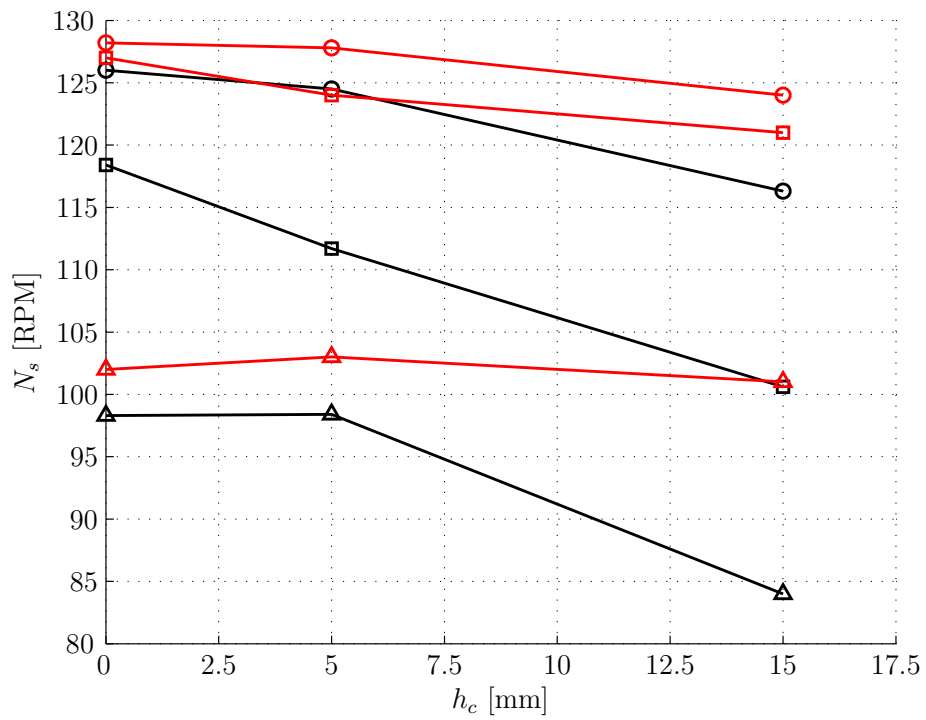


Figure 4.20: Variation of suspension speed,  $N_s$ , with conical bottom height,  $h_c$ , for  $d_i=100$  mm,  $h=45$  mm: ( $\circ$ )  $d_o=15$  mm, ( $\square$ )  $d_o=25$  mm, ( $\triangle$ )  $d_o=50$  mm; and  $h=70$  mm: ( $\circ$ )  $d_o=15$  mm, ( $\square$ )  $d_o=25$  mm, ( $\triangle$ )  $d_o=50$  mm.

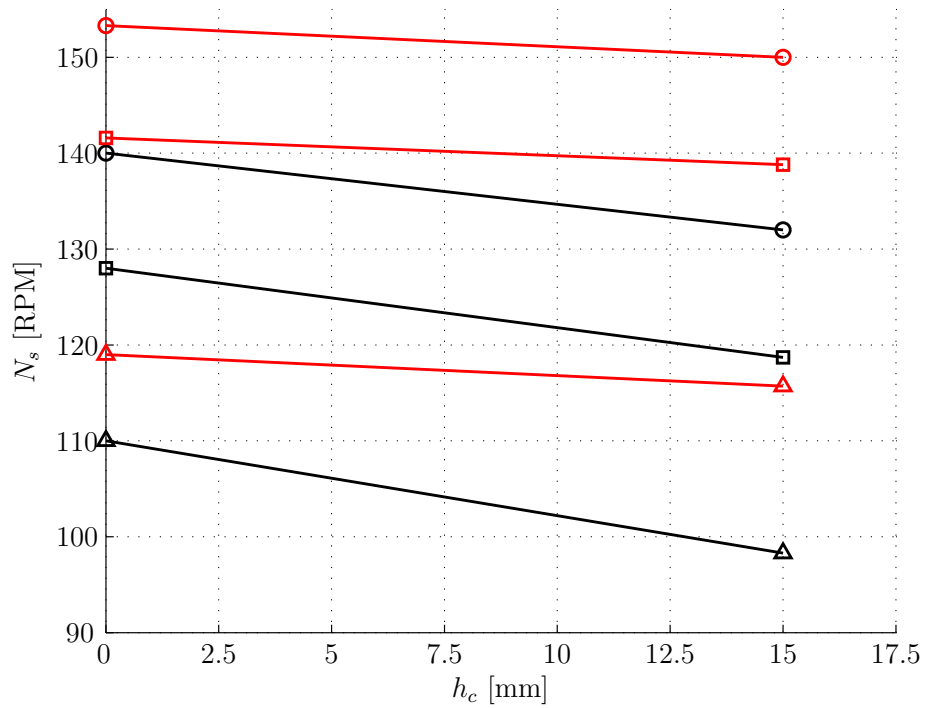


Figure 4.21: Variation of suspension speed,  $N_s$ , with conical bottom height,  $h_c$ , for  $d_i=70$  mm,  $V_f=115$  mL: ( $\circ$ )  $d_o=15$  mm, ( $\square$ )  $d_o=25$  mm, ( $\triangle$ )  $d_o=50$  mm; and  $V_f=192$  mL: ( $\circ$ )  $d_o=15$  mm, ( $\square$ )  $d_o=25$  mm, ( $\triangle$ )  $d_o=50$  mm.

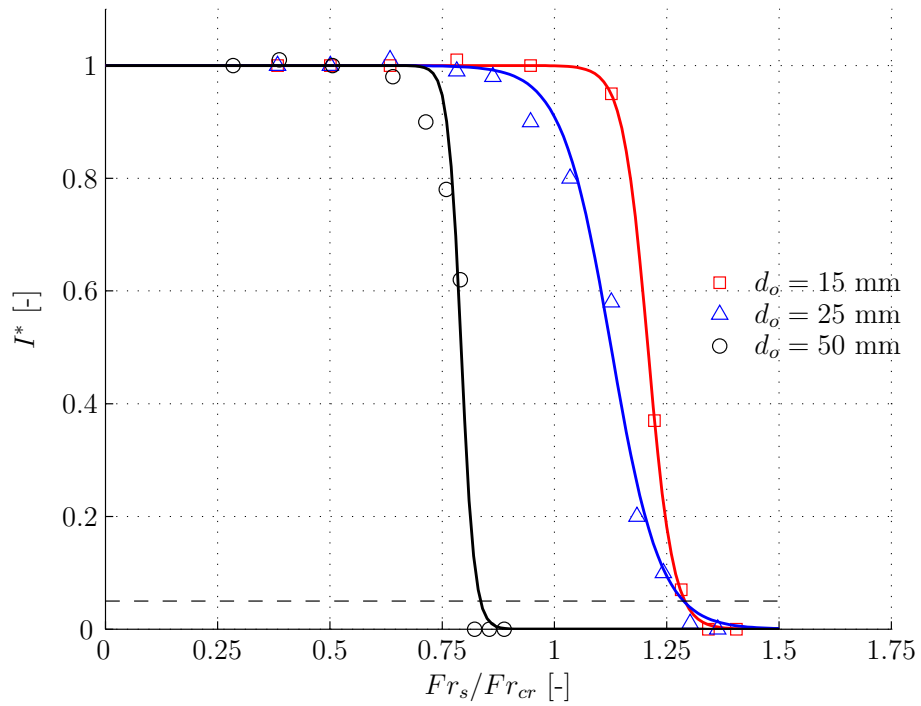
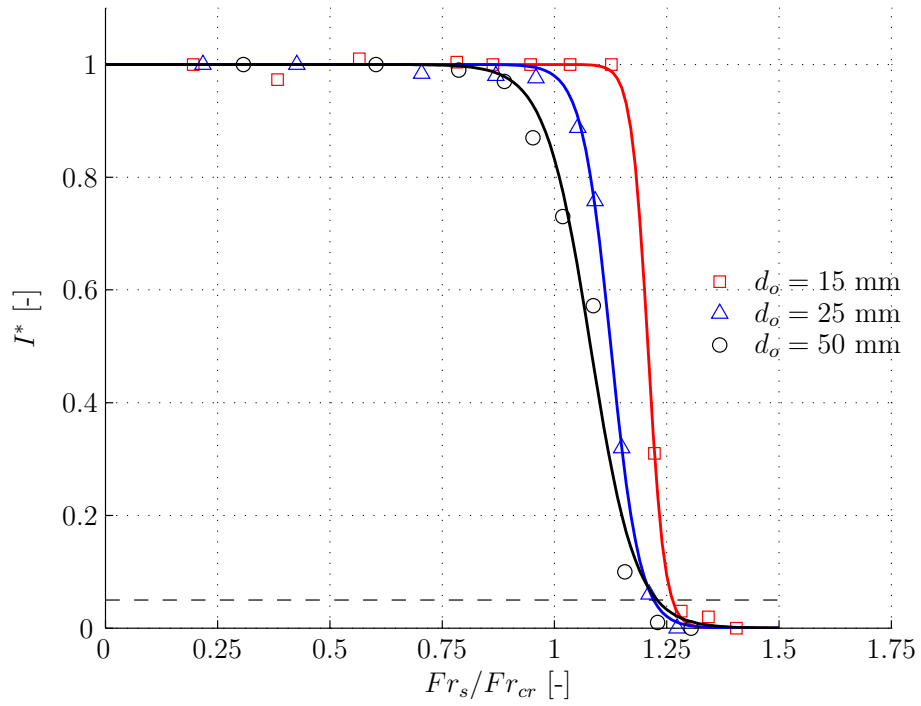
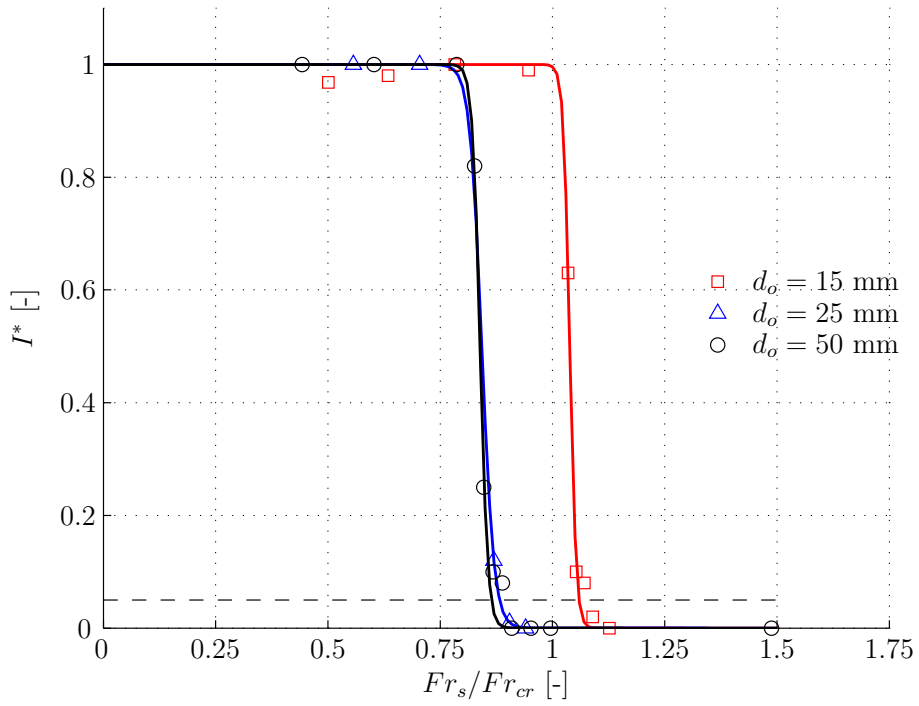
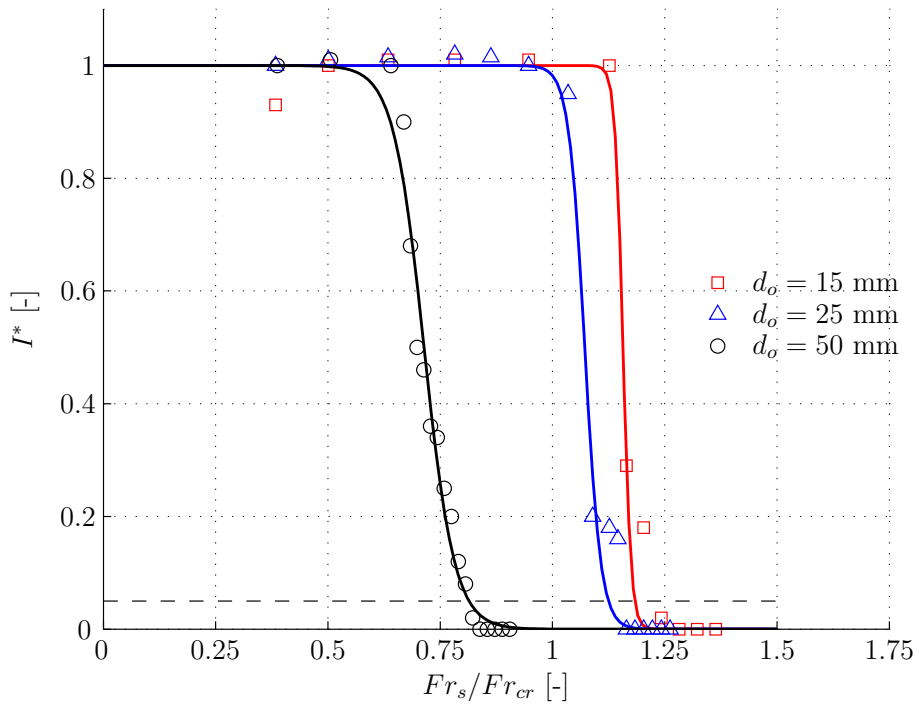


Figure 4.22: Variation of  $I^*$  with  $Fr_s/Fr_{cr}$  for different orbital diameters in a Flat bottom  $d_i=100$  mm OSR with (a)  $h=45$  mm and (b)  $h=70$  mm.



(a)



(b)

Figure 4.23: Variation of  $I^*$  with  $Fr_s/Fr_{cr}$  for different orbital diameters in a Conical B bottom  $d_i=100$  mm OSR with (a)  $h=45$  mm and (b)  $h=70$  mm.

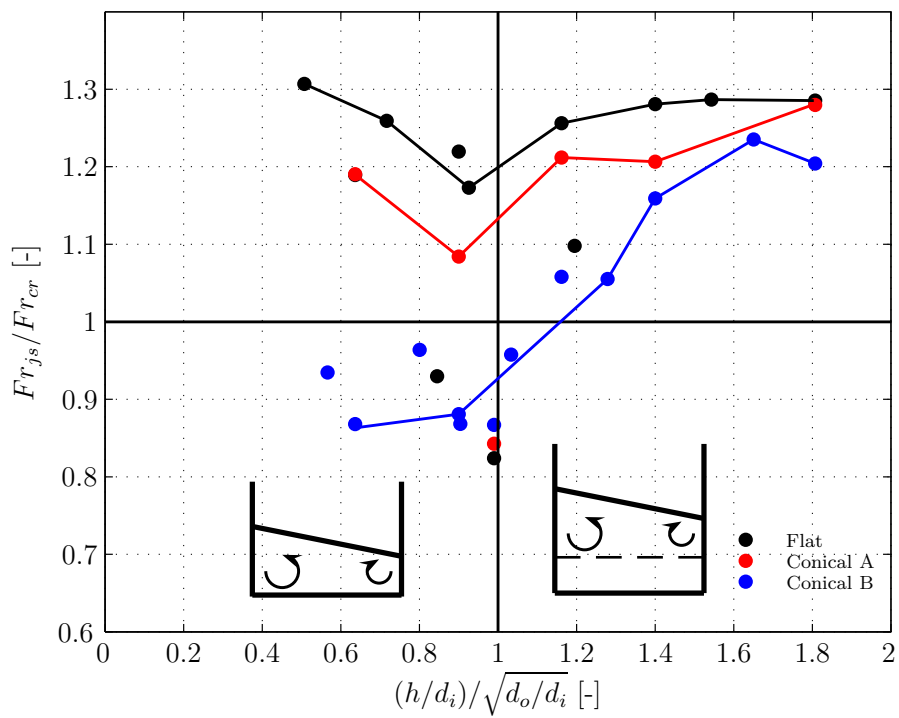


Figure 4.24: Variation of the suspended to critical Froude number ratio,  $Fr_s / Fr_{cr}$ , with critical height ratio,  $(h/d_i) / \sqrt{d_o/d_i}$ , for all the conditions investigated.

# Chapter 5

## Flow and mixing dynamics in fluids of high viscosity

### 5.1 Introduction

This chapter deals with the study of highly viscous fluids in orbital shaken reactors. Whilst mammalian cell culture broths typically have a viscosity comparable to that of water, other bioprocesses may require high density cultures, where the nature of the fluid is no longer water-like, but behaves like a non-Newtonian fluid with variation of viscosity for different rotational speeds.

The DISMT methodology, discussed in Section 2.3.4, was used in Section 5.2 to evaluate the mixing characteristics of a flat bottom OSR of  $d_i=100$  mm with fluids of viscosity  $\sim 2, 4$  and  $14$  times larger than water. The flow presents characteristics similar to that of water, but significant differences occur as the viscosity is increased. The mixing number is found to increase with increasing viscosity and formation of caverns are observed, which are described in Section 5.2.2. The persistence of the caverns within the toroidal vortices' boundaries is used to ob-

tain a preliminary estimate of the diffusion coefficient of the DISMT reagents in Section 5.2.4.

Planar Laser Induced Fluorescence (pLIF) was used to visualise the segregation dynamics of a blob of rhodamine in the flow at different agitation rates, to provide an insight on the micro-mixing characteristics of the flow at different regimes (see Section 5.3). The phase-locked fluorescence visualisation is used to measure the deformation induced by the toroidal vortical structure on a blob of dye over a complete revolution, and assess its variation for different operating conditions.

The highly viscous fluids used were aqueous glycerol solutions at a glycerol concentration of 20, 40, 60 v/v% corresponding to kinematic viscosity  $\nu = 1.9 \times 10^{-6}$ ,  $4.37 \times 10^{-6}$  and  $1.37 \times 10^{-5} \text{ m}^2 \text{ s}^{-1}$ , respectively. Full fluid characteristics are listed in Table 5.1.

It is appropriate at this point to make a digression to clarify the terminology relating to the flow types present in OSRs. In his work, Buchs (Büchs *et al.*, 2001, 2000a,b) identified a flow transition based on power consumption measurements and observed a decrease in power consumption when the movement of the fluid in the OSR is not synchronised with the shaker, distinguishing between in- and out-of-phase conditions. Weheliye *et al.* (2013) reported that the free surface wave presents an elliptical shape in-phase flow, whilst for out-of-phase condition the free surface is highly three dimensional. When the free surface is elliptical it projects an inclined line at  $\varphi=0^\circ$  when the bioreactor is observed from the side, whilst the corresponding projection for out-of-phase flow presents a sinusoidal shape.

Weheliye *et al.* (2013) distinguished between before flow transition (BFT) and after flow transition (AFT) based on velocity field measurements from PIV data.

The BFT is characterised by separated vortical cells at the sides of the bioreactor, which are a cross-section of a toroidal vortex inclined below the free surface, whilst AFT presents an axial vortex precessing around the bioreactor's vertical axis with a delay to the shaker's orbital motion. In the case of water-like viscosities, the definitions of Buchs and Weheliye are in agreement, as BFT presents an elliptical free surface and fluid motion in sync with the shaker, whilst AFT is characterised by a three-dimensional free surface and fluid motion delayed with respect to the shaker position. The current chapter builds on these observations to determine how the flow dynamics and transitions are affected by an increase of fluid viscosity, and whether similar definitions of in-phase and out-of-phase flow apply.

## 5.2 Mixing dynamics in highly viscous fluids

As discussed in Section 2.3.4, the DISMT consists in a fast acid-base reaction in presence of pH indicators. To extend such methodology to fluids of high viscosity, the hydrochloric acid and sodium hydroxide were prepared at a concentration of 0.75M in aqueous glycerol solutions to match the viscosity and density of the bulk of the fluid. Other than this the DISMT procedure and data analysis was performed as described in Section 3.2.

Figures 5.1 to 5.3 show images collected by the iCube camera as part of the DISMT experiments performed in a cylindrical OSR, of internal diameter  $d_i=100$  mm, with a fluid height  $h=32$  mm and orbital diameter  $d_o=25$  mm for  $\nu = 1.9 \times 10^{-6}$ ,  $4.37 \times 10^{-6}$  and  $1.37 \times 10^{-5}$  m<sup>2</sup>s<sup>-1</sup>, respectively. In Figure 5.1-5.3 images shown at each given speed were not necessarily taken at a prefixed time interval, but were selected to visualise significant features and key elements of the mixing process during its transient. It is therefore implicit that the image sequences displayed in Figure 5.1-5.3 were not taken at corresponding time across

the different viscosity and speed conditions investigated.

Figure 5.1 and the experiment video (in appendix cd: DIMST\_highly\_viscous\_1\_105RPM.avi) refer to the time evolution of the mixing process for a  $\nu = 1.9 \times 10^{-6} \text{ m}^2 \text{ s}^{-1}$  at  $N=105$  ( $Fr_{do}=0.15$ ,  $Re=580$ ) (a-d) and  $N=120$  RPM ( $Fr_{do}=0.2$ ,  $Re=660$ ) (e-h). At the start of the experiment (Figure 5.1 a) the Sodium Hydroxide is quickly broken up by the flow. The shear in proximity of the vortical cell edge generates streaklines of locally alkaline concentrations that visualise the boundary of the vortical structure on the left hand side (LHS) of the vessel. Few revolutions later, Figure 5.1 (b), the alkaline concentration on the right side (RHS) of the vessel delineates a vortical structure, smaller in size, with the outer and inner sides of the vortical cells being alkaline (blue) and acidic (red), respectively. The alkaline fluid present on the outside of the LHS vortex of Figure 5.1 (b) is transported to the RHS of Figure 5.1 (c) a few revolutions later and starts to neutralise locally the predominant acidic solution. Striations are present in the central section of the vessel, indicating slower mixing in this region. After some time, Figure 5.1 (d), the fluid close to the bottom is well mixed (yellow), whilst the interior of the toroidal vortex remains acidic (red) with local base concentrations at the boundaries on the RHS vortical cell. This specific experiment was run for a very long time, until full mixing was reached, indicating little fluid exchange through the toroidal vortex boundaries. The free surface profile appears to be wavy, implying that the flow is out-of-phase to a certain degree, although the flow structure is very similar to that exhibited by water-like fluids BFT, including the direction of rotation of the toroidal vortex, with the left cell rotating anticlockwise (CCW) and the right are clockwise (CW).

For  $N=120$  RPM, the fluid presents mixing characteristics induced by a ‘whirlpool’ axial vortex at the centre of the vessel (Figure 5.1 e-h). NaOH concentrations alternate between the LHS and RHS of the vessel as time progresses (Figure 5.1

f-g), with the central area, associated to an axial vortex, being slower at reaching steady state homogenous pH.

The flow visualisation of Figure 5.1 suggests that for  $\nu=1.9 \times 10^{-1} \text{ m}^2 \text{ s}^{-1}$  the toroidal vortices are still present at a speed,  $N=105 \text{ RPM}$ , which is above that predicted by the scaling law (Ducci and Weheliye, 2014; Weheliye *et al.*, 2013) for that viscosity ( $N_{cr}=92 \text{ RPM}$ ), despite the slope of the free surface being denoted by a certain degree of out-of-phase. According to Figure 5.1 the flow transition occurs somewhere in between  $N=105\text{-}120 \text{ RPM}$ .

The time evolution of the mixing process for  $\nu = 4.37 \times 10^{-6} \text{ m}^2 \text{ s}^{-1}$  is shown in Figure 5.2 (a-d) for  $N=110 \text{ RPM}$  ( $Fr_{do}=0.17$ ,  $Re=260$ ) (a-d) and in Figure 5.2 (e-h) for  $120 \text{ RPM}$  ( $Fr_{do}=0.2$ ,  $Re=286$ ). For the lowest speed examined, the free surface profile is clearly three-dimensional (i.e. Figure 5.2 a), suggesting after-flow-transition condition and the alkaline feed is broken up in filaments, which initially neutralise the fluid at the sides of the vessel (Figure 5.2 b). After few revolutions, Figure 5.2 (c), the different pH and colours delineate an inclined toroid below the free surface with elliptical vortical cells on the LHS and RHS side of the OSR. Figure 5.2 (d) shows that mixing was first achieved in the bulk of the fluid, whilst the toroid behaves as a segregated zone, denoted by a longer time to reach complete pH homogeneity. An important feature of the flow, which cannot be perceived by the static images, but becomes clear from the experiment video (in appendix cd: DIMST\_highly\_viscous\_2\_110RPM.avi), is the direction of rotation of the toroidal vortex. The cells rotate in the opposite direction to that observed in water-like fluid: CW on the LHS and CCW on the RHS of the vessel. For the highest agitation rate ( $N=120 \text{ RPM}$ ) the fluid presents an axial vortex that achieves complete mixing at the vessel sides first and in the core of the fluid later on in the experiment.

The DISMT experiments for  $\nu = 1.37 \times 10^{-5} \text{ m}^2 \text{ s}^{-1}$  are shown in Figures 5.3 (a-d) for  $N=110$  RPM ( $Fr_{do}=0.17$ ,  $Re=84$ ), Figures 5.3 (e-h) for  $N=112$  RPM ( $Fr_{do}=0.18$ ,  $Re=85$ ) and Figures 5.3 (i-l) for  $N=115$  RPM ( $Fr_{do}=0.18$ ,  $Re=87$ ). This fluid is 14 times more viscous than water and presents significantly different flow regimes than those observed in water. At the lowest agitation rate considered ( $N=110$  RPM) the free surface is three-dimensional suggesting an out-of-phase regime. After insertion, the added base is dragged downward through the centre of the vessel (see Figure 5.3 b). A toroidal vortex is clearly visible below the free surface in Figure 5.3 (c), which rotates CW on the LHS and CCW on the RHS of the vessel, retaining a highly acidic (red) liquid inside it. Mixing is achieved earlier outside the toroidal vortex, which acts as a segregated mixing zone, or cavern (Figure 5.3 c-d). An additional toroidal vortex can be observed in Figure 5.3 (d), and more clearly in Figure 5.4 above the main toroidal flow feature, also inclined with the free surface and rotating in the opposite direction. These secondary toroidal vortices had not been previously reported in the literature.

A flow characteristic not observed before is found to be present at an agitation rate of  $N=112$  RPM (Figure 5.3 e-h). At these conditions the Sodium Hydroxide concentrations, in blue in Figure 5.3 (e), outlines a CW vortical cell compressed at the vessel walls on the LHS of the vessel. In Figure 5.3 (f), and in the supplementary video (`DIMST_higly_viscous_3_112RPM.avi`), an area of fast moving flow is observed on the RHS, below the free surface. Figures 5.3 (g-h) show a slow mixing region close to the vessel bottom, with features resembling those of a toroidal vortex, acting as a cavern and hindering pH homogenisation. The vortical cell on the left, the fast moving flow on the right and a toroidal structure at the bottom of the vessel had been observed by Ducci and Weheliye (2014) for a vessel of similar geometry operating with silicon oils,  $\nu=10^{-5}$  and  $10^{-4} \text{ m}^2 \text{ s}^{-1}$ , as working fluid, where a strong radial flow was recorded below the lowest side

of the free surface.

The flow transition to a axial vortex occurs at a rotational speed of  $N=115$  RPM (see Figure 5.3 i-1). A ‘whirlpool’ like structure generates fast mixing at the OSR sides, and a long lasting un-mixed region at the centre of the bioreactor. The three flow dynamics described in Figure 5.3 for  $\nu = 1.37 \times 10^{-5} \text{ m}^2 \text{ s}^{-1}$  occur over a relatively small range of speed,  $N=110-115$  RPM, and are denoted by substantial differences from those observed for water-like fluids.

### 5.2.1 Effects of fluid viscosity on mixing time

The effect of the viscosity of the fluid on mixing time is discussed in this section for an agitation range of  $N=100-200$  RPM ( $Fr_{d_o}=0.13-0.56$ ) and  $\nu=1.9 - 13.7 \times 10^{-6} \text{ m}^2 \text{ s}^{-1}$ . As discussed in Chapter 3, the mixing number,  $Nt_m$ , decrease with increasing agitation speed up to a value of  $N$  ( $Fr_{d_o}$ ) above which  $Nt_m$  becomes constant. The effects of agitation rate on the mixing number for different  $h/d_i$  and  $d_o/d_i$  combinations in Chapter 3.6 shows that at low  $Fr_{d_o}$ , when the flow is dominated by a toroidal vortex, mixing numbers are significantly higher when fluid entrainment occurred in the vortical structure. At higher  $Fr_{d_o}$ , when an axial precessional vortex is present, mixing numbers are significantly lower than those associated to the toroidal vortex regime. Weheliye *et al.* (2013) derived a scaling law which can accurately determine the  $Fr_{d_o}$  at which flow transitions, for fluids of water-like viscosity. Ducci and Weheliye (2014) further expanded the scaling law for fluids of high viscosity finding that Weheliye’s scaling law was valid for  $\nu < 1.76 \times 10^{-6} \text{ m}^2\text{s}^{-1}$ . As some of the viscosities used in this section are higher than those investigated by Ducci and Weheliye (2014), the range of  $Fr_{d_o}$  investigated was selected to include flow transition.

Figure 5.5 shows the variation of mixing number,  $Nt_m$ , with  $Fr_{d_o}$  for a cylindrical

OSR of  $d_i=100$  mm with  $d_o=25$  mm and  $h=32$  mm for three viscosities  $\nu = 1.9 \times 10^{-6}$ ,  $4.37 \times 10^{-6}$  and  $1.37 \times 10^{-5}$  m<sup>2</sup> s<sup>-1</sup>, respectively. At the lowest  $N$  considered very long mixing time are measured for all the viscosities investigated. This aspect is evident in Figure 5.1, where data points associated to  $Fr_{d_o} < 0.15$  for  $\nu = 1.9 \times 10^{-6}$  m<sup>2</sup> s<sup>-1</sup> and  $Fr_{d_o} < 0.17$  for  $\nu = 4.37 \times 10^{-6}$  and  $1.37 \times 10^{-5}$  m<sup>2</sup> s<sup>-1</sup> have mixing number outside of the ordinate axis range ( $Nt_m > 300$ ). The reason for the slow mixing process is due to the presence of the toroidal vortex, which acts as a cavern preventing fluid exchange with the bulk of the fluid. Data associated with  $\nu = 1.9 \times 10^{-6}$  and  $\nu = 3.7 \times 10^{-6}$  m<sup>2</sup> s<sup>-1</sup> show a similar variation with  $Fr$ , and tend to plateau for  $Fr_{d_o} > 0.27$ , while this is delayed for  $\nu = 1.37 \times 10^{-5}$  m<sup>2</sup> s<sup>-1</sup> with the mixing number levelling for  $Fr_{d_o} > 0.37$ .

The  $Nt_m$  data of Figure 5.5 are scaled with the critical Froude number in Figure 5.6, where the  $Fr_{cr}$  is calculated from Equation 1.7 with a constant of proportionality  $a_o$  dependant on fluid viscosity according to Equation 1.12 (Ducci and Weheliye, 2014). The shaded area in the figure represents non-dimensional mixing times estimated for water-like fluids (discussed in Section 3.7). The higher value of  $N$  required for more viscous fluids to achieve similar  $Nt_m$  can be explained by the higher resistance due to the viscosity, resulting in slower fluid velocities, whilst only direct correlation with the direction of rotation of the toroidal vortical cells can be established from mixing time experiments carried out.

### 5.2.2 Caverns in toroidal vortex flows

The term ‘cavern’ is commonly used within the mixing field to indicate regions of fast mixing close to the impeller as opposed to the surrounding semi-static liquid, when visco-elastic non-newtonian fluids are used in STRs. It however will be used in this work to indicate the slow mixing region observed inside the toroidal vortex

before flow transition in a cylindrical OSR. As shown in Figure 5.1 (d), 5.2 (d) and 5.3 (d) the toroidal vortex below the free surface generates a region of slow mixing, where local stretching and folding mechanisms acting on the inserted base are lower due to the vortical nature of the local flow. On the contrary the shear and strain rate are high close to the wall and at the border of the toroidal vortex. As a result, an active mixing region (the bulk of the fluid) and an isolated mixing region (inside the toroid) can be distinguished inside the bioreactor. The fluids of lower viscosity are associated to long lasting entrapment of acidic pH inside the toroid suggesting limited pH exchange with the bulk of the fluid.

The impact of the toroidal vortex ‘cavern’ on the global mixing time is shown in Figure 5.7 (a) and 5.8 (a) at  $N=110$  RPM ( $Fr_{d_o}=0.17$ ) for  $\nu = 4.37 \times 10^{-6}$  and  $1.37 \times 10^{-5} \text{ m}^2 \text{ s}^{-1}$ , respectively. The mixing map indicates the local mixing number,  $Nt_{m_{ij}}$ , as defined in the colourbar. The regions surrounding the toroidal vortex (Figure 5.7 c and 5.8 c) achieve a local degree of homogeneity much faster than that of the fluid entrained within (Figure 5.7 b and 5.8 b). The size of the region of the slower mixing cavern is larger for  $\nu = 4.37 \times 10^{-6} \text{ m}^2 \text{ s}^{-1}$  (Figure 5.7), with the slow mixing area (and the toroid) extending almost fully to the vessel sides and bottom. For  $\nu = 1.37 \times 10^{-5} \text{ m}^2 \text{ s}^{-1}$ , a more compact slow mixing area can be observed although the mixing number of the fluid within in the toroid is nearly 1.5 times larger than that obtained for  $\nu = 4.37 \times 10^{-6} \text{ m}^2 \text{ s}^{-1}$ . This behaviour is expected as the critical  $Fr$  number,  $Fr_{cr}$ , increases with increasing viscosity, and therefore the flow within the vessel is more developed for  $\nu = 4.37 \times 10^{-6} \text{ m}^2 \text{ s}^{-1}$  rather than  $\nu = 1.37 \times 10^{-5} \text{ m}^2 \text{ s}^{-1}$  at a given speed (i.e.  $N=110$ RPM). This can also be inferred from the size of the toroid which is larger in Figure 5.7 (b) than in Figure 5.8 b).

This suggests that, at a given  $N$  and  $Fr_{d_o}$ , particularly at  $Fr_{d_o} \approx Fr_{cr}$ , the size of the slow mixing cavern is inversely proportional to the viscosity of the fluid.

### 5.2.3 Segregated mixing time

As seen in Figures 5.7 and 5.8, the mixing number of the fluid within the toroid can be 3-5 folds that of the fluid close to the vessel bottom and sides. The two regions achieve homogeneity independently at different times. The mixing maps of Figures 5.7 and 5.8 are used to discriminate between the slow and fast mixing regions (Figure 5.7 and 5.8 b and c, respectively). In both cases the  $Nt_m=1000$  is used as a threshold for separating fast- from slow-mixing regions. The two segregated mixing regions were evaluated independently to further assess their mixing dynamics. Figure 5.9 compares the variation in time of the standard deviation of the normalised green channel,  $\sigma_{G^*}$ , and the degree of mixedness,  $M$ , for the two segregated regions ( $\nu = 4.37 \times 10^{-6} \text{ m}^2 \text{ s}^{-1}$ ). The  $\sigma_{G^*}$  profile of the fast mixing region presents a peak at the beginning of the measurement, indicating a sharp increase of the colour heterogeneity. The inserted base is quickly broken up and distributed around this region and is sufficient to achieve pH neutralisation (yellow colour in the DISMT) within  $500 Nt$ . On the contrary the fluid within the toroidal vortex presents a peak in  $\sigma_{G^*}$  later and the region remains heterogeneous until the end of the experiment. The experimental images show streaklines of NaOH and HCL concentrations within the toroid. The red/blue streaks appear to move on a spiral path within the toroidal vortex and very slowly mix together to reach pH homogeneity. The degree of mixedness,  $M$ , in Figure 5.9 (b) varies from 0 to 1, as defined in Section 3.3.2. The fast mixing region outside the toroidal structure presents a quick increase in the degree of mixedness, reaching within 5% of complete mixing at  $500 Nt$ . The region corresponding to the toroidal vortex presents a slow, almost linear, increase of  $M$  and reaches homogeneity in more than 1250 revolutions.

A similar trend was observed with the highest viscous fluid considered, ( $\nu = 1.37 \times 10^{-5} \text{ m}^2 \text{ s}^{-1}$ ), in Figure 5.10. The  $\sigma_{G^*}$  sharply increases outside the toroid

and soon reaches steady state value whilst the mixing process is significantly slower within the vortex. The degree of mixedness  $M$  in Figure 5.10 (b) reaches 95% within 750  $Nt$  outside the vortical structure, but requires above 2500  $Nt$  to achieve complete mixing inside the toroid.

#### 5.2.4 Diffusion coefficient

Highly viscous fluids at low  $Fr_{d_0}$  present a toroidal vortical structure, which acts as an obstacle for fast mixing by generating a segregated zone within it. In some cases the added base is broken up by the shear at the surroundings of the toroidal vortex and mixing is promoted in the regions close to the walls, without any of the highly concentrated base entering the vortex. This results in excess of base outside the toroid (although still within the pH range of the indicators) and excess of acid inside. The stability of the toroid increases with highly viscous fluids, and this causes little fluid exchange between the toroid and the bulk of the fluid in the bioreactor vessel. Such barrier slows the overall mixing time. It is observed that the fluid within the toroid, initially highly acidic (hence red), slowly reduces in size as the experiment progresses. It is assumed that such reduction in size is due to the diffusion of the NaOH from the bulk to the interior of the fluid in the toroidal structure.

Molecular diffusion is described as the movement of molecules from a region of high concentration to a region of low concentration. Frick's 1<sup>st</sup> law relates the diffusion rate,  $J$ , to the concentration gradient according to the relationship of Equation 5.1 (for 1D case):

$$J = -D \frac{\partial C}{\partial x} \quad (5.1)$$

where  $D$  is the diffusivity of a substance,  $\partial C$  the concentration gradient,  $x$  is the direction of diffusion  $\partial x$ .

The diffusion flux rate of NaOH from the high concentration region to the interior of the toroid could not be measured in the DISMT experiments, nor could the concentration gradient as the pH indicators are effective over a range of pH values. However the effect of the diffusion from the bulk to the inner toroid is observable via the size reduction of the acidic region within the toroid (see Figure 5.3 c-d). The vortical structure can be best represented by an elliptical toroid, whose cross section is largest below the higher crest of the free surface wave and is approximated here by an ellipse. The surface of the toroid is the unit area for the flux  $J$ . For simplicity, the perimeter or circumference of the vortical cell is assumed to be proportional to the surface area of the toroid. The elliptic cross-section of the LHS toroidal cell was measured for  $\nu = 4.37 \times 10^{-6}$  and  $1.37 \times 10^{-5}$   $\text{m}^2 \text{s}^{-1}$  as shown in Figure 5.11 (a) ( $N=110$  RPM,  $d_o=100$  mm,  $h=32$  mm,  $d_o=25$  mm). The cross-section perimeter was estimated according the approximation of Equation 5.2.

$$p_v = 2 \pi \sqrt{\frac{A^2 + B^2}{2}} \quad (5.2)$$

where A and B are the major and minor axes of the ellipse. The maximum size of the toroidal vortex is clearly visible after a few revolutions from the start of the experiment where there is a clear contrast between the red acidic concentration within the vortex and the yellow surroundings (see Figure 5.11 a). This occurs at  $Nt=60$  and  $Nt=500$  for the  $\nu = 4.37 \times 10^{-6}$  and for  $\nu = 1.37 \times 10^{-5}$   $\text{m}^2 \text{s}^{-1}$ , respectively. Figure 5.11 (b) shows the decrease of the vortex perimeter, normalised with the initial size of the vortical cell,  $p_v^*$ , over the shaker table revolutions. The  $p_v^*$  is measured every 30-60 revolutions. The region of higher acid concentration decreases in size, due to the slow diffusion of the excess of NaOH in the bulk of the fluid. It must be noted that the toroidal vortex per se does not vary in size throughout the agitation. A linear relationship can be observed in Figure 5.11 (b), with the diffusion coefficient for  $\nu = 4.37 \times 10^{-6}$   $\text{m}^2 \text{s}^{-1}$

( $dp_v^*/dNt = -4.46 \times 10^{-4}$ ) being nearly four times greater than the corresponding coefficient for  $\nu = 1.37 \times 10^{-5} \text{ m}^2 \text{ s}^{-1}$  ( $dp_v^*/dNt = -1.12 \times 10^{-4}$ ).

### 5.3 Micro-mixing of highly viscous fluids

Phase-resolved measurements at different agitation rates were taken using planar Laser Induced Fluorescence ( $d_i=100 \text{ mm}$ ,  $d_o=50 \text{ mm}$ ,  $h=50 \text{ mm}$ ). This allowed to better characterise micro-mixing efficiency for highly viscous fluids. The fluid employed was an aqueous glycerol solution of viscosity  $\nu = 1.37 \times 10^{-5} \text{ m}^2 \text{ s}^{-1}$ , 14-fold that of water. The Rhodamine dye was inserted in the flow using a syringe pump from above the surface at the centre of the vessel.

Figures 5.12 (a-c) show three distinctive moments of the mixing process obtained at  $N=80 \text{ RPM}$  ( $Fr_{d_o}=0.18$ ). A video extract of the experiment can be found in the cd attached to the thesis: `pLIF_80RPM.avi`. After insertion of the fluorescent dye, the centrifugal force pushes the dye on the free surface towards the vessel walls. The following description will focus on the LHS of the vessel, on the side where the free surface wave is at its highest position. A large blob of dye can be observed being drawn towards the bottom (Figure 5.12 a) on a vertical path parallel to the side walls before curling back up CCW towards the free surface (*streak 'a'* in the figure). At the same time part of the dye undergoes stretching resulting in a wavy filament (*streak 'b'* in the figure). These striations appear to increase in length and in striation frequency the longer they have undergone stretching in the flow. Each fold of the Rodamine streak is associated to a single revolution of the orbital shaker, hence it can be considered as the cumulative stretching experienced by the initial blob of dye over each revolution. In Figure 5.12 (b) *streak 'a'* continues to elongate towards the free surface in a CCW motion over a single revoution. *Streak 'b'* appears to be pulled partially

upwards towards the surface and partially downwards towards the vessel bottom, resulting into thin striations' pattern present next to *streak 'a'* close to the left wall (see Figure 5.12 b and c). Figure 5.12 (c), 87 revolutions after Figure 5.12 (a), visualises the main features of the flow  $N = 80$  RPM: a principal toroidal vortical cell ( $P_L$ ), larger in size in the bulk of the fluid, and a secondary ( $S_L$ ), smaller and located below the free surface close to the vessel walls. Close to the surface and the LHS wall, vortical cell  $S_L$  rotates CW and acts up to a depth of  $z/d_i=0.2$  creating a wavy streak which is then elongated further by the larger  $P_L$  structure, which extends deeper, the bottom of the bioreactor. Symmetrical vortical cells are present on the RHS, rotating in the opposite direction ( $P_R$  rotating CW and  $S_R$  CCW). The vortical cells appear completely separated and elliptical in shape, with  $P_L$  elongated on the  $z$ -direction and  $P_R$  on the  $r$ -direction.

Similar observations can be made at  $N=85$  RPM ( $Fr_{do}=0.2$ ), as shown in Figure 5.13 and in `pLIF_85RPM.avi` in the supplementary cd: the dye remains on the free surface after injection and it is pushed against the wall by the centrifugal force; it is then drawn into the bulk of the reactor over a limited height below the free surface and is deformed in a striation pattern by the action of  $S_L$ ; the structure  $P_L$  further elongates the dye towards the bottom of the vessel and completes its transport across the entire size of the bioreactor. The amplitude of the wavy *streak 'b'* appears greater than in Figure 5.12, whilst the principal vortical cells extend to the bottom of the vessel, as previously observed for water-like viscosities, when the agitation rate is increased (see Section 4.2).

A very different flow can be observed at  $N=90$  RPM ( $Fr_{do}=0.23$ ). The dye enters the fluid from the side walls (see Figure 5.14 a) and the Rhodamine dye is drawn downwards by vortical cell  $S_L$  commencing a wavy filament aligned in the  $z$ -direction and being transported towards the reactor axis. The streaks are observed to further deform and elongate in a bell shape form due to the simultaneous

action of vortical cell  $S_L$  and a tertiary vortical cell,  $T_L$ , which are counter-rotating with respect to each other. This results in the high shear region at the border between the two vortical cells that promotes lamellar stratification. Specular vortical structure can be observed on the LHS ( $P_R$ ,  $S_R$  and  $T_R$  in Figure 5.14 d), all close to the free surface and oriented at an angle parallel to the free surface. A video extract of the experiment can be found in the supplementary cd: `pLIF_90RPM.avi`.

At  $N=100$  RPM ( $Fr_{do}=0.28$ ) the inserted dye does not spread on the free surface towards the walls, but it can be observed being drawn through the centre of the fluid (Figure 5.15 a) under the action of vortical cell  $P_L$  (in Figure 5.15 d). The Rhodamine dye reaches the vessel bottom in Figure 5.14 (b) and then undergoes elongation towards the walls. Significantly, the direction of rotation of the principal vortical cells at these conditions is opposite of that observed at  $N=80-85$  RPM for  $\nu = 1.37 \times 10^{-5} \text{ m}^2 \text{ s}^{-1}$  and water-like viscous fluids BFT. This is indicated by the orientation of the striations but can be clearly observed in `pLIF_100RPM.avi` in the supplementary cd. The periodic striations visible inside the LHS and RHS vortical cell region in Figure 5.15 (c) are generated by a smaller cell,  $S_L$ , close to the free surface which rotates in the same direction as the correspondent  $P$  vortex. A vortical cell pair ( $T_L$  and  $T_R$ ) is observed at the centre of the vessel, just below the free surface, which is argued to initiate the draw of Rhodamine dye from the free surface after feed.

At  $N=105$  RPM ( $Fr_{do}=0.31$ ), as shown in Figure 5.16 (a), the dye is drawn through the centre of the fluid and stretched toward the bottom of the vessel after insertion in the fluid. A pair of vortical cells can be seen close to the centre of the free surface 5.16(b) which draws the Rhodamine dye from the surface. The main flow structure  $P_L$  (and  $P_R$ ) elongates the dye filaments to the bottom, then up the vessel walls to the free surface. The striation thickness in Figure 5.16 (c) indicates

that at that instant high level of homogeneity is achieved in the periphery of the vortical cell, whilst the dye requires several more revolutions to enter the inner part of the vortical cell. An additional pair of vortices is observed below the free surface (denoted as  $S_L$  and  $S_R$  which rotate in the opposite direction to that of the main cells  $P_L$  and  $P_R$ , respectively (see Figure 5.16 d).

The pLIF images in Figure 5.17 (a-c) refer to the OSR agitated at  $N=115$  RPM ( $Fr_{do}=0.37$ ). Figure 5.17 (a) shows the dye being pushed to the vessel walls by centrifugal force and not entering the fluid through the centre, as observed at  $N=100-105$  RPM. The Rhodamine gets drawn in the fluid from the side walls and undergoes fast and repeated folding and stretching on the sides of the vessel (Figure 5.17 b). This flow condition did not present stable flow structures but was characterised by chaotic mixing.

Figures 5.18 (a-c) summarise the flow structures observed from the pLIF images at  $N=80, 85, 90, 100$  and  $105$  RPM ( $\nu = 1.37 \times 10^{-5} \text{ m}^2 \text{ s}^{-1}$ ). The diagram obtained for  $N=80$  RPM, Figure 5.18 (a) is characterised by the following features: a CW rotating vortical cell  $S_L$  below the free surface close to the wall, a large CCW rotating vortical cell,  $P_L$ , extending deeper in the liquid with specular flow structures on the RHS.  $P_L$  and  $P_R$  are part of an elliptical toroidal vortex inclined below the free surface, with the LHS vortical cell elongated vertically and the RHS one horizontally. The direction of rotation of  $P_L$  and  $P_R$  inhibit the dye from entering the flow below the insertion position at the centre of the vessel, which instead is pushed towards the walls from the free surface. The increase in agitation rate to  $N=85$  RPM results in an increase in size of  $P_L, P_R, S_L$  and  $S_R$  (Figure 5.18 b). At  $N=90$  RPM, as shown in Figure 5.18 (c),  $S_L$  and  $S_R$  expand significantly and acts to a higher depth below the free surface. As a result  $P_L$  and  $P_R$  reduce in size and are positioned just below the free surface. Figure 5.18 (d) represents the flow observed at  $N=100$  RPM, which presents a large CW

rotating vortical cell on the LHS and a CCW on the RHS ( $P_L$  and  $P_R$ ). From the change of rotation direction of the primary vortex it is hypothesized that these are indeed the secondary vortices described at speed of  $N=90$ RPM, which have further increased in size to become the primary vortex. Similarly the primary vortices of Figure 5.18 (c) have decreased in size and have been pushed towards the centre of the vessel, keeping their direction of rotation, to become the tertiary vortex denoted by the  $T$  pair of Figure 5.18 (d).

The principal toroidal vortex expands further in size at  $N=105$  RPM (see Figure 5.18 d) reaching the bottom of the vessel, whilst  $S_L$  and  $S_R$ , responsible for the initial draw of dye from the free surface, move towards the LHS crossing the vessel centerline and increasing in size.

### 5.3.1 Material line elongation of Rhodamine dye

A more detailed study was performed of the deformation of the Rhodamine dye by the action of the vortical cells present close to the wall for conditions  $N=80-90$  RPM. As described in Section 5.3, at such range of speed, the inserted dye is moved on the free surface by the centrifugal force and enters in the bulk of the flow due to the action of the vortical cells close to the vessel walls. Figure 5.19 shows in detail the elongation of the dye on the LHS of the vessel due to the simultaneous action of vortical cells  $P_L$  and  $S_L$  at an agitation of  $N=80$  RPM (as labelled in Figure 5.18 a). The images refer to the deformation of a blob of dye, originating from the surface, over 7 revolutions. As the shaker orbits, the free surface wave reaches its highest position at  $\varphi=0^\circ$ , collecting a parcel of dye from the surface under the action of  $S_L$  (Figure 5.19 a). The fluid parcel then undergoes elongation due to the high shear rates at the edges of vortices  $P_L$  and  $S_L$ . The intensity of the dye, and consequently its concentration, does not vary

significantly over the frames under consideration. The blur visible on the right of the bright Rhodamine streak was due to the dye present at different angular positions in the vessel (behind or in front of the laser plane), having moved in a direction perpendicular to the laser plane. The diffusion rate  $D$  for Rhodamine is in the order of  $8 \times 10^{-10} \text{ m}^2/\text{s}$ , and is several orders of magnitude smaller than that of the rate of stretching.

Figure 5.20 refers to the detail of the dye being elongated on the RHS of the bioreactor, just below the free surface. The wavy streakline is generated by the shear at the interface of vortical cell  $P_R$  and  $S_R$  (as labelled in Figure 5.18 a). At each revolution, the dye streak is elongated, with the amplitude of the folds and their frequency increasing. Similar details of the evolution of the Rhodamine streak on the LHS and RHS of the vessel are presented for an agitation rate  $N=85$  RPM in Figures 5.21 and 5.22, respectively. The LHS streak, shown in Figure 5.21, appears to experience fewer folds before being recirculated by the  $S_L$  vortical cell, suggesting higher vorticity in the region when compared to  $N=80$  RPM.

As discussed previously, the flow at  $N=90$  RPM is dominated by two concentric counter-rotating toroidal vortices. The inner one is identifiable by vortical cell  $P_L$  and  $P_R$ , the outer by  $S_L$  and  $S_R$ , (as labelled in Figure 5.18 c)  $S_L$  and  $S_R$  are elliptical and oriented parallel to the vessel walls, whilst  $P_L$  and  $P_R$  are inclined with the free surface. This results in the dye streak, as shown for the LHS of the vessel in Figure 5.23, developing in a filament oscillating vertically with large folds and extending towards the centre of the vessel. On the RHS, shown in Figure 5.24, the Rhodamine streak follows a wavy path, due to the effect of vortical cell  $S_R$  and  $P_R$ , whose overall direction is tangent to the vortical cells. The streak on the RHS presents short folds which increase in width at the end of the selected range of images (Figure 5.24 i-k). The striations observed are the concentrations

of dye present on the plane of measurement, which bisects the bioreactor along its axis. The toroid is acting three-dimensionally in the fluid and elongates and folds the dye in all directions, although motion and shear in the  $r$ - $z$  is dominant at  $\varphi=0^\circ$ . The wavy characteristic of the dye streak can be explained based on the findings of Reclari *et al.* (2014), who performed particles tracking simulations in the flow of a cylindrical OSR. It was found that an individual particle moves along a trochoical path with amplitude proportional to the shaking diameter and inversely proportional to the depth from the free surface. It was found in Section 3.5 that local concentrations or streaks of NaOH were following a spiral path around the toroidal vortex, requiring 1.67 shaker revolutions to complete a loop around the toroid axis and 6.68 shaker revolutions to completely revolve around the cylindrical vessel. The wavy trajectory of the the Rhodamine observed in the pLIF images dye might be the cross section of the trochoical streaklines observed by Reclari *et al.* (2014), which intersect the measurement plane.

The variation in time, in terms of revolutions, of the striation length growth ratio,  $(\ell_t - \ell_o)/\ell_o$ , of the dye material lines is shown in Figure 5.25 (a) and (b) for the LHS and RHS of the bioreactor vessel, respectively. Although commencing at different times after Rhodamine insertion, the data is plotted with a common origin, starting at the same time instant (or revolution). The lengths were measured at the dye streak centreline, for each elongated section (as shown by the different coloured sections in Figures 5.19 to 5.24). On the LHS of the vessel, Figure 5.25 (a), the growth ratio of the striation length has a larger slope the higher the  $N$ . It can be observed that after 5 revolutions, the dye *streak* ‘a’ at the  $N=90$  RPM condition has experienced the largest elongation, due to the wide streak meanders shown in Figure 5.23 (f). On the RHS of the vessel, the dye streak undergoes the largest elongation at  $N=85$  RPM (Figure 5.25 b). At  $N=90$  RPM a slow growth of the material lines was observed, due to the tight folds shown in Figure 5.24 (l),

this might be due to the fact that on this side the dye is aligned in the tangential direction and therefore its growth ratio is only partially measurable from the vertical plane measurements of this study.

The scalar lamellae or streaks are formed by the repeated action of advective motions of the counter rotating vortical cells present in the flow. The growth ratio of the material lines in vortices can be used to predict their mixing time (Meunier and Villermaux, 2003). For a scalar blob of dye,  $s_0$ , if the material lines grow linearly, as  $\gamma t$  (where  $\gamma$  is the rate of deformation), the characteristic time,  $t_s$ , after which fluctuations decay from initial scalar spatial distribution is  $t_s \sim \gamma^{-1} Pe^{1/3}$ ; if the material lines grow as  $(\gamma t)^2$ , then  $t_s \sim \gamma^{-1} Pe^{1/3}$ , where  $Pe = \gamma s_0^2 / D$  is a Peclet number and  $D$  the diffusivity. Although the material lines in OSR presented in this work are due to the interaction of vortical pairs and not elongation inside a point vortex, Meunier and Villermaux (2003)'s correlation can be used to obtain an indication of the mixing performance. A power law,  $(\gamma t)^n$ , is fitted through the data in Figure 5.25 (a) to determine the growth rate coefficient,  $n$ . This is found to increase with the shaker speed and to be 1.4, 1.6 and 2 for  $N=80$ , 85 and 90 RPM, respectively.

## 5.4 Concluding Remarks

The mixing dynamics and flow characteristics of fluids of high viscosity in OSRs were evaluated using DISMT and planar Laser Induced Fluorescence. The DISMT experiments were used to identify the main features in the flow, and to determine the global mixing time, the mixing time of segregated regions in the flow and the rate of reduction of the regions of slower mixing for different fluid viscosities ( $\nu = 1.9 \times 10^{-6} - 1.37 \times 10^{-5} \text{ m}^2 \text{ s}^{-1}$ ). The use of pLIF enabled detailed visualisations of flow features and estimates of the growth rate of material lines stretched

highly viscous fluid ( $\nu = 1.37 \times 10^{-5} \text{ m}^2 \text{ s}^{-1}$ ).

The DISMT experiments show distinct flow structures for the viscosity and agitation rate combinations evaluated: toroidal vortices, axial vortices and tangential flow. At low viscosity and low  $N$ , a toroidal vortex is observed, inclined with the free surface which both generates the mixing in the bulk of the liquid but also acts as a segregated mixing zone. The toroidal vortex rotates CCW on the LHS and CW on the RHS of the OSR vessel. With increasing  $N$  (at constant viscosity), the flow transitions to an axial vortex, and fast mixing is achieved at the sides of the vessel. At the intermediate viscosity investigated,  $\nu = 4.37 \times 10^{-6} \text{ m}^2 \text{ s}^{-1}$ , the toroidal vortices are present at low  $N$ , but are observed to rotate in an opposite direction than that exhibited at lower viscosities. This results in the added base being drawn through the centre of the fluid to the bottom of the vessel just after insertion. The fluid presents a flow structure not observed with lower viscosity fluid: a vortical cell compressed at the vessel walls on the LHS of the vessel rotating CW and a radial flow on the RHS moving towards the centre of the vessel. For  $\nu = 1.37 \times 10^{-5} \text{ m}^2 \text{ s}^{-1}$  the different flow features are observed over a relatively small range of speed,  $110 < N < 115$ .

The viscosity of the fluid affects the mixing time, with the highest viscosity fluid requiring higher agitation rates to reach homogeneity ( $Nt_m \simeq 100Nt$ ). The mixing numbers for all viscosities decay to a value  $Nt \simeq 50$ , doing so earlier for the lowest viscosity fluid. The direction of rotation of the toroidal vortices does not affect mixing times. Although CW rotation on the LHS (present in highly viscous fluids) favours the initial distribution of the added base, the segregated mixing inside the toroid are found to offset their advantage.

At low  $N$ , the segregated mixing regions caused by the toroidal vortices present higher concentration of the initial pH, resulting in red (acidic) colour, whilst the

fluid outside of the toroid undergoes fast mixing. For the same  $N$ , the segregated region is larger for fluids of lower viscosity, but tends to mix quicker than higher viscosity fluids. The analysis of the mixing dynamics in the segregated zones proved that the base is quickly broken up by the action of the toroidal vortex and reaches homogeneity in the bulk of the fluid. On the contrary the base reaches the interior of the toroid later and homogenizes far slower, increasing the mixing number tenfold. The segregated regions in the toroidal vortices were further studied by means of measuring their rate of decay. Due to the limited fluid transfer between the interior of the vortex and the bulk of the fluid the segregated region decays slowly, and it was found that the rate of decay of the cross-sectional area of the toroid decreases linearly.

Phase-resolved pLIF measurements showed that at low  $N$ , when the LHS toroidal vortex cell rotates CCW (and the RHS rotates CW) the centrifugal force pushes the dye to the vessel walls and subsequently enters the fluid from the sides under the action of small vortical cells at the sides of the vessel. The interaction between the small vortical cell close to the walls and the larger ones inside the reactor, which extends further down, stretches and folds the dye in a wavy streak which increases in length and wave amplitude at each revolution, before engulfing in the toroid. At higher  $N$ , when the LHS toroidal vortex cell rotates CW (and the RHS CCW) the dye is dragged in the flow through the centre of the fluid, and stretched to the bottom and sides of the vessel. When the agitation rate is further increased an axial vortex dominates the flow with mixing being chaotic in nature.

The growth ratio of the material lines of the dye undergoing stretching and folding from the vortical cells shows a non-linear correlation for  $N=80-90$  RPM, which follows a quadratic power law. The research presented in this chapter furthers the findings of Chapters 3 and 4, where water-like viscosity fluids were evalu-

ated in terms of mixing and fluid velocity. The range of viscosities and agitation rates investigated is used to characterize the different types of flow pattern occurring in highly viscous liquids, such as those present in high concentration cell cultures.

Glycerol		Density	Dynamic viscosity	Kinematic viscosity	$\nu/\nu_w$
vv%	vw%	kg/L	[cPo]	[St or m <sup>2</sup> s <sup>-1</sup> ]	[-]
20	23.97	1.0572	2.025	$1.9 \times 10^{-6}$	1.9
40	45.68	1.1146	4.876	$4.37 \times 10^{-6}$	4.37
60	65.43	1.1686	16.051	$1.37 \times 10^{-5}$	13.7

Table 5.1: Fluid properties of the aqueous glycerol solutions.

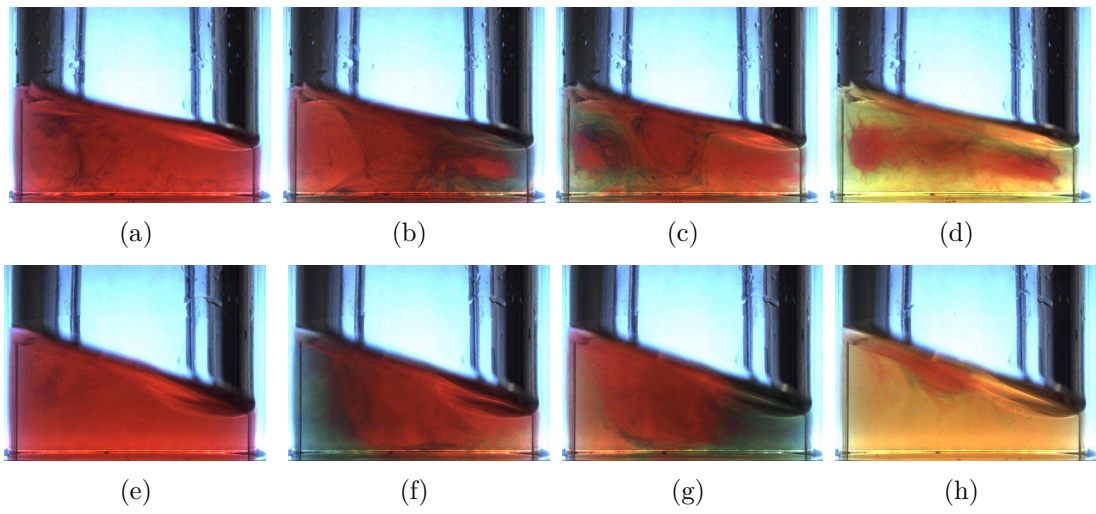


Figure 5.1: Time evolution of the mixing dynamics inside the  $d_i=100$  mm bioreactor for a glycerol solution of viscosity  $\nu=1.9 \times 10^{-6} \text{ m}^2\text{s}^{-1}$  for two speeds; (a-d)  $N=105$  RPM, (e-h)  $N=120$  RPM. ( $h/d_i=0.32$ ,  $d_o/d_i=0.25$ ).

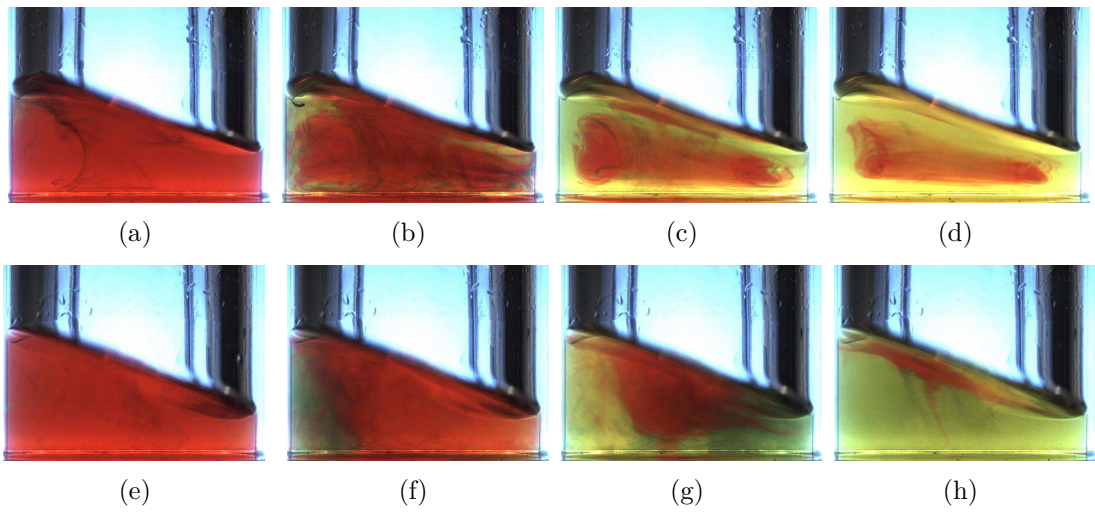


Figure 5.2: Time evolution of the mixing dynamics inside the  $d_i=100$  mm bioreactor for a glycerol solution of viscosity  $\nu=4.37 \times 10^{-6} \text{ m}^2\text{s}^{-1}$  for two speeds; (a-d)  $N=110$  RPM, (e-h)  $N=120$  RPM. ( $h/d_i=0.32$ ,  $d_o/d_i=0.25$ ).

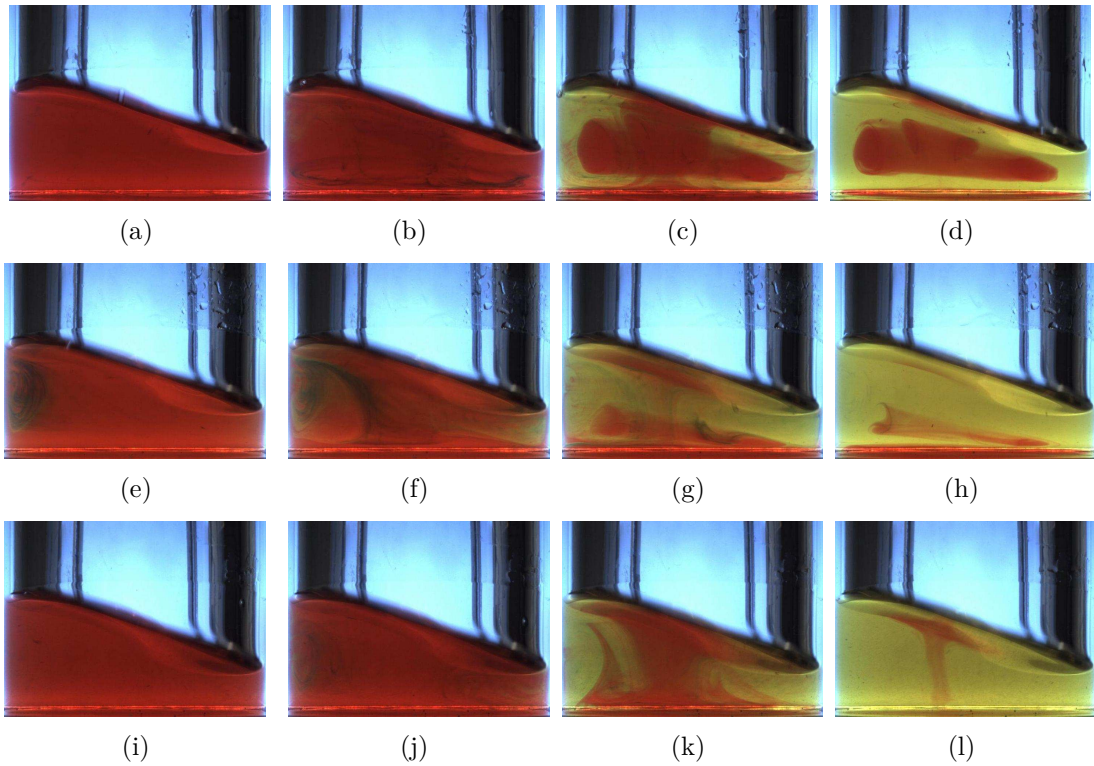


Figure 5.3: Time evolution of the mixing dynamics inside the  $d_i=100$  mm bioreactor for a glycerol solution of viscosity  $\nu=1.37 \times 10^{-5} \text{ m}^2\text{s}^{-1}$  for three speeds; (a-d)  $N=110$  RPM, (e-h)  $N=112$  RPM, (i-l)  $N=115$  RPM. ( $h/d_i=0.32$ ,  $d_o/d_i=0.25$ ).

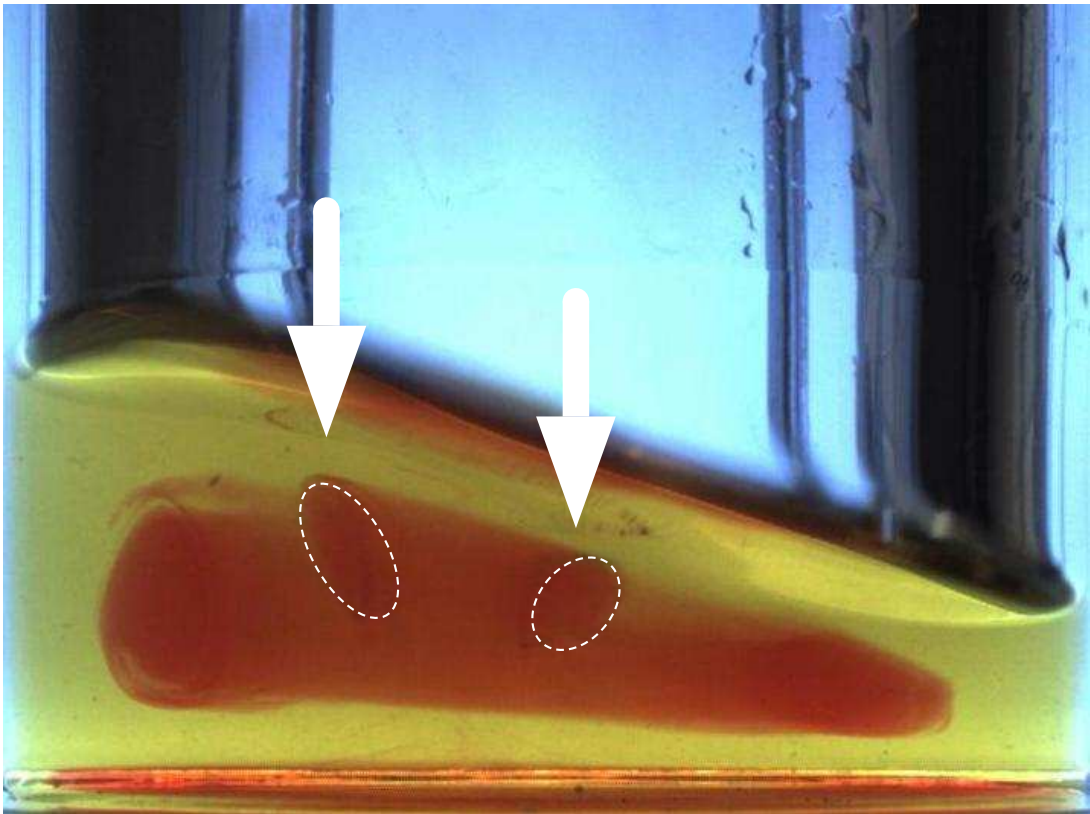


Figure 5.4: Detail of Figure 5.3 (d), showing the location of secondary vortical cells.

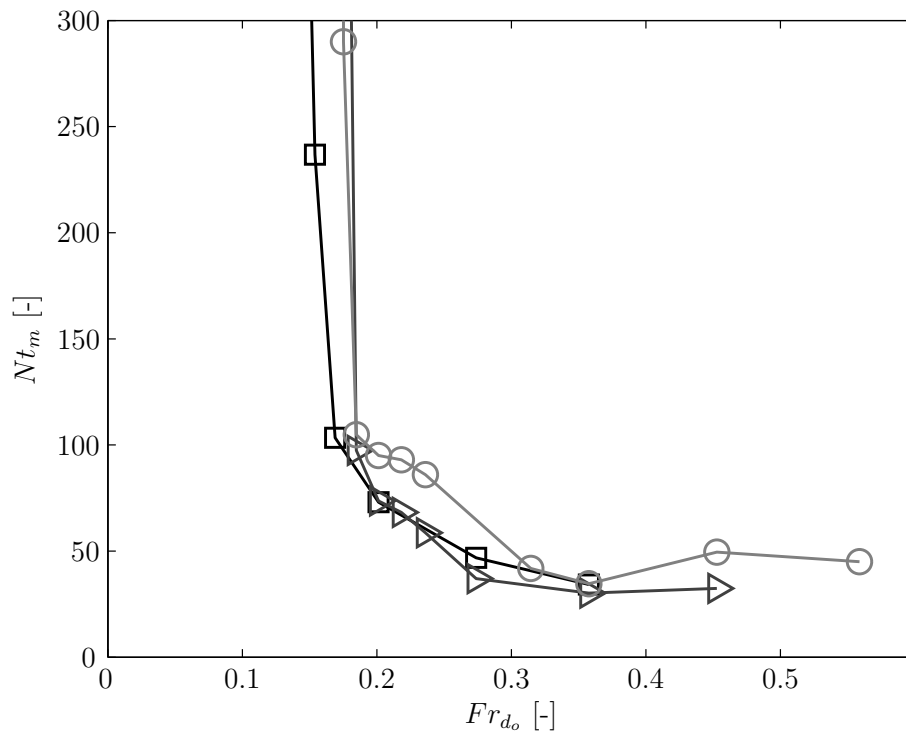


Figure 5.5: Variation of mixing number,  $Nt_m$ , with increasing Froude for fluids of different viscosity: ( $\square$ )  $\nu=1.9 \times 10^{-6} \text{ m}^2 \text{ s}^{-1}$ , ( $\triangleright$ )  $\nu=4.37 \times 10^{-6} \text{ m}^2 \text{ s}^{-1}$  and ( $\circ$ )  $\nu=1.37 \times 10^{-5} \text{ m}^2 \text{ s}^{-1}$ .

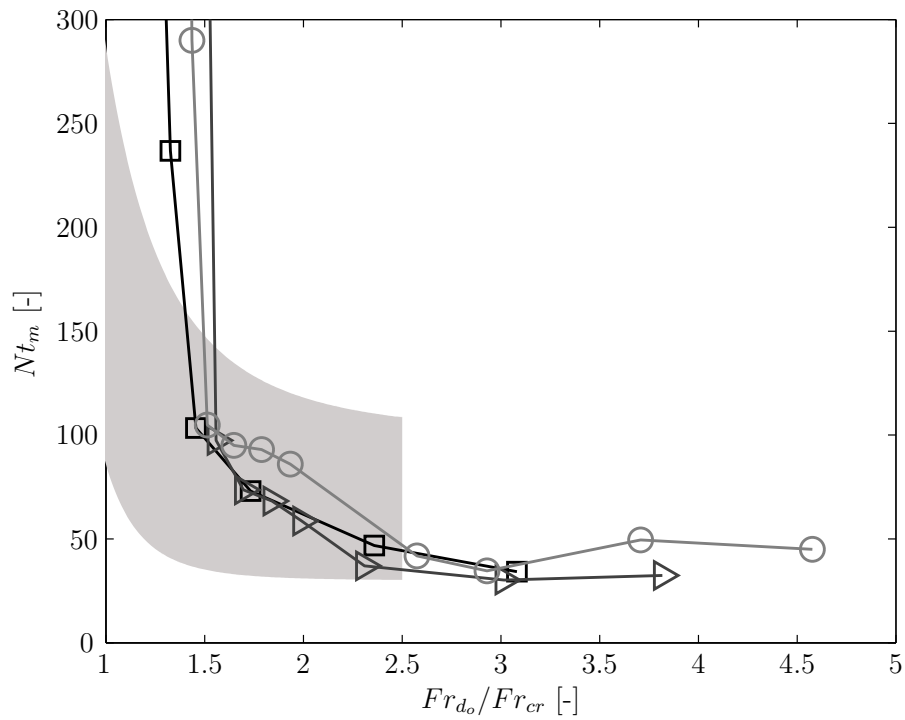


Figure 5.6: Variation of mixing number,  $Nt_m$ , with  $Fr_{d_o}/Fr_{c_r}$  for fluids of different viscosity: ( $\square$ )  $\nu=1.9 \times 10^{-6} \text{ m}^2 \text{ s}^{-1}$ , ( $\triangleright$ )  $\nu=4.37 \times 10^{-6} \text{ m}^2 \text{ s}^{-1}$  and ( $\circ$ )  $\nu=1.37 \times 10^{-5} \text{ m}^2 \text{ s}^{-1}$ . Shaded area representing mixing numbers for water-like fluids (see Figure 3.28).

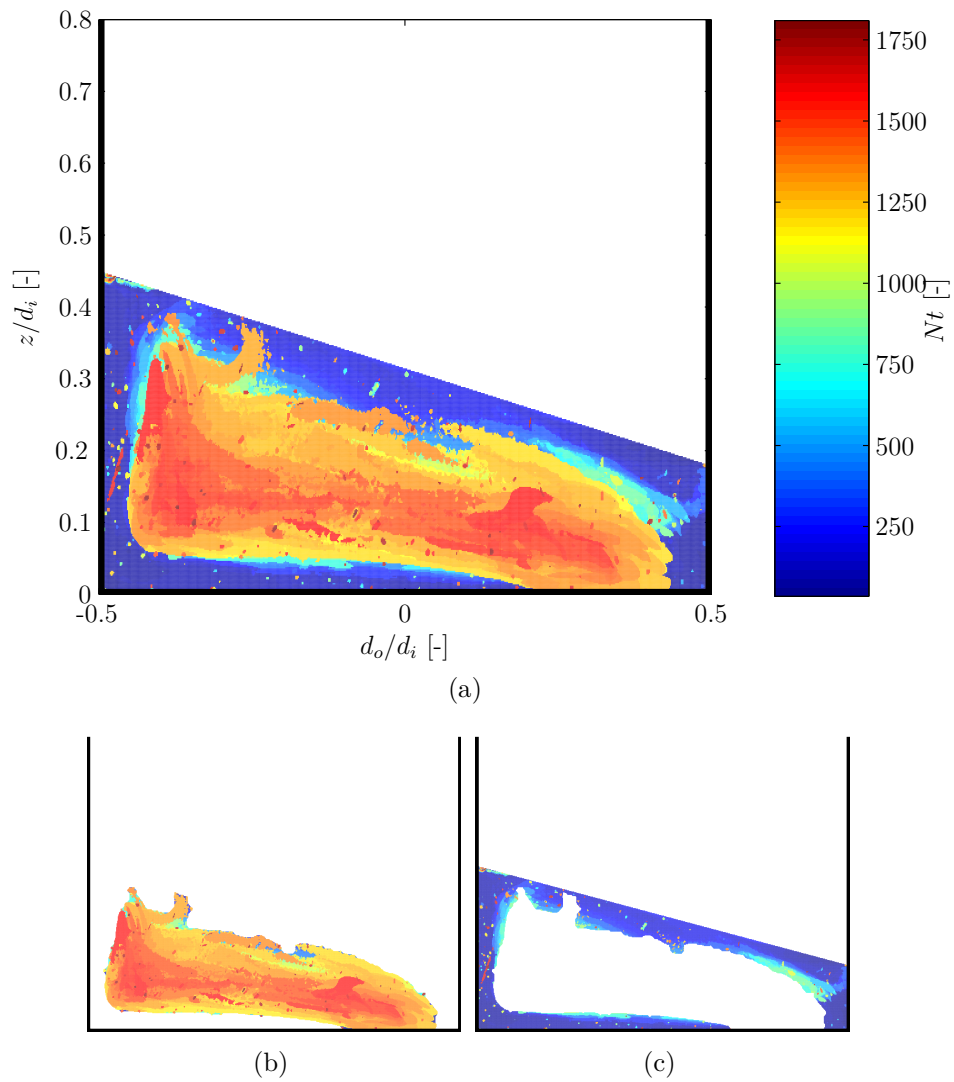


Figure 5.7: Mixing time map of a  $d_i=100$  mm bioreactor for glycerol solution  $\nu=4.37 \times 10^{-6} \text{ m}^2\text{s}^{-1}$ ,  $h/d_i=0.32$ ,  $d_o/d_i=0.25$ ,  $N=110$  RPM (a) whole field of view, (b) slow mixing region, (c) fast mixing region.

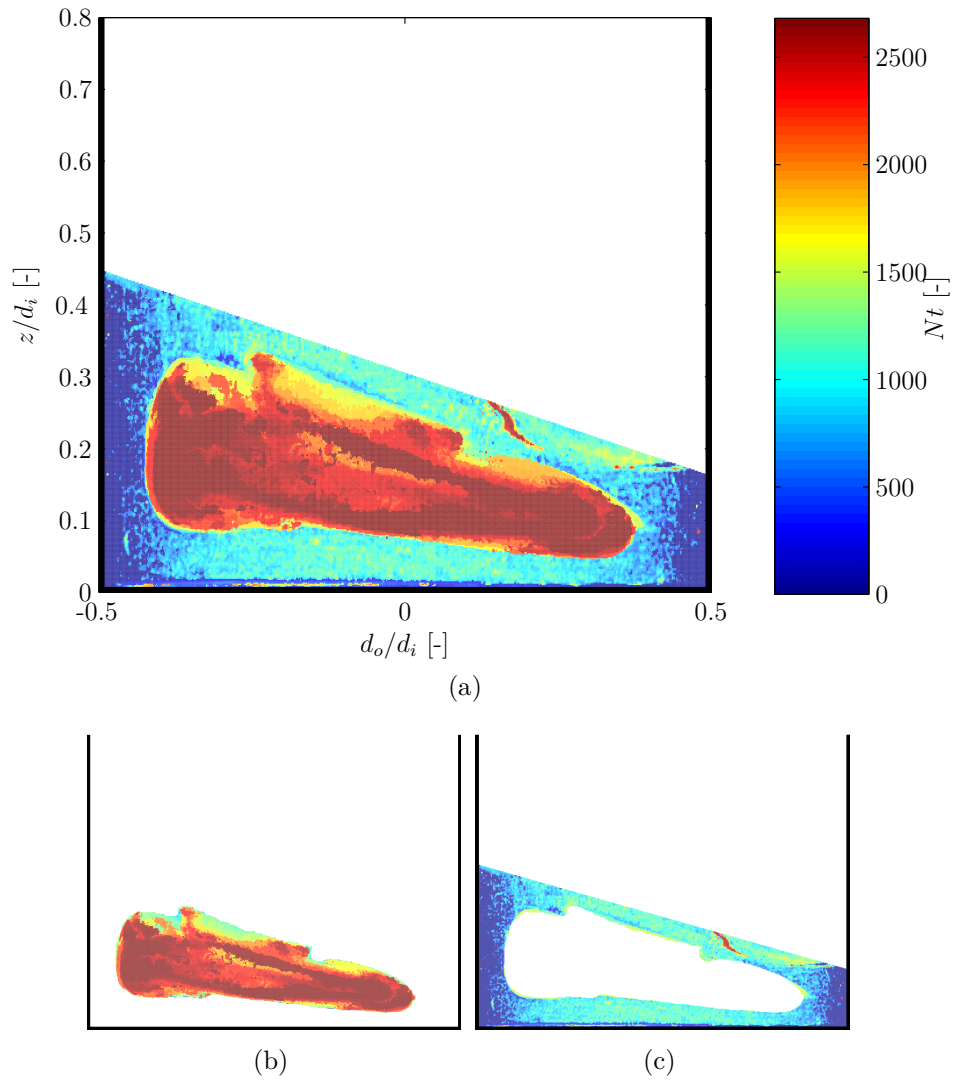


Figure 5.8: Mixing time map of a  $d_i=100$  mm bioreactor for glycerol solution  $\nu=1.37 \times 10^{-5} \text{ m}^2\text{s}^{-1}$ ,  $h/d_i=0.32$ ,  $d_o/d_i=0.25$ ,  $N=110$  RPM (a) whole field of view, (b) slow mixing region, (c) fast mixing region.

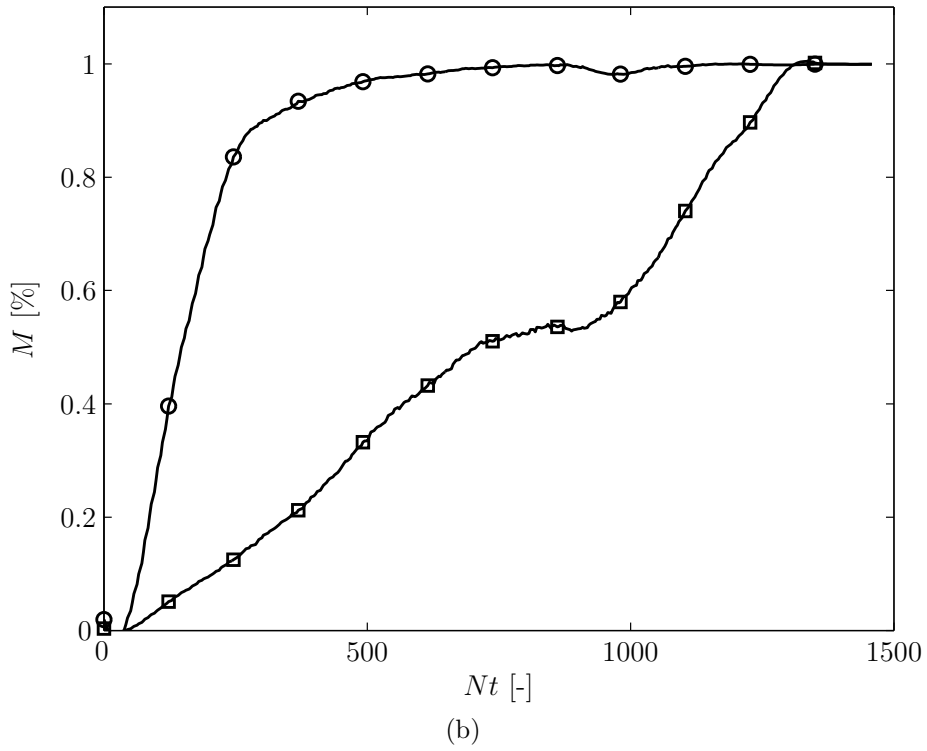
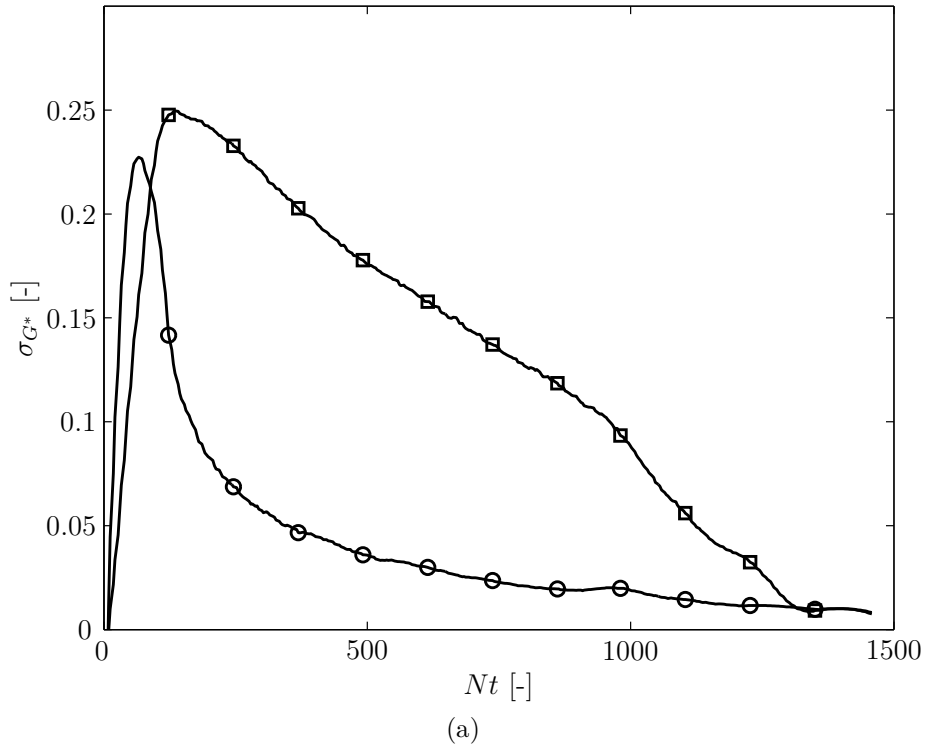


Figure 5.9: Variation in time of the (a) standard deviation of the Green channel output,  $\sigma_{G^*}$ , and of (b) the percentage of mixed pixels,  $M$ , in the ( $\square$ ) slow mixing and ( $\circ$ ) fast mixing regions. All data are for  $d_o=100$  mm,  $\nu=4.37 \times 10^{-6}$ ,  $h/d_i=0.32$ ,  $d_o/d_i=0.25$ ,  $N=110$  RPM.

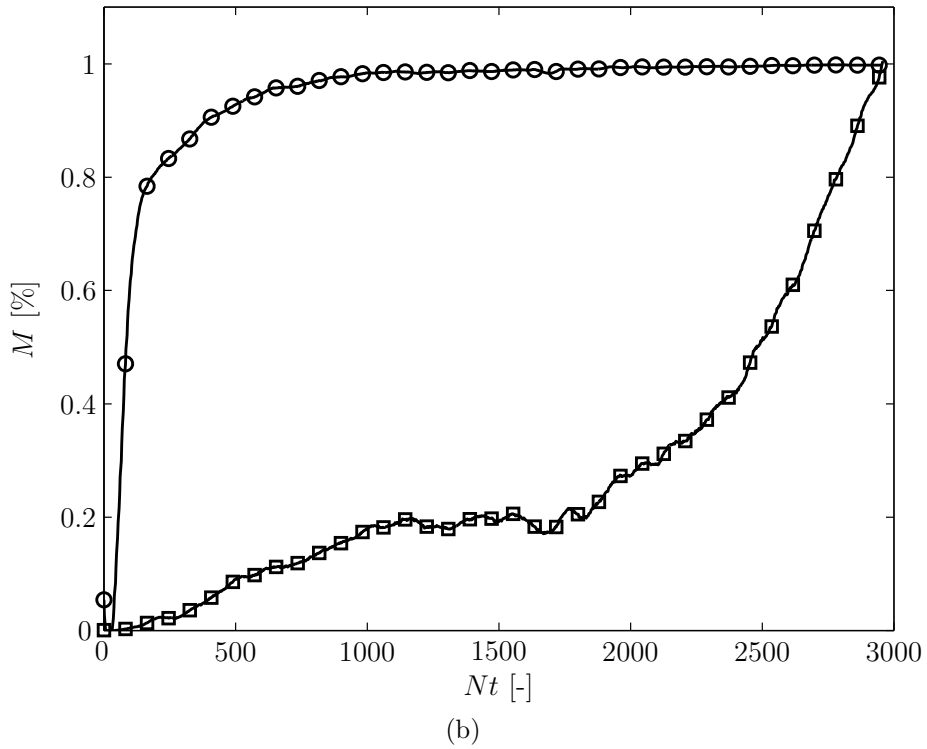
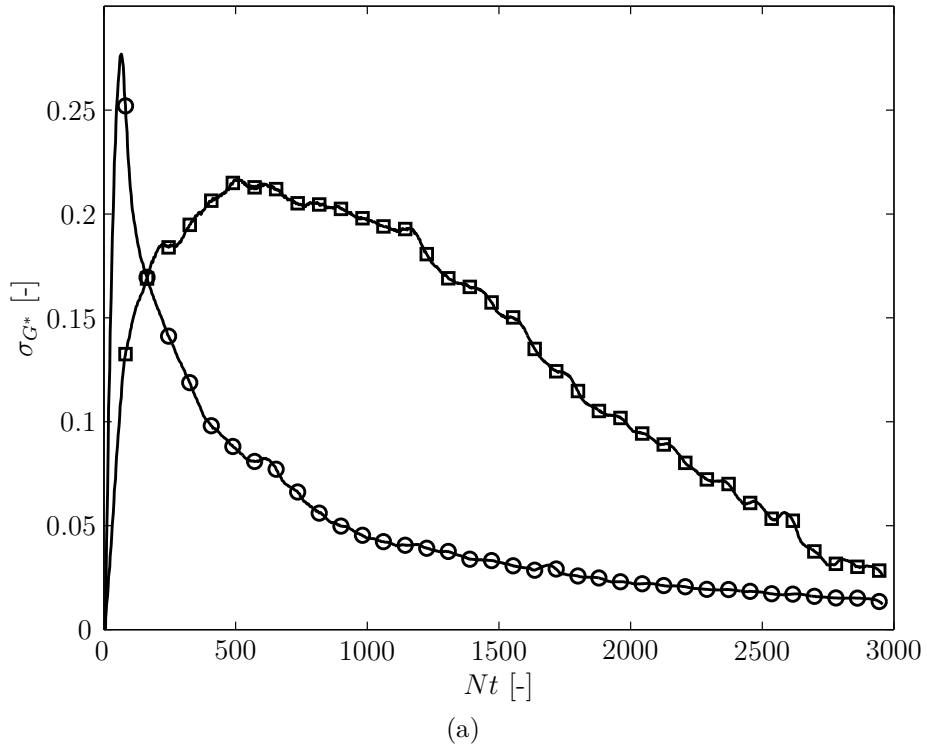
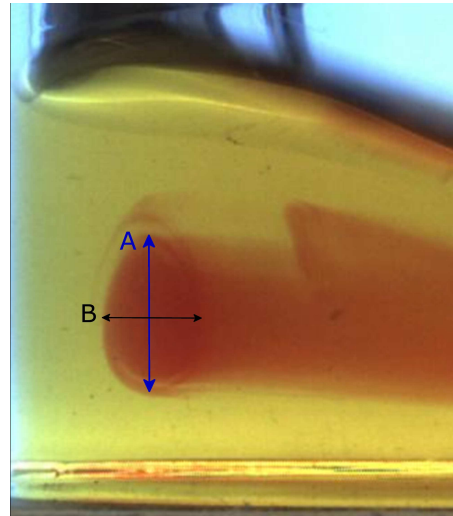
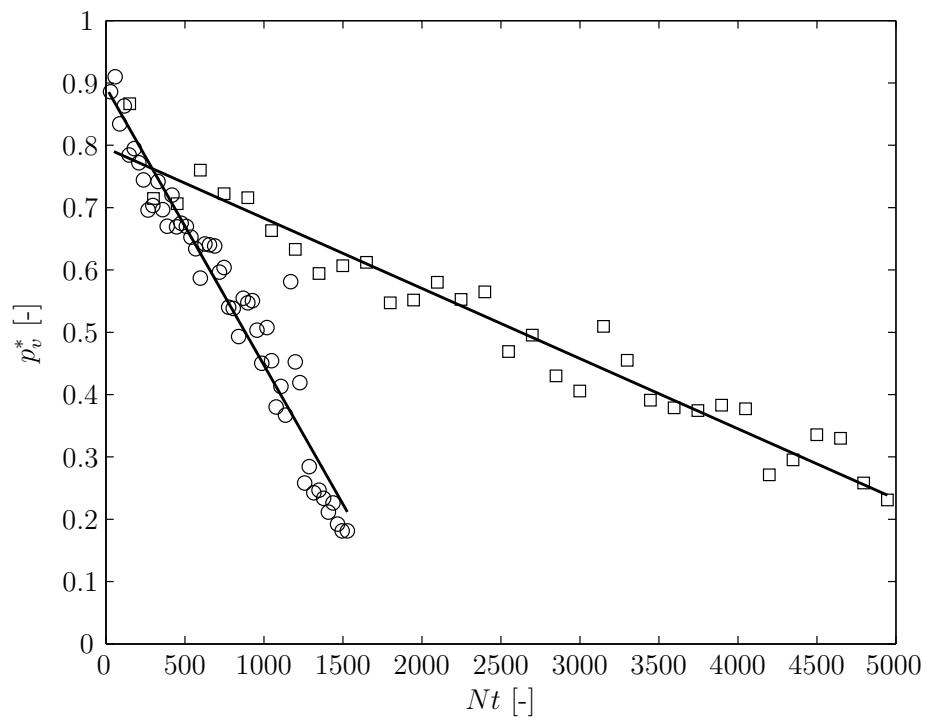


Figure 5.10: Variation in time of the (a) standard deviation of the Green channel output,  $\sigma_{G^*}$ , and of (b) the percentage of mixed pixels,  $M$ , in the ( $\square$ ) slow mixing and ( $\circ$ ) fast mixing regions. All data are for  $d_o=100$  mm,  $\nu=1.37 \times 10^{-5}$ ,  $h/d_i=0.32$ ,  $d_o/d_i=0.25$ ,  $N=110$  RPM.



(a)



(b)

Figure 5.11: (a) Visualisation of the major and minor axis of the elliptical cross-section of the LHS vortical cell. (b) Time evolution of the normalised perimeter of the vortical cell with linear fit for: (○)  $\nu=4.37 \times 10^{-6}$ ; (□)  $\nu=1.37 \times 10^{-5}$  ( $d_o=100$  mm,  $h/d_i=0.32$ ,  $d_o/d_i=0.25$ ,  $N=110$  RPM).

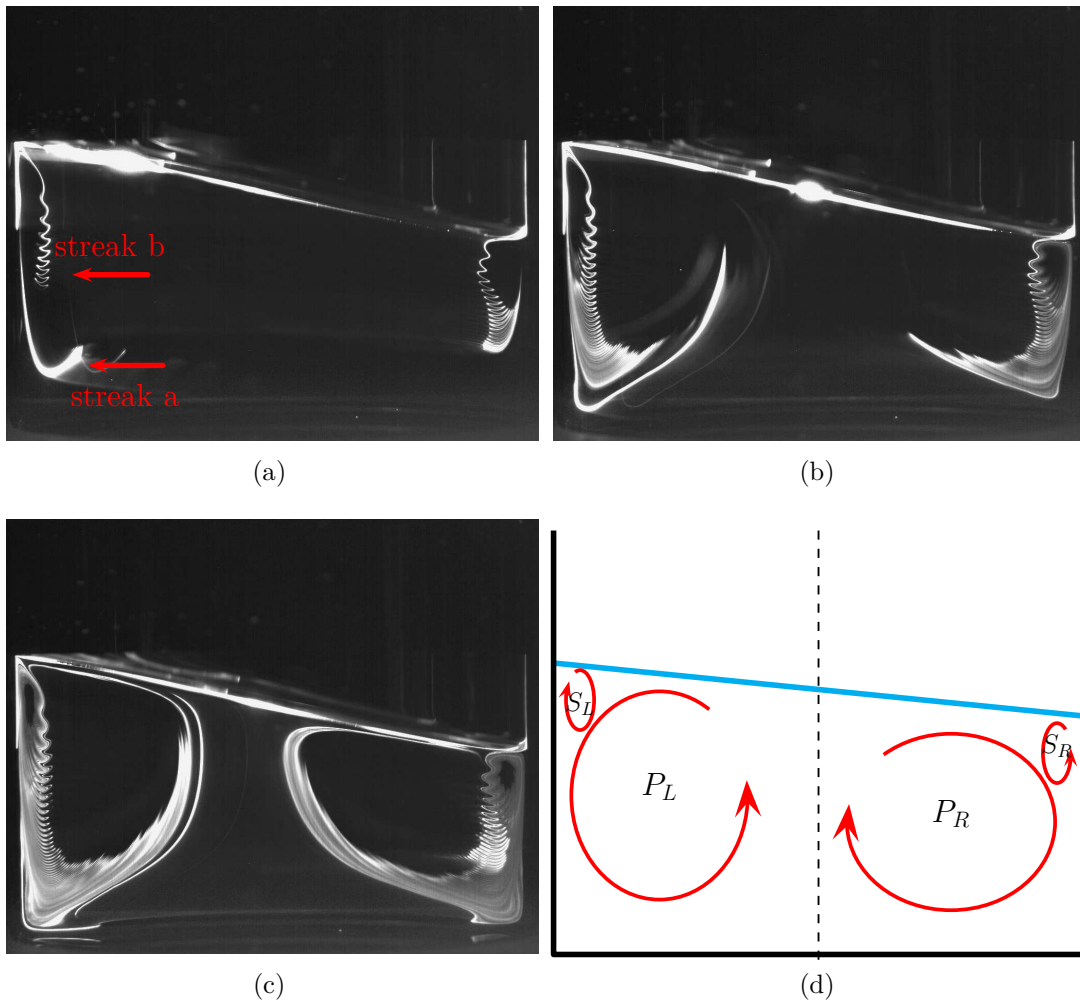


Figure 5.12: pLIF images of the cylindrical OSR, for  $d_i=100$  mm ,  $\nu=1.37 \times 10^{-5}$   $\text{m}^2\text{s}^{-1}$ ,  $h/d_i=0.5$ ,  $d_o/d_i=0.5$ ,  $N=80$  RPM: (a)  $Nt=63$ , (b)  $Nt=105$ , (c)  $Nt=150$ . (d) Schematic diagram of the flow configuration.

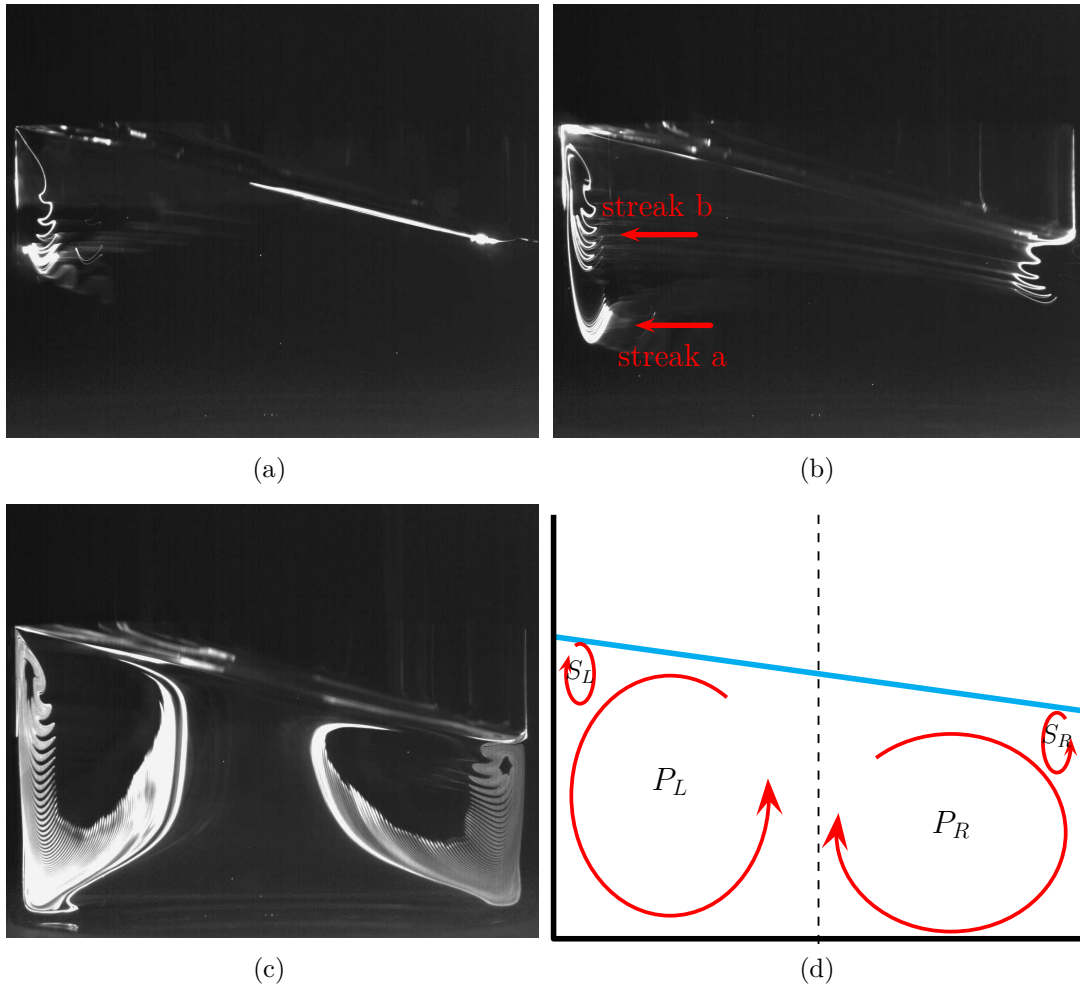


Figure 5.13: pLIF images of the cylindrical OSR, for  $d_i=100$  mm ,  $\nu=1.37 \times 10^{-5}$   $\text{m}^2\text{s}^{-1}$ ,  $h/d_i=0.5$ ,  $d_o/d_i=0.5$ ,  $N=85$  RPM: (a)  $Nt=20$ , (b)  $Nt=31$ , (c)  $Nt=93$ . (d) Schematic diagram of the flow configuration.

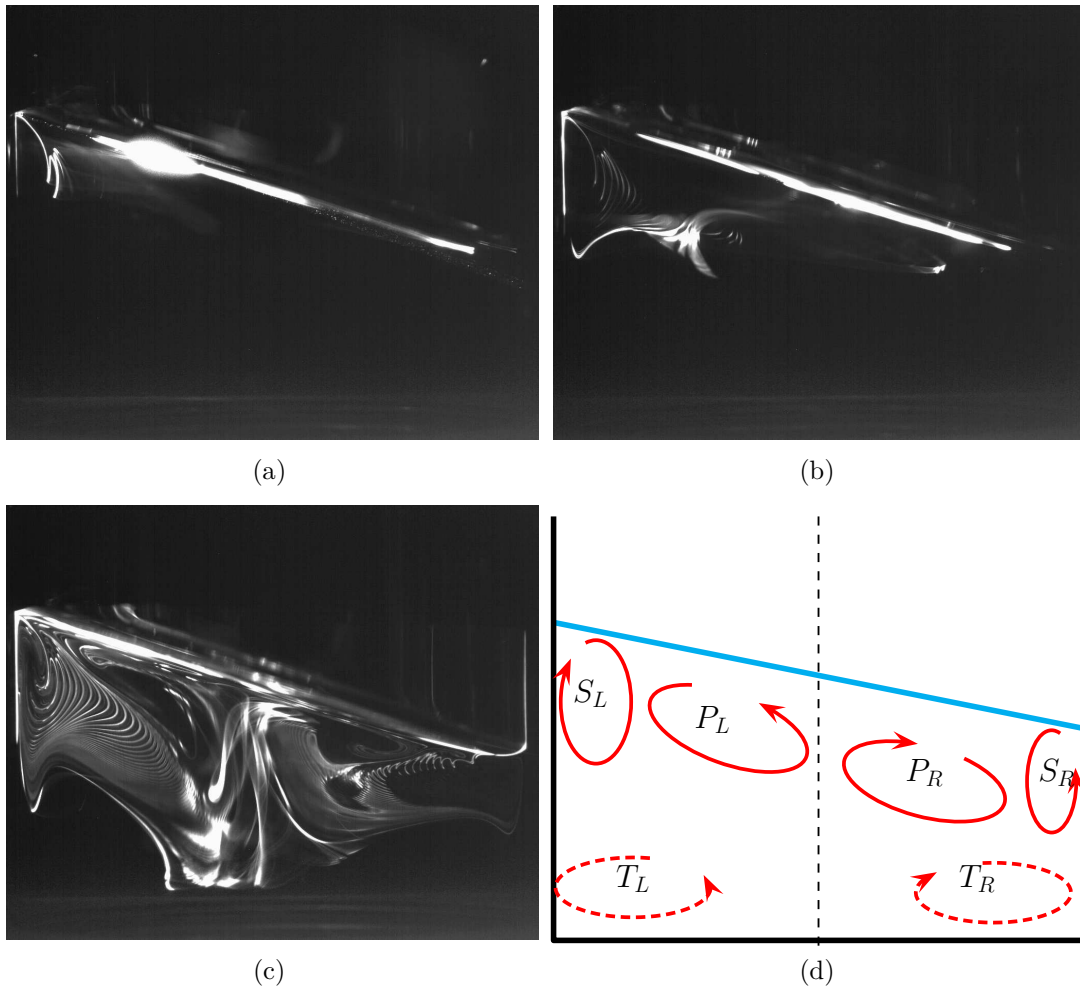


Figure 5.14: pLIF images of the cylindrical OSR, for  $d_i=100$  mm ,  $\nu=1.37 \times 10^{-5}$   $\text{m}^2\text{s}^{-1}$ ,  $h/d_i=0.5$ ,  $d_o/d_i=0.5$ ,  $N=90$  RPM: (a)  $Nt=33$ , (b)  $Nt=44$ , (c)  $Nt=108$ . (d) Schematic diagram of the flow configuration.

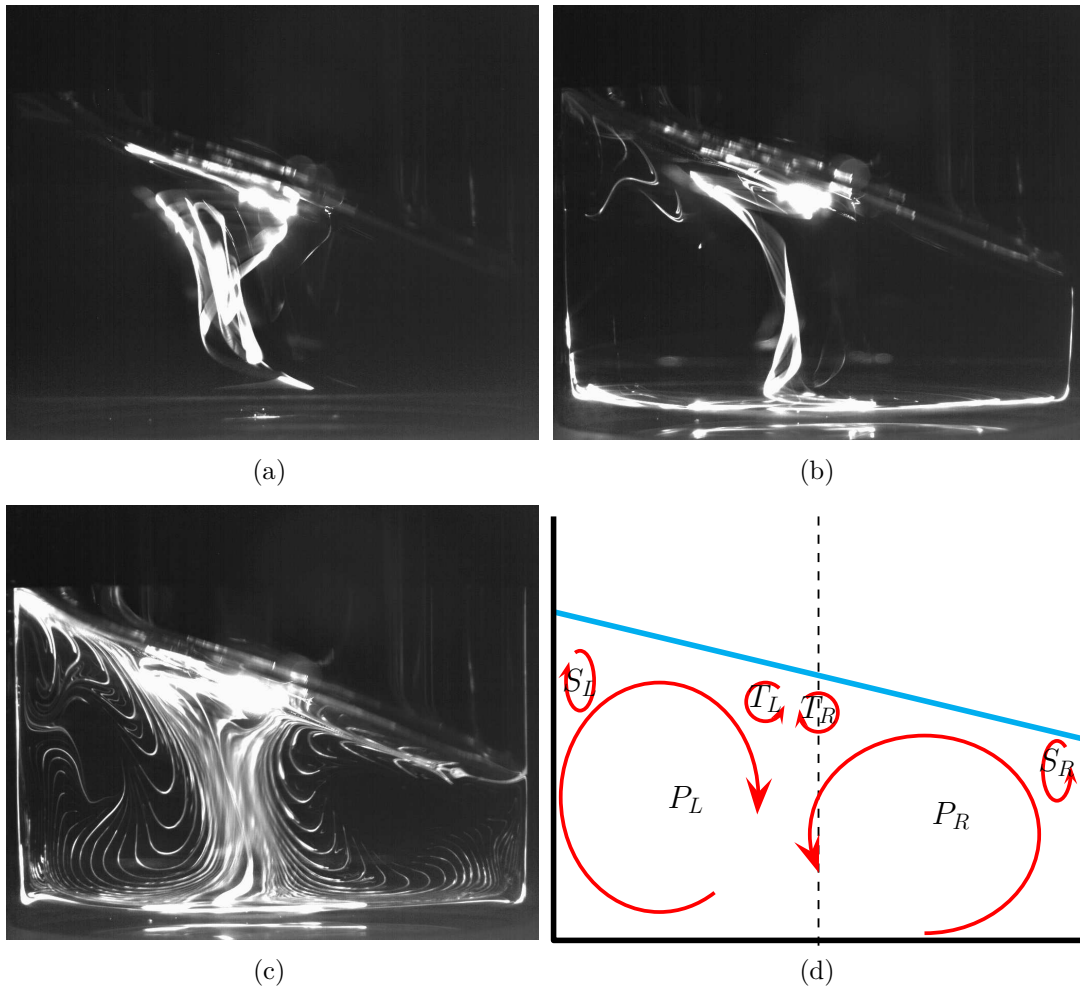


Figure 5.15: pLIF images of the cylindrical OSR, for  $d_i=100$  mm ,  $\nu=1.37 \times 10^{-5}$   $\text{m}^2\text{s}^{-1}$ ,  $h/d_i=0.5$ ,  $d_o/d_i=0.5$ ,  $N=100$  RPM: (a)  $Nt=37$ , (b)  $Nt=62$ , (c)  $Nt=93$ . (d) Schematic diagram of the flow configuration.

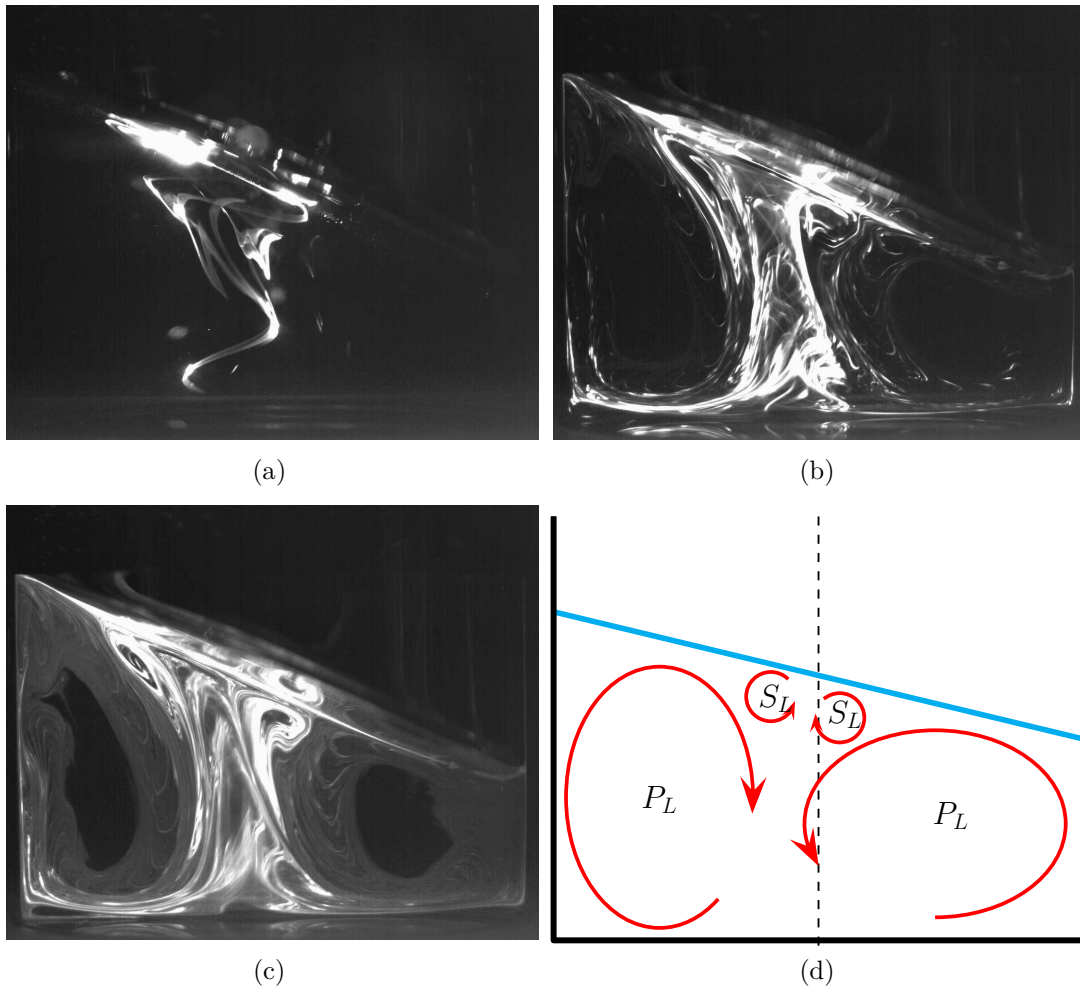
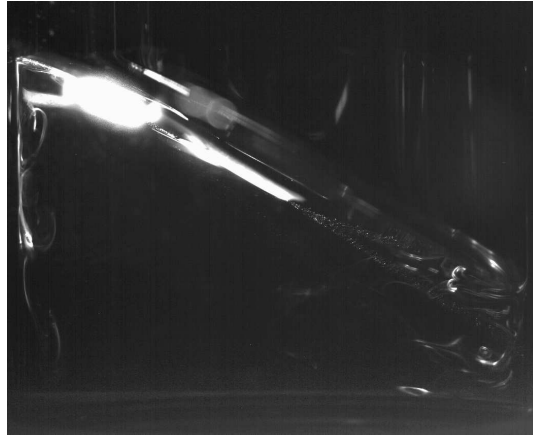


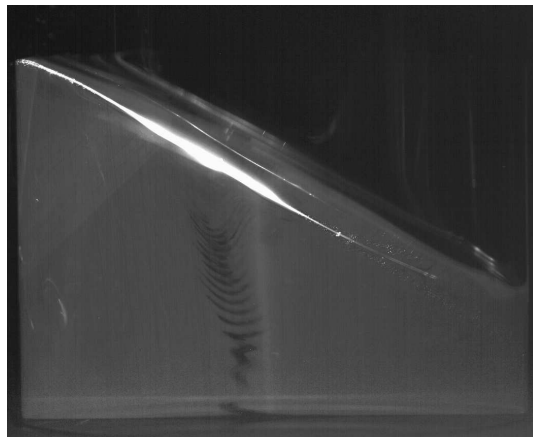
Figure 5.16: pLIF images of the cylindrical OSR, for  $d_i=100$  mm ,  $\nu=1.37 \times 10^{-5}$   $\text{m}^2\text{s}^{-1}$ ,  $h/d_i=0.5$ ,  $d_o/d_i=0.5$ ,  $N=105$  RPM: (a)  $Nt=21$ , (b)  $Nt=74$ , (c)  $Nt=182$ . (d) Schematic diagram of the flow configuration.



(a)



(b)



(c)

Figure 5.17: pLIF images of the cylindrical OSR, for  $d_i=100$  mm ,  $\nu=1.37 \times 10^{-5}$   $\text{m}^2\text{s}^{-1}$ ,  $h/d_i=0.5$ ,  $d_o/d_i=0.5$ ,  $N=115$  RPM: (a)  $Nt=9$ , (b)  $Nt=16$ , (c)  $Nt=62$ .

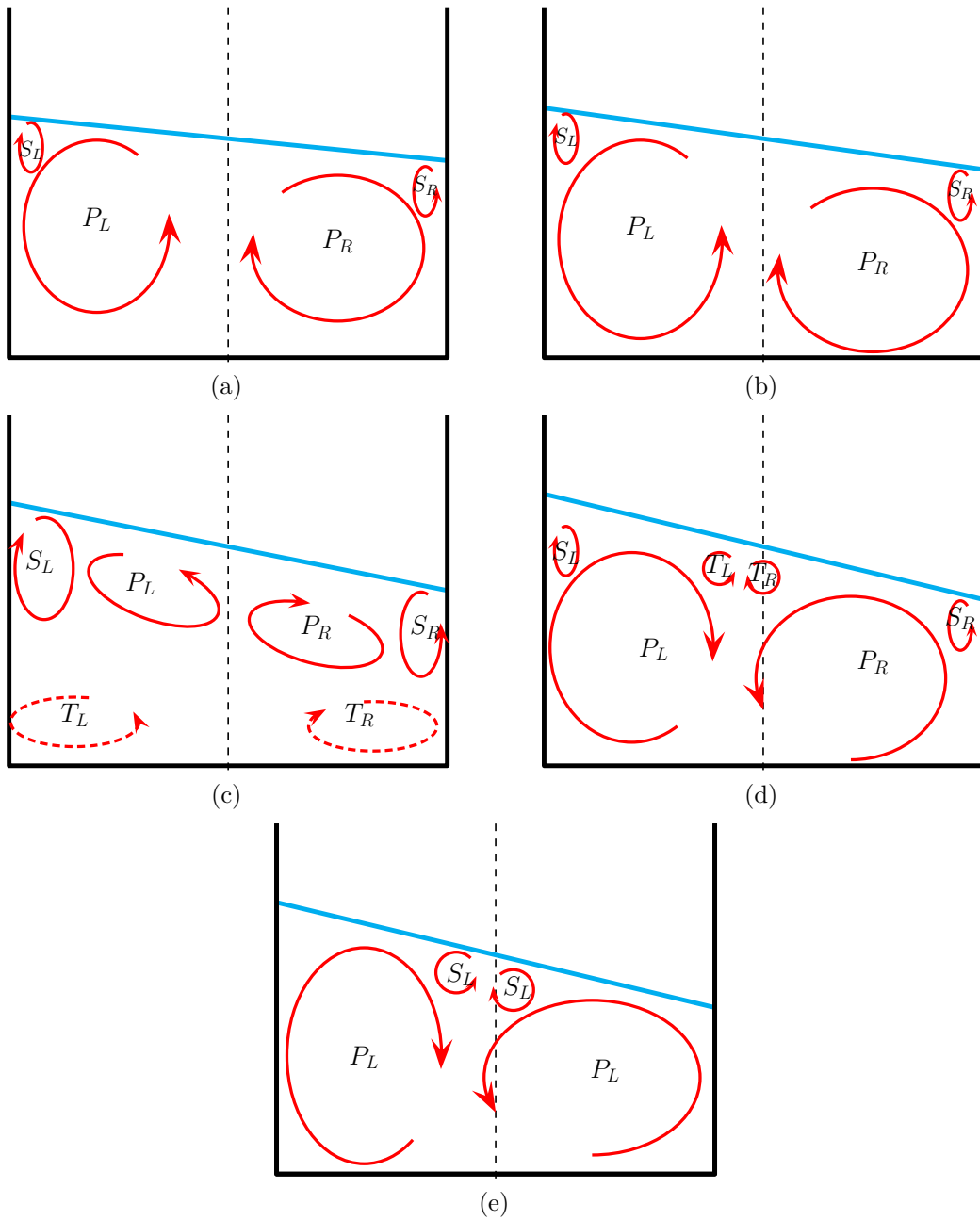


Figure 5.18: Schematic diagrams of the flow structures observed from the pLIF images for  $\nu=1.37 \times 10^{-5} \text{ m}^2\text{s}^{-1}$  at different  $N$ : (a) 80 RPM, (b) 85 RPM, (c) 90 RPM, (d) 100 RPM, (e) 105 RPM.

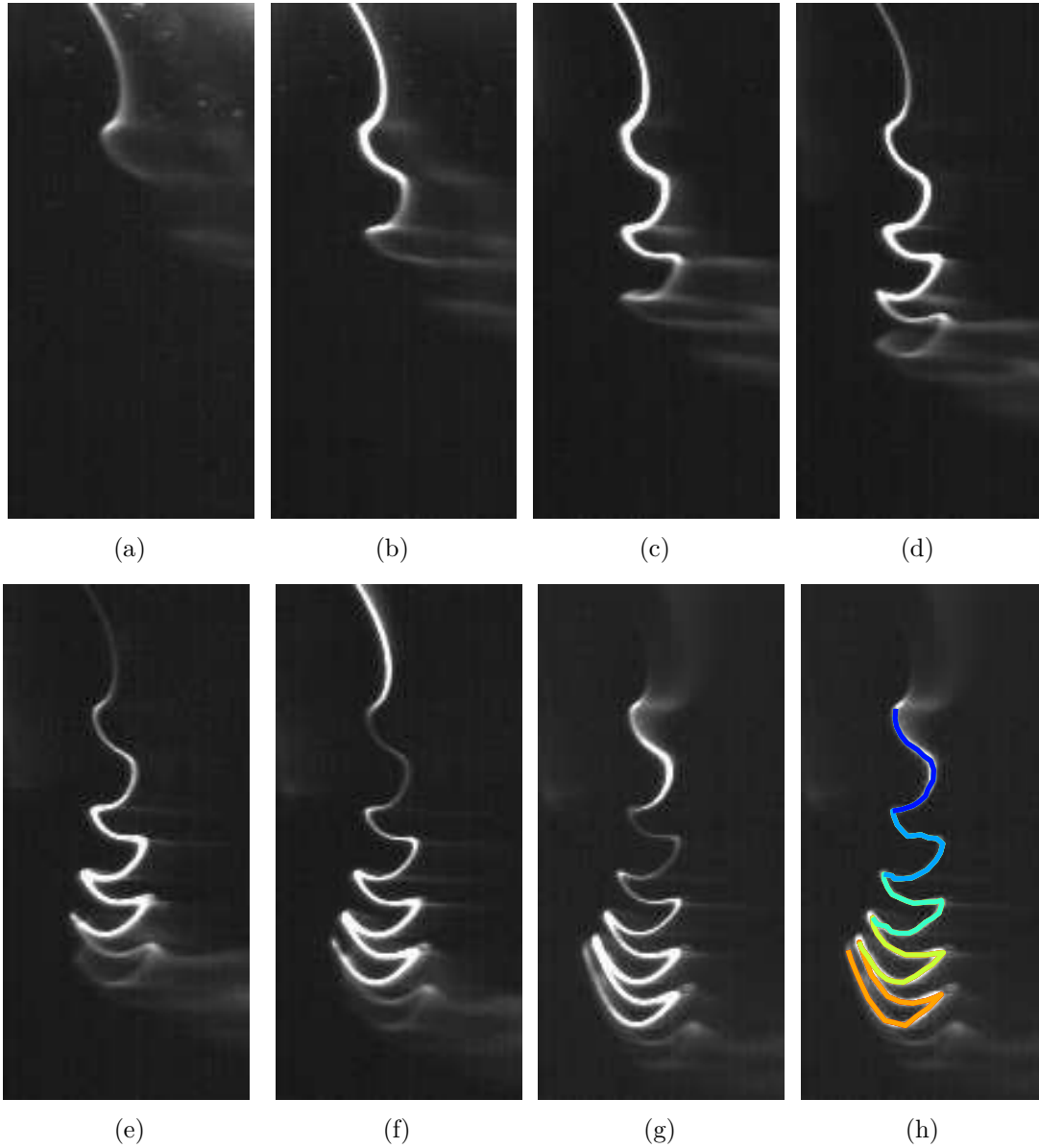


Figure 5.19: Detail of the elongation of Rhodamine dye on the LHS of a  $d_i=100$  mm OSR, glycerol solution  $\nu=1.37 \times 10^{-5} \text{ m}^2\text{s}^{-1}$ ,  $h/d_i=0.5$ ,  $d_o/d_i=0.5$   $N=80$  RPM: (a-g)  $Nt=25-31$ . (h) Elongation of material lines per shaker revolution, with the colour change indicating each complete revolution.

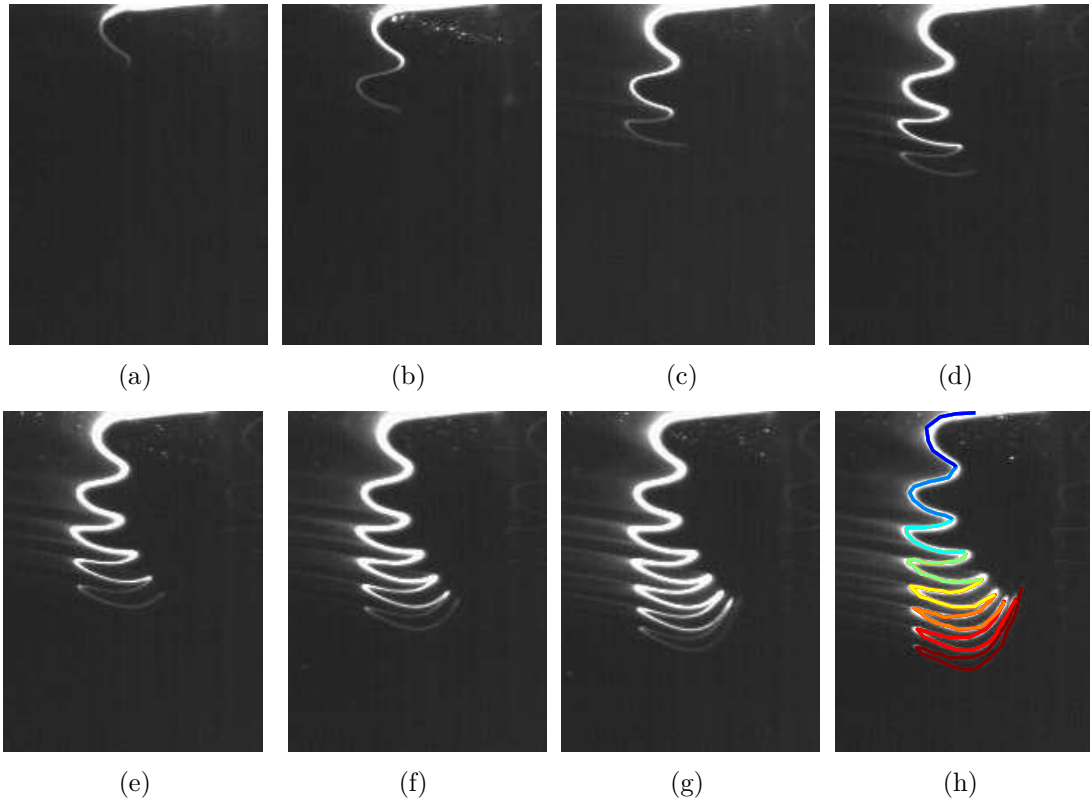


Figure 5.20: Detail of the elongation of Rhodamine dye on the RHS of a  $d_i=100$  mm OSR, glycerol solution  $\nu=1.37 \times 10^{-5}$  m<sup>2</sup>s<sup>-1</sup>,  $h/d_i=0.5$ ,  $d_o/d_i=0.5$   $N=80$  RPM: (a-g)  $Nt=42-48$ . (h) Elongation of material lines per shaker revolution, with the colour change indicating each complete revolution.

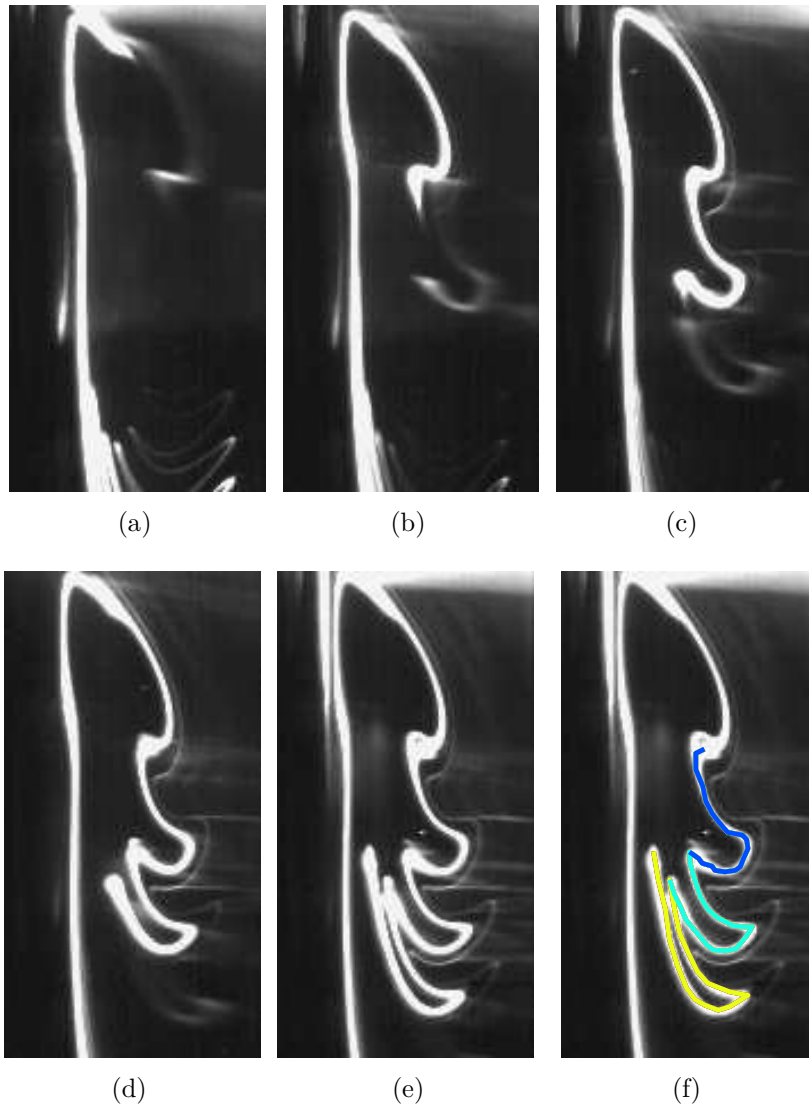


Figure 5.21: Detail of the elongation of Rhodamine dye on the LHS of a  $d_i=100$  mm OSR, glycerol solution  $\nu=1.37 \times 10^{-5} \text{ m}^2\text{s}^{-1}$ ,  $h/d_i=0.5$ ,  $d_o/d_i=0.5$   $N=85$  RPM: (a-e)  $Nt=26-30$ . (f) Elongation of material lines per shaker revolution, with the colour change indicating each complete revolution.

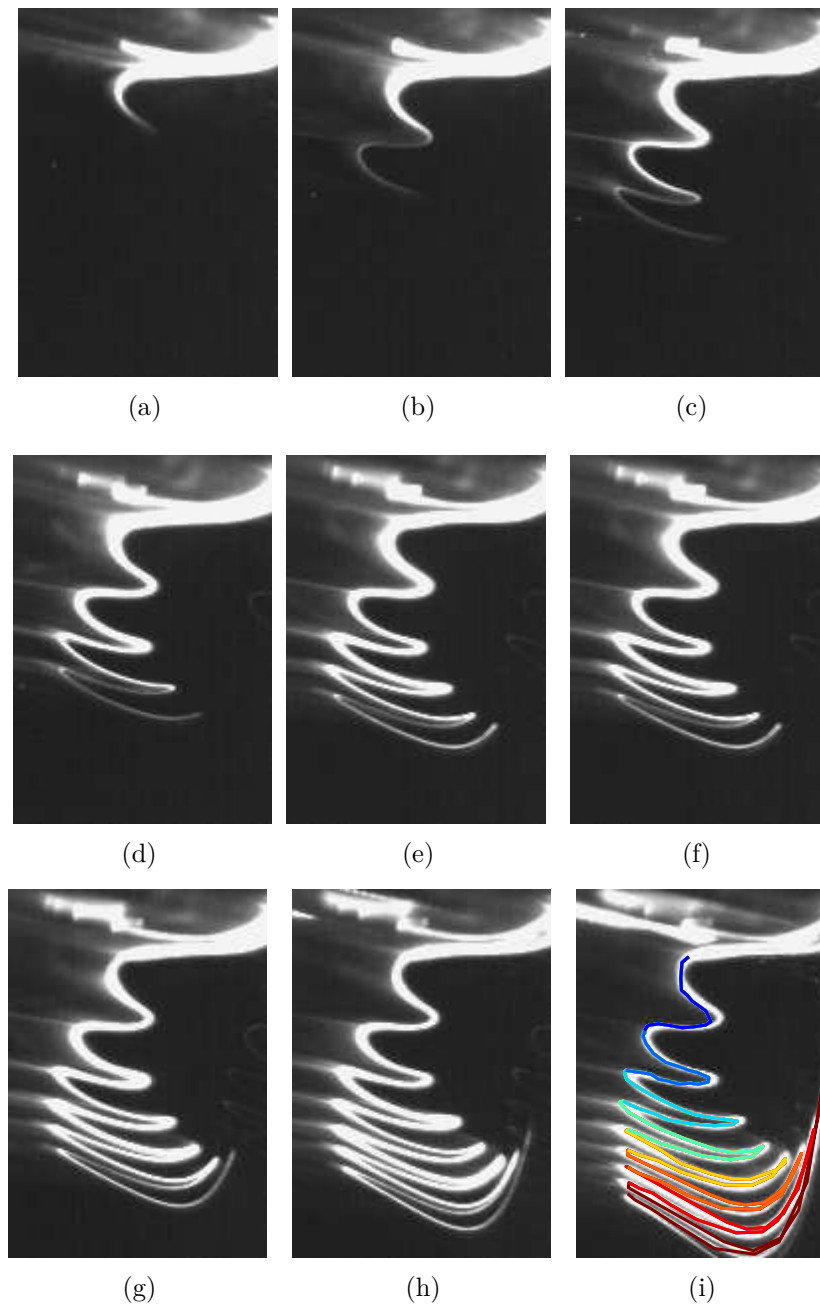


Figure 5.22: Detail of the elongation of Rhodamine dye on the RHS of a  $d_i=100$  mm OSR, glycerol solution  $\nu=1.37 \times 10^{-5} \text{ m}^2\text{s}^{-1}$ ,  $h/d_i=0.5$ ,  $d_o/d_i=0.5$   $N=85$  RPM: (a-h)  $Nt=28-35$ . (i) Elongation of material lines per shaker revolution, with the colour change indicating each complete revolution.

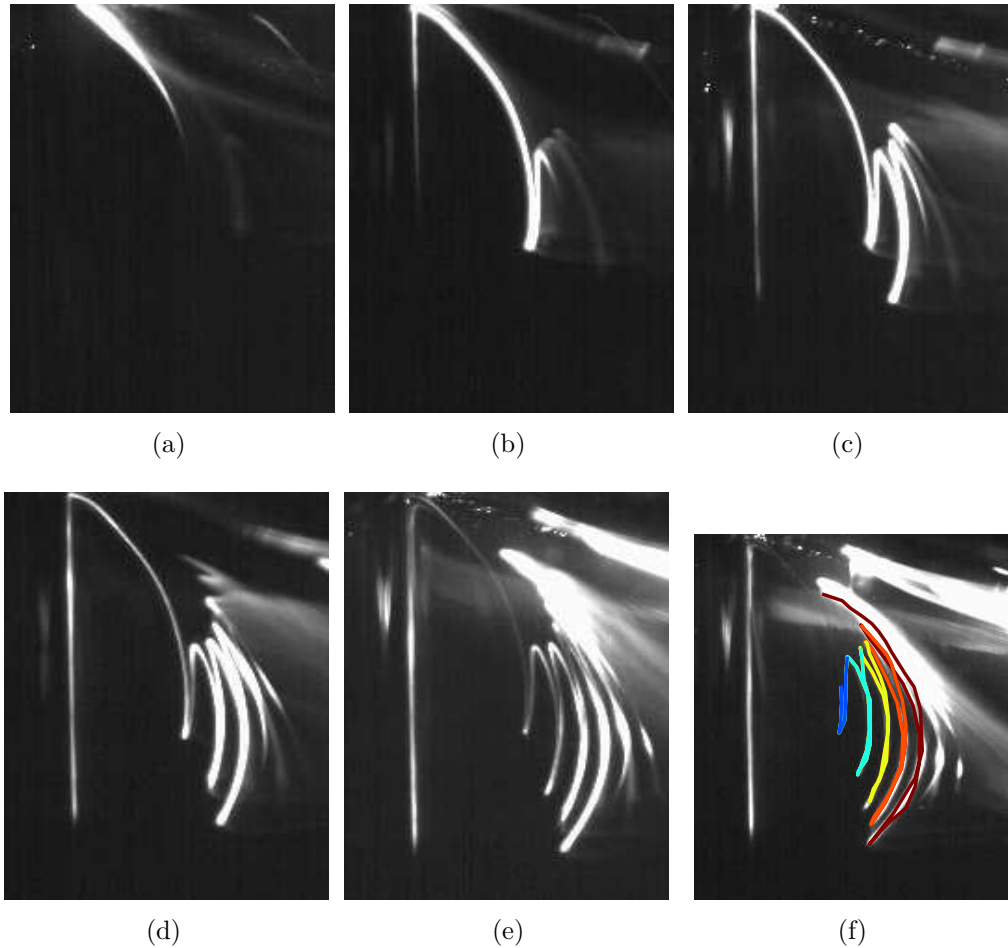


Figure 5.23: Detail of the elongation of Rhodamine dye on the LHS of a  $d_i=100$  mm OSR, glycerol solution  $\nu=1.37 \times 10^{-5} \text{ m}^2\text{s}^{-1}$ ,  $h/d_i=0.5$ ,  $d_o/d_i=0.5$ ,  $N=90$  RPM: (a-e)  $Nt=31-35$ . (f) Elongation of material lines per shaker revolution, with the colour change indicating each complete revolution.

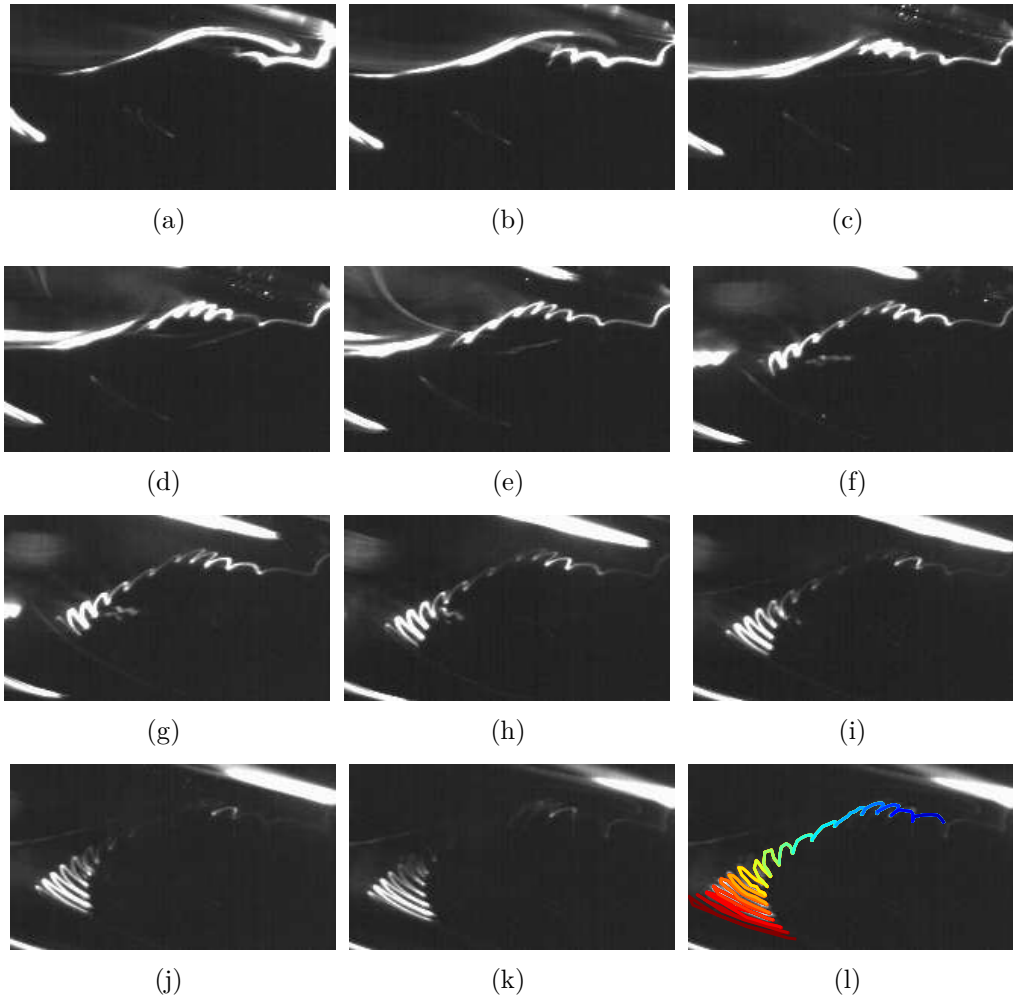
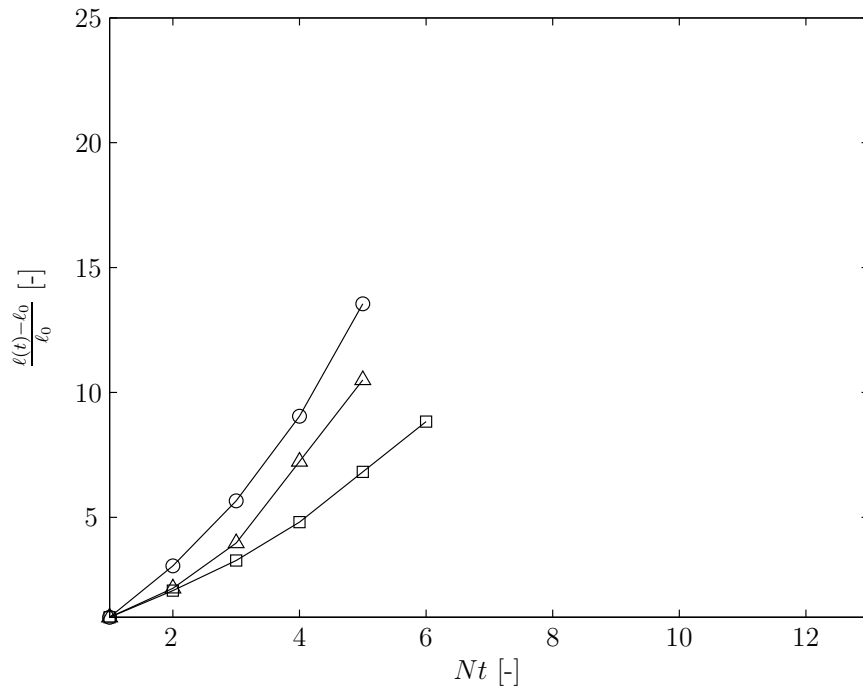
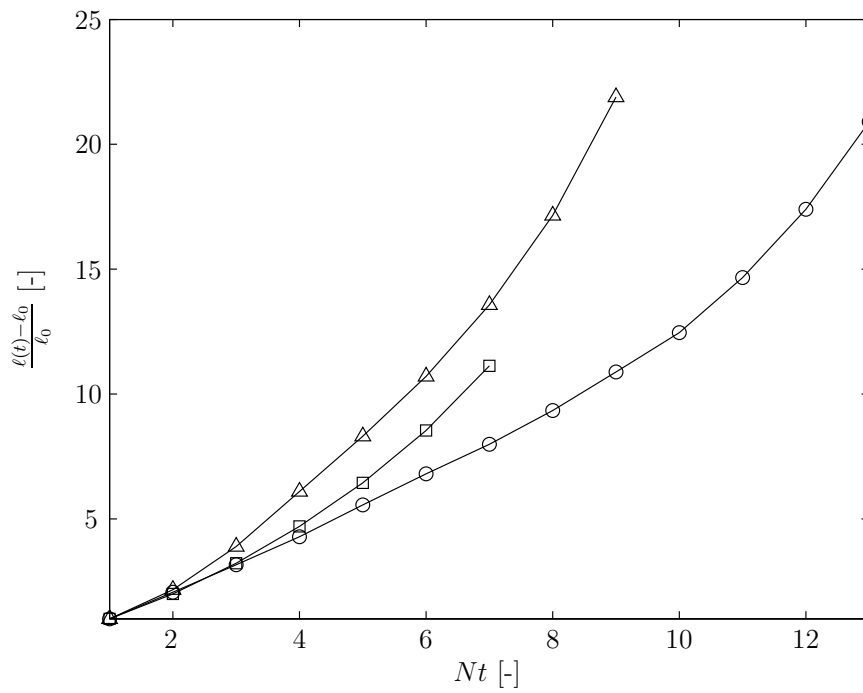


Figure 5.24: Detail of the elongation of Rhodamine dye on the RHS of  $d_i=100$  mm OSR, glycerol solution  $\nu=1.37 \times 10^{-5} \text{ m}^2\text{s}^{-1}$ ,  $h/d_i=0.5$ ,  $d_o/d_i=0.5$   $N=90$  RPM: (a-k)  $Nt=49-59$ . (l) Elongation of material lines per shaker revolution, with the colour change indicating each complete revolution.



(a)



(b)

Figure 5.25: Evolution in time of the material line growth ratio,  $\frac{\ell(t)-\ell_0}{\ell_0}$  for the (a) LHS of bioreactor; (b) RHS of bioreactor: ( $\square$ )  $N=80$  RPM, ( $\triangle$ )  $N=85$  RPM and ( $\circ$ )  $N=90$  RPM.

# Chapter 6

## Conclusions and recommendations for future work

### 6.1 The present contribution

The major objective of the research presented in this thesis was to provide a detailed analysis of the flow, mixing and suspension dynamics of orbitally shaken bioreactors for the improvement of scale-up methodologies of biopharmaceuticals manufacturing. The research has been organised in such a way to provide a detailed account of each aspect under consideration, to present the potential improvements achievable from the thorough understanding of the phenomena and establish a framework to successfully implement scale-up. Quantification of the mixing dynamics was provided by means of the Dual Indicator System for Mixing Time with the purposely developed code and post-processing analysis, thus establishing an accurate and objective estimation methodologies to obtain

mixing time information in OSRs. Phase-resolved Particle Image Velocimetry was employed to determine the flow velocity field, vorticity and kinetic energy content. Solid suspension studies shed light on the suspension efficiency of OSRs and for the first time, to the best of the author's knowledge, an effort was made to relate the suspended conditions to the flow pattern using dimensionless parameters.

In the first stages of this work a mixing time colorimetric method (DISMT) based on the fast acid/base reaction in the presence of pH indicators, applied in depth and results are analysed in depth towards the development of an image analysis algorithm able to provide an objective measure of mixing. In order to build confidence in the robustness of the methodology, details of the software are clearly described and results compared with those obtained using other mixing time estimation methods. The DISMT and image processing software are then employed to quantitatively measure mixing in OSRs operating at different conditions. The impact of feeding location is also investigated, leading to the conclusion that a careful selection of feed insertion positioning must be made to fully exploit the features of the flow in shaken systems and significantly enhance mixing.

Building on the findings derived from the mixing time data, a scaling factor is proposed based on the critical  $Fr$  for flow transition. This scaling factor is employed to compare mixing time results measured in this work with those reported in the literature. The comparison, unsuccessful when made in dimensional terms due to significant differences in bioreactor size, geometry and mixing time estimation methodology, shows a very good agreement between results from different studies when dimensionless scaling factor is used.

Phase-resolved PIV is employed to evaluate the impact of a different bioreactor design on the flow, for fluids with water-like viscosity. PIV measurements validate flow characteristics previously reported in literature and provide a quantitative

analysis of the flow using the novel vessel bottom geometry. Phase-averaged velocity fields show that the conical bottom significantly affect the flow when the highest conical bottom is employed. A stronger circulation is observed in the flow, together with higher space averaged kinetic energy due to the conical bottom occupying the regions of otherwise slow moving fluid.

The impact of the observed improved circulation caused by the presence of a conical bottom is evaluated in terms of solid suspension. Cytodex 3 microcarriers, a 150 $\mu\text{m}$  particles commonly used for the cultivation of anchorage-dependant cells, are employed for suspension studies in OSRs. The method development includes a software component able to automate the image analysis thus removing operator subjectivity. The decision to focus on a vertical measurement plane, rather than horizontal, which was covering the whole field of view, is found to successfully determine not only the agitation necessary for solid suspension, but also to obtain solids distribution information on the whole flow field. The conical bottom geometry is found to facilitate suspension of the solids under a range of conditions, namely  $(h/d_i) > \sqrt{d_o/d_i}$  and  $(h/d_i) < \sqrt{d_o/d_i}$ .

DISMT and planar Laser Induced Fluorescent measurements are performed with high viscosity fluids, to investigate the flow characteristics of fluids representative of high density cell cultures. Glycerol solutions of viscosities equal to 2, 4 and 14 times that of water are selected. The DISMT results provide evidence of several flow transitions, occurring for highly viscous fluids over small increments of agitation rate. A novel flow configuration is revealed for highly viscous fluids, where the toroidal vortex would rotate in the opposite direction to what has been reported in water-like viscosity fluids. Micro-mixing characteristics are also investigated using phase-locked pLIF using glycerol solutions. The nature of the pLIF measurements provide a higher level of detail on the nature of the flow which had been missed in phase-averaged measurements and has not been reported in

the literature.

The main findings of the research are outlined in the following section. The chapter closes with recommendations for future work which are given in Section 6.3.

## 6.2 Main findings of the investigation

In the first stage, the image processing code was developed to accurately determine mixing time from DISMT experiments. It was found that the colour change in the fluid due to the acid-base reaction in presence of Thymol blue and Methyl red was best represented by the Green channel in the RGB colour map. A normalised value for the green channel was introduced to account for material defects in the experimental rig and light variations. The variation of the  $\sigma_{G^*}$ , reported in Equation 3.1 was used to measure the variation of colour homogeneity, proportional to the pH levels and hence the degree of mixing homogenisation. A coefficient of mixedness  $M$  was introduced to quantify how many pixels in each image had reached a value corresponding to a status of complete mixing. The mixing was defined as complete when the  $\sigma_{G^*}$  reached 95% of its steady state value and when  $M$  was above 95%. The  $\sigma_{G^*}$  algorithm provided an indication of the transient states of mixing at different experimental conditions, whilst the  $M$  algorithm provided a definite time at which the whole field volume of the fluid had mixed completely. The DISMT and image processing algorithm was evaluated against other mixing time estimation methods. DISMT was proven to be a direct and effective representation of pH homogenisation based on a stoichiometric acid-base reaction, and outperformed results, obtained with local pH measurement techniques.

DISMT provided a detailed flow visualisation and highlighted the presence of a toroidal vortex, with distinct vortical cells at each side of the bioreactor, below the free surface at low shaking speed. An axial vortex was observed when the shaken speed was increased above a defined critical value. Colour variations, corresponding to local pH concentrations, provided a description of the movement of a fluid particle in the vicinity of the toroidal vortex structure. It was estimated that the time needed for to rotate around the vortical cell and around the vessel diameter corresponds to 4 shaker revolutions and 1.67 revolutions, respectively.

The mixing results showed a decrease of  $Nt_m$  with  $Fr_{d_o}$ . Slow mixing was observed when feeding of the base occurred in correspondence of the toroidal vortex at low agitation, and high experimental variability was noted up to  $Fr_{d_o}=0.2$ . Faster mixing times were obtained above  $Fr_{d_o}=0.2$ , when a precessional axial vortex was present. The investigation of the effects of feed addition location demonstrated significant  $Nt_m$  improvements can be achieved when insertion was performed close to vessel walls or at locations above the boundary of the toroidal vortical cell. Mixing in AFT configurations was improved when additions were made in correspondence to vessel axis. A mixing time scaling methodology was proposed, based on Weheliye *et al.* (2013), which successfully scaled the mixing times/numbers found in this work with other data available in the literature.

Phase-resolved velocity fields and tangential vorticity were obtained for cylindrical OSRs with a flat and a novel conical bottom design. The PIV measurements showed separate vortical cells present at the sides of the bioreactor at a phase angle  $\varphi = 0^\circ$ . In flat bottom OSRs the toroidal vortices extended from the free surface towards the bottom increasing in size as  $Fr$  is increased. Similar vortical expansion was observed in conical bottom geometry although the toroidal vortex reached the bottom at lower  $Fr$ . The vortices were found to be present at larger

shaker speeds due to the conical bottoms affecting the shape of the vortical cells. Vorticity intensity was found to increase with increasing  $Fr_{d_o}$  and no differences between flat and conical geometries were observed at low  $Fr_{d_o}$  ( $> 0.12$ ) when the toroidal vortex is located close to the free surface. Vorticity of the two vortical cells was only affected by the bottom geometry for speeds sufficiently large to cause full vortex expansion to the bioreactor base. The strain rate tensor, a measure of the local rate of stretching, compression and shear, was calculated from the velocity fields. Highest compression rates were measured at the margins of the toroidal vortex cells. Significant stretching rates were observed on the lower section of the toroidal vortex, in correspondence to the conical bottom tip. Maximum values of shear rates were found in correspondence to the conical tip whilst the lowest rates were measured at the core of the vortical cell. The high shear regions are aligned orthogonally to the bioreactor base and the maximum value shear stress value was  $0.001\text{Nm}^{-1}$ , well below shear rates reported to be detrimental to cell proliferation in the literature for some cell types. The novel conical bottom affected the local flow by diverting the velocity field by an angle which increased with increasing conical bottom height. Solid suspension studies showed that higher vorticity intensity, as measured by PIV, corresponded to an improvement in solid suspension dynamics. In fact, the shaker speed required to suspend microcarriers from the vessel bottom and homogeneously distribute around the volume was found to be lower when a conical bottom was used and the condition  $(h/d_i) < \sqrt{d_o/d_i}$  was present.

The flow and mixing dynamics in OSRs with highly viscous fluids was evaluated by means of DISMT and PLIF. Glycerol solutions at viscosities 2,4 and 14 times that of water were used. It was found that fluids of high viscosity present flow structures different than those observed in water. Above  $\nu = 1.9 \times 10^{-6} \text{ m}^2 \text{ s}^{-1}$  for  $Fr_{d_o}=0.2$ , separated vortical cells were observed at the sides of the bioreactor

rotating in a direction opposite than that observed in water-like viscosity fluids. It was found that in highly viscous fluids a three-dimensional free surface, normally an indication of out-of-phase condition, is present, whilst the flow presents BFT toroidal vortices with completely separated vortical cells. The mixing number of high viscosity fluids was found to be larger than water at conditions  $Fr_{d_o}/Fr_{cr} < 1$ . At such conditions the toroidal vortices acted as ‘caverns’ with segregated mixing zones where the mixing number was measured to be more than twice than that outside the toroidal vortex. The reduction in size of the slow mixing segregated zone was observed to be linear, with the  $\nu = 4.37 \times 10^{-6} \text{ m}^2 \text{ s}^{-1}$  fluid reducing in size at a faster rate than  $\nu = 1.37 \times 10^{-5} \text{ m}^2 \text{ s}^{-1}$  by a factor of 4. pLIF measurements performed on a  $\nu = 1.37 \times 10^{-5} \text{ m}^2 \text{ s}^{-1}$  aqueous glycerol solution provided a clear picture of small scale mixing. Evidence of several toroidal vortices was found. At low  $Fr_{d_o}$  a small vortical cell is observed close to the wall below the surface with a larger one in the bulk of the fluid. Both vortical cells extended in size with increasing  $Fr_{d_o}$  up to  $Fr_{d_o}=0.23$  when the toroidal vortices locate themselves just below the free surface. A further increase of  $Fr_{d_o}$  generated a flow characterised by counter-rotating vortical cells rotating in a direction resulting in a downward stream through the centre of the bioreactor. The study of the elongation of the dye under effect of the vortical structures present in the flow showed quadratic growth for  $Fr_{d_o}=0.18-0.23$ .

### 6.3 Recommendations for future work

The work presented in this thesis has investigated three important features of orbital shaken reactors: flow, mixing and suspension dynamics. By utilising non-dimensional parameters, such as the Froude number,  $Fr$ , the mixing number,  $Nt$ , the critical Froude number ratio,  $Fr/Fr_{cr}$ , it was proved that it is possible to

derive scaling laws applicable to OSRs of different geometry and scale. The literature has in the past few years increased the number of publications on OSRs, although without being able to directly correlate results obtained by different researchers. The scaling methodology for mixing time could be used to achieve this, perhaps including other bioreactor types, such as STRs and WAVE bioreactors, and other scales, namely microtitre plates, which are routinely used in early bioprocess development but are affected by further physical constraints due to the small size, in particular surface tension.

For the bioprocess engineer's benefit a collation of mixing and scale up data from the literature should be made and presented in an organised manner as a software where parameters of small (large) scale can be input and produce recommended parameters for the required large (small) scale.

Volumetric PIV measurements should be performed for three dimensional particle tracking within OSRs, to investigate the interaction between the toroidal vortex and the bulk of the fluid and evaluate the residence time of a specific tracer particle in the slow/fast mixing region and in high shear regions. PIV and LIF experiments are required in orbitally shaken microwell plates geometry to quantify the effect of surface tension and verify the effectiveness of the scaling law at such scales. Further investigation is needed of highly viscous fluids, which have been demonstrated in this work to be characterised by several flow types at different  $Fr$ . An effective scaling law for fluids of high viscosity should be derived, also taking into account the complex viscosity of real high density cell cultures.

Further work on the engineering parameters for microcarrier cultures should be performed, in light of the growing need for three dimensional cultures of stem cells to meet regenerative medicine's therapy requirements. Parallel fluid dynamics and cell culture experiments would verify the scaling law effectiveness and

determine just suspended speed variation for different microcarrier concentrations. Studies can be carried out using a cell line expressing Green Fluorescence Protein (GFP) to be able to quantify the just suspended speed under real process conditions with and without microcarriers. Similarly PIV will allow to fully assess microcarriers suspension which is the result of complex phenomena involving turbulent eddies, forces acting on particles (drag, buoyancy, gravity), wall-particle and particle particle interactions.

# Appendix A

## DISMT experimental procedure

The Dual Indicator System for Mixing Time was adapted from Tissot *et al.* (2010).

The solution was prepared as follows:

- Prepare Thymol Blue indicator in 70% ethanol at 0.92mg/mL ( $\beta$ -indicator)
- Prepare Methyl Red indicator in 70% ethanol at 1.01mg/mL ( $\rho$ -indicator)
- Measure the required volume of distilled water
- Add 0.467mL/cL of  $\beta$ -indicator in the distilled water
- Add 0.426mL/cL of  $\rho$ -indicator in the distilled water

The solution's pH was then measured and 5 $\mu$ L/cL of 0.75M NaOH was added to reach a pH value  $6.5 < \text{pH} < 7.5$ , corresponding to a bright yellow. The prepared solution was poured into the cylindrical vessel fixed on the shaker table.

The solution was acidified with 20 $\mu$ L/cL volume of 0.75M HCl added using an automatic pipette. The shaker was run at a high speed ( 150RPM) for one minute to ensure that the acid was mixed thoroughly through the solution and it's colour a strong red.

The Thymol Blue and Methyl Red pH indicator, NaOH and HCl used were all produced by Fisher Scientific. A stoichiometric amount of 0.75M NaOH (20 $\mu$ L/cL) was added using the syringe pump and microfluidics tubing (IDEX Health and Science). The addition of base was triggered by the encoder, enabling consistency in base feed angular position between experiments. Insertion was nearly instantaneous, lasting around 2 ms (i.e.  $\Delta\varphi < 2^\circ$ ).

# References

- Aloi, L. E. and R. S. Cherry (1996). Cellular response to agitation characterized by energy dissipation at the impeller tip. *Chemical Engineering Science* 51(9), 1523–1529.
- Baldyga, J. and J. R. Bourne (1999). *Turbulent mixing and chemical reactions*. Wiley.
- Bibila, T. A., C. S. Ranucci, K. Glazomitsky, C. Buckland, and J. G. Aunins (1994). Monoclonal antibody process development using medium concentrates. *Biotechnology progress* 10(1), 87–96.
- Borysenko, J. Z. and W. Woods (1979). Density, distribution and mobility of surface anions on a normal/transformed cell pair. *Experimental cell research* 118(2), 215–227.
- Bouremel, Y., M. Yianneskis, and A. Ducci (2009). On the utilisation of vorticity and strain dynamics for improved analysis of stirred processes. *Chemical Engineering Research and Design* 87(4), 377–385.
- Büchs, J. (2001). Introduction to advantages and problems of shaken cultures. *Biochemical Engineering Journal* 7(2), 91–98.
- Büchs, J., S. Lotter, and C. Milbradt (2001). Out-of-phase operating conditions, a hitherto unknown phenomenon in shaking bioreactors. *Biochemical Engineering Journal* 7(2), 135–141.

- Büchs, J., U. Maier, C. Milbradt, and B. Zoels (2000a). Power consumption in shaking flasks on rotary shaking machines: I. power consumption measurement in unbaffled flasks at low liquid viscosity. *Biotechnology and Bioengineering* 68(6), 589–593.
- Büchs, J., U. Maier, C. Milbradt, and B. Zoels (2000b). Power consumption in shaking flasks on rotary shaking machines: II. Nondimensional description of specific power consumption and flow regimes in unbaffled flasks at elevated liquid viscosity. *Biotechnology and Bioengineering* 68(6), 594–601.
- Cabaret, F., S. Bonnot, L. Fradette, and P. A. Tanguy (2007). Mixing time analysis using colorimetric methods and image processing. *Industrial & engineering chemistry research* 46(14), 5032–5042.
- Cherry, R. S. and C. T. Hulle (1992). Cell-death in the thin-films of bursting bubbles. *Biotechnology Progress* 8(1), 11–18.
- Cherry, R. S. and E. T. Papoutsakis (1988). Physical-mechanisms of cell-damage in microcarrier cell-culture bioreactors. *Biotechnology and bioengineering* 32(8), 1001–1014.
- Cronin, D. (1992). An experimental study of the mixing in a proto-fermenter agitated by dual rushton turbines. *Trans. Inst. Chem. Eng., PartC* 72, 35–40.
- Davidson, P. A. (2015). *Turbulence: an introduction for scientists and engineers*. Oxford University Press.
- Delaplace, G., L. Bouvier, A. Moreau, R. Guerin, and J. Leuliet (2004). Determination of mixing time by colourimetric diagnosis application to a new mixing system. *Experiments in fluids* 36(3), 437–443.
- Doulgerakis, Z., M. Yianneskis, and A. Ducci (2009). On the interaction of trailing and macro-instability vortices in a stirred vessel-enhanced energy levels and improved mixing potential. *Chemical Engineering Research and Design* 87(4), 412–420.

- Ducci, A. and W. H. Weheliye (2014). Orbitally shaken bioreactors - viscosity effects on flow characteristics. *AIChE Journal* 60(11), 3951–3968.
- Ducci, A. and M. Yianneskis (2007). Vortex tracking and mixing enhancement in stirred processes. *AIChE journal* 53(2), 305–315.
- Elias, C. B., R. B. Desai, M. S. Patole, J. B. Joshi, and R. A. Mashelkar (1995). Turbulent shear stress effect on mammalian cell culture and measurement using laser doppler anemometer. *Chemical Engineering Science* 50(15), 2431–2440.
- Escudié, R. and A. Liné (2003). Experimental analysis of hydrodynamics in a radially agitated tank. *AIChE Journal* 49(3), 585–603.
- Ferrari, C., F. Balandras, E. Guedon, E. Olmos, I. Chevalot, and A. Marc (2012). Limiting cell aggregation during mesenchymal stem cell expansion on microcarriers. *Biotechnology progress* 28(3), 780–787.
- Frauschuh, S., E. Reichmann, Y. Ibold, P. M. Goetz, M. Sittlinger, and J. Ringe (2007). A microcarrier-based cultivation system for expansion of primary mesenchymal stem cells. *Biotechnology progress* 23(1), 187–193.
- Funke, M., S. Diederichs, F. Kensy, C. Müller, and J. Büchs (2009). The baffled microtiter plate: increased oxygen transfer and improved online monitoring in small scale fermentations. *Biotechnology and bioengineering* 103(6), 1118–1128.
- Gardner, J. and G. Tatterson (1992). Characterization of mixing in shaker table containers. *Biotechnology and bioengineering* 39(7), 794–797.
- Godleski, E. and J. Smith (1962). Power requirements and blend times in the agitation of pseudoplastic fluids. *AIChE Journal* 8(5), 617–620.
- Houcine, I., H. Vivier, E. Plasari, R. David, and J. Villermaux (1996). Planar laser induced fluorescence technique for measurements of concentration fields in continuous stirred tank reactors. *Experiments in Fluids* 22(2), 95–102.

- Hu, Y., Z. Liu, J. Yang, Y. Jin, and Y. Cheng (2010). Study on the reactive mixing process in an unbaffled stirred tank using planar laser-induced fluorescence (plif) technique. *Chemical Engineering Science* 65(15), 4511–4518.
- Ismadi, M.-Z., P. Gupta, A. Fouras, P. Verma, S. Jadhav, J. Bellare, and K. Hourigan (2014). Flow characterization of a spinner flask for induced pluripotent stem cell culture application. *PloS one* 9(10), e106493.
- Kasat, G. R. and A. B. Pandit (2004). Mixing time studies in multiple impeller agitated reactors. *The Canadian Journal of Chemical Engineering* 82(5), 892–904.
- Keane, J. T., D. Ryan, and P. P. Gray (2003). Effect of shear stress on expression of a recombinant protein by chinese hamster ovary cells. *Biotechnology and bioengineering* 81(2), 211–220.
- Kim, H. M. and J. P. Kizito (2009). Stirring free surface flows due to horizontal circulatory oscillation of a partially filled container. *Chemical Engineering Communications* 196(11), 1300–1321.
- King, J. A. and W. M. Miller (2007). Bioreactor development for stem cell expansion and controlled differentiation. *Current opinion in chemical biology* 11(4), 394–398.
- Klockner, W. and J. Buchs (2012). Advances in shaking technologies. *Trends in biotechnology* 30(6), 307–314.
- Klößner, W., S. Tissot, F. Wurm, and J. Büchs (2012). Power input correlation to characterize the hydrodynamics of cylindrical orbitally shaken bioreactors. *Biochemical Engineering Journal* 65, 63–69.
- Kresta, S. M. and P. E. Wood (1993). The flow field produced by a pitched blade turbine: characterization of the turbulence and estimation of the dissipation rate. *Chemical Engineering Science* 48(10), 1761–1774.

- Lara, A. R., E. Galindo, O. T. Ramírez, and L. A. Palomares (2006). Living with heterogeneities in bioreactors. *Molecular biotechnology* 34(3), 355–381.
- Le Coënt, A.-L., A. Rivoire, S. Briancon, and J. Lieto (2005). An original image-processing technique for obtaining the mixing time: The box-counting with erosions method. *Powder technology* 152(1), 62–71.
- Lee, K. and M. Yianneskis (1997). A liquid crystal thermographic technique for the measurement of mixing characteristics in stirred vessels. *Chemical Engineering Research and Design* 75(8), 746–754.
- Lehwald, A., G. Janiga, D. Thévenin, and K. Zähringer (2012). Simultaneous investigation of macro-and micro-mixing in a static mixer. *Chemical engineering science* 79, 8–18.
- Li, D., J. Zhou, F. Chowdhury, J. Cheng, N. Wang, and F. Wang (2011). Role of mechanical factors in fate decisions of stem cells. *Regenerative medicine* 6(2), 229–240.
- Li, J.-K. and A. E. Humphrey (1991). Use of fluorometry for monitoring and control of a bioreactor. *Biotechnology and bioengineering* 37(11), 1043–1049.
- Ludwig, A., J. Tomeczkowski, and G. Kretzmer (1992). Influence of shear stress on adherent mammalian cells during division. *Biotechnology letters* 14(10), 881–884.
- Maier, U. and J. Büchs (2001). Characterisation of the gas–liquid mass transfer in shaking bioreactors. *Biochemical Engineering Journal* 7(2), 99–106.
- Mancilla, E., C. Palacios-Morales, M. Córdova-Aguilar, M. Trujillo-Roldán, G. Ascanio, and R. Zenit (2015). A hydrodynamic description of the flow behavior in shaken flasks. *Biochemical Engineering Journal* 99, 61–66.
- Margaritis, A. and J. D. Sheppard (1981). Mixing time and oxygen transfer character-

- istics of double draft tube airlift fermentor. *Biotechnology and Bioengineering* 23(9), 2117–2135.
- Mehmood, N., E. Olmos, P. Marchal, J.-L. Goergen, and S. Delaunay (2010). Relation between pristinamycins production by streptomyces pristinaespiralis, power dissipation and volumetric gas–liquid mass transfer coefficient, *Process Biochemistry* 45(11), 1779–1786.
- Melton, L. A., C. Lipp, R. Spradling, and K. Paulson (2002). Dismt-determination of mixing time through color changes. *Chemical Engineering Communications* 189(3), 322–338.
- Meunier, P. and E. Villermaux (2003). How vortices mix. *Journal of Fluid Mechanics* 476, 213–222.
- Micheletti, M., L. Nikiforaki, K. C. Lee, and M. Yianneskis (2003). Particle concentration and mixing characteristics of moderate-to-dense solid-liquid suspensions. *Industrial & engineering chemistry research* 42(24), 6236–6249.
- Monteil, D. T., G. Tontodonati, S. Ghimire, L. Baldi, D. L. Hacker, C. A. Bürki, and F. M. Wurm (2013). Disposable 600-ml orbitally shaken bioreactor for mammalian cell cultivation in suspension. *Biochemical Engineering Journal* 76, 6–12.
- Muller, N., P. Girard, D. L. Hacker, M. Jordan, and F. M. Wurm (2005). Orbital shaker technology for the cultivation of mammalian cells in suspension. *Biotechnology and bioengineering* 89(4), 400–406.
- Nienow, A. W. (2006). Reactor engineering in large scale animal cell culture. *Cytotechnology* 50(1-3), 9–33.
- Nienow, A. W., C. Langheinrich, N. C. Stevenson, A. N. Emery, T. M. Clayton, and N. K. Slater (1996). Homogenisation and oxygen transfer rates in large agitated

- and sparged animal cell bioreactors: Some implications for growth and production. *Cytotechnology* 22(1-3), 87–94.
- Nienow, A. W., Q. A. Rafiq, K. Coopman, and C. J. Hewitt (2014). A potentially scalable method for the harvesting of hmscs from microcarriers. *Biochemical Engineering Journal* 85, 79–88.
- Nienow, A. W., W. H. Scott, C. J. Hewitt, C. R. Thomas, G. Lewis, A. Amanullah, R. Kiss, and S. J. Meier (2013). Scale-down studies for assessing the impact of different stress parameters on growth and product quality during animal cell culture. *Chemical Engineering Research and Design* 91(11), 2265–2274.
- Olmos, E., K. Loubiere, C. Martin, G. Delaplace, and A. Marc (2015). Critical agitation for microcarrier suspension in orbital shaken bioreactors: Experimental study and dimensional analysis. *Chemical Engineering Science* 122, 545–554.
- Ozturk, S. S. (1996). Engineering challenges in high density cell culture systems. *Cytotechnology* 22(1-3), 3–16.
- Pavlou, A. K. and J. M. Reichert (2004). Recombinant protein therapeutic success rates, market trends and values to 2010. *Nature biotechnology* 22(12), 15131519.
- Pieralisi, I., G. Rodriguez, M. Micheletti, A. Paglianti, and A. Ducci (2015). Microcarriers' suspension and flow dynamics in orbitally shaken bioreactors. *Chemical Engineering Research and Design*.
- Reclari, M., M. Dreyer, S. Tissot, D. Obreschkow, F. M. Wurm, and M. Farhat (2014). Surface wave dynamics in orbital shaken cylindrical containers. *Physics of Fluids (1994-present)* 26(5), 052104.
- Reichert, J. M., C. J. Rosensweig, L. B. Faden, and M. C. Dewitz (2005). Monoclonal antibody successes in the clinic. *Nature biotechnology* 23(9), 1073–1078.
- Rodriguez, G., W. Weheliye, T. Anderlei, M. Micheletti, M. Yianneskis, and A. Ducci

- (2013). Mixing time and kinetic energy measurements in a shaken cylindrical bioreactor. *Chemical Engineering Research and Design* 91(11), 2084–2097.
- Sargent, C. Y., G. Y. Berguig, M. A. Kinney, L. A. Hiatt, R. L. Carpenedo, R. E. Berson, and T. C. McDevitt (2010). Hydrodynamic modulation of embryonic stem cell differentiation by rotary orbital suspension culture. *Biotechnology and bioengineering* 105(3), 611–626.
- Sart, S., Y.-J. Schneider, and S. N. Agathos (2009). Ear mesenchymal stem cells: an efficient adult multipotent cell population fit for rapid and scalable expansion. *Journal of biotechnology* 139(4), 291–299.
- Schröder, M., K. Matischak, and P. Friedl (2004). Serum- and protein-free media formulations for the chinese hamster ovary cell line dukxb11. *Journal of biotechnology* 108(3), 279–292.
- Serrato, J. A., L. A. Palomares, A. Meneses-Acosta, and O. T. Ramírez (2004). Heterogeneous conditions in dissolved oxygen affect n-glycosylation but not productivity of a monoclonal antibody in hybridoma cultures. *Biotechnology and bioengineering* 88(2), 176–188.
- Simaria, A. S., S. Hassan, H. Varadaraju, J. Rowley, K. Warren, P. Vanek, and S. S. Farid (2014). Allogeneic cell therapy bioprocess economics and optimization: Single-use cell expansion technologies. *Biotechnology and bioengineering* 111(1), 69–83.
- Siva, S., A. Zhang, E. Koepf, L. Conley, D. Cecchini, Y.-M. Huang, R. Kshirsagar, and T. Ryll (2015). Leveraging high-throughput technology to accelerate the time to clinic: A case study of a mab. *Engineering in Life Sciences* 16(2), 143–151.
- Stolberg, S. and K. E. McCloskey (2009). Can shear stress direct stem cell fate? *Biotechnology progress* 25(1), 10–19.
- Storm, M. P., C. B. Orchard, H. K. Bone, J. B. Chaudhuri, and M. J. Welham (2010).

- Three-dimensional culture systems for the expansion of pluripotent embryonic stem cells. *Biotechnology and bioengineering* 107(4), 683–695.
- Tan, R.-K., W. Eberhard, and J. Büchs (2011). Measurement and characterization of mixing time in shake flasks. *Chemical engineering science* 66(3), 440–447.
- Tissot, S., M. Farhat, D. L. Hacker, T. Anderlei, M. Kühner, C. Comninellis, and F. Wurm (2010). Determination of a scale-up factor from mixing time studies in orbitally shaken bioreactors. *Biochemical Engineering Journal* 52(2), 181–186.
- Toh, Y.-C. and J. Voldman (2011). Fluid shear stress primes mouse embryonic stem cells for differentiation in a self-renewing environment via heparan sulfate proteoglycans transduction. *The FASEB Journal* 25(4), 1208–1217.
- Walsh, G. (2014). Biopharmaceutical benchmarks 2014. *Nature biotechnology* 32(10), 992–1000.
- Weheliye, W., M. Yianneskis, and A. Ducci (2013). On the fluid dynamics of shaken bioreactors, flow characterization and transition. *AIChE Journal* 59(1), 334–344.
- Weheliye, W. H. (2013). *Mixing, Velocity and Turbulence Characteristics of Shaken Bioreactors*. Ph. D. thesis, UCL (University College London).
- Wurm, F. M. (2004). Production of recombinant protein therapeutics in cultivated mammalian cells. *Nature biotechnology* 22(11), 1393–1398.
- Yianneskis, M., Z. Popiolek, and J. Whitelaw (1987). An experimental study of the steady and unsteady flow characteristics of stirred reactors. *Journal of Fluid Mechanics* 175, 537–555.
- Zhang, H., S. R. Lamping, S. C. Pickering, G. J. Lye, and P. A. Shamlou (2008). Engineering characterisation of a single well from 24-well and 96-well microtitre plates. *Biochemical Engineering Journal* 40(1), 138–149.

Zhang, J. (2010). Mammalian cell culture for biopharmaceutical production. In *Manual of Industrial Microbiology and Biotechnology, Third Edition*, pp. 157–178. American Society of Microbiology.